# Development of a Methanol to Hydrocarbons Process over Zeolite Coatings in a Microstructured Reactor

by

**Guannan Hu**

A thesis submitted in fulfilment of the requirements for the degree of Doctor of Philosophy

University of Warwick, School of Engineering

November 2017

# Contents

**List of Tables** ..... **V**

**List of Figures** ..... **VII**

**Acknowledgement** ..... **XIV**

**Declaration** ..... **XV**

**Abstract** ..... **XVI**

**Abbreviations** ..... **XVIII**

**Chapter 1 Introduction** ..... **1**

**Chapter 2 Literature review** ..... **5**

2.1 Zeolite catalysts ..... 5

2.1.1 Porous structure ..... 5

2.1.2 Acidity ..... 7

2.2 Reaction mechanism ..... 10

2.2.1. Oxonium ylide mechanism ..... 10

2.2.2 Carbene mechanism ..... 11

2.2.3 Hydrocarbon pool mechanism ..... 11

2.2.4 Kinetic model ..... 14

2.3 Synthesis of ZSM-5 coatings on structured substrates ..... 16

2.3.1 Synthesis of microporous zeolites ..... 17

2.3.2 Ion-exchange ..... 21

2.3.3 Hierarchical ZSM-5 structure ..... 22

2.3.4 Catalyst stability ..... 24

2.4 MTH process ..... 27

2.4.1. Methanol-to-gasoline (MTG) process ..... 28

2.4.2 Methanol to Olefins (MTO) process ..... 30

2.5 Numerical modelling of microstructured reactors ..... 32

2.5.1 Two dimensional models ..... 34
2.5.2 Three dimensional models ..... 35
**Chapter 3 Experimental ..... 37**
3.1 Catalyst synthesis ..... 37
3.1.1 Substrate modification ..... 37
3.1.2 Hydrothermal synthesis ..... 38
3.1.3 Alkaline treatment ..... 39
3.1.3 Calcium ion-exchange ..... 40
3.2 Catalyst characterisation ..... 40
3.2.1 X-ray Diffraction (XRD) ..... 40
3.2.2 Scanning Electron Microscopy (SEM) ..... 40
3.2.3 Nitrogen adsorption-desorption isotherms ..... 41
3.2.4 Inductively coupled plasma (ICP) ..... 42
3.2.5 Pyridine Temperature programmed desorption (TPD) ..... 42
3.3 Catalytic activity measurements ..... 43
3.4 Temperature programmed oxidation and catalyst regeneration ..... 45
**Chapter 4 Synthesis and catalytic activity of microporous ZSM-5 catalyst and its coating ..... 46**
4.1 Introduction ..... 46
4.2 ZSM-5 powder catalyst ..... 47
4.2.1 Optimisation of synthesis conditions ..... 47
4.2.3 Catalytic performance ..... 58
4.3 ZSM-5 coating catalyst ..... 69
4.3.1 Optimisation of synthesis conditions ..... 69
4.3.2. Catalytic performance ..... 76
4.4 Conclusions ..... 77

**Chapter 5 Post-synthesis modification of ZSM-5 catalysts ..... 79**

5.1 Introduction ..... 79

5.2 Calcium ion exchange ..... 80

5.2.1 Characterization ..... 80

5.2.2 Catalytic performance ..... 82

5.3 Desilication ..... 86

5.3.1 ZSM-5 powder ..... 87

5.3.2 Micro-mesoporous ZSM-5 coating ..... 98

5.4 Conclusions ..... 103

**Chapter 6 Modelling of heat transfer in a microstructured reactor/ heat-exchanger ..... 105**

6.1 Introduction ..... 105

6.2 2D modelling ..... 106

6.2.1 Reactor design ..... 106

6.2.3 Heat transfer modelling ..... 113

6.2.4 Parametric study ..... 121

6.3 3D modelling ..... 128

6.3.1 Geometry and physics ..... 128

6.3.2 Parametric study ..... 129

6.3.3 Optimised model ..... 132

6.3.4 Comparison to 2D modelling ..... 134

6.4 Pilot unit ..... 135

6.5 Conclusions ..... 136

**Chapter 7 Conclusions and outlook ..... 138**

7.1 Conclusions ..... 138

7.2 Outlook ..... 141

**References**.....**144**

**Appendices**.....**164**

# List of Tables

**Table 2.1**. Properties of MTG gasoline vs. US conventional refinery gasoline [130]..... 29

**Table 3.1**. Stainless steel substrates used in this study ..... 38

**Table 3.2**. Synthesis conditions..... 39

**Table 4.1**. Synthesis parameters of ZSM-5 samples..... 48

**Table 4.2**. Textural properties of ZSM-5 samples..... 53

**Table 4.3**. Pyridine-TPD for different type of peaks for ZSM-5 with different Si/Al ratios..... 55

**Table 4.4**. Calculated values of the rate constant, deactivation coefficient and conversion capacity for ZSM-5 catalysts ($W_0$=0.1 g, $\tau$0=110 g·h·mol$^{-1}$) ..... 66

**Table 4.5**. Parameters for Thiele modulus calculation..... 75

**Table 4.6**. Initial conversion and selectivity over ZSM-5 catalyst in the MTH reaction (T=370 $^{o}$C, WHSV of methanol=7.0 h$^{-1}$, P=1 bar) ..... 76

**Table 5.1.** Pyridine-TPD for different type of peaks for ZSM-5 with different Si/Al ratios..... 82

**Table 5.2** Calculated values of the rate constant, deactivation coefficient and conversion capacity for ZSM-5 catalysts ($W_0$=0.1 g, $\tau$0=7.7 g·h·mol$^{-1}$) ..... 84

**Table 5.3**. Textual properties of blank and Ca-ZSM-5 samples..... 85

**Table 5.4**. Textural properties of blank and desilicated ZSM-5 samples 87

**Table 5.5**. Calculated values of the rate constant, deactivation coefficient and turnover number (TON) for $C_{8-11}$ fraction of ZSM-5 catalysts ($W_0$=0.1 g, $\tau$0=1.15 g·h·mol$^{-1}$)..... 94

**Table 5.6**. Summary of selectivity over ZSM-5 catalyst in different reactor (T=370 $^{o}$C, WHSV=28 h$^{-1}$, P=4 bar)..... 102

**Table 6.1**. Properties of gas phases species at 653 K..... 109

**Table 6.2**. Reactor design specifications and fluid properties.....110

**Table 6.3**. Computational domains and corresponding physical models .....117

**Table 6.4.** Overview of design unit (half channel) in micro-reactor/heat-exchanger .....127

**Table 6.5**. Studied parameters and range in 3D modelling.....129

**Table 6.6**. Summary of pilot scale of MRHE.....136

# List of Figures

**Figure 2.1**. a) Assembly unit by five-rings. b) T-T linkage scheme of a pentasil chain [7,10] ..... 6

**Figure 2.2**. Illustration of channel system in H-ZSM-5 [255] ..... 6

**Figure 2.3**. The activity of H-ZSM-5 plotted against the tetrahedral Al NMR signal (Activity value of 1 corresponds to the activity of amorphous silica-alumina catalyst) [24] ..... 9

**Figure 2.4**. Variation in the Gibbs free energy (ΔG) at an increase in the molecular aggregate radius in the nucleation process at the different solution supersaturation degrees α1 < α2 < α3. As the supersaturation increases, the critical nucleus radius (r*) decreases [67]. ..... 17

**Figure 2.5**. SEM images of samples obtained after 72 (left), 96 (middle) and 120 h (right) [75] ..... 20

**Figure 2.6**. Flow diagram of MTG process operated in New Zealand [256] ..... 29

**Figure 2.7**. INEOS MTO fluidized bed process over SAPO-34 combined with UOP/Total OCP [6] ..... 30

**Figure 2.8**. Lurgi MTP process: Adiabatic dehydration reactor for DME synthesis and parallel adiabatic reactors with interstage feed (quench) addition and recycle of process condensate and $C_2$ and $C_4$+ olefins [6]. 31

**Figure 3.1**. Initial stainless steel plate (left). Sand blasted plate (middle). Stainless steel microchannel plate (right) ..... 38

**Figure 3.2**. Schematic view of reactor set-up (Red line: Hot line preheated at 373 K. Blue line: Cold line.) ..... 43

**Figure 3.3**. a) The fixe-bed reactor for ZSM-5 powder catalyst, b) The tube reactor loaded with two plates coated with ZSM-5 catalyst ..... 43

**Figure 4.1**. Si conversion in a synthesis mixture with Si/Al=20 as a function of synthesis time (T=140 $^{o}$C) ..... 48

**Figure 4.2**. XRD patterns of the zeolite powder samples ZSM-20-0.50 (24 h), ZSM-20-0.84 (48 h), ZSM-20-1.04 (72 h), ZSM-20-1.14 (96 h), ZSM-20-1.20 (120 h) ..... 49

**Figure 4.3**. The thickness of the zeolite coatings and crystal size of ZSM-5 sample with Si/Al ratio of 20, $H_2O$/Si ratio of 30 and different synthesis time ..... 50

**Figure 4.4**. SEM microphotographs of the ZSM-5 samples a) ZSM-20-0.50, b) ZSM-20-1.20 ..... 50

**Figure 4.5**. Average value and distribution of crystal size of ZSM-5 powder samples with different Si/Al ratio ..... 51

**Figure 4.6**. SEM image of ZSM-5 powder samples: a) ZSM-20-0.84, b) ZSM-30-1.10, c) ZSM-40-1.70, d) ZSM-50-2.40, e) ZSM-60-2.60 ..... 52

**Figure 4.7**. Isotherms of nitrogen adsorption and desorption of ZSM-5 samples a) ZSM-20-0.8, b) ZSM-30-1.1, c) ZSM-40-1.7, d) ZSM-50-2.4, e) ZSM-60-2.6 ..... 53

**Figure 4.8**. Pyridine-TPD thermograms obtained at 125-550 $^oC$ over ZSM-5 catalysts with the increasing Si/Al ratio ..... 54

**Figure 4.9**. a) Desorption profiles at different starting temperature over the ZSM-5 catalyst with Si/Al ratio of 20. b) Differential curves of pyridine-TPD thermograms between two adjacement starting temperatures in **Figure 4.8** over the samples with the increasing Si/Al ratio. ..... 55

**Figure 4.10**. SEM images of samples a) ZSM-20-0.40, b) ZSM-20-0.84, c) ZSM-20-1.07 ..... 57

**Figure 4.11**. Crystal size distribution of powder samples ZSM-20-0.40, ZSM-20-0.84 and ZSM-20-1.07 ..... 58

**Figure 4.12**. Methanol conversion over ZSM-5 samples with different Si/Al ratios. (T=370 $^oC$, P=0.4 bar, WHSV=1.5 $h^{-1}$) ..... 59

**Figure 4.13**. Hydrocarbons selectivity towards a) $C_{8-11}$, b) $C_{6-10A}$ plot in MTH reaction over ZSM-5 samples and c) weighing function with different Si/Al ratios and crystal sizes (T=370 $^oC$, P=0.4 bar, WHSV=1.5 $h^{-1}$) ..... 61

**Figure 4.14**. Colour contour displaying selectivity towards four hydrocarbon fractions and the weighing function of selectivity in MTH reaction at different WHSV and pressure (T=370 $^{o}$C) ..... 62

**Figure 4.15**. Selectivity distribution at different residence time in ZSM-5 catalyst in MTH reaction ..... 64

**Figure 4.16**. Comparison of the calculated methanol conversion (solid line) with measured methanol conversion (open symbols) with time on stream over ZSM-5 catalysts with different Si/Al ratios at 370 $^{o}$C and 4 bar. ..... 66

**Figure 4.17**. Methanol conversion and product selectivities in MTH reaction over ZSM-50-2.4 (T=370 $^{o}$C, WHSV=14 $h^{-1}$, P=3.0 bar) ..... 67

**Figure 4.18**. a) TPO profiles of deactivated zeolite samples after different time on stream, b) $CO_2$ release from deactivated zeolites at different temperature range during TPO ..... 68

**Figure 4.19**. XRD patterns of coating samples with different pretreatment and reference patterns of ZSM-5 catalyst ..... 69

**Figure 4.20**. XRD patterns of zeolite coating on substrates obtained in different synthesis time (*: reflection of stainless steel)..... 71

**Figure 4.21**. SEM images of ZSM-5 coating on microchannel with cross-section ..... 72

**Figure 4.22**. a) SEM image of the cross-section of 5-layer coating and b) coating thickness as a number of synthesis cycles..... 74

**Figure 5.1**. XRD patterns of parent and Ca-ZSM-5 samples with different Ca ion-exchange ratio..... 80

**Figure 5.2**. Differential curves of pyridine-TPD thermograms between 125-175, 175-225, 225-550 $^{o}$C starting temperatures over the samples with the increasing Ca ion-exchange ratio..... 81

**Figure 5.3**. Methanol conversion over Ca-ZSM-5 samples with different Ca exchange ratios (T=370 $^{o}$C, P=1 bar, WHSV=3 $h^{-1}$)..... 83

**Figure 5.4**. Lifetime of Ca-ZSM-5 with different Ca content ..... 83

**Figure 5.5**. Selectivity of hydrocarbons over Ca-ZSM-5 with different exchange ratio ..... 84

**Figure 5.6**. XRD patterns of microporous and desilicated H-ZSM-5 samples with mesoporous structure and ZSM-5 reference patterns ..... 88

**Figure 5.7**. SEM images of a) Micro(0.5)-2.4 and desilicated samples, b) Meso(4.1)-2.4, c) Meso(4.4)-2.4, d) Meso(5.0)-2.4 ..... 88

**Figure 5.8**. Nitrogen adsorption-desorption isotherms of micro-mesoporous ZSM-5 catalysts..... 89

**Figure 5.9**. BJH pore size distribution curves of the blank and desilicated ZSM-5 samples..... 90

**Figure 5.10**. Pyridine-TPD profiles of parent and desilicated ZSM-5 powder and coating catalysts ..... 92

**Figure 5.11**. Conversion of methanol over the blank and desilicated ZSM-5 samples along time on stream in MTH reaction (T=370 $^{o}$C K, WHSV=20 $h^{-1}$, P=4 bar)..... 94

**Figure 5.12**. Selectivity of hydrocarbons over blank and desilicated ZSM-5 samples obtained in MTH reaction at conversion of 50% ..... 96

**Figure 5.13**. Product yield of $C_{8-11}$ fraction over blank and desilicated samples (T=370 $^{o}$C, WHSV=20 $h^{-1}$, P=2 bar)..... 97

**Figure 5.14**. SEM images of coating sample MesoC-10 on its surface .. 98

**Figure 5.15**. Conversion of methanol over blank and modified coating samples (T=370 $^{o}$C, WHSV=28 $h^{-1}$, P=4 bar)..... 99

**Figure 5.16**. Product distribution of a) $C_{1-4}$, b) $C_{5-7}$, c) $C_{8-11}$ and d) $C_{6-10A}$ in MTH reaction over the MesoC-30 coating under different conditions (T= 370 $^{o}$C) e) the values of the design parameter (Eq. 5.3)..... 101

**Figure 5.17**. Methanol conversion over micro and micro-mesoporous pellets (Solid symbols) and coatings (Open symbols) in MTH reaction (T=370 $^{o}$C, WHSV=28 $h^{-1}$, P=4 bar)..... 102

**Figure 6.1**. An example of concentration profiles for methanol and reaction products as a function of reactor length. (T=653 K, $F_{v,M}$=2.66*$10^{-9}$ $m^3$ $s^{-1}$, P=1 bar) ..... 108

**Figure 6.2.** Schematic view of sandwich microchannel reactor/heat-exchanger geometry. Plate dimensions (w×h) are 14 × 8 $mm^2$, with 14 microchannels with a diameter of 0.5 mm and a length of 200 mm ..... 110

**Figure 6.3**. Different meshing levels: a) Coarse, b) Normal, c) Fine..... 112

**Figure 6.4**. Effect of coolant temperature on reactant temperature in different cooling mode a) Co-current, b) Counter-current ($v_c$=1.0 m $s^{-1}$, $D_c$=0.5 mm, W=3.5 mm, TH=0.01 mm ..... 114

**Figure 6.5**. Optimised temperature profiles in a single reactor configuration with co-current and counter-current coolant configuration. ($v_c$=1.0 m $s^{-1}$, $D_c$=0.5 mm, W=3.5 mm, TH=0.01 mm)..... 115

**Figure 6.6**. a) Temperature profiles plotted with different length of the first reactor (b) The effect of the length of the first reactor on temperature non-uniformity in the coating ($v_c$=1.0 m·$s^{-1}$, $D_c$=0.5 mm, W=3.5 mm, Th=0.01 mm)..... 116

**Figure 6.7a**. Schematic view of boundary conditions in laminar flow domains. The left image part represents the first reactor, the right part represents the second reactor. The images are not on scale. Domains (from top to bottom): Semi cylindrical reaction channel (R1, R2), catalytic film (F1, F2), Metal wall (M1, M2), Semi cylindrical cooling channel (C1, C2) ..... 118

**Figure 6.8**. Schematic of thermal resistance in Y axis..... 121

**Figure 6.9**. Reactant temperature profiles in reactors with different coolant flow mode in a) First reactor. b) Second reactor ($v_c$=1.0 m·$s^{-1}$, $D_c$=0.5 mm, W=3.5 mm, TH=0.01 mm) ..... 122

**Figure 6.10** a) Temperature profiles in reaction channel in the reactor with different wall thickness. ($v_c$=1.0 m·$s^{-1}$, $D_c$=0.5 mm, TH=0.01 mm). b) Non-uniformity as a function of W in the first reactor ..... 123

**Figure 6.11**. a) Temperature profiles in reaction channel with catalyst film of different thickness. (W=3.5 mm, $D_c$=0.5 mm, $v_c$=1.0 m·s$^{-1}$, $T_{C1,\ in}$ = 635 K, $T_{C2,\ in}$=652 K). b) Non-uniformity as a function of C in the first reactor .....124

**Figure 6.12.** a) Temperature profiles in coating domain when coolant at different temperature. (W=3.5 mm, $D_c$=0.5 mm, $v_c$=1.0 m·s$^{-1}$, TH =0.01 mm).....125

**Figure 6.13.** a) Temperature profiles in first reactor when coolant at different velocity. (W=1.0 mm, $D_c$=0.5 mm, TH =0.01 mm, $T_{C1,\ in}$ = 635 K, $T_{C2,\ in}$=652 K). b) Non-uniformity as a function of $v_c$ in the first reactor..125

**Figure 6.14.** Temperature profiles in coating domain with optimise parameters. (W=3.5 mm, $D_c$=0.5 mm, $v_c$=4.0 m·s$^{-1}$, TH =0.01 mm, $T_{C1,\ in}$ = 635 K, $T_{C2,\ in}$=652 K) .....126

**Figure 6.15**. Geometry of 3D modelling with design unit and parameters .....128

**Figure 6.16**. Mesh of 3D geometry.....129

**Figure 6.17**. Temperature distribution profile in the first reactor with different diameters of cooling channel (W=3.5 mm, $v_c$=4.0 m·s$^{-1}$, TH =0.01 mm).....130

**Figure 6.18.** 2D Sketch of geometries with one (left), two (middle) and three (right) cooling channels.....131

**Figure 6.19**. Temperature profiles in the coating with one, two and three cooling channels obtained with the 3D model (Dc=0.3 mm, W=3.5 mm, $v_c$=4.0 m·s$^{-1}$, TH =0.01 mm).....131

**Figure 6.20**. Temperature distribution in first reactor with optimised conditions with temperature contour in YZ cross-section obtained with the 3D model (v=0.0271m·s$^{-1}$, Dc=0.8 mm, W=3.5 mm, TH=0.01 mm).....132

**Figure 6.21**. Temperature profiles of coating, wall and coolant domains with optimised parameters in the first reactor obtained with the 3D model (v=0.0271m·s$^{-1}$, Dc=0.8 mm, W=3.5 mm, TH=0.01 mm).....133

**Figure 6.22**. Sketch of heat transfer path from different locations of heat source ..... 134

# Acknowledgement

First of all, I want to pay my deepest gratitude to my supervisor, Prof Evgeny Rebrov, who offer me this valuable opportunity to do my PhD project in his group. Without his consistent support, guidance, assistance and encouragement, I would not get this far for a doctoral degree. Thank you very much for all the patient demonstration and inspiring discussion through the four years of my journey.

I would like to thank Prof Andre Van Veen for his valuable suggestion on my experiments and my PhD study. He always looks after everyone in Chemical Engineering Group and is really a mentor who is generous on sharing inspiring ideas. I would also thank Dr Volkan Degirmenci, Dr Nikolay Cherkasov, and Dr Javier Fernandez Garcia for their guidance and help in respective period in during my PhD. I am very thankful to all my colleagues in Chemical Engineering Groups, Dr Yawen Liu, Ryan Oozeerally, Dongwei Du, Dr Changdong Li and Dr Maoshuai Li who are very dear friends to me.

I also acknowledge the financial support provided by School of Engineering at the University of Warwick and to all the supports from BIOGO committees, especially from Jin in Teer Coating Ltd., Fraunhofer ICT-IMM and C.E. Ortega Rojas from Technische University of Eindhoven.

At last, but not the least, I would like to thank my parents who have been remotely encouraging me to become the person I am today. Finally, special thanks to my girlfriend Linwei Gan who step into my life at the end of my PhD. Your encouragement and comfort have been the most precious accompany in my most difficult time.

## Declaration

This thesis is submitted to the University of Warwick in support of my application for the degree of Doctor of Philosophy. It has been composed by myself and has not been submitted in any previous application for any degree.

# Abstract

In this work, the hydrothermal synthesis of ZSM-5 and its coating with controllable crystal size and Si/Al ratio has been performed. The obtained catalysts have been studied in the methanol to hydrocarbon (MTH) reaction. This reaction is the last step in an integrated fuel processor for the conversion of bio resources to liquid fuels. The development of ZSM-5 coatings has been supported by advanced characterization and testing of catalysts for the determination of property/performance relationships. An optimal synthesis time of 72 h was found to provide the highest crystallinity of ZSM-5 coatings. The larger crystal size of ZSM-5 coatings leads to a higher selectivity towards gasoline ($C_{8-11}$) hydrocarbons. The selectivity towards the gasoline fraction over ZSM-5 coatings with a thickness of 14 µm was similar to that of an industrial ZSM-5 catalyst, however the yield of the undesirable aromatics by-products was reduced by half due to shorter diffusion pathways in thin catalyst layers.

In an attempt to improve the yield of the $C_{8-11}$ hydrocarbons, two post-synthesis modifications have been performed: Ca ion-exchange and desilication by alkaline treatment. The maximum gasoline selectivity over Ca-H-ZSM-5 was observed at a Ca/H ratio of 0.1 while the longest lifetime in the reaction was observed at the ratio of 0.2. Mesoporosity has been introduced into microporous ZSM-5 catalysts. The obtained meso-microporous ZSM-5 coating show 3 times lifetime and 2.7 times selectivity towards $C_{8-11}$ hydrocarbon fraction than microporous coating in the MTH reaction.

Lumped kinetics of MTH reaction over H-ZSM-5 were used to design a microstructured reactor/heat-exchanger (MRHE) with reaction channels coated with the ZSM-5 catalyst. 2D and 3D convection and conduction heat transfer models coupled with the MTH reaction kinetics were employed to investigate temperature distribution in the MRHE. The effect of the dimension of the microreactor/ heat-exchanger and flow condition on the temperature field has been studied. The 2D model under-predicts the

magnitude of temperature gradient. The optimised reactor configuration shows a temperature gradient of 21 K in the reaction channels.

# Abbreviations

| | |
|---|---|
| $A_{cat}$ | Area of cross section in catalyst coating, $m^2$ |
| Cp | Heat capacity, $J \cdot mol^{-1} \cdot K^{-1}$ |
| D | Diameter of channel, mm |
| $D_m$ | Molecular diffusivity, $m^2\ s^{-1}$ |
| $D_{eff}$ | Effective diffusivity, |
| $FM_c$ | Flow mode of coolant |
| $F_v$ | Volumetric flow rate of reactant, $m^3 \cdot s^{-1}$ |
| $\Delta_r H_1$ | Reaction enthalpy of methanol dehydration, $J \cdot mol^{-1}$ |
| $\Delta_r H_2$ | Reaction enthalpy of octene formation, $J \cdot mol^{-1}$ |
| h | Heat convection coefficient, $J \cdot m^{-2} \cdot K^{-1}$ |
| k | Thermal conductivity, $J \cdot m^{-1} \cdot K^{-1}$ |
| $k_1$ | Reaction rate constant of methanol dehydration , $s^{-1}$ |
| $k_{-1}$ | Reaction rate constant of methanol formation, $s^{-1}$ |
| $k_2$ | Reaction rate constant of octene formation, $mol^{-0.5} \cdot m^{-1.5} \cdot s^{-1}$ |
| L | Reactor length, m |
| $F_m$ | Mass flow rate, $kg \cdot s^{-1}$ |
| N | Total number of positions taken in the optimisation |
| Nu | Nusselt number |
| $P_{out}$ | Pressure at channel outlet, Pa |
| q'' | Heat flux, $W \cdot m^{-2}$ |
| R | Thermal resistance, $K \cdot J^{-1}$ |
| $R_1$ | Reaction rate of methanol dehydration, $mol \cdot s^{-1} \cdot m^{-3}$ |
| $R_2$ | Reaction rate of octene formation, $mol \cdot s^{-1} \cdot m^{-3}$ |
| Re | Reynolds number |
| t | Retention time of reactant in channel, s |
| $\bar{T}$ | Average temperature in reactant channel, K |
| $T_j$ | Temperature at position j along the axial reactor coordinate, K |
| $T_{C,\ in}$ | Coolant inlet temperature, K |
| $V_{cat}$ | Volume of catalyst film, $m^3$ |
| $v_{,in}$ | Flow inlet velocity, $m \cdot s^{-1}$ |
| W | Thickness of wall between reaction and cooling channel, mm |
| TH | Zeolite coating (film) thickness, mm |

*Subscripts*

| | |
|---|---|
| r | Reaction channel |
| c | Cooling channel |
| R1 | Reaction channel in the first reactor |
| R2 | Reaction channel in the second reactor |
| C1 | Cooling channel in the first reactor |

| | |
|---|---|
| C2 | Cooling channel in the second reactor |

*Greek letters*

| | |
|---|---|
| α | Gas-solid heat transfer coefficient, $W \cdot m^{-2} \cdot K^{-1}$ |
| ρ | Density, $kg \cdot m^{-3}$ |
| μ | Dynamic viscosity, Pa·s |
| Φ | Thiele modulus |

# Chapter 1
# Introduction

Raising concerns for the environment and diminishing oil reserves since the first global energy crisis in the early 1970s drew much attention on the necessity of the alternatives to fuels derived from oil. Due to increasing demand, all forms of energy supply should be taken into account in not so recent future, including solar, wind, biomass, etc. [1]. Future sustainable and low-carbon energy and chemistry largely depend on the development of new innovative solutions to enable an effective and direct use of renewable energy for the conversion of small molecules such as methanol to liquid fuels.

As one of the main alternative energy carriers, methanol is a building block in the chemical industry. Methanol is currently produced from fossil-based (natural gas and coal) syngas [2] but it can also be produced from various other routes (**Scheme 1.1**). The partial oxidation of methane to methanol has always been problematic in research for many years because oxidation products (methanol, formaldehyde and formic acid) are more reactive in oxidation than methane itself [2]. Instead, methanol can be produced from wind or solar powder via formation of hydrogen from electrolysis of water followed methanol synthesis by hydrogenation of $CO_2$ [3]. Thus the chemical energy of hydrogen can be stored in methanol, which is much easier to store and transport. Therefore, methanol to hydrocarbon process has received renewed interest as it could become economically feasible [4].

Process and energy intensification are the challenge for the transition to future sustainable and low-carbon industrial chemical production. Innovation is required for large-scale processes regarding energy intensive and multiple process steps, as methanol conversion to olefins and the development of new sustainable paths for $CO_2$ reuse.

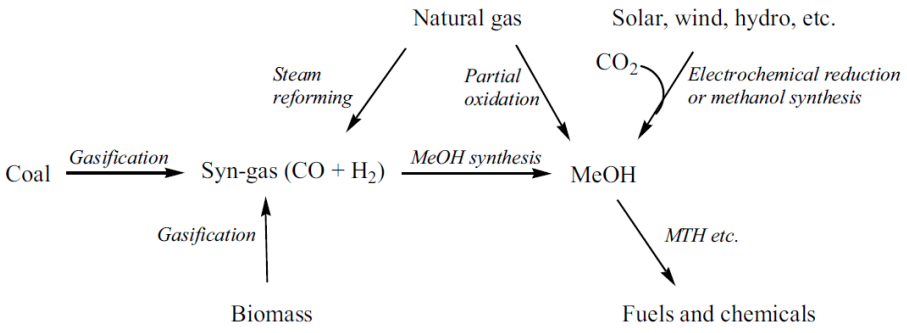


**Scheme 1.1**. Main routes for the production of methanol [1]

Methanol can be directly used as fuel either in a combustion engine or by employing a 'direct methanol fuel cell' (DMFC) [5] but it can also be converted to fuel grade hydrocarbons through Mobil's methanol to hydrocarbon (MTH) process. Synthetic gasoline from this process is identical to petrochemical gasoline. Therefore no new type of engine and vehicle are necessary.

The research described in this thesis was part of a project funded by the European Commission as part of the 7th Framework Programme for Research and Development under the acronym BIOGO-for-Production. The project objective was to design a miniaturized integrated reactor for the conversion of methanol to liquid hydrocarbons with enhanced amount of gasoline ($C_{8-11}$) fraction and reduced amount of aromatics. The reactor should be small, light-weight, and energy efficient. A procedure to deposit thin zeolite layers has to be adopted and the coatings obtained were characterised by various physico-chemical methods. The results of the BIOGO project are described in this thesis.

### Scope and layout of the thesis

Despite the recent development in advanced microreactor design and fabrication, the reactor performance is often limited by the activity of the state-of-the-art catalysts. To fully exploit the benefits of catalytic microreactors, and to increase the drive towards their applications in MTH processes as a superior alternative to conventional reactor systems, a strong focus is required towards the development and optimisation of

highly active catalytic coatings. However, the development of novel catalytic coatings is often an empirical process, which is based on known catalyst performance in similar relations. Therefore, fast testing of libraries of coatings is required at realistic process conditions to speed up this development and optimisation trajectories.

In Chapter 2, a literature review is presented which provides recent developments in the MTH process, including reaction mechanisms, optimal catalysts and reaction conditions. The synthesis of ZSM-5 catalysts and post-synthesis modifications are reviewed. The application of microstructured reactors and numerical solution methods for their design is described. Chapter 3 describes equipment using in catalytic tests and respective experimental procedures. It also covers catalyst synthesis procedures and characterisation methods. Chapter 4 describes the synthesis of microporous H-ZSM-5 coatings and the effects of different synthesis parameters (Si/Al ratio, $H_2O$/Si ratio, synthesis time) on the morphology and catalytic properties of the catalysts obtained. The performance of ZSM-5 coatings is compared to that of ZSM-5 pellets and industrial ZSM-5 catalysts. Chapter 5 describes the effect of two post-synthesis modifications: ion-exchange with metal salt solutions and desilication with alkali treatment, on physical properties and catalytic activity of the catalysts. Hierarchical (micro- mesoporous) ZSM-5 coatings have a better performance in terms of product distribution and deactivation behaviour. The design of a microstructured reactor/heat-exchanger (MRHE) using a convection and conduction heat transfer model is presented in Chapter 6. Micro heat exchangers differ from larger-scale heat exchangers, as axial conduction of heat through the solid material becomes more important, while convective heat transfer becomes less important. Therefore, in this chapter we do not solely address practical issues like reactor performance, start-up time, and heat recovery possibilities, but we also present a modelling study of the heat transfer in the micro heat exchangers. A parametric study describing the effect of different design parameters (channel length and diameter, plate thickness, coating thickness, cooling flow rate) is initially performed using a 2D model

with the goal to reduce the temperature gradient in the catalytic coating. Then the optimal 2D design is verified using a 3D reactor model which resembles the actual reactor geometry and accurately describes hydrodynamics and heat transfer in the reactor. The purpose of this work is also to study the heat transfer behaviour of micro heat exchangers and the effect of integrating several heat exchangers in a single device in terms of start-up time and mechanical design. In Chapter 7, main conclusions from the thesis are summarised and suggestions for future work are given.

# Chapter 2

# Literature review

In the 1970s, two teams of Mobil scientists who were working on methylated isobutene to improve the octane number of gasoline accidentally discovered the formation of diverse hydrocarbons over ZSM-5 zeolite. Later on, several types of other zeolites were synthesised and the product range was extended to other fuels. The respective processes were called methanol-to-gasoline (MTG), methanol-to-olefins (MTO), and methanol to hydrocarbons (MTH) process since then.

The first and second oil crises between 1973 and 1978 were the driving force for commercialising the MTG process. As the oil price was increasing, looking for other feed stocks such as natural gas, biomass or coal was crucial which could be converted via different pathways to fuel (gasoline and diesel), olefins and other hydrocarbon products. The Methanol-To-Hydrocarbons (MTH) reaction is an important step to produce a range of hydrocarbons such as fuel and olefins from various carbon sources. Various range of hydrocarbons can be obtained as the final products using different zeolite topologies and reaction conditions.

## 2.1 Zeolite catalysts

A zeolite possesses a well-defined crystalline structure in which $[SiO_4]^{4-}$ and $[AlO_4]^{5-}$ tetrahedral units are connected by sharing all oxygen atoms. The activity and selectivity over zeolites in the catalysis are often governed by two key factor: porous structure and site acidity.

### 2.1.1 Porous structure

Also called as ‘molecular sieve’, the zeolite has 1D, 2D or 3D framework that consists of nanometre sized micropores and cages, giving a high porosity and a large specific surface area to the material. Zeolites are classified according to different topologies (channels and cavities

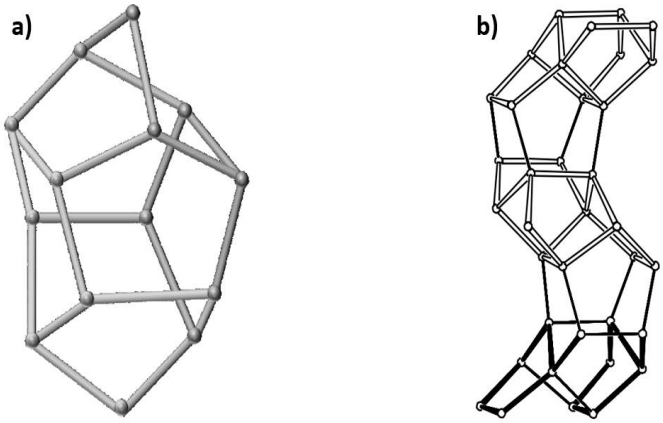


**Figure 2.1**. a) Assembly unit by five-rings. b) T-T linkage scheme of a pentasil chain [7,10]

dimensions and interconnections), compositions (concentration and distribution of acidic sites) and morphologies (crystal dimensions, micro- and mesoporosity).

MFI is one of the most investigated framework type of zeolite for MTH reaction [6]. ZSM-5 is a typical zeolite that belongs to this framework type. The MFI structure can be described as an assembly of pentasil five-ring chains which are linked to each other by oxygen bridges and form an assembly unit (**Figure 2.2a**) [7,8]. These units connect via edges to form chain structure (**Figure 2.2b**). Extending this chain structure in both x- and y-directions, these five-rings create straight ten-ring channels (5.3 Å × 5.6 Å) parallel to the [010] direction and sinusoidal ten-ring channels (5.1 Å

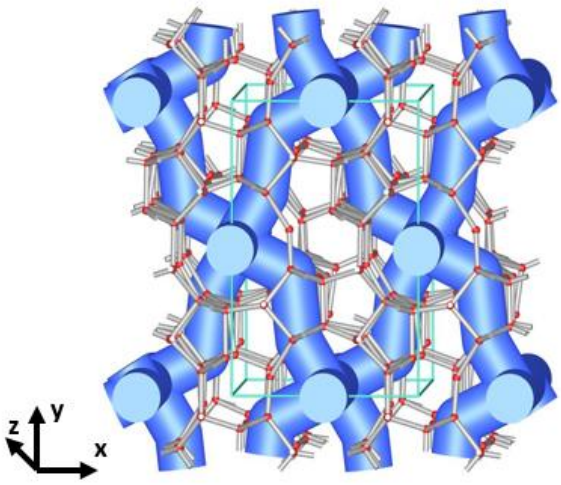


**Figure 2.2**. Illustration of channel system in H-ZSM-5 [255]

×5.5 Å) parallel to the [100] direction [8,9] (**Figure 2.2**). This particular structure is described as interconnected tubes with intersections between orthogonal channels which create larger volume and thus, gives ZSM-5 distinct differences from other zeolite regarding to shape selectivity [10]. For example, ZSM-5 (MFI topology) and SAPO-34 zeotype (CHA topology) are the only two catalysts applied at industrial scale. SAPO-34 consists of much larger cavities with narrow connecting pores [13]. The highest selectivity to light olefins (ethylene and propene) was observed over H-SAPO-34 catalysts. On the contrary, monocyclic aromatics was formed over H-ZSM-5 catalysts as a by-product of light olefins [6,11,12]. This can be explained by shape selectivity in the SAPO-34 narrow pores in comparison to the medium pores of ZSM-5 [20]. However, the H-ZSM-5 catalyst has a much longer lifetime than SAPO-34 [13].

### 2.1.2 Acidity

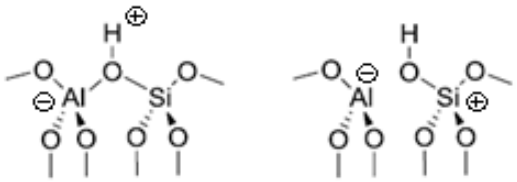

**Scheme 2.1.** Common representation of Brønsted (left) and Lewis acid site (right) in zeolites [15].

In zeolite materials, two different acid sites are formed, Lewis and Brønsted sites [13]. Typically, if a proton is used as a charge balancing species in the framework, Brønsted acid sites will be formed. The Lewis sites are the electron pair acceptors and can interact with basic molecules by hydrogen bonding. The Lewis sites are more available in zeolites with very high Al contents or in materials that have had a background of thermal/steam treatments [14]. Cationic extra-framework species, such as $AlO^{+}$ and $Al(OH)^{2+}$, could as act as Lewis acid sites displaying weak acidity (**Scheme 2.1**) [15].

The acid density and acid strength determine catalytic activity of zeolites. The acid density of zeolites refers to the number of acid sites that is ideally equal to the number of substituted Si atoms by Al atoms in the lattice.

Therefore the Si/Al ratio is reversely proportional to the acid density. The acid strength is described as the intrinsic property of zeolite shown in presence of basic molecules. The main factor which determines the acid strength is the overall chemical composition of the framework structure, however some other parameters such as the exchanged metal cations and topology of the framework effects are also of importance [16].

In case of presenting Al in the framework structure, in order to balance the total charge, an extra-framework cation (i.e. $K^+$, $Na^+$) or proton located in pore space may be exerted. The cations can be exchanged due to the high mobility and this property gives rise to the use of zeolites as the acid-base catalyst and ion-exchanged material.

There are various methods to identify the acid site strength as well as the density of acid sites. Among them, the elemental composition of the zeolite is a common way to determine the acid density. However this method does not distinguish the framework and extra-framework sites and does not take into account the accessibility of the sites for test molecules [17].

By choosing proper characterisation techniques, it is also possible to distinguish between Lewis and Brønsted sites. Fourier transform infrared spectroscopy (FTIR) is used to identify the types of acid sites. In FTIR spectra, weak acid sites encompassing Lewis acid site and hydrogen-bonded sites could be observed at 2300 $cm^{-1}$ while strong sites including Brønsted acid sites and Si-OH bond could be observed around 3610 $cm^{-1}$ and 3740 $cm^{-1}$ respectively. A study focusing on how the acidity of ZSM-5 effects reaction rate was carried out by Alharbi et al. They observed maximum turnover rate and methanol conversion over ZSM-5 with a high content of Al. They also reported that turnover rate of methanol dehydration over ZSM-5 is primarily determined by the strength of catalysts acid sites, regardless of the pore structure [18].

The characterisation of acidity could also be carried out by probe molecule (pyridine or ammonia) temperature programmed desorption (TPD) where probe molecules adsorb on strong acid sties as cations while its adsorption

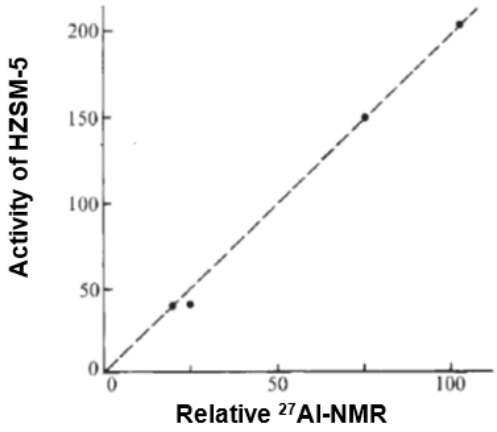


**Figure 2.3**. The activity of H-ZSM-5 plotted against the tetrahedral Al NMR signal (Activity value of 1 corresponds to the activity of amorphous silica-alumina catalyst) [24]

on the weak sites occurs via a hydrogen-coordinated bond. The ratio of measured strong acidity over theoretical acidity was reported to be close to 1 for ZSM-5 with high Si/Al ratio, however lower for samples with increasing Al content [13, 14]. After desorption of probe molecules, the disappearance of weak acid sites was reported by several groups and that strong acidity remained [21–23]. The more emphasis in catalytic process has been on Brønsted than Lewis acid sites as it was shown a linear relationship between the concentrations of protonated tetrahedral aluminium in $SiO_2$ framework and the catalytic activity of zeolite materials (**Figure 2.3**) [24].

## 2.2 Reaction mechanism

### 2.2.1. Oxonium ylide mechanism

The oxonium ylide mechanism proposed by Van den Berg et al. [25] has received intensive attention. As shown in **Scheme 2.2**, after dehydration from two methanol molecules, a DME molecule interacts with a Brønsted acid site provided by the catalyst to form a dimethyl oxonium ion which further reacts with a methanol molecule to form a trimethyl oxonium ion. It is then deprotonated by a basic site to form a dimethyl oxonium methyl ylide. In the next step, the first C-C bond is formed either by Stevens rearrangement [26] or methylation step [27] leading to either a methylethyl ether or an ethyldimethyle oxonium ion respectively. Both intermediates then go through beta-elimination and produce ethylene [26].

However, Olah suggested that, instead of Stevens rearrangement, the first C-C bond is a result of bimolecular methylation of trimethyl oxonium ion [26] (**Scheme 2.2**). In order to prove the existence of oxonium ylide, direct synthesis of ylide via different approaches have been performed by Olah et al. By using $^{13}C$ and $^{2}H$ labelled compounds, the product isotope distributions appeared to rule out Stevens rearrangement [26].

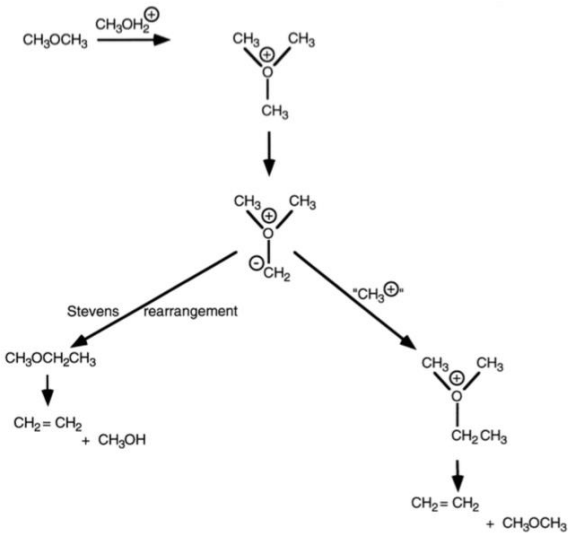


**Scheme 2.2**. Oxonium ylide mechanism [26]

### 2.2.2 Carbene mechanism

The carbine mechanism proposed by Swabb and Gates [28] involves the interaction of both acid and basic sites in zeolite (**Scheme 2.3**). A methanol molecule is alpha-eliminated to form water and carbene. Either by polymethylation or concurrent sp3 insertion into methanol of DME molecule, the initial C-C bond is formed [26,29,30]. Evidence in favour of the carbene mechanism for the MTH reaction over ZSM-5 catalysts was reported by several groups [26,31]. These authors used $^{13}C$ methanol and other isotope techniques.

$$[Zeo-O^{-} \leftarrow H-CH_2-OH \rightarrow H-O-Zeo]$$
$$\rightarrow H_2O + :CH_2$$

**Scheme 2.3**. The carbene mechanism [26]

### 2.2.3 Hydrocarbon pool mechanism

A consecutive mechanism was suggested by Dahl and Kolboe [32,33] where one carbon from methanol adds up during each step. Due to a narrow range of products, the mechanism was initially studied by feeding $^{13}C$ methanol over a SAPO-34 catalyst rather than over ZSM-5. The hydrocarbon-pool stands for $(CH_2)_n$ adsorbates containing less hydrogen than indicated [33]. Later from experimental outcomes obtained in several

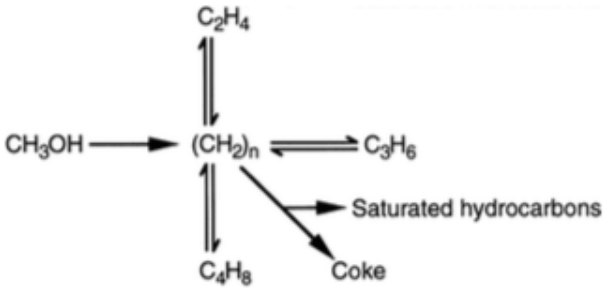


**Scheme 2.4**. Hydrocarbon pool mechanism [32]

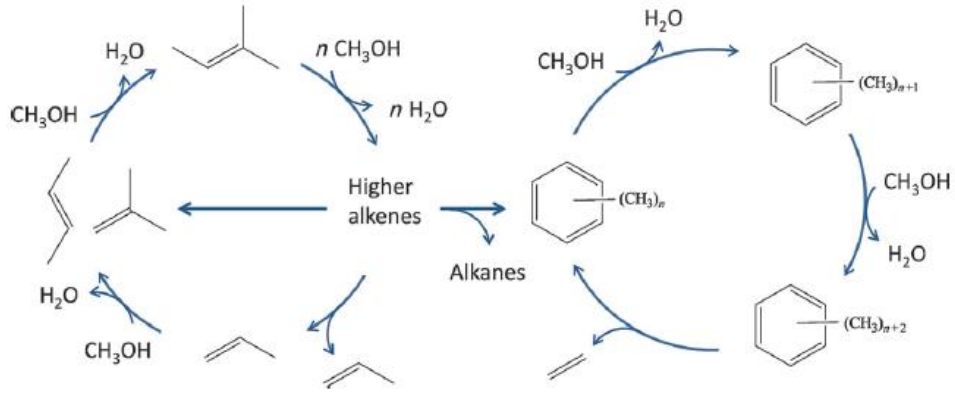


**Scheme 2.5**. Dual-cycle hydrocarbon-pool mechanism for MTH over H-ZSM-5 catalyst [6]

studies, authors believe that the MTH reaction over H-ZSM-5 undergoes continuous adding up and splitting off reactants and products (**Scheme 2.4**) [26,34,35].

Clearly, the detailed mechanism might vary with various pore structures, so a re-examination of the detailed mechanism of MTH over H-ZSM-5 was undertaken in 2006 [36]. It was concluded that the aromatics-based hydrocarbon-pool mechanism, rather than cracking from high alkenes, was the main source of hydrocarbon production. This brought the suggestion of two simultaneous mechanism cycles running in the MTH reaction over H-ZSM-5. The dual-cycle mechanism (**Scheme 2.5**) demonstrating both the aromatic cycle including ethene formation form lower methylbenzenes, and the alkene cycle which consists of methylation/ cracking involving only $C_{3+}$ alkenes [37]. It was also claimed that a completely independent operation of the aromatic cycle is not possible in the MTH reaction since aromatics

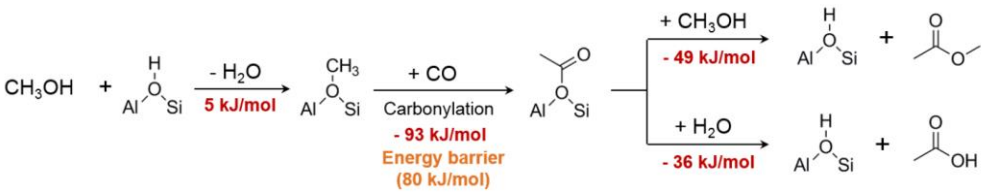


**Scheme 2.6**. Carbonylation of methanol to yield the first carbon-carbon bond. Enthalpy changes are shown in red. Energy barrier in orange. Reproduced from [38].

are constantly formed by aromatisation of higher alkenes. However, by choosing a catalyst of particular topology or tuning the reaction conditions, one can suppress any of the cycles to control the selectivity of products [6].

Recently, Liu et al. [38] reported that acetic acid and methyl acetate represent the first intermediates containing C-C bonds. The authors proposed that the C-C bond is formed via CO carbonylation of methoxy groups adsorbed on the acid sites. The reaction happens between the electrophilic carbon atom present in methanol, DME and formaldehyde and the nucleophilic carbon atom of CO. The carbonylation forms an acetyl group on the surface of the catalyst. Then, it can dissociate to form acetic acid (HOAc) and methyl acetate (MeOAc), as schematically shown in **Scheme 2.6** MeOAc and HOAc. The surface acetyl groups on H-ZSM-5 were observed via in-situ IR spectroscopy [38]. These were primary products, followed by the formation of olefins. An activation energy of 80 $kJ \cdot mol^{-1}$ was estimated for the carbonylation step [38], in line with a previous theoretical study on carbonylation of methanol and DME on Mordenite, where the activation energy was estimated in 84 $kJ \cdot mol^{-1}$ [39].

Chowdhury et al. [40] used NMR, UV/Vis diffusive reflectance and mass spectrometry to investigate the reaction mechanisms over a H-SAPO-34 catalyst. They also identified surface acetate, methyl acetate and dimethoxymethane (DMM, $CH_3OCH_2OCH_3$) as the initial intermediates with C-C bonds and proposed a plausible mechanism for the formation of the first C-C bond (**Scheme 2.7**).

The reaction may proceed as follows: first, methylation of a Brønsted acid site (ZeOH) forms a surface methoxy species (SMS) that interact with another methanol or DME molecule. Then, the formation of the first C-C occurs by an insertion reaction from SMS to the methanol/DME molecule

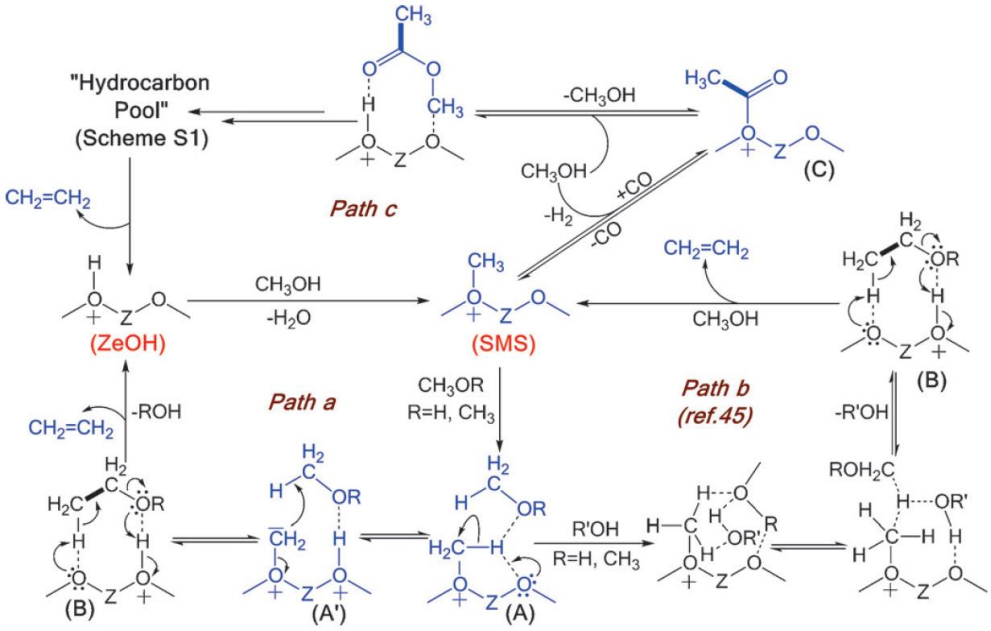


**Scheme 2.7**. Schematic diagram of a plausible mechanism for first carbon-carbon bond formation. Reproduced from [40].

(Path a). Direct interaction of the SMS with methanol is also possible (Path b), as proposed by Blaszkowski and van Santen [41]. Alternatively, carbonylation of the SMS can take place to form the first C-C bond, and further reaction with methanol results in MeOAc, supporting the results presented by Liu et al [38].

Once the first C-C bonds are formed, a hydrocarbon pool develops in the cages of the zeolites, which is methylated to yield polymethylbenzenes, as shown by the dual cycle mechanism, presented in **Scheme 2.7**.

### 2.2.4 Kinetic model

The first step of MTH reaction is the dehydration of methanol.

$$2CH_3OH \leftrightarrow CH_3OCH_3 + H_2O$$

Fan and co-workers carried out a theoretical study that identified different intermediates related to the first C–C bond formed during the initial induction period formaldehyde ($CH_2O$) and methoxymethyl ($CH_3OCH_2^+$) from methanol and DME, respectively [42]. Under steady-state conditions,

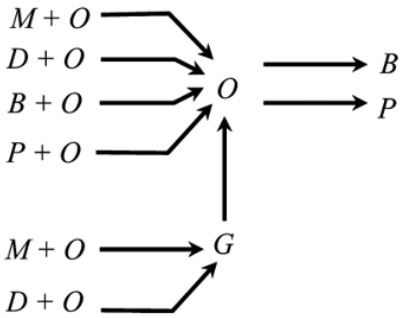


**Scheme 2.8.** MTH reaction scheme over an H-ZSM-5 catalyst [50]. Preudo components: M: methanol, D: dimethyl ether, P: propylene, B: Butane, O: $C_2$-$C_4$ olefins, G: gasoline

DME has been identified as a faster alkene and arene methylation agent than methanol over H-ZSM-5 [43]. This is in line with the observations that, with a H-ZSM-5 catalyst, DME is converted faster to hydrocarbons than methanol, and that addition of methanol or $H_2O$ to a DME feed results in a lower initial activity of the catalyst [44,45].

Many simplified kinetic models based on different principles have been proposed [46–48]. It should be noted that the hydrocarbon pool mechanism was generally accepted over the last decade, therefore earlier kinetic schemes were oversimplified and lacked relation with the true chemistry behind the formation of hydrocarbons. Therefore, they provide little information on the real reaction steps and the product distribution observed. A lumped kinetic model for methanol at industrial conditions was built based on a one-step reaction of methanol dehydration in a fixed-bed reactor by Tavan et al. [49]. The experiments were carried out in the 200-400 $^oC$ range at 1 bar with a WHSV varying from 15 to 90 $h^{-1}$. Their experimental data were described rather well with a simple kinetic model. As the pressure has little effect of the enthalpy of the overall reaction, this model was also utilised at elevated pressures [49].

Another lumped kinetic model was developed for the MTH process over a ZSM-5 catalyst in the 400-550 °C range. Seven pseudo components including oxygenates, n-butane, $C_2$-$C_4$ olefins, $C_2$-$C_4$ paraffin (except for n-butane), $C_5$-$C_{10}$ fraction and methane were used to quantify the distribution of products (**Scheme 2.8**).

In this kinetic scheme, $C_2$-$C_4$ olefins are primary products, formed from methanol and dimethylether, intermediates in the autocatalytic steps to form more olefins and in the formation of gasoline product by methylation, oligomerisation, cyclization, and aromatisation. A cracking step of gasoline product was also considered to form lower olefins. This kinetic model describes experimental data obtained in a fixed-bed reactor in the 400-550 $^{o}$C range at short residence times [50].

There is general consensus about the auto-catalytic nature of the MTH reaction [51]. This means that the reaction between methanol or DME and hydrocarbons residing in the zeolite pores under steady-state conditions (the so-called “hydrocarbon pool”) is faster than C–C bond forming reactions between two methanol and/or DME molecules.

## 2.3 Synthesis of ZSM-5 coatings on structured substrates

As one of the most important commercial zeolites, ZSM-5 has been synthesised over various ceramic substrates such as quartz, cordierite as well as metal substrates: aluminium, titanium and stainless steel [52–54]. However, the reaction is often mass transfer limited by intraparticle diffusion. Therefore other deposition techniques such as in-situ hydrothermal growth, washcoating, dipcoating and spray deposition were developed to obtain zeolitic coatings [55–57]. A thin layer of zeolite catalysts has a better accessibility to active catalytic sites and improved heat and mass transfer rates [58]. Commonly, the envisioned application of zeolitic coatings determines the deposition method. For example, fast exothermic reactions can be intensified when they are performed over zeolitic coatings with a thickness of few microns, which are directly grown in the channels of a microstructured reactor.

A microstructured reactor is a chemical reactor that is characterised by its very small channel diameter (typically 0.3-1.0 mm) and a channel length of 10-200 mm. The small dimensions allow very fast external heat and mass transfer. Microstructured reactors were employed in many fast reactions

and improved performance was reported [59–62]. A thin layer of PdZn catalyst was studied in methanol steam reforming [63]. High conversion and selectivity were achieved in dehydration of ethanol over a $TIO_2$/γ-$Al_2O_3$ coatings [60]. A propene selectivity above 97% was observed for a non-oxidative propane dehydrogenation in a microstructured membrane reactor [64]. In oxidative dehydrogenation of methanol to formaldehyde, a silicon microreactor demonstrated higher selectivity than a fixed-bed reactor due to isothermal conditions even at high oxygen concentrations [65]. A highly exothermic oxidation of hydrogen over a Pt/$Al_2O_3$ coatings in the explosive region was performed in a microstructured reactor coupled with a micro heat-exchanger [66].

### 2.3.1 Synthesis of microporous zeolites

Sol-gel hydrothermal synthesis (HT) is the most common method to obtain zeolitic coatings. Synthesis of zeolitic coatings onto different substrates by thesol-gel method was studied by Rebrov [67]. In a heterogeneous synthesis, the Gibbs free energy of the system is the key factor of forming phases. The Gibbs volume free energy of the system under nucleation

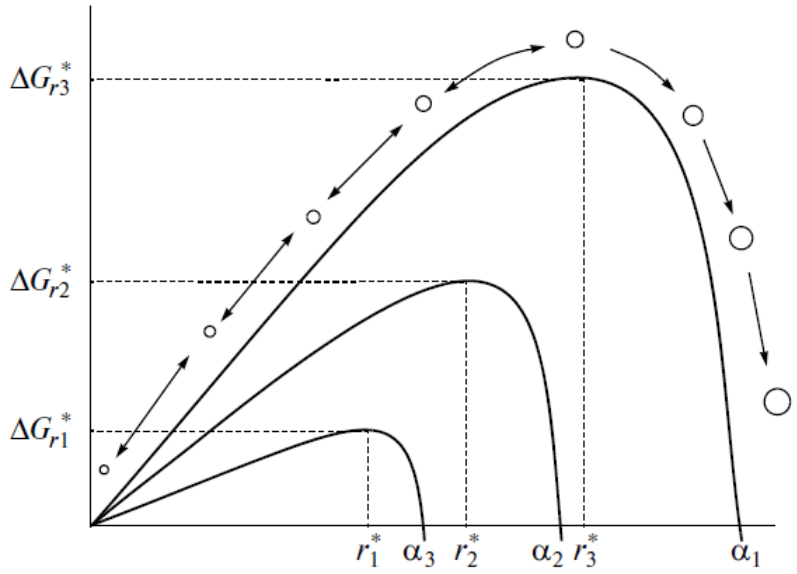


**Figure 2.4**. Variation in the Gibbs free energy (ΔG) at an increase in the molecular aggregate radius in the nucleation process at the different solution supersaturation degrees α1 < α2 < α3. As the supersaturation increases, the critical nucleus radius (r*) decreases [67].

increases due to the formation of the phase interface. When a new solid phase is formed under nucleation in a sol-gel phase of precursors, the free energy decreases due to the formation of a more stable thermodynamic state. However, the radius of formed molecule aggregate is highly effected by saturation. In a supersaturated situation, the critical nucleus radius decreases. Any smaller nucleus with lower Gibbs volume free energy than the critical value may be dissolved to have a lower chemical potential (**Figure 2.4**). Moreover, the Gibbs free energy for the formation of critical nucleus under heterogeneous nucleation is always lower than under homogeneous one which indicates that nucleation is more likely to occur within surface defects (micro slots and cracks) [67].

Initiation of ZSM-5 coating growth is highly dependent on surface pretreatment and concentration of precursors. Jiao et al. [68] used SEM to study the initial steps in the formation of ZSM-5 coatings on a SiC foam substrate pretreated with the precursor gel. Between synthesis times of 3 and 36 hrs, ZSM-5 crystals were observed to emerge on the gel layer, grow larger into the outer porous layer and eventually cover the foam. However, coating growth slows down and ceases after a certain time of synthesis when synthesis mixture is exhausted. Calis et al. [69] performed the synthesis of ZSM-5 coatings on a stainless steel monoliths and observed that the coverage exceeded 25 g/m$^2$ after rotating synthesis of 24 hrs and eventually reached 28 g/m$^2$ after 44 hrs.

The quality of the zeolite product is determined by the elemental composition of the initial sol, synthesis conditions and the substrate properties (such as wettability and surface roughness). Usually, the initial sol consists of a silica and aluminium sources, a structure directing agent (template) and a solvent. Crystallization time can influence different aspects of ZSM-5 crystallization and can lead to changes in the properties of the final zeolite product. The effect of crystallization time on ZSM-5 morphology was studied in a synthesis performed from fumed silica, sodium aluminate and tetrapropylammonium hydroxide (TPAOH) [70]. The authors concluded that there exists an optimum synthesis time of 45 hours which provides the highest crystallinity and highest surface area of zeolites.

ZSM-5 with very high Si/Al ratios (80 to 1200) were obtained by HT synthesis using a mixture of two templates: tri-ethyl butyl ammonium bromide (TEBA) and ethylene diamine (EDA) [71]. A synthesis in the absence of structural template was also successfully performed to obtain nanosized ZSM-5 with a crystal size of 15 nm. In this case, sodium cations were reported to play a structure directing role instead of a template enhancing nucleation and crystallization [72]. Developed from hydrothermal synthesis, a two-step synthesis method was demonstrated by mixing tetraethylorthosilicate (TEOS) and TPAOH as the seed suspension at 80 $^{o}$C for 72 hrs prior to the synthesis [73]. It is interesting that the crystal size was controlled in the range from 200 to 1000 nm by adjusting the amount of the seed suspension. Various metal cations were studied to replace sodium and to modify the acidity of ZSM-5 catalysts. A manganese (III) acetylacetonate precursor was used in a one-step ZSM-5 synthesis. Characterisation suggested that manganese was incorporated in the zeolite framework and it also formed a large extra framework clusters, depending on the initial Mn concentration in the sol [74].

The catalytic performance of ZSM-5 zeolite depends highly on its physicochemical properties such as crystallinity, crystal size, acidity, specific surface area, and the presence of other zeolite phases. In order to tailor these properties to maximise different reaction products, large efforts have been done to study and control synthesis conditions during hydrothermal synthesis.

Synthesis time is one of the most significant factors during crystal growth. The crystallinity of ZSM-5 was reported to increase with synthesis time [70,75,76]. By increasing synthesis time from 72 to 120 hrs, Karimi et al. observed an increased crystallinity which was ascribed to increased nucleation and growth rates (**Figure 2.5**) [75]. The increasing crystallinity with longer synthesis time was also proved by optical density ratio measured at the 542 and 450 $cm^{-1}$ bands in FTIR spectra [70,77]. However, after reaching a high crystallinity at some point, it was reported that further increase in synthesis time has no significant effect on crystallinity [70]. However the crystal size was reported to increase or decrease with synthesis time depending on synthesis conditions. This indicates that an equilibrium between crystallization and dissolution of zeolite crystals may exist [75,76].

The synthesis temperature is another important parameter in zeolite synthesis. Karimi et al. [75] performed ZSM-5 synthesis in a wide temperature range (125-200 $^{o}C$). They reported that the crystallinity reached the maximum at 175 $^{o}C$. At maximised crystallinity, twinned crystals with smooth surfaces and the strongest band intensity at 550 $cm^{-1}$ were observed.

The effect of Si/Al content on the morphology of ZSM-5 crystals has been reported [78,79]. Al-Dughaither et al. [79] obtained a series of ZSM-5 samples in a wide range of Si/Al ratios of 30-280. They concluded that the Si/Al ratio has little effect on the crystallinity of ZSM-5 crystal. The unit cell

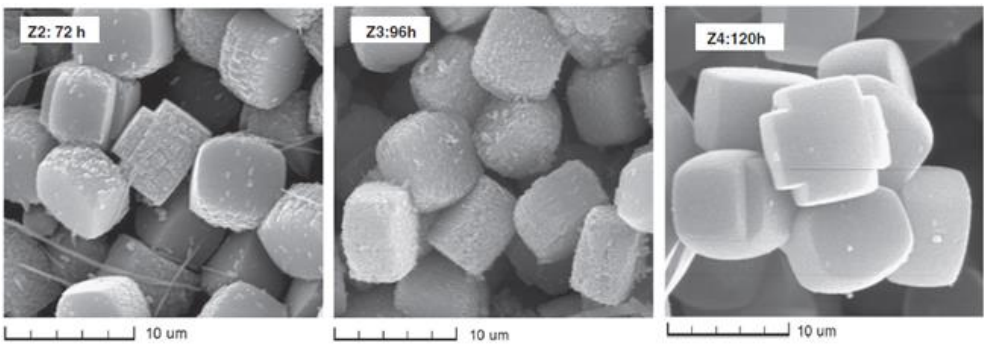


**Figure 2.5**. SEM images of samples obtained after 72 (left), 96 (middle) and 120 h (right) [75]

volume increases in crystals with lower Si/Al ratio due to the replacement of smaller silicon atoms (2.22 Å) by larger aluminium atoms (2.86 Å). This explains the higher intensity of peaks in XRD patterns of samples with high Si/Al ratio. Shirazi et al. [78] reported that high Al content led to highly undergrown and twinning crystals with smaller mean size. A lower BET surface area was also observed in ZSM-5 with low Si/Al ratio. The catalytic and chemical properties will be discussed in section **2.3.4**.

One of the major challenges in the conversion of methanol to hydrocarbons is deactivation by coking. Deactivation of MTH catalysts correlates with the formation of (poly-)aromatic coke precursor molecules, which eventually block the pores and active sites and are gradually converted to graphitic type coke [80]. For H-ZSM-5, it has been observed that coke formation starts in the first part of the catalyst bed and progresses towards the outlet with time on stream, leading to an inverse S-shaped conversion versus time-on-stream curve [81]. Various treatments of ZSM-5 zeolites have been investigated in order to prolong the catalytic lifetime of ZSM-5 by reducing and weakening the number of acid sites [82,83].

### 2.3.2 Ion-exchange

Research intending to modify strong acid sites on the surface of ZSM-5 was performed by ion-exchange with various alkaline earth metals [84]. Among tested metals, Ca-exchanged ZSM-5 exhibited the best coke resistance and longest lifetime in the MTH reaction when compares to magnesium, strontium and barium. By replacing the strong acid sites, calcium ions suppressed formation of aromatics which are intermediates to produce coke deposits. Moreover, a decrease in strong acid sites of the regenerated Ca-ZSM-5 implied a fact that some calcium ions were released from sites over time on stream [84].

Ni-exchanged ZSM-5 catalysts were investigated in an n-hexane conversion where nickel was reported to cause an extreme increase in aromatisation selectivity [85]. Location of nickel in ZSM-5 was examined by comparing samples prepared by ion-exchange and wet impregnation. Both samples exhibited improved selectivity towards olefins in secondary

cracking of butene and pentene and that formation of NiO at the external surface of ZSM-5 was favoured when nickel loading exceeded 1 wt.% during wet impregnation [86]. Precise information on the location of nickel ions was beneficial in catalyst design to control selectivity. Nickel was reported to catalyse the conversion of a $CO/CO_2$ mixture into methane [87] and therefore its catalytic activity will be studied in this thesis.

### 2.3.3 Hierarchical ZSM-5 structure

The micropores in zeolite structures have a diameter below 1 nm which could impose diffusion limitations, especially in relatively large crystals. In order to enhance diffusivity, tailoring the porosity is required during zeolite synthesis. Mesoporosity could be introduced into the ZSM-5 structure either by direct hydrothermal synthesis [88,89] using a second templating agent, or a post-synthesis desilication approach [90]. In a desilication, silicon atoms are extracted from the zeolite framework by a treatment with a base solution. In this approach, an intense removal of silicon occurs which decreases the Si/Al ratio and consequently increases the exposure of acid sites. **Scheme 2.9** represents a schematic view of the desilication process. Step 1a to 1b represents the initial stage of random dissolution of

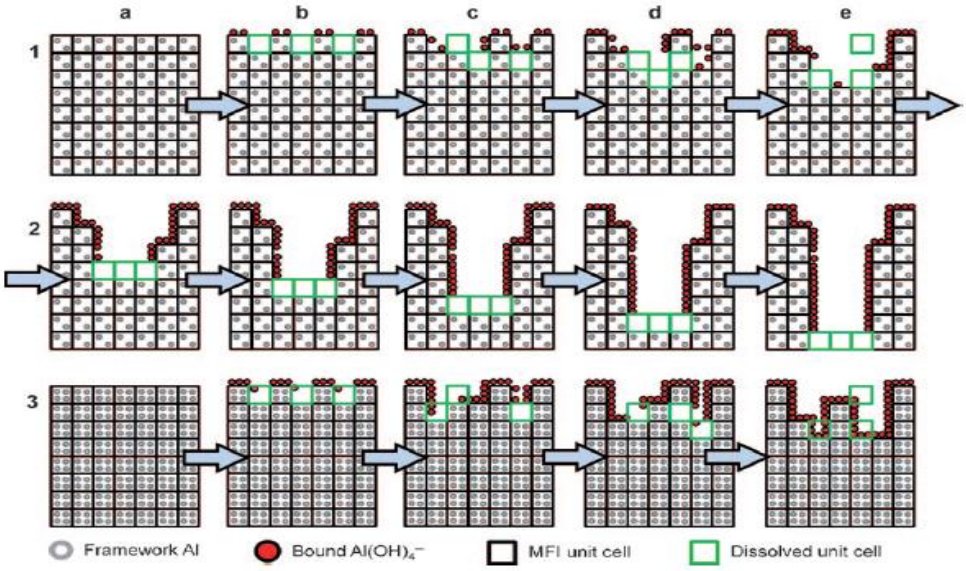


**Scheme 2.9**. Schemes of influence of desilication on ZSM-5 with 1,2) high Si/Al ratio, 3) low Si/Al ratio regarding dissolution, pore formation and realumination [91]

a MFI unit cell by alkaline treatment where framework Al is released and adsorbed on the cell surface protecting further dissolution. However, in further steps, 1c to 2e, the MFI unit cells get further dissolved due to low Al density in a ZSM-5 with high Si/Al ratio. They form a mesopore with diameter around 40 nm. Contrarily, for ZSM-5 with high Al content, the dissolved MFI unit cell will release enough framework Al to cover the entire external surface and consequently stops formation of mesopores (steps 3a to 3e) [91]. In order to introduce intracrystalline mesopores in ZSM-5 with a low Si/Al, the alkalinity has to be increased [92].

The formation of mesopores improves internal transport of larger molecules, thus shifts product selectivity to longer chain hydrocarbons. The formation of mesopores mainly occurs at the expense of micropores [93]. Desilication would not affect the number of Brønsted acid sites but would substantially increase Lewis acidity [93]. However, the total acidity remains constant as confirmed by several groups using $NH_3$ adsorption [94–96]. This result indicates that all sites are acidic enough for strong adsorption of $NH_3$. A discrepancy between elemental composition by NMR and total acidity for desilicated ZSM-5 was also reported, which was explained by the existence of extra framework or even amorphous aluminium species that does not contribute to acidity [94]. The deactivation and reactivation kinetics of micro- and bi-porous zeolites is different due to different mass transfer rates in their porous networks.

Introducing mesoporosity by desilication was widely reported to have an improvement on catalytic stability, lifetime and selectivity towards gasoline range hydrocarbons [94,97–99]. By modifying micropores to mesopores, larger cavity and channel diameter allow heavier hydrocarbon molecules to pass through and higher resistance against coking which could block pores. A fundamental study comparing catalytic activity of microporous and desilicated ZSM-5 was carried out by Bjørgen et al. [94]. They observed both higher methanol conversion with time on stream and accumulated methanol conversion over ZSM-5 desilicated sample and that this effect was improved by harder desilication treatment using a NaOH solution up to 0.2 M. This result was explained as an improved accessibility to and from

the acid sites due to higher external surface areas and mesopore volumes observed [94]. The $C_{5+}$ selectivity was also reported to rise by a factor of 1.4. In another reported synthesis of ZSM-5/MCM-48 composites, an interconnected microporous and mesoporous channel system was proved to have improved selectivity towards $C_{5+}$ gasoline range products with almost half of the aromatics content in the products when compares to H-ZSM-5 zeolite [100]. The reaction temperature was also studied in this work where the optimal temperature for selectivity towards $C_{5+}$ was 380-400 $^{o}$C over both catalysts. Higher operating temperature resulted in a higher conversion of methanol, however, with more aromatics in liquid products. A work studying space velocity of methanol over a mesoporous ZSM-5 was performed in a fixed-bed reactor at 370 $^{o}$C. At a high WHSV, a higher amount of $C_{4+}$ was observed together with a lower conversion of methanol due to the lower contact time. Similar overall products were observed indicating a common reaction pathway over various WHSV [88].

### 2.3.4 Catalyst stability

H-forms of various zeolites (both 1D and 3D) with different acid density and surface areas were studied in the MTH reaction, among others ZSM-22, ZSM-23, IM-5, ITQ-13, Beta and ZSM-5. All these catalysts are active for methanol conversion and give initially full methanol conversion but their lifetime varies considerably and decreases in the order of ZSM-5 >> ITQ-13 >> IM-5 > ZSM-23 ~ Beta > ZSM-22 > Mordenite. In general, 12-ring zeolites (H-Beta and H-Mordenite) deactivate faster than 10-ring zeolites, with higher aromatic yields and a lower $C_{5+}$ aliphatics fraction. Ten-ring 1D zeolites, ZSM-22 and -23, produce mainly aromatic free $C_{6+}$ fractions but show reduced stability toward deactivation.

One of the main drawbacks of MTH over zeolite catalysts is related to the deactivation. It is also the major issue in the industrial application of MTH conversion. Two main causes of the deactivation are the removal of framework aluminium and formation of carbon species. Framework aluminium is mandatory for generating the Brønsted acid sites. Therefore the dealumination caused by steam attacking Al-O-Si bonds, leads to the

collapse of the acidic structure and irreversible deactivation of catalyst [101–103]. Carbon species deposited inside zeolite cavities also block the micropores and acid sites [104,105].

Severe deactivation due to micropore filling by alkylated benzene molecules was observed over H-ZSM-5 above 543 K [106]. Dealkylation of products over a H-ZSM-5 catalyst started at 623 K and cracking to alkene was favoured at higher temperatures as it was concluded from temperature-programmed desorption experiments (TPD). Above 623 K, a longer lifetime and less hydrocarbon residue were observed [6]. A similar effect of reaction temperature was observed over H-SAPO-34 [107]. Two other important factors related to catalyst deactivation are the strength of the acid sites and their density. With a high acid strength and density of acid sites, deactivation was reported to be faster in several studies [26,108–110].

Major deactivation in MFI catalysts is caused by coke formation at the external surface of zeolite [6]. In a study by Schmidt et al., characterisation of deactivated ZSM-5 was performed to investigate the deactivation and reactivation of both micro and mesoporous ZSM-5.

Diffusion limitation created by micropores is the main reason of the less efficient use of interior layer of crystals. Therefore, coke was mainly observed in the outer shell of ZSM-5 crystals, which prohibits the access to acid sites and leads to poor catalytic performance (**Scheme 2.10**). More coke was formed in mesopores due to a higher external surface. The mesoporous ZSM-5 was also evenly deactivated over the whole crystal, explaining the higher conversion capacity of methanol and lifetime (**Scheme 2.10**) [111].

Framework dealumination causes irreversible damage to the activity of catalyst which cannot be restored. On the other hand, coking of the catalyst is reversible by burning off the carbon residues under mild conditions [112]. Industrial regeneration of the catalyst proceeds either via thermal treatment or washing with a solvent. Reported by Schmidt et al. [97], though having

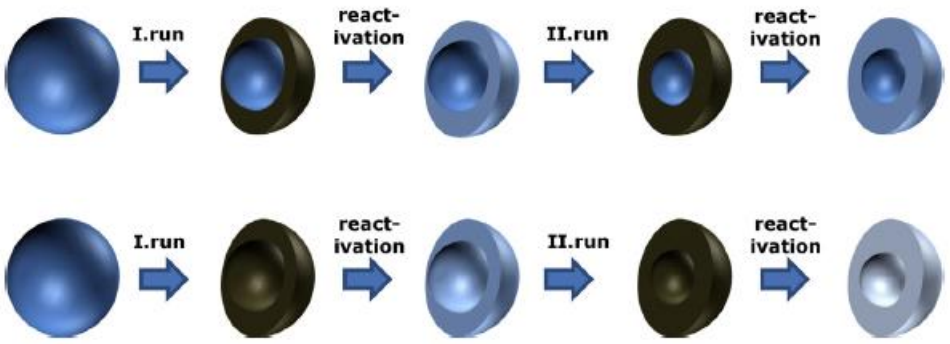


**Scheme 2.10**. Deactivation behaviour of micro (Top row) and mesoporous (Bottom row) ZSM-5 and the impact on the acid sites after the reactivation. (The intensity of the particle colour represents the acid site density. The dark parts of the particle represent the location of coke after deactivation.) [111]

a reduced lifetime, most activity of reactivated microporous ZSM-5 was recovered. This is in line with the fact that the coke shell stops conversion and that high amounts of inner particles do not deactivate (**Scheme 2.10**). However for mesoporous ZSM-5, a loss of catalytic activity was observed from reactivated zeolite. This was explained by irreversible loss of Brønsted acid sites due to the removal of framework aluminium during burning the coke [41].

Recent studies suggested that deactivation of MTH catalysts, in which the reactants are the dominating source of coke, might be related to formaldehyde or similar intermediates formed via reactions [113,114]:

$2CH_3OH \rightarrow CH_2O + CH_4$ $\Delta G^o_{298}$ =160.8 kJ·mol$^{-1}$

$CH_3OH \rightarrow CH_2O + H_2$ $\Delta G^o_{298}$ = 49.3 kJ·mol$^{-1}$

$CH_3OH + C_nH_{2n} \rightarrow CH_2O + C_nH_{2n+2}$

$\Delta G^o_{298}$ =-51.8 (n=2), -48.8 (n=3) kJ·mol$^{-1}$

Those studies support early observations by Hutchings et al. who proposed that formaldehyde is formed during the MTH and induces deactivation due to the promotion of polymerization of hydrocarbon species [115,116]. Later, it has been reported that formaldehyde is formed on Lewis and Brønsted

sites in MFI. The hypothesis is that formaldehyde promotes the formation of oxygen-rich coke, which is observed during the early stages of reaction and gradually evolves into hydrogen-deficient carbon residues [117]. Methanol may also react with mono- and polycyclic aromatic compounds to form additional aromatic rings, as exemplified by the reaction

$$C_6(CH_3)_6 + CH_3OH \rightarrow C_{10}H_5(CH_3)_3 + \mathrm{H_2O} + 6\,\mathrm{H'}$$

Methylation and hydride transfer reactions are important in this type of coking process. However, the mechanism leading to the extra aromatic ring is still not fully revealed [118].

## 2.4 MTH process

The methanol to hydrocarbons (MTH) reaction is currently among the fastest evolving industrial processes for converting $C_1$ carbon sources to higher hydrocarbons, with at least 12 industrial plants being commissioned since 2009 [14,119].

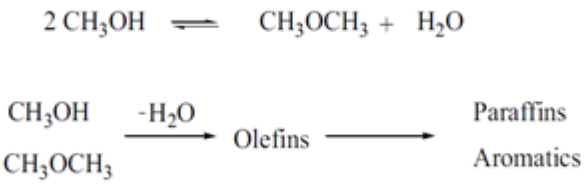


**Scheme 2.9**. Simplified MTH reaction pathway

The methanol conversion, selectivity towards the $C_{5+}$ range products and stability of catalyst against deactivation are several key aspects that need to be considered to optimise the catalytic performance of ZSM-5 in the MTH process. Various approaches have been investigated regarding tuning reaction conditions and modification of the catalyst.

The classical representation of reaction path in the conversion of methanol to hydrocarbons could be summarised to several consecutive reaction steps (**Scheme 2.9**).

The first step is the fast equilibration of methanol with the dimethylether (DME) which is the dehydration product of methanol. In the second step, the equilibrium mixture of methanol and DME converts to olefins as well as aromatic and alphabetic hydrocarbons. This step is well known as a mainly autocatalytic reaction then the C-C-coupling produces some light olefins. The oxygenates are considered to bound by the previously formed olefins or by a so-called hydrocarbon pool consisting of polymethylated benzenes, residing in the micropores of the zeolite lattice [120]. Subsequently cracking forms light olefins. The coke is formed by the polymerisation of the aromatic species contained in the hydrocarbon pool inside the micropores and deactivates the catalyst. The MTH process can be further modified toward preferential gasoline production (MTG), propylene production (MTP) and olefin production (MTO) by appropriate choice of catalyst/support system and operating conditions such as pressure and temperature [121]. H-ZSM-5 (MFI) catalysts are most common for the methanol-to-gasoline (MTG) process, and H-SAPO-34 (CHA) catalysts are well known for the methanol-to-olefins (MTO) process [122].

### 2.4.1. Methanol-to-gasoline (MTG) process

The MTG process is considered one of the widely used technologies for the production of high-octane gasoline from biomass, natural gas and coal [6,123–127]. Biomass thermochemical-derived intermediates containing a large fraction of oxygenated compounds (less than $C_6$) are chemically and thermally unstable and cannot be used as fuel directly. However, after deoxygenation, liquid hydrocarbon molecules can be a direct feed into current petroleum refineries or be a direct replacement of diesel gasoline [128].

The MTG process was discovered in the early 1970s by researchers at Mobil [4] and later commercialised in New Zealand where Mobil, in partnership with New Zealand government, built a 14500 bpd plant based on natural gas converting synthesis gas into methanol [6]. In the fixed-bed process, the reaction is split into two parts (**Figure 2.6**). In the first part,

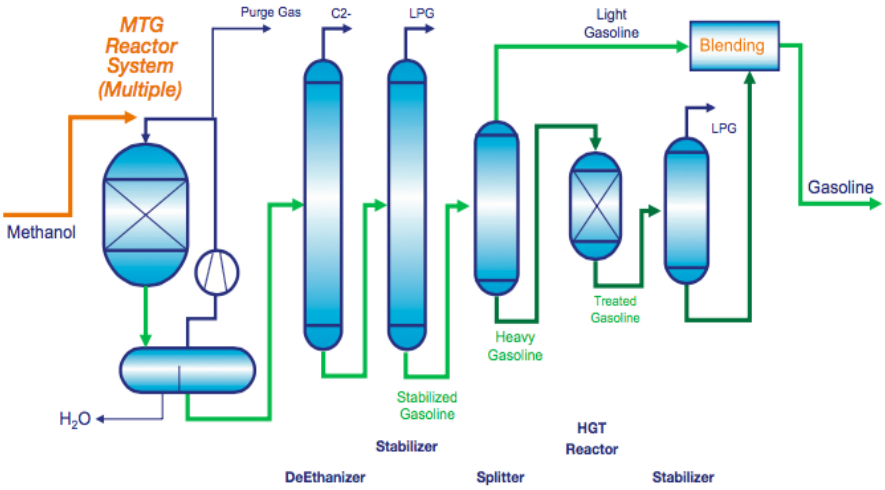


**Figure 2.6**. Flow diagram of MTG process operated in New Zealand [256]

methanol converts into dimethyl ether (DME) and forms an equilibrium mixture containing methanol, DME and water, releasing 15-20% of the overall heat of reaction. The second step is the conversion of DME into gasoline-range hydrocarbons and water over the designed ZSM-5 zeolite catalyst [129].

**Table 2.1**. Properties of MTG gasoline vs. US conventional refinery gasoline [130]

| | Summer 2005 | Winter 2005 | MTG gasoline |
|---|---|---|---|
| Oxygen (WI%) | 0.95 | 1.08 | - |
| API Gravity | 58.4 | 61.9 | 61.8 |
| Aromatics (%Vol) | 27.7 | 24.7 | 26.5 |
| Olefin (vol.%) | 12.0 | 11.6 | 12.6 |
| RVP (psi) | 8.3 | 12.12 | 9 |
| T50 | 211.1 | 199.9 | 201 |
| T90 | 330.7 | 324.1 | 320 |
| Sulfur (ppm) | 106 | 97 | 0 |
| Benzene (%Vol) | 1.21 | 1.15 | 0.3 |

The reactor effluent is then cooled down and separated into gas, liquid hydrocarbons and water. The gas phase, mostly light hydrocarbons, is recycled to gas compressor. Essentially all of the non-hydrocarbons, $C_1$-$C_4$ gases are removed by distillation. Methane, ethane and some propane are

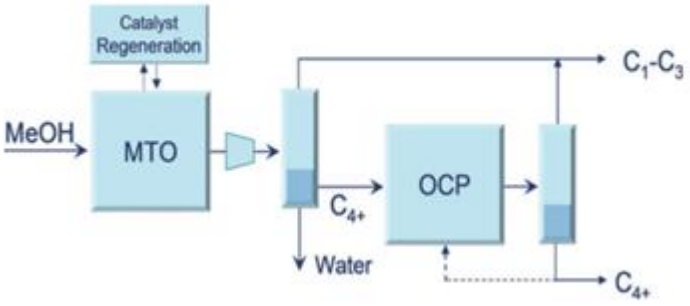


**Figure 2.7**. INEOS MTO fluidized bed process over SAPO-34 combined with UOP/Total OCP [6]

removed in a de-ethanizer. The stabiliser could then remove propane and part of the butane. Stabilized gasoline then flows to a splitter where it is separated into light and heavy gasoline fractions [129].

The MTG reactors were a successful example regarding scaling up from 500 kg/d to 1700 t/d. Gasoline yield, purity and catalytic performance were consistent at a high level in all pilot plant data. **Table 2.1** compares the MTG gasoline properties with the average properties of conventional gasoline sold in the US markets in 2005 [130]. The MTG gasoline has virtually identical properties as US conventional refinery gasoline with two outstanding difference being lower benzene content and zero sulphur.

### 2.4.2 Methanol to Olefins (MTO) process

The selectivity of methanol conversion could be tuned to light olefins (over 80%) over an H-SAPO-34 catalyst. However, opposed to H-ZSM-5, H-SAPO-34 has a lower resistance against coking, which indicates that this process requires frequent catalyst regeneration and efficient temperature control. In the 1990s, UOP and Norsk Hydro (now INEOS) developed an industrial MTO process based on H-SAPO-34 in a low-pressure fluidized-bed [131]. Later in 2009, combining with an olefin cracking process (OCP) by UOP/Total Petrochemicals (**Figure 2.7**) [132], this process was semi-commercialised in Feluy, Belgium with methanol feed of 3.65 kt/y and a

plant was also constructed in Nanjing, China with a production of olefins at 295 kt/y.

Lurgi developed the MTO process further to maximize the selectivity of propene over H-ZSM-5 zeolite with high Si/Al ratio, which eventually became the methanol-to-propylene (MTP) process [133]. As shown in **Figure 2.8**, undesired products, such as primary olefins, ethane and butenes, are recycled to the MTO conversion reactor. Feed injection between beds and recycling of $C_2$ and $C_{4+}$ provide a heat sink for exothermic reactions. To increase selectivity to olefins, low pressure (close to atmosphere) and high temperature (460-480 $^oC$) was applied. The first

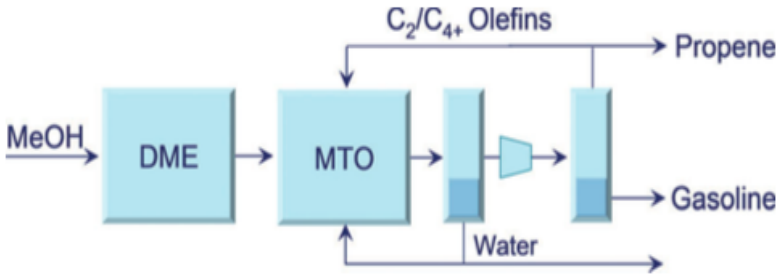


**Figure 2.8**. Lurgi MTP process: Adiabatic dehydration reactor for DME synthesis and parallel adiabatic reactors with interstage feed (quench) addition and recycle of process condensate and $C_2$ and $C_4$+ olefins [6].

plant of this process was started up in China in 2010 with a production at 500 kt/y of propylene and 185 kt/y of gasoline as a major by-product.

The conversion step of methanol is strongly exothermic. The produced heat can result in hot spots due to inefficient heat transfer in the reactor. The hotspot issue leads directly to damage of the acidic structure of catalyst, thus low stability of catalyst and shifted selectivity of products [102].

Over the last decade, increasing interests have been drawn on microstructured reactors that form now-a-days a new class of chemical reactors [134,135]. Their small dimensions and high surface-to-volume ratios provide several advantages over conventional fixed bed reactors, such as higher heat and mass transfer rates, operation under specific conditions that are hard to achieve in the conventional reactors [136–138]

and a possibility of integrated chemical analytic platforms for fast data analysis [139]. Due to their small diameter, microchannels have very good heat and mass transfer properties. Therefore, the rate of reactions that are limited by heat or/and transfer in a conventional reactor, can be increased by performing the reaction in a microreactor, leading to process intensification. Furthermore, non-uniformities in temperature (in the case of fast, highly exothermic reactions [140]) can be avoided in a microreactor, which can result in improved selectivity and yield. The temperature uniformity also makes microreactors well suited for measuring intrinsic reaction kinetics. The catalytic material is usually deposited as a thin coating at the walls of reactor channels. Zeolite interfaces are excellent candidates for microreactor applications because of their remarkable possibilities in MTH catalysis.

## 2.5 Numerical modelling of microstructured reactors

Microreactors also differ from conventional reactors in a number of ways, which are of importance for the development of mathematical reactor models [134]. Reactor modelling is an important aspect of chemical engineering, since it is the basis for the design and optimization of chemical process equipment. Since the flow in the channels is laminar, the accuracy of microreactor models is higher than of conventional reactors, which makes the design of microreactors more reliable.

In microstructured reactors, simple 1D correlations such as constant surface temperature or constant heat flux through surface are not always the case. Heat transfer in microreactor consists of both convection in the gas flow and axial conduction in the solid. The volume fraction of solid wall material is much higher in microreactors than in macroscopic equipment, which makes solid heat conduction an important factor in microreactors, while it can usually be neglected in conventional reactors. The choice of the wall material and flow mode (co-current or counter-current) depends on the ratio of convective and conductive heat fluxes [141]. A ratio of the

fluid conductive flux to the convective one is typically in the range of 0.001-0.01 in long channels with the length to diameter ratio of 100 [142]. Therefore conductive heat flux in the fluid could usually be safely neglected in microchannels.

Small reactors are more sensitive to their outside environment than conventional reactors therefore heat losses to the surroundings need to be included in their designs. Many studies were carried out to analyse heat transfer in microreactors and their results demonstrated considerable deviations from well-established correlations [143,144].

Due to the reactor's small size, numerical simulations are critical to understand heat and mass transfer phenomena occurring in the systems and help guide further improvements. Fluid flows in microreactors are governed by partial differential equations (PDE) which represent conservation laws for the momentum, mass, and energy. Computational Fluid Dynamics (CFD) is used to replace such PDE systems by a set of algebraic equations which can be solved using numerical methods. The basic principle behind CFD modelling is that the simulated region is divided into small cells. Differential equations are discretized and represented in terms of the variables at any predetermined position within the cell. Then these equations are solved iteratively in a numerical solver until the solution reaches the desired accuracy. The existence of a singular point in the microchannel was reported by several group when a cold gas was heated by a hot channel wall [145,146]. After this point, the heat flux changed the direction back to the surface. This singular point can also be shifted downstream to the channel outlet with increased Re number. However, the heat flux can still be described by conventional 1D heat transfer correlations [141]. The boundary conditions comprised uniform temperature and axially uniform heat flux with circumferential temperature uniformity (so-called thin wall boundary conditions). The CFD simulations showed ca 10% deviations, which are acceptable for initial designs. The thin-wall CFD model was recommended by the authors instead of 1D correlations to model heat transfer in microchannel heat-exchangers [147].

However, 2D and 3D numerical simulations are often needed for situations including changing flow composition along the reaction channel. Most of the models found in the literature are two dimensional.

### 2.5.1 Two dimensional models

Two dimensional models provide more accurate predictions and more complicated designs compared to one dimensional models, while not requiring the high computing power needed for three dimensional simulations. They assume that variables change predominantly in two directions.

One of the earliest two dimensional models was developed by Karim et al. [148] and was used to compare the performance between a packed bed and a wall coated microreactor. They used the model to study the temperature profiles, impact of reactor size on apparent activity and for the wall coated reactor, the effect of catalyst wall-coating thickness and reactor diameter on apparent activity.

Liu and Garimella [149] performed a CFD study of fluid flow and heat transfer in both conventional and micro channels and confirmed that the heat transfer coefficients were the same in both cases. This is also in line with the finding that experiments with single microchannels are in good agreement with predictions using published correlations [141]. The forced convective heat transfer was studied and compared to various geometric configurations of microchannel which showed a significant effect on heat transfer and flow characteristics [150]. Several groups also claimed that extended internal surface of microchannels such as cavities, ribs and fins could improve heat transfer rates [151–153].

Stefanidis and Vlachos [154] developed a model of a parallel plate microreactor/heat-exchanger where propane combustion and methane steam reforming occur on opposite sides of the wall. For the heat and mass transfer, they used standard continuity equations, gas-phase and solid phase energy balance, and the gas and surface species mass balance.

They determined that a co-current flow configuration would minimize hot spots and give better overlap of reaction zones, so this configuration was chosen for the follow up study.

A CFD study on heat transfer in a wall-coated methanol steam reformer microreactor with a porous catalytic coating was carried out by Chen et al. [149]. The temperature profile was observed to be non-linear with lower heat transfer coefficient at inlet and outlet of reformer. It was also claimed that thickness of catalytic coating also played a role effecting heat flux and temperature distribution.

While the 2D models are far superior to one dimensional models, they still have many limitations. They are able to show changes in the x and y directions while it is assumed that changes in the z direction are not significant. This works well for near cylindrical geometries. However 2D models require less computational power than three dimensional designs, which can be an advantage, especially in the design phase. However, most small scale microreactors are planar systems which means that the physical phenomena changes in the z-direction. Therefore, to achieve greater accuracy in predicting and understanding reactor performance, 3D models are needed [147].

### 2.5.2 Three dimensional models

With an increase in computing power over the last decade, 3D reactor modelling became possible. One of the first 3D models was developed by Alfadhel and Kothare [155]. They modelled a Si-based water-gas-shift reactor. In 2009, researchers from Yan's group published two papers on numerical studies on plate type microreformers [156]. They examined a multi-channel parallel plate reactor with the focus on the impact of the aspect ratio on methanol conversion, hydrogen and carbon monoxide generation rate. The channel surfaces were coated with a 30 μm thick $Cu/ZnO/Al_2O_3$ catalyst. In the 3D model, it was assumed the methanol-water mixture entered the reactor as a gas and the reaction occurs on the

catalyst layer. They found out that there were non-uniform reaction rates in each microchannel which had a major impact on the reactor performance. The concentration of non-uniformities were heavily dependent on temperature, flow rate and methanol to steam ratio. In the follow up paper they varied the channel aspect ratio (height to width ratio) to understand their impacts on methanol conversion [156]. The simulation results predicted that lower height to width ratio resulted in better overall performance. This was ascribed to the improved surface area for heat transfer.

Jang et al. [157] reported a CFD study on a reactor geometry using a 3D model. The reactor was designed of stainless steel with 20 microchannels each 33 mm long, 0.5 mm wide and 0.6 mm deep. The multi-step kinetics of methanol reforming, methanol decomposition, and reverse water gas shift reaction was applied to obtain concentration and temperature profiles in the reactor. The numerical simulation tools have proven to be extremely useful in evaluating different designs, understanding the manifold impact on flow distribution, projecting thermal distribution and efficiency. Flow maldistribution was reported to be one of the main drawbacks in numbering up of microreactors. Several studies found out that flow maldistribution has a great impact on reactions by shifting and broadening product distribution [152–154].

In this work, a 2D heat transfer and PFR model will be built concerning the influence of geometric dimensions on the temperature uniformity in a microchannel/ heat-exchanger with zeolite inner coating for a MTH reaction. The aim of this work is to reduce the hot-spot formed by the exothermic reaction. A following 3D model will be then built and compared to 2D model for verification.

# Chapter 3

# Experimental

The following chapter provides a general description of the experimental procedures and methods employed in this work. Descriptions of catalyst synthesis (section **3.1**), characterisation (section **3.2**), and catalytic activity measurements (section **3.3**) are provided.

## 3.1 Catalyst synthesis

### 3.1.1 Substrate modification

The AISI 304 stainless steel plates (substrates) were supplied by the Fraunhofer-ICT-IMM (Germany). The size of substrates is given in , and a characteristic image is shown in **Figure 3.1**. Then they were coated with a $TiO_2$ layer by Teer Coating Limited (TCL, UK) to increase of surface hydrophilicity. The plates were first dry blasted for 10 s with glass beads (150 -250 μm) to produce a surface roughness of 10-20 nm. Then a 130 nm $TiO_2$ layer was deposited with chemical vapour deposition using a reactive magnetron sputter ion plating UDP 650 system [158]. A titanium target (99.5 wt.%) was driven by a pulsed DC power supply at 150 kHz frequency and 2.0 μs pulse duration. The oxygen pressure in the chamber was controlled to provide complete oxidation of titanium to titania.

All substrates were boiled in xylene (98 % wt, Sigma-Aldrich) for 1 hour to remove all organic impurities. After drying, the surface was treated by UV-light (450 W Hg lamp) for 30 min to improve surface wettability. Before the synthesis, the substrates were dipped into a 1.0 M tetrapropylammonium hydroxide solution (TPAOH, Sigma-Aldrich) for 10 s and dried. The plates were attached to a PEEK holder and placed into a stainless steel autoclave equipped with a PTFE liner of 45 ml. The volume of the synthesis mixture is 45 ml which was filled with mixture of 20 ml.

**Table 3.1**. Stainless steel substrates used in this study

| Substrate | Size (mm × mm × mm) |
|---|---|
| Flat plate | 10×10×1 |
| Power blasted plate | 10×10×1 |
| Microstructured plate | 60×14×2 |

As shown in **Figure 3.1**, a microreactor plate consists of 14 half-microchannels of a diameter of 0.5 mm and a length of 25 mm. The distance between centres of each channel is 0.2 mm. When stacking two microreactor plates on the channel side, a microreactor with 14 microchannels was constructed.

### 3.1.2 Hydrothermal synthesis

Tetraethylorthosilicate (TEOS, Sigma-Aldrich, 98 wt%) and sodium aluminate (Sigma-Aldrich, >98 wt%) were used as silica and aluminium sources respectively. Synthesis conditions and the relative molar ratio of precursors are summarised in **Table 3.2**.

ZSM-5 was synthesised following the synthesis procedure in Ref. [159], with gel composition: (0.1-0.4) $NaAlO_2$: 8 TEOS: 1 TPAOH: 240 $H_2O$. The following procedure describes the main synthesis steps of ZSM-5 zeolite coatings (and powders):

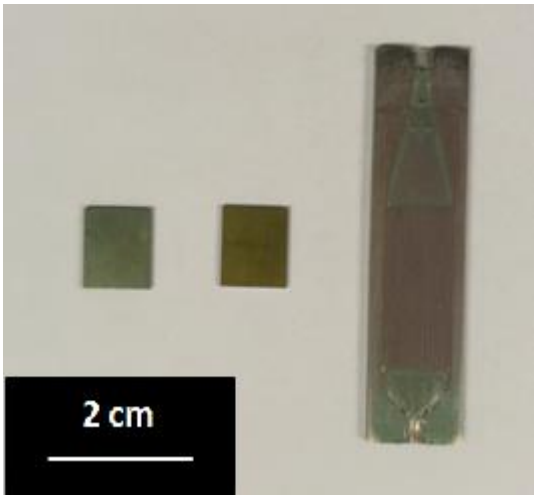


**Figure 3.1**. Initial stainless steel plate (left). Sand blasted plate (middle). Stainless steel microchannel plate (right)

- TPAOH was dissolved in a sodium aluminate solution ($NaAlO_2$, 0.038M).Then the designed amount of TEOS was added and the mixture was stirred for 24 h at room temperature until a homogenous solution was obtained.
- 20 ml of the mixture was transferred to a Teflon lined stainless steel autoclave and the crystallization was performed in an oven at 140 $^oC$ for 2-5 days.
- At the end of the synthesis, the autoclave was quenched with cold water. Obtained materials were washed with deionized water to remove remaining precursors, filtered and dried. The organic template was removed by calcination under a flow of air at 550 $^oC$ for 6 h with a heating rate of 1 $^oC \cdot min^{-1}$.
- The calcined samples were ion-exchanged three times with an ammonium nitrate solution ($NH_4NO_3$, 0.5 M, Fluka, >99 wt%) for 12 hrs at 65 $^oC$ and then calcined at 550 $^oC$ to obtain the H-form of zeolite.

**Table 3.2**. Synthesis conditions

| Si/Al | Si/TPAOH | $H_2O$/Si | Time | Temperature |
|---|---|---|---|---|
| 20-60 | 8.16 | 24-35 | 24-120 h | 140 $^oC$ |

### 3.1.3 Alkaline treatment

The samples (1 g) were treated with a 30 ml NaOH solution (Sigma-Aldrich, 99 wt.%) of different concentrations (0.1, 0.2, 0.4 M) and left at 65°C for 0.5 h. The solutions were then cooled in an ice bath, centrifuged and washed with distilled water until the pH was close to neutral. The samples were dried before ion exchange in a 1 M $NH_4NO_3$ solution (0.5 M) for 3 x 2h at 60 $^oC$. The dried samples were calcined at 550 $^oC$ for 4 h in a flow of artificial air. In additional experiments, a mixture of NaOH (60 mol.%) and TPAOH (40 mol.%) solution [160] with a total $OH^-$ concentration of 0.2 M was used instead of the NaOH solution. The other steps were the same as described above.

### 3.1.3 Calcium ion-exchange

Calcium ion-exchange was performed on powder and coating samples to partially exchange $NH_4^+$ with $Ca^{2+}$. The degree of ion-exchange in the zeolite is determined by $Ca^{2+}$ concentration in the solution. A mixture of $Ca(NO_3)_2$ (0.005-1.0 M) and $NH_4NO_3$ (0.5 M) solution was added to 1 g zeolite. The mixture was stirred for 3 h at room temperature. The large volume of exchanging solution with low $Ca^{2+}$ concentration provides equilibrium due to a threefold surplus of $NH_4^+$ ions in the solution as compared to the ion-exchange capacity of zeolite.

## 3.2 Catalyst characterisation

The catalysts obtained were characterised by X-ray diffraction (XRD), Scanning Electron Microscopy (SEM), $N_2$-adsorption isotherm measurements, ammonia temperature programmed desorption ($NH_3$-TPD) and elemental analysis (ICP-AES).

### 3.2.1 X-ray Diffraction (XRD)

The crystallinity and purity of the material were determined using XRD on a PANalytical Empyrean diffractometer equipped using a Fe filtered Co Kα radiation (λ = 0.179 nm). XRD analysis was performed in the 5-50° 2θ range. Step width and scanning speed were set to 0.02° and 1.5°/min, respectively. The obtained patterns were recalculated to Cu Kα radiation (λ = 0.154 nm) source.

### 3.2.2 Scanning Electron Microscopy (SEM)

Surface morphology was investigated using a Carl Zeiss Sigma scanning electron microscope (SEM) equipped with a field emission electron source and an Oxford instruments energy-dispersive X-ray (EDX) detector. SEM was used to determine crystal size and shape for powder samples. Coatings were studied by cutting the coated plates using a precision saw, placing them into a cylindrical mold and filling with an electro-conductive

phenolic resin mixed with carbon. The resin was cured within a few minutes by heating the mold to 80 °C. Then the solid sample was automatically polished using a series of abrasives. In such way, the samples could be investigated under SEM to determine the thickness of zeolite layers.

Energy dispersive X-ray analysis (EDX) was used to determine the chemical composition (e.g. the Si/Al ratio). The zeolite powder and coating samples were eventually covered with a thin layer of Pt or Au to avoid charging prior to analysis.

### 3.2.3 Nitrogen adsorption-desorption isotherms

$N_2$ adsorption-desorption isotherms were used to determine the surface area and pore size of the zeolites. About 40 mg catalyst was weighed and measured in a relative partial pressure range from 0-0.99 $P/P_0$ at -196 °C. Prior to the measurement, the sample was degassed at 90°C for 0.5 h to remove moisture and then at 400 °C for 5 h. A BELSORP mini-II ASAP2010 porosimeter was used in the measurement.

The t-plot method was used to calculate the surface area of microporous ZSM-5 cataslyst. The Harkins-Jura equation is often used for the analysis of zeolite materials [161].

$$t(\text{Å}) = 3.54 \times \left(\frac{5}{\ln(P_0/P)}\right)^{\frac{1}{3}} \tag{3.1}$$

$$S\left(\frac{m^2}{g}\right) = 15.47 \cdot s \tag{3.2}$$

where $t$ is the statistical thickness, $P_0/P$ is the relative pressure of adsorbing environment, $s$ is the slope of obtained t-plot.

Brunauer–Emmett–Teller (BET) theory was applied to calculate the surface area of mesoporous ZSM-5 catalyst as shown in following equations [162].

$$\frac{1}{v\left(\frac{P_0}{P}-1\right)} = \frac{c-1}{v_m c}\frac{P}{P_0} + \frac{1}{v_m c} \tag{3.3}$$

$$S_{BET} = \frac{v_m N s}{aV} \tag{3.4}$$

$v$ is the adsorbed gas quantity, and $v_m$ is the monolayer adsorbed gas quantity. $c$ is the BET constant, N is the Avogadro's number, $s$ is the adsorption cross section of the adsorbent.

### 3.2.4 Inductively coupled plasma (ICP)

Elemental analysis was carried out with an ICP-AES apparatus (Thermo iCAP 7000). To extract the metals, the catalysts were dissolved in a mixture of HF/$HNO_3$/$H_2O$ (1.5 ml).

### 3.2.5 Pyridine Temperature programmed desorption (TPD)

The acidity of ZSM-5 samples was assessed by the pyridine temperature programmed desorption (TPD) method. The pyridine-TPD profiles were obtained in a tube reactor. The analysis was performed with a quadrupole mass-spectrometer (OMNIStar$^{TM}$) using a m/z =79 signal. Prior to pyridine adsorption, 50 mg of catalyst was pretreated at 450 °C for 1 h in a $O_2$/He mixture flow and then quenched in He flow for 2 h while the sample was cooling down to the desired temperature (125, 175, 225 $^oC$). Subsequently 1.5 vol% pyridine in He flow was introduced until saturation of the sample, indicated by the stabilization of the mass spectrometer signal. The chemisorbed pyridine was desorbed by heating the catalyst from the adorption temperature at a rate of 8 $^oC$/min to 550 $^oC$.

## 3.3 Catalytic activity measurements

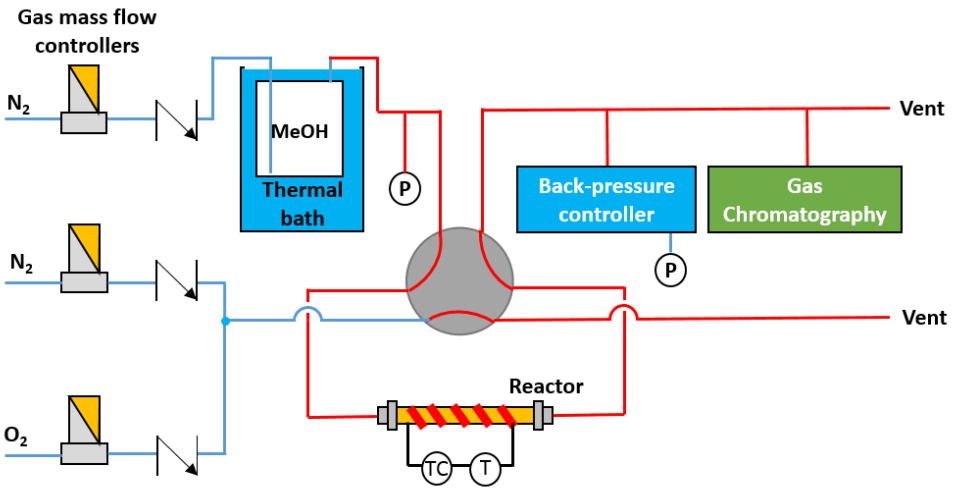


**Figure 3.2**. Schematic view of reactor set-up (Red line: Hot line preheated at 373 K. Blue line: Cold line.)

The reaction was performed in the experimental set-up schematically presented in **Figure 3.2**. A gas mixture preparation section consists of three mass flow controllers that were used to feed carrier gas (99.9 vol.% $N_2$) directly, a methanol (99.99 vol.%)-nitrogen mixture and oxygen flow for calcination. To control the methanol partial pressure, the methanol evaporator was placed in a thermostat (LAUDA ECO RE420) maintained at desired temperature.

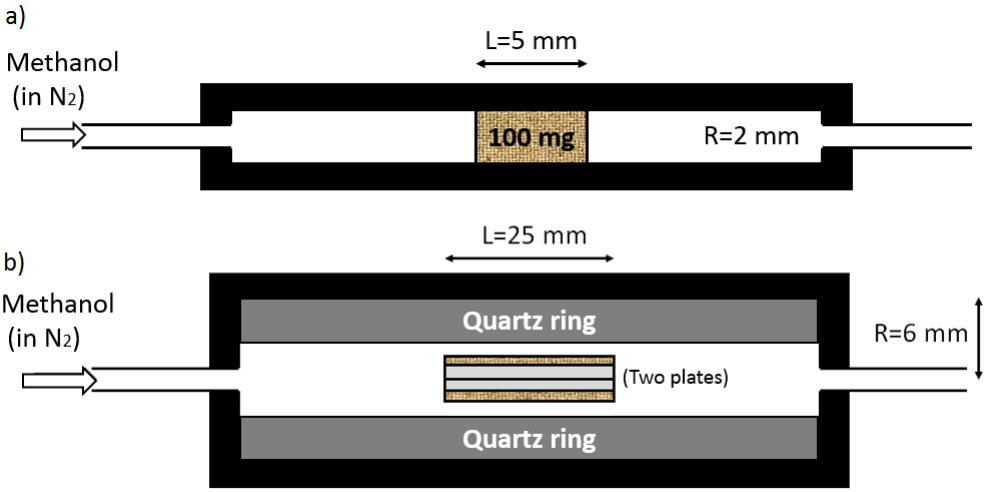


**Figure 3.3**. a) The fixe-bed reactor for ZSM-5 powder catalyst, b) The tube reactor loaded with two plates coated with ZSM-5 catalyst

Two types of reactor were used in this study (**Figure 3.3**). A fixed-bed reactor was used to study pelleted catalysts. The fixed bed reactor was positioned in oven filled with of zeolite pellets (fraction 0.25-0.50 mm). The catalyst was packed in a quartz tubular reactor and fixed with two quartz wool packings. A tube reactor was used to study the performance of catalytic coatings. This reactor has a diameter of 12 mm.

Prior to the reaction, nitrogen flow was used to purge the reactor for 30 min. The pressure in the reactor was maintained with a back-pressure controller (Equilibar). When the pressure and temperature were stable, the inlet flow was switched to the mixture of methanol and nitrogen. The temperature of the reactor was controlled with thermocouples attached to the reactor outer wall.

A small fraction of reaction products were sent to analysis via an additional line connected to the reactor outlet line. The products were analysed with a GC (Shimadzu 2010) equipped with a Supelco Equity-1 column (90 m, 0.53 mm id) and an FID detector. The column was programmed to be kept at 313 K for 6 min, then heated to 240 $^{o}$C at a heating rate of 12.5 $^{o}$C $\cdot$min$^{-1}$ and maintained for 5 min. An example of a chromatogram and further analysis details are presented in Appendix A.

The concentrations of reaction products were calculated based on peak areas. The GC was calibrated using a series of $C_{1-4}$ gases, methanol, DME, a series of liquid hydrocarbons such as n-pentane, n-heptane, p-xylene. The effective carbon number approach provided accuracy of the analysis within 5 % [163] for all hydrocarbons, but for methanol and DME effective carbon numbers were found to be 0.88 and 1.10, respectively.

Methanol conversion (X), product selectivity (S) and product yield (Y) were calculated based on GC-FID areas. During the calculations, methanol and dimethyl ether (DME), which is the condensation product of methanol molecules are considered as reactants, and all non-oxygen containing effluent hydrocarbons are considered as reaction products. The calculations were performed as follows:

Conversion: $X_i(\%) = \frac{C\ in\ products - C\ in\ reactants}{C\ in\ all\ compounds} \times 100$ (3.5)

Selectivity: $S_i(\%) = \frac{C_i}{C\ in\ all\ compounds} \times 100$ (3.6)

Yield: $Y_i(\%) = \frac{X_i \cdot S_i}{100}$ (3.7)

Residence time: $\tau(\mathrm{s}) = \frac{1}{WHSV} \frac{\rho_{MeOH}}{\rho_{cat}}$ (3.8)

Turnover number: $\mathrm{TON}(g \cdot {g_{cat}}^{-1}) = \mathrm{WHSV} \cdot \int_0^t Y_i\, dt$ (3.9)

## 3.4 Temperature programmed oxidation and catalyst regeneration

The rate of coke formation was studied by temperature programmed oxidation (TPO) analysis. 100 mg of spent samples were placed in a reactor. Then a flow of 20 % $O_2$ in $N_2$ (10 mL $min^{-1}$) was fed to the reactor Ar was used as an internal standard. The temperature of the sample was increased to 650 °C at a heating rate of 5 °C $min^{-1}$. The concentration of $CO_2$ in the outlet was monitored continuously by a Quadrupole mass spectrometer (OmniSTAR).

# Chapter 4

# Synthesis and catalytic activity of microporous ZSM-5 catalyst and its coating

## 4.1 Introduction

Thin catalytic coatings on a structured (metal) substrate provide a number of advantages compared to powdered catalysts. Catalytic coatings supported onto channel walls show a very low pressure drop. The substrate allows to reduce the hot spot in an exothermic reaction by additional heat removal mechanism via conduction. This prevents catalyst deactivation due to high temperature sintering of an active component during a reaction or regeneration step.

The hydrothermal synthesis [58,164] is the most promising method to obtain binder-free zeolite coatings for the application in the methanol-to-hydrocarbon (MTH) reaction. This method provides higher catalytic loadings and a direct thermal contact between the coating and the substrate as compared to slurry deposition. In this chapter, a method of zeolite coating synthesis was adopted onto microreactor plates with semi-circular microchannels following the approach originally presented in [159]. The synthesis procedure included the following steps: (i) deposition of a thin titania coating, (ii) UV-treatment of the substrates prior to the synthesis and (iii) the hydrothermal synthesis.

The effect of synthesis conditions (Si/Al ratio, synthesis time, $H_2O$/Si ratio) on zeolite will be discussed. The aim is to obtain ZSM-5 coatings with a thickness in the range 5-30 μm and the Si/Al ratios in the range of 20-60. The coatings obtained are characterised with XRD, BET, SEM and EDX. The effect of design parameters on the yield of the $C_{8\text{-}11}$ hydrocarbons and deactivation kinetics will be studied. The ZSM-5 coatings will also be compared with pellets in a tube reactor in the MTH reaction.

## 4.2 ZSM-5 powder catalyst

### 4.2.1 Optimisation of synthesis conditions

This study takes a literature recipe [165] as a starting point where the growth of ZSM-5 crystals on a molybdenum (Mo) substrate was carried out. Among synthesis precursors, TPAOH was selected as a structure directing agent (template) for the formation of ZSM-5 with high crystallinity and large surface area comparing to other templates [166]. A low amount of TPAOH would result in the formation of an amorphous phase while excessive TPAOH concentration gives elongated crystals that are unlikely to be of high crystallinity [159]. For the silica source, TEOS was selected based on its ability to make ZSM-5 with high crystallinity and a high surface area compared to other silica sources (e.g. colloidal silica, sodium metasilicate) [167]. Sodium aluminate was selected as the aluminium source because it could provide small crystals with high crystallinity compared with other sources [168,169]. ZSM-5 powder samples will be called as ZSM-(Si/Al)-(Crystal size) and respective coating samples ZSMC-(Si/Al)-(Crystal size).

*4.2.1.1 Effect of synthesis time*

**Table 4.1**. Synthesis parameters of ZSM-5 samples

| Sample code | Synthesis time (h) | Si/ Al | $H_2O$/ Si | Crystal size (μm) | Coating thickness (μm) | Relative crystallinity (%) |
|---|---|---|---|---|---|---|
| ZSM-20-0.50 | 24 | 20 | 30 | 0.50 | - | 78 |
| ZSM-20-0.84 | 48 | 20 | 30 | 0.84 | - | 91 |
| ZSM-20-1.04 | 72 | 20 | 30 | 1.04 | - | 100 |
| ZSM-20-1.14 | 96 | 20 | 30 | 1.14 | - | 88 |
| ZSM-20-1.20 | 120 | 20 | 30 | 1.20 | - | 80 |
| ZSM-20-0.40 | 24 | 20 | 25 | 0.40 | - | 75 |
| ZSM-20-1.07 | 24 | 20 | 35 | 1.07 | - | 82 |
| ZSM-30-1.10 | 48 | 30 | 30 | 1.10 | - | 79 |
| ZSM-40-1.70 | 48 | 40 | 30 | 1.70 | - | 102 |
| ZSM-50-2.40 | 48 | 50 | 30 | 2.40 | - | 103 |
| ZSM-60-2.60 | 48 | 60 | 30 | 2.60 | - | 102 |

The Si conversion was calculated as a molar ratio between Si in the zeolite and Si in the precursor. The conversion reaches 35% in 24 h and then remains at a 45% level (**Figure 4.1**). It could be speculated that the nucleation stage is completed in a very short time due to the high crystallization temperature (140 $^oC$). In the subsequent crystallization stage, crystals start to grow and their growth rate is determined by the composition of initial synthesis mixture. This gives a fast rise in the Si

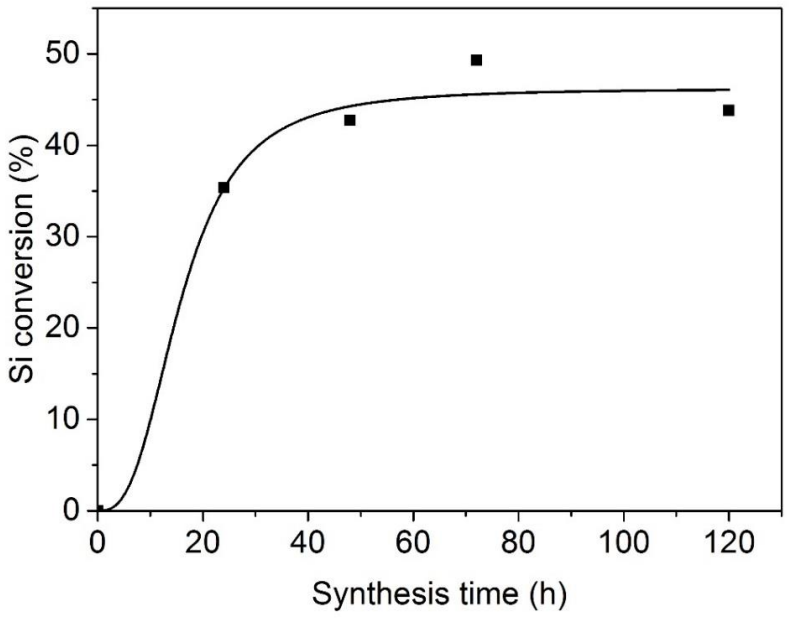


**Figure 4.1**. Si conversion in a synthesis mixture with Si/Al=20 as a function of synthesis time (T=140 $^oC$)

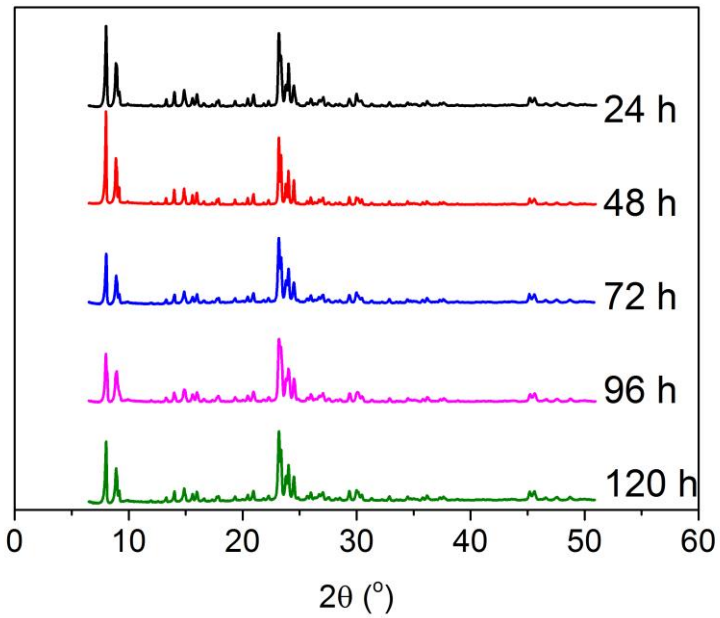


**Figure 4.2**. XRD patterns of the zeolite powder samples ZSM-20-0.50 (24 h), ZSM-20-0.84 (48 h), ZSM-20-1.04 (72 h), ZSM-20-1.14 (96 h), ZSM-20-1.20 (120 h)

conversion in the range of 16-24 h. After this point, further crystallization time results in slower particle growth until they reach a crystallization equilibrium [166]. This result is in agreement with the work of Hu et al. who observed increasing crystal size at low temperature along crystallization time but no change in crystal size after 24 h in a zeolite synthesis at 140 $^{o}$C [170].

**Figure 4.2** shows XRD patterns of zeolite powders obtained at different synthesis times. Main diffraction peaks at 23.18, 23.37, 23.79, 24.03, and 24.50 $^{o}$ 2θ are characteristic for the MFI-type zeolites and confirm the formation of a ZSM-5 structure [159]. All diffraction peaks are almost identical and consistent with a standard ZSM-5 pattern reported [171]. The ZSM-20-1.04 powder sample was selected as the reference samples for its highest crystallinity. The relative crystallinity (**Table 4.1**) also confirms that highly crystalline ZSM-5 were produced and no phases other than ZSM-5 were detected even for a synthesis time of 120 h.

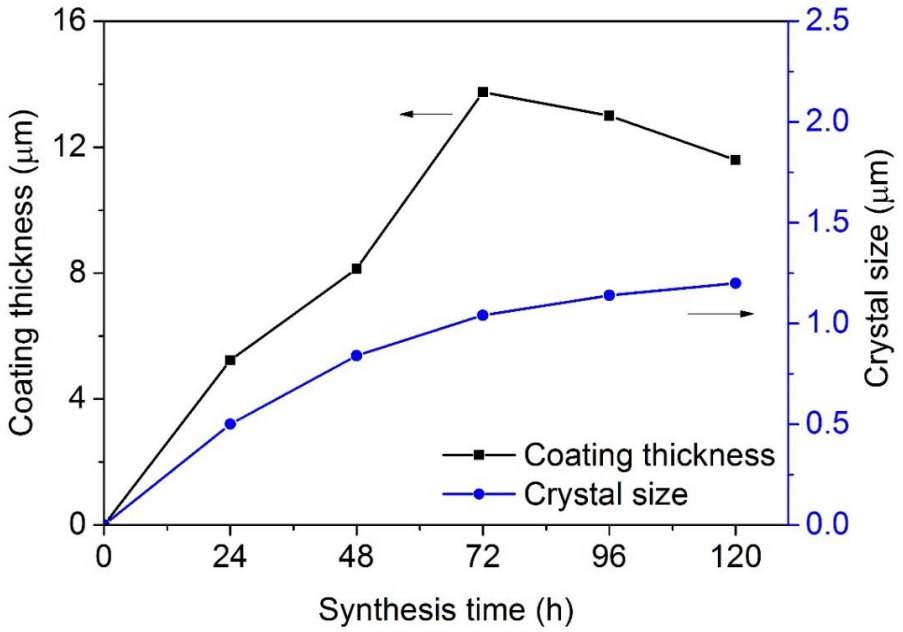


**Figure 4.3**. The thickness of the zeolite coatings and crystal size of ZSM-5 sample with Si/Al ratio of 20, $H_2O$/Si ratio of 30 and different synthesis time

The effect of synthesis time on crystal size of ZSM-5 catalyst was studied on samples with a Si/Al ratio of 20. **Figure 4.4** shows the SEM images of the ZSM-5 zeolites obtained at a synthesis time of 24 h (**Figure 4.4a**) and 120 h (**Figure 4.4b**). The crystal size of ZSM-5 increases to 1.0 μm in 72 h and maintains around 1.1 μm as the synthesis time increases to 120 h (**Figure 4.3**). For synthesis at the high temperature of 140 $^{o}$C, high crystallization rate could reduce the growth period when a longer synthesis time does not have a further impact on crystal size [170].

#### *4.2.1.2 Effect of Si/Al ratio*

##### *Crystal size*

The effect of Si/Al ratio on the crystal size was studied over a series of ZSM-5 zeolites with different Si/Al ratios in the range between 20 and 60. The average crystal size was observed to show an increasing trend with increasing Si/Al ratio (**Figure 4.5**) in line with previous data [78,172]. ZSM-20-0.84 catalyst is observed to have a narrow crystal size distribution with

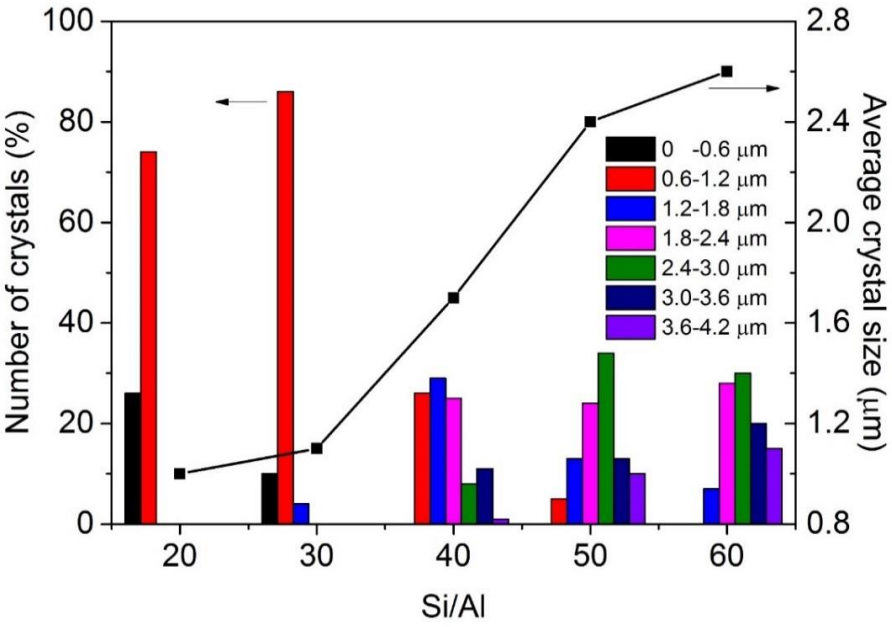


**Figure 4.5**. Average value and distribution of crystal size of ZSM-5 powder samples with different Si/Al ratio

a standard deviation (SD) of 0.177 and an average value of 1.0 μm. The crystal size of ZSM-30-1.10 catalyst increases to 1.1 μm in a narrow distribution with a SD of 0.124. While increasing Si/Al ratio from 40 to 60, the average crystal size increases from 1.7 to 2.6 μm. A wider dispersion (SD=0.8) of crystal size in the ZSM-40-1.70, ZSM-50-2.40 and ZSM-60-2.60 samples with lower Al content are observed. This could be attributed to the fact that new small crystals are formed (**Figure 4.6e**) and also larger crystals are formed during inter-crystal growth (**Figure 4.6d**). A possible explanation is that high Si content during crystal growth accelerates the completion of crystalline structure [166]. This effect could also result in a wide particle size distribution in these 3 samples (**Figure 4.6e**) due to an incomplete growth of some crystals. This result is also in line with the study by Chauhan et al. [71]. The Si/Al ratio will be optimised in the subsequent section based on the catalytic performance.

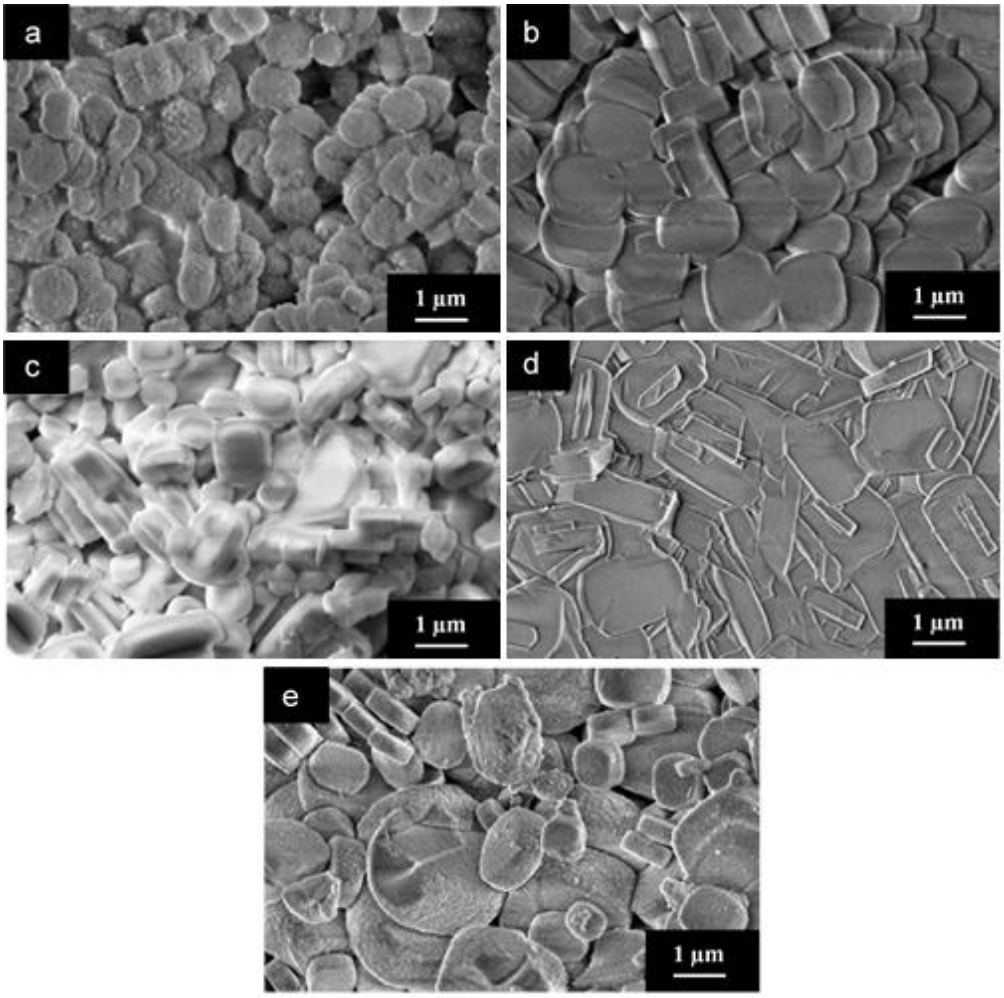


**Figure 4.6**. SEM image of ZSM-5 powder samples: a) ZSM-20-0.84, b) ZSM-30-1.10, c) ZSM-40-1.70, d) ZSM-50-2.40, e) ZSM-60-2.60

### *Porosity*

The nitrogen physisorption isotherms of all samples are classified by Type I (**Figure 4.7**). The early steep uptake in low relative pressure region ($p/p_0<0.01$) is attributed to high microporosity in samples indicating the presence of microporous framework and high crystallinity. A flat region without hysteresis loop is observed at the high relative pressures suggesting the absence of the mesoporous structure, as also confirmed by a low mesopore volume of 0.03 $cm^3 \cdot g^{-1}$ (**Table 4.2**). The external surface area are found to follow a similar trend with increasing Si/Al ratio and crystal size except for the ZSM-60-2.6 sample. The external surface area increases from 121 to 222 $cm^3 \cdot g^{-1}$ with increasing Si/Al ratio to 50. The crystal size increases slightly which is in line with the literature data

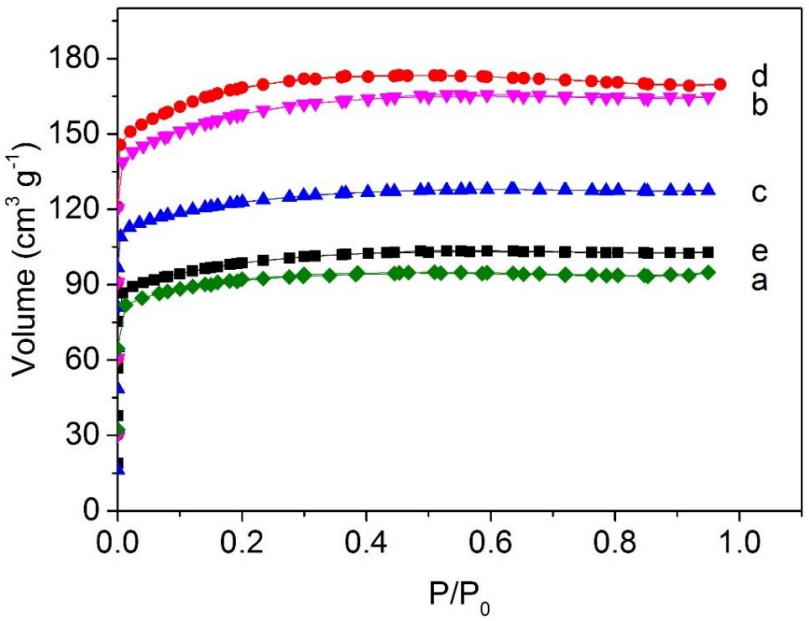


**Figure 4.7**. Isotherms of nitrogen adsorption and desorption of ZSM-5 samples a) ZSM-20-0.8, b) ZSM-30-1.1, c) ZSM-40-1.7, d) ZSM-50-2.4, e) ZSM-60-2.6

[173,174]. The highest value of 600 $m^2 \cdot g^{-1}$ observed for sample ZSM-50-2.40. The external surface area of ZSM-5 zeolite decreases with increasing crystal size [175,176]. The surface area does not follow a monotonous pattern as a result of two competing trends: increase in both crystallinity and crystal size with increasing Si content.

**Table 4.2**. Textural properties of ZSM-5 samples

| **Sample code** | **$S_{ext}$ ($m^2 \cdot g^{-1}$)** | **$V_{micro}$ ($cm^3 \cdot g^{-1}$)** | **$V_{meso}$ ($cm^3 \cdot g^{-1}$)** |
|---|---|---|---|
| ZSM-20-0.84 | 121 | 0.120 | 0.020 |
| ZSM-30-1.10 | 178 | 0.144 | 0.029 |
| ZSM-40-1.70 | 163 | 0.163 | 0.027 |
| ZSM-50-2.40 | 222 | 0.230 | 0.024 |
| ZSM-60-2.60 | 114 | 0.102 | 0.027 |

*Acidity*

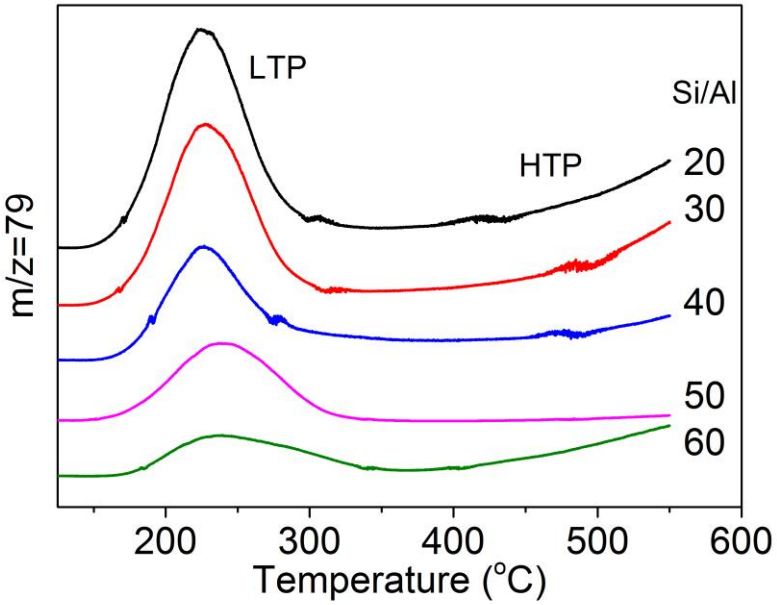


**Figure 4.8**. Pyridine-TPD thermograms obtained at 125-550 °C over ZSM-5 catalysts with the increasing Si/Al ratio

The distribution of acid sites of ZSM-5 catalysts with different Si/Al ratios was determined by pyridine-TPD. The desorption patterns over the samples show a typical low temperature peak (LTP) at 150-300 °C and a high temperature peak (HTP) above 450 °C (**Figure 4.8**). These result are in line with the reported literature data [177].The same terminology in describing different acid sites is applied as introduced by Shirazi [78]. The LTP and HTP correspond to the weak and strong acid sites, respectively. They both show decreasing trend as the Si/Al ratio increases, which is attributed to the decrease of both framework and extra-framework aluminium sites[78]. The total amount of pyridine adsorbed weak and strong acid sites over ZSM-5 catalysts with different Si/Al ratios is calculated and listed in **Table 4.3**. In line with literature [18], this result shows the decreasing total acidity of ZSM-5 samples with increasing Si/Al ratio.

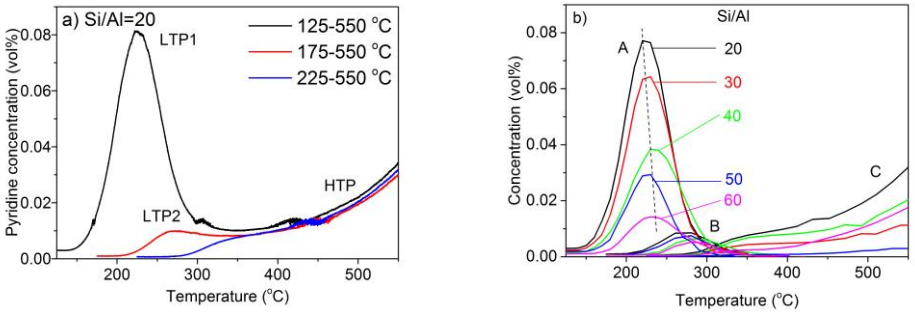


**Figure 4.9**. a) Desorption profiles at different starting temperature over the ZSM-5 catalyst with Si/Al ratio of 20. b) Differential curves of pyridine-TPD thermograms between two adjacement starting temperatures in **Figure 4.8** over the samples with the increasing Si/Al ratio.

In order to distinguish different acid sites, TPD spectra were measured by increasing the starting temperature (125,175,225 $^{o}$C). For example, the curves for the ZSM-20-0.8 sample is shown in **Figure 4.9a**. Two desorption peaks at low temperature (LTP1 and LTP2) and a HTP are observed. The amount of each type of acid site is estimated by subtracting the two adjacent curves in **Figure 4.9a**. Within each of the 125-175, 175-225 and 225-550 $^{o}$C segment, the acid sites are assumed to have an identical strength. The area of each peak represents the amount of acid sites with certain strength. The segment A (125-175 $^{o}$C) representing the amount of weak acid sites, clearly decreases as Si/Al ratio increases from 20 to 60.

**Table 4.3**. Pyridine-TPD for different type of peaks for ZSM-5 with different Si/Al ratios

| Sample code | Total acidity (mmol·$g_{cat}^{-1}$) | LTP A (mmol·$g_{cat}^{-1}$) | LTP B (mmol·$g_{cat}^{-1}$) | HTP C (mmol·$g_{cat}^{-1}$) |
|---|---|---|---|---|
| ZSM-20-0.84 | 0.793 | 0.452 | 0.058 | 0.283 |
| ZSM-30-1.10 | 0.538 | 0.372 | 0.045 | 0.121 |
| ZSM-40-1.70 | 0.407 | 0.258 | 0.038 | 0.111 |
| ZSM-50-2.40 | 0.327 | 0.224 | 0.064 | 0.039 |
| ZSM-60-2.60 | 0.237 | 0.091 | 0.029 | 0.117 |

The segment B (175-225 $^{o}$C) does not show clear trend with increasing Si/Al ratio. The segment C also shows a decreasing trend, indicating decrease in the amount of strong acid sites. As reported by Jin and Li [178], the acid sites that desorbs pyridine molecule at low temperature below 200 $^{o}$C consist both weak Bronsted acid sites and weak Lewis acid sites, which corresponds to the A segment in **Figure 4.9b**. A shift of the segment A to higher temperatures (**Figure 4.9b**) indicates the existence of aluminium in extra-framework positions[78]. Segment B represents Lewis acid sites which desorbs pyridine at 200-300 $^{o}$C. The segment C classified as strong Bronsted acid sites is observed over 450 $^{o}$C. However this segment could not be fully captured due to the heating limitation on the quartz reactor. As similar to the segment A, the amount of acid sites in the segment C decreases as Si/Al ratio increases. The strong Bronsted acid sites are also determined as the key acid sites catalysing methanol conversion. A decrease in their number was reported to result in almost the same decrease in methanol conversion [179].The large width of segment C indicates a rather wide acidity spectrum for strong Bronsted acid sites in line with the previously reported microcalorimetry data [180].

*4.2.1.3 Effect of $H_2O$/Si ratio*

The water content in the synthesis solution is another key factor that has a major influence on the zeolite particle size. A low supersaturation decreases the concentration of structural template and the solubility of silica and aluminium species which eventually leads to large particles [166].

The effect of $H_2O$/Ai ratio on the crystal size was studied by diluting the synthesis mixture to different levels ($H_2O$/Si=25-35). The SEM images of zeolite catalysts after hydrothermal synthesis are shown in **Figure 4.10**. The corresponding particle size distribution is shown in **Figure 4.12**. When the $H_2O$/Si ratio increases from 24 to 35, the average crystal size of ZSM-5 samples increases from 0.4 to 1.1 µm. A narrow distribution of crystal size with a low SD of 0.052 µm was observed on the ZSM-20-0.40 sample

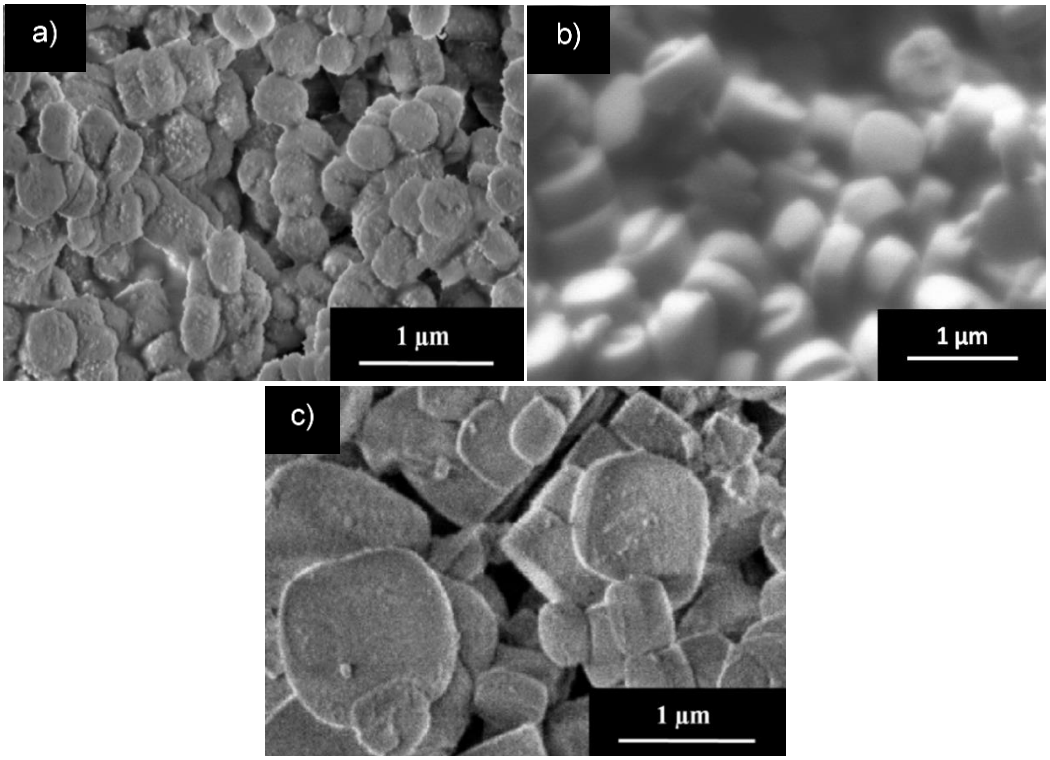


**Figure 4.10**. SEM images of samples a) ZSM-20-0.40, b) ZSM-20-0.84, c) ZSM-20-1.07

while this value increases to 0.210 and 0.370 when the mixture is further diluted by water (ZSM-20-0.40 and ZSM-20-1.07) respectively. In the synthesis solution with lower water content, the higher alkalinity leads to the formation of more crystal nucleus, which in turn results in small crystal size [175]. However some of these particles are amorphous (**Figure 4.10a**). Low water content in the synthesis solution increases in the possibility of forming structures other than MFI [181]. With higher dilution ratio, larger crystals were synthesised (**Figure 4.10c**). The wide distribution of crystal size in samples obtained from diluted solutions indicates low nucleation and crystallization rates due to decreased dissolution of the nutrient pool at low saturation [166,182].

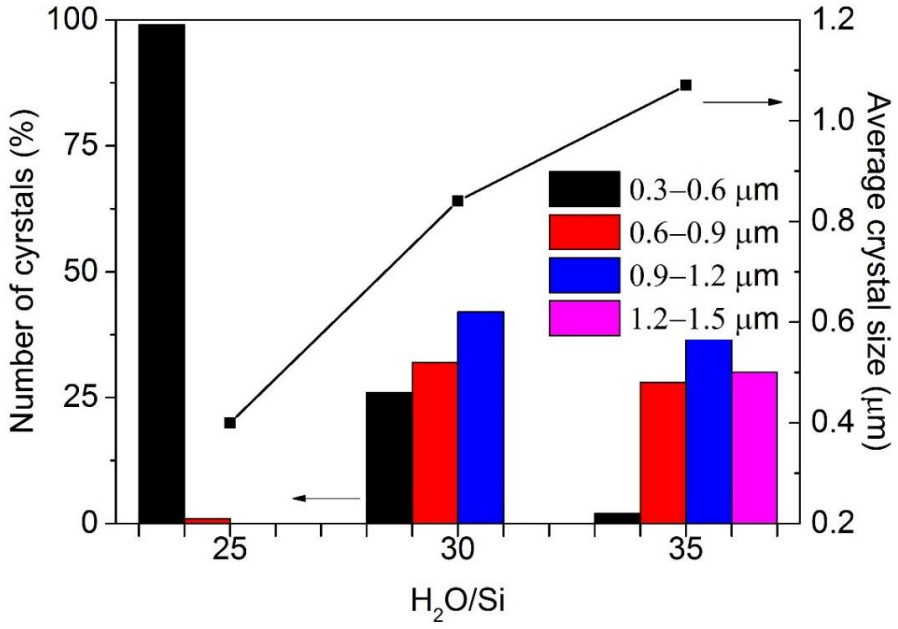


**Figure 4.11**. Crystal size distribution of powder samples ZSM-20-0.40, ZSM-20-0.84 and ZSM-20-1.07

### 4.2.3 Catalytic performance

*4.2.3.1 Effect of Si/Al ratio and crystal size*

Synthesised ZSM-5 powder samples with different Si/Al ratio were tested in the MTH reaction to study the influence of Si/Al ratio and crystal size on catalytic activity. In **Figure 4.12**, an initial methanol conversion above 80% was observed over all samples. An increase in methanol conversion occurs at the initial stage of the reaction as could be seen in the insert. This delay of initial equilibrium between oxygenates and hydrocarbons could be caused by internal diffusion limitations in larger crystals. This diffusion limitation could form an initial methanol 'by-pass' around crystals and consequently results in slightly lower methanol conversion. Deactivation of the catalyst is mainly caused by the formation of carbonaceous residues on the surface and inside pores covering acid sites. They are commonly known as coke composited by polyaromatic hydrocarbons [183]. It is also a complex process due to factors like topology, crystal size, defects, strength and density of Brønsted acid sites which have been proposed in

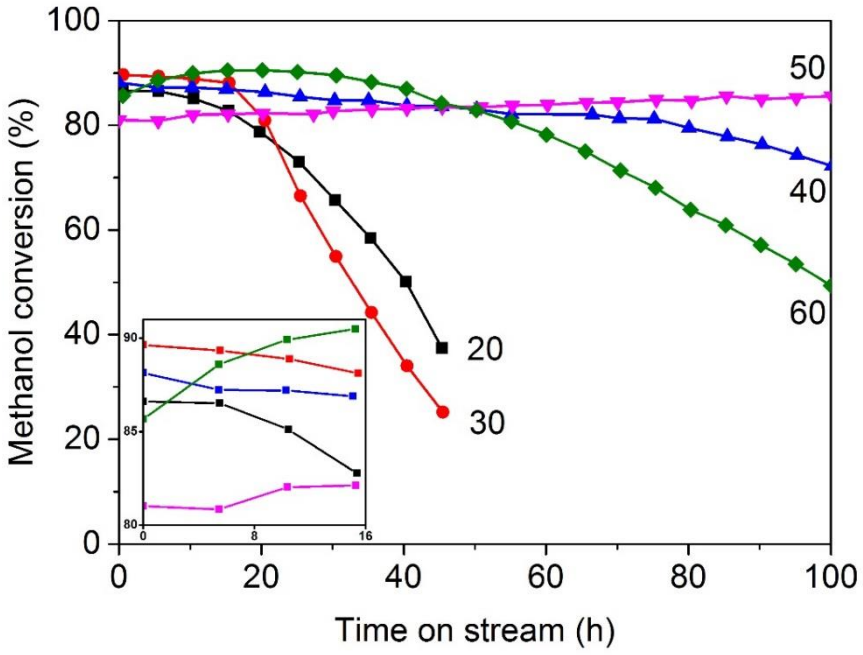


**Figure 4.12**. Methanol conversion over ZSM-5 samples with different Si/Al ratios. (T=370 $^{o}$C, P=0.4 bar, WHSV=1.5 $h^{-1}$)

literature [184,185]. The deactivation for the sample with Si/Al ratios of 20 and 30 starts after 20 h and terminates the reaction fully within 50 h. As the amount of acid sites is proportional to Al content in the zeolite, the high initial conversion but fast deactivation could be attributed to high acidity [79,97]. The ZSM-40-1.7 and ZSM-50-2.4 samples demonstrate stable catalyst activity in the first 100 h on. The ZSM-5 samples with high surface area (ZSM-50-2.4) (**Table 4.2**) could enhance the coke capacity, thus reduce the coking rate [175]. The other reason of improved stability is that the reduction of acidity could also limit the subsequent and unwanted conversion of olefins into heavier poly-aromatics and coke [79,186]. However, after 50 h, the sample with the lowest acidity (Si/Al=60) shows no catalytic activity to the desired products due to a low amount of total active sites and low coke capacity due to a relatively low surface area.

The initial conversion rate over all ZSM-5 catalysts is 44 mol·kgcat$^{-1}$·h$^{-1}$ in this study. The selectivity towards the $C_{8-11}$ aliphatic and the $C_{6-10A}$ aromatic hydrocarbon fractions is shown in **Figure 4.13**. The selectivity towards $C_{8-11}$ gasoline fraction increases over larger crystals. The highest selectivity of 16% is observed at a Si/Al of 20 and 50. The increase of $S_{8-11}$ over ZSM-50-2.4 comparing ZSM-50-1.8 also suggests that longer diffusion path and contact time in a larger crystal could promote the formation of larger hydrocarbons according to the hydrocarbon pool build-up mechanism [187]. The selectivity towards $C_{6-10}$ aromatics is shown to be mainly affected by Si/Al ratio. A high selectivity towards aromatics of 26% observed over samples with a Si/Al ratio of 20 is attributed to the strong acid sites favouring hydrogen transfer and aromatisation reactions, as previously reported for ZSM-5 catalysts with high Al content [173]. Longer diffusion distance and contact time in a larger crystal could also promote the formation of aromatics, which leads to high coking rate [26]. The formation of aromatics is reduced over the samples with higher Si/Al ratio due to a lower density of strong acid sites. For ZSM-60-2.6, the lowest density of acid sites results in a low $S_{6-10A}$ of 17%. High Si/Al ratio is preferred for the production of light olefins as reported in literature [188,189]. The formation of light hydrocarbons ($C_{1-4}$) usually occurs with dealkylation of aromatics due to sterical restrains by an intermediate pore size in ZSM-5 structure [190].

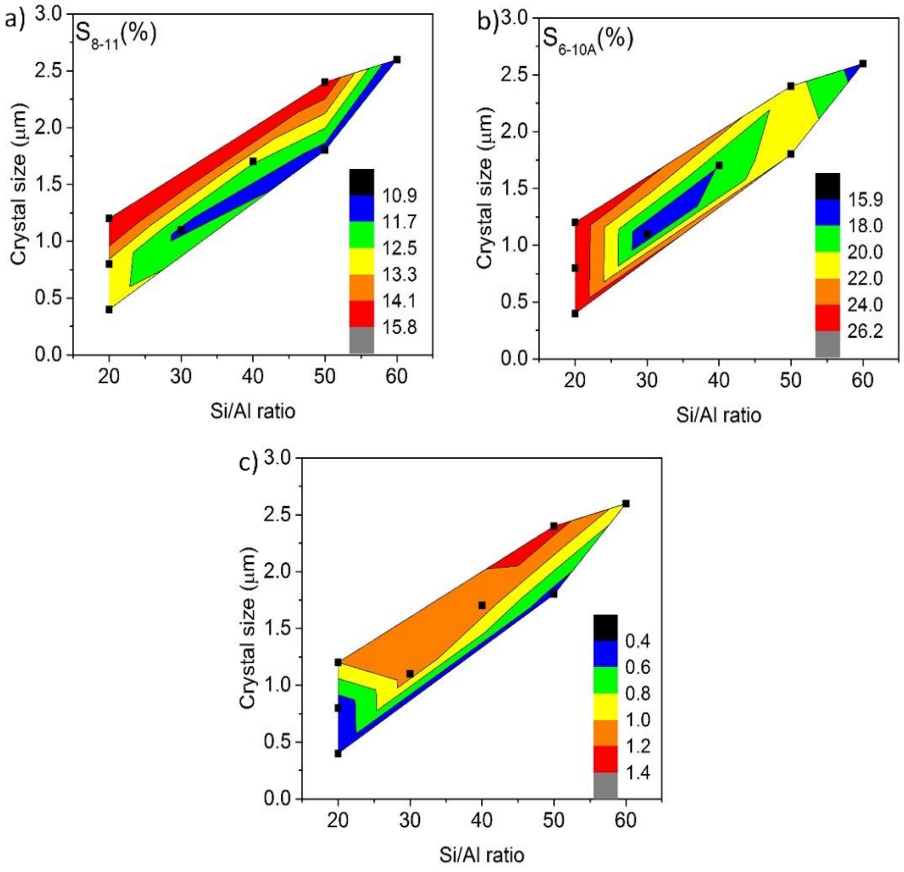


**Figure 4.13**. Hydrocarbons selectivity towards a) $C_{8-11}$, b) $C_{6-10A}$ plot in MTH reaction over ZSM-5 samples and c) weighing function with different Si/Al ratios and crystal sizes (T=370 °C, P=0.4 bar, WHSV=1.5 $h^{-1}$)

To optimise the catalyst performance a design parameter ($f$) is introduced which is defined as follows:

$$f = \frac{S_{8-11,i} - S_{8-11,min}}{S_{8-11,max} - S_{8-11,min}} + \frac{S_{6-10A,max} - S_{6-10A,i}}{S_{6-10A,max} - S_{6-10A,min}} \quad (4.1)$$

where $S_i$ is selectivity over each sample. The function has a value between 0 and 2. A low value corresponds to high selectivity to aromatics and low selectivity to $C_{8-11}$ gasoline fraction. As shown in **Figure 4.13c**, low $f$ value is mainly observed for sample with low Si/Al ratio and small crystal size which provides higher $S_{6-10A}$ and lower $S_{8-11}$. A high $f$ value appears over samples with Si/Al ratios of 40-50 and large crystal sizes. These ZSM-5 samples could provide higher $S_{8-11}$ whereas considerably lower $S_{6-10A}$. The highest $f$ value of 1.36 is observed over the ZSM-50-2.4 sample which

gives the most preferable selectivity in MTH reaction. Therefore this sample was chosen for the study on zeolite coatings.

*4.2.3.2 Effect of residence time*

In order to explore the effect of reaction conditions on the activity and selectivity of the ZSM-5 catalysts, a series of experiments at a WHSV in the range of 0.7-20 $h^{-1}$ and a pressure in the range in the range of 1 to 4 bar were performed.

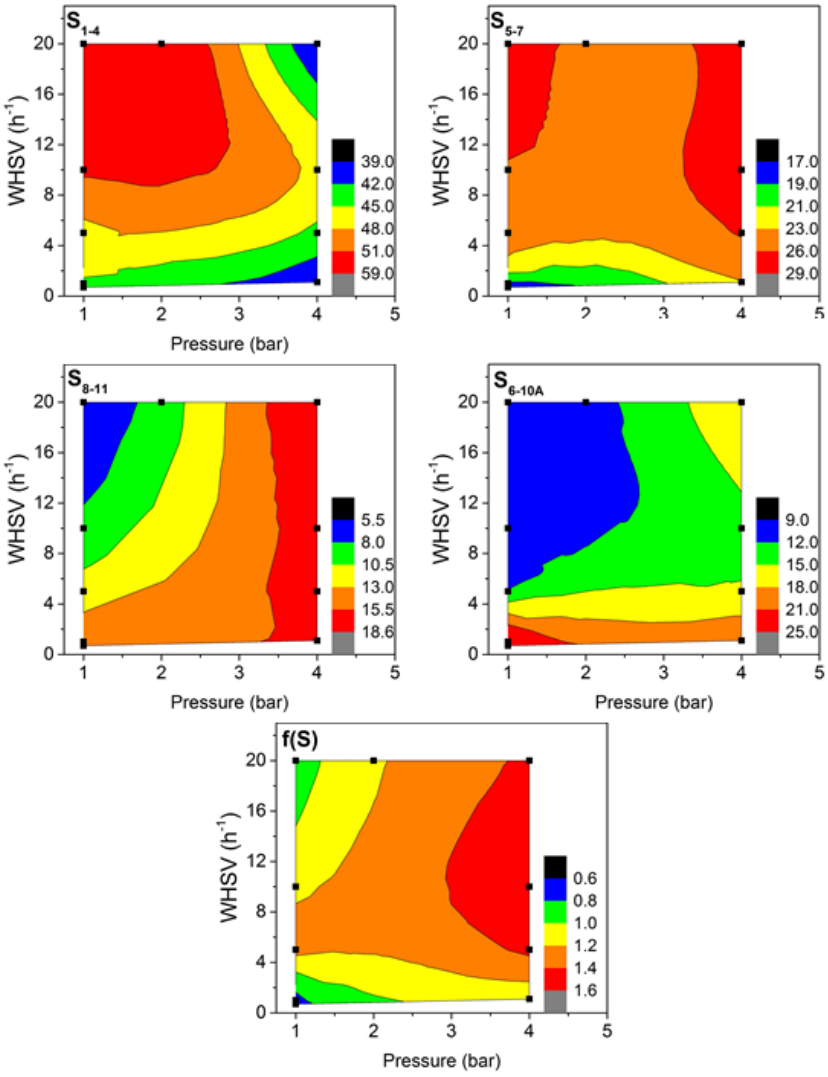


**Figure 4.14**. Colour contour displaying selectivity towards four hydrocarbon fractions and the weighing function of selectivity in MTH reaction at different WHSV and pressure (T=370 $^{o}$C)

In **Figure 4.14**, the selectivity towards different fractions is presented by colour contour from blue to red (low to high) as a function of methanol WHSV and reaction pressure. The highest selectivity towards the gaseous product of 54.9% is observed at 1 bar and a WHSV of 20 $h^{-1}$ when the residence time is 0.1 s. The selectivity to $C_{1-4}$ clearly decreases with decreasing WHSV and with increasing pressure and the residence time. The lowest $S_{1-4}$ is observed at a methanol pressure of 4 bar when the formation of the liquid product is favoured due to increased residence time. The lighter hydrocarbons could undergo oligomerisation, cyclisation, aromatisation, aromatic methylation, hydrogen transfer and aromatic dealkylation to gradually build up to larger products with longer residence time [173]. Therefore, at low pressure and high feed rate, the $C_{1-4}$ fraction might be flushed out of the catalyst before these products diffuse further into the crystal, resulting in high $S_{1-4}$. As for the $C_{5-7}$ fraction, the selectivity is increased with increasing WHSV. The formation of the $C_{8-11}$ fraction is clearly favoured at the higher pressures with the highest value of 18.6% at a pressure of 4 bar. In industrial processes, the reaction is performed at a pressure above 20 bar [191]. At a low pressure at 1 bar, an increase in flow rate of methanol could decrease the formation of $C_{8-11}$. The selectivity distribution towards $C_{6-10A}$ has a similar pattern as $C_{8-11}$ with the lowest value of 9.3% at a pressure of 1 bar and a WHSV of 20 $h^{-1}$. However, the highest $S_{6-10A}$ value is observed at a pressure of 1 bar and a WHSV of 1 $h^{-1}$ when the residence time has the highest value of 8.4 s. This suggests the effect of contact time is more pronounced as compared to reaction pressure. The design function shows that the highest pressure and moderate methanol flow rate is desirable for high selectivity to the $C_{8-11}$ gasoline product in the MTH reaction over ZSM-5 catalyst (**Figure 4.14**).

The selectivity of hydrocarbon fractions was previously reported to be effected by residence time of methanol in catalyst pores [192]. The selectivity towards four hydrocarbon fractions is plotted in **Figure 4.15** as a function of residence timeThe selectivity of hydrocarbon fractions was previously reported to be effected by residence time of methanol in catalyst

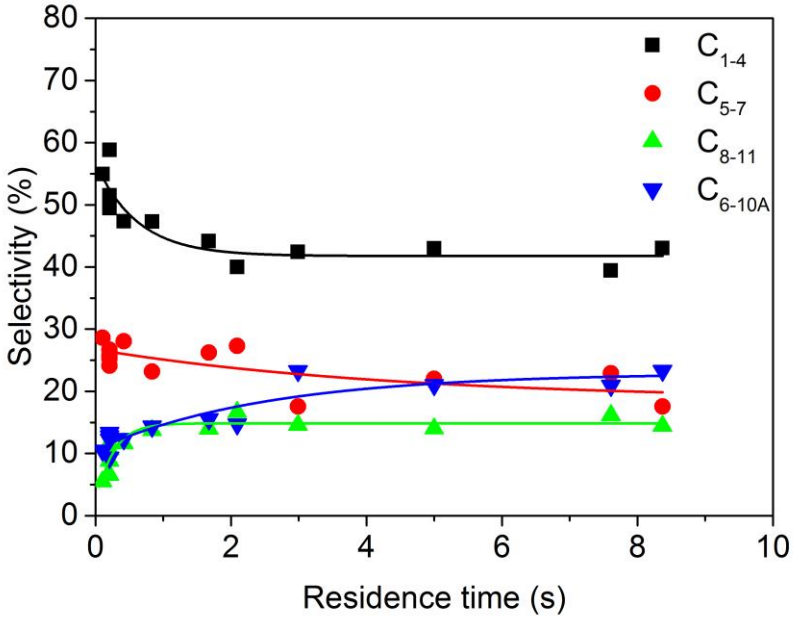


**Figure 4.15**. Selectivity distribution at different residence time in ZSM-5 catalyst in MTH reaction

pores [192].. At a very short residence time, the selectivity towards $C_{1-4}$ is 60% with $C_{5-7}$, $C_{8-11}$ and $C_{6-10A}$ fractions of 30, 10 and 10% respectively. As the residence time increases, lighter hydrocarbons are consumed while $C_{8+}$ aliphatics and aromatics start to build up. Beyond a residence time of 3 s, any further increase in the residence time does not influence the selectivity distribution. The equilibrium mixture consists of the $C_{1-4}$ (40%), $C_{5-7}$ (22%), $C_{8-11}$ (15%) and $C_{6-10A}$ fractions (22%). The formation of large molecules could be restrained by pore volume and channel dimensions in spite of long residence time and the presence of hydrocarbon-pool intermediates. This finding is in line with the study by Wan et al. who claimed that the highest $C_{5+}$ gasoline selectivity could not be reached in the largest ZSM-5 crystals even with a long residence time [173].

*4.2.3.3 Deactivation model*

The deactivation of ZSM-5 catalysts in a MTH reaction could be described as a loss of active catalyst, or equivalently a reduction of the effective contact time with time on stream reported by Janssen [192]. The deactivation could be modelled with two key factors, the deactivation rate coefficient ( $a$ ) and the first-order reaction rate constant ( $k$ ). The deactivation model is described in following equations where the deactivation rate is proportional to the methanol conversion. The methanol conversion is finally expressed as a function of time.

$$\frac{d\tau}{dt} = -aX \tag{4.2}$$

$$\frac{dX}{dt} = k(1 - X) \tag{4.3}$$

$$X = \frac{(\exp(k\tau_0)-1)\exp(-kat)}{1+(\exp(k\tau_0)-1)\exp(-kat)} \cdot 100\% \tag{4.4}$$

$$t_{0.5}(h) = \frac{\ln(\exp(k\tau_0)-1)}{ka} = \frac{\tau_0}{a} \tag{4.5}$$

$\tau$ is the contact time. X is the methanol conversion. $\tau_0$ stands for the initial contact time when the catalyst is fully active. $t_{0.5}$ is defined as the lifetime of a catalyst when the methanol conversion reaches 50%.

**Table 4.4**. Calculated values of the rate constant, deactivation coefficient and conversion capacity for ZSM-5 catalysts ($W_0$=0.1 g, $\tau_0$=110 g·h·mol$^{-1}$)

| Sample | $t_{0.5}$ (h) | k (mol·$g_{cat}^{-1}$·$h^{-1}$) | a (mmol·$g^{-1}$) |
|---|---|---|---|
| ZSM-20-0.84 | 39 | 0.13 | 0.54 |
| ZSM-30-1.10 | 32 | 0.15 | 0.66 |
| ZSM-40-1.70 | 147 | 0.14 | 0.14 |
| ZSM-50-2.40[a] | - | - | <0.05 |
| ZSM-60-2.60 | 97 | 0.15 | 0.22 |

a. No deactivation behavior was observed over the ZSM-50-2.4 catalyst in 200 h

**Figure 4.16**. Comparison of the calculated methanol conversion (solid line) with measured methanol conversion (open symbols) with time on stream over ZSM-5 catalysts with different Si/Al ratios at 370 °C and 4 bar.

By fitting all experiment data into above deactivation model, the deactivation coefficient and the first-order reaction rate is obtained in **Table 4.4**. The calculated methanol conversion is compared to the measured one in **Figure 4.16**. The calculated conversion over all ZSM-5 catalysts shows great fitting with the measured conversion in the deactivation period except for the ZSM-50-2.40 catalyst. The ZSM-20-0.84 and ZSM-30-1.10 sample display similar deactivation behaviour with the deactivation coefficient of 0.54 and 0.66. For the ZSM-40-1.70 and ZSM-60-2.60 samples, the deactivation coefficient decreased to 0.14 and 0.22 respectively. The longest lifetime is observed over the ZSM-50-2.40 sample which did not deactivate in 200 h so a deactivation coefficient could not be calculated. An estimation of its deactivation coefficient is obtained as 0.05 by iteration method. Though the assumption of first-order reaction is rough for the complex autocatalytic reaction [193], this deactivation model gives a qualitative indication to compare the activity and deactivation behaviour of ZSM-5 catalysts.

*4.2.3.4 Coking analysis*

The experiments at different times on stream of 0.5, 4.0, 6.0, 6.5 and 9.0 hours in the MTH reaction (vertical lines in **Figure 4.17**) were performed to monitor the deactivation kinetics. These particular time intervals were chosen to get the samples with different degree of deactivation: during a stable operation ($S_{0.5h}$), in the beginning of rapid deactivation ($S_{4.0h}$), during deactivation ($S_{6.0h}$, $S_{6.5h}$) and after full deactivation ($S_{9.0h}$).

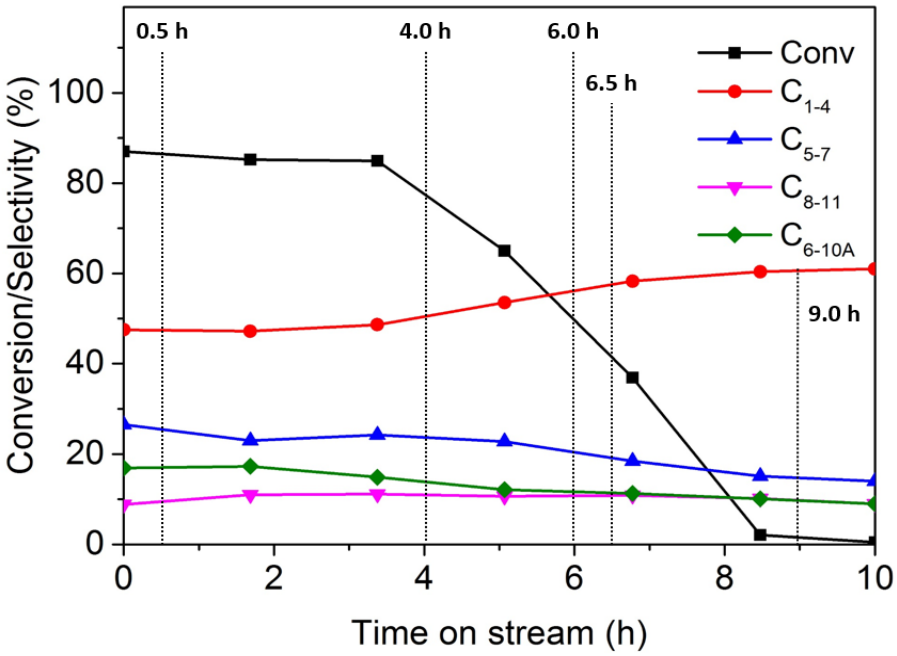


**Figure 4.17**. Methanol conversion and product selectivities in MTH reaction over ZSM-50-2.4 (T=370 °C, WHSV=14 $h^{-1}$, P=3.0 bar)

**Figure 4.18a** shows TPO profiles of spent catalysts after different times on stream. It can be seen that the activation energy for $CO_2$ formation increases with the reaction time as the maximum of $CO_2$ peaks shifted to higher temperatures. Our reference study showed that $CO_2$ desorption in the H-ZSM-5 zeolite occurs below 200 °C, the oxidisation of hydrocarbons happens between 200 and 500 °C, while graphitic coke oxidises at higher temperatures. Hence, the profiles obtained were split into these three temperature ranges and analysed based on the MTH reaction time as shown in **Figure 4.18b**. The total amount of coke quickly increased to about 2 mmol·$g^{-1}$ and remained virtually the same during the reaction. The

coke content further increased only after full catalyst deactivation, likely, due to the formation of coke on the external surface of the catalyst. However, the nature of the coke changed in the course of the reaction. A marginal increase in graphitic coke occurred during the first 4 h when product selectivities remained similar (**Figure 4.17**). However, when the formation of $C_{8\text{-}11}$ fraction was suppressed, the amount of the graphitic coke increased, while the amount of adsorbed hydrocarbon species decreased.

The coke formation model from literature assumes that the coke is formed first inside the catalyst pores followed by coking of the catalyst surface [183,194]. At the very initial reaction stages, the coke amount quickly increased creating hydrocarbon pool providing several pathways for the conversion of methanol. During the reaction, aromatic molecules inside the catalyst pore condensed, but the total amount of coke barely increased. When several channels of the three-dimensional structure of ZSM-5 were blocked by coke, quick deactivation started accompanied with the conversion of all hydrocarbons into graphitic coke. This process resulted in a minor increase in the total coke content, but a substantial increase in the graphitic coke amount.

After 6 h on stream, methanol conversion decreased resulting in the

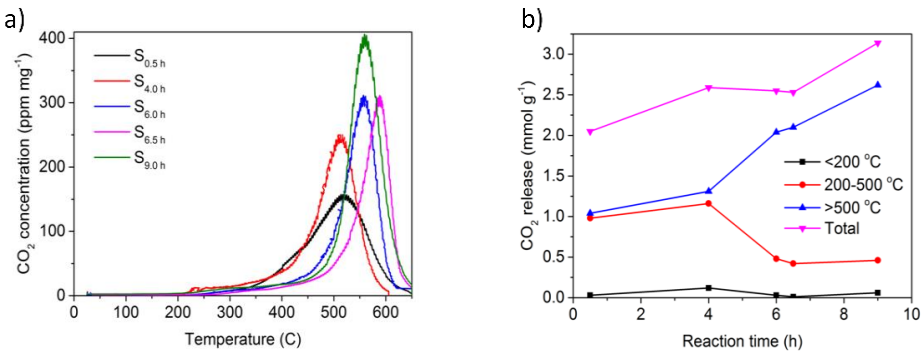


**Figure 4.18**. a) TPO profiles of deactivated zeolite samples after different time on stream, b) $CO_2$ release from deactivated zeolites at different temperature range during TPO

decrease in the formation of larger hydrocarbon fractions ($C_{5+}$) in the $s_{6.0h}$ and $s_{6.5h}$ samples. However, the difference in coke content was very minor,

likely because a gradual decrease in pore availability at some point led to a blockage for $C_{8-11}$ molecules. Therefore, selectivity towards lighter hydrocarbons increased. Quickly afterwards, only smaller pores accessible to $C_{1-4}$ remained, which was accompanied by minor changes in coke characteristics. After full deactivation, i.e. when zeolite provided only external surface to form the equilibrium mixture of methanol and DME, the amount of coke increased forming mainly graphitic coke on the external surface.

## 4.3 ZSM-5 coating catalyst

### 4.3.1 Optimisation of synthesis conditions

*4.3.1.1 Effect of plate pretreatment*

To provide better adhesion of zeolite coatings on substrates, the surface roughness and hydrophilicity of substrates were increased prior to hydrothermal synthesis. XRD patterns (**Figure 4.19**) of ZSM-5 coating on a blasted substrate shows similar crystallinity as the coating on a flat

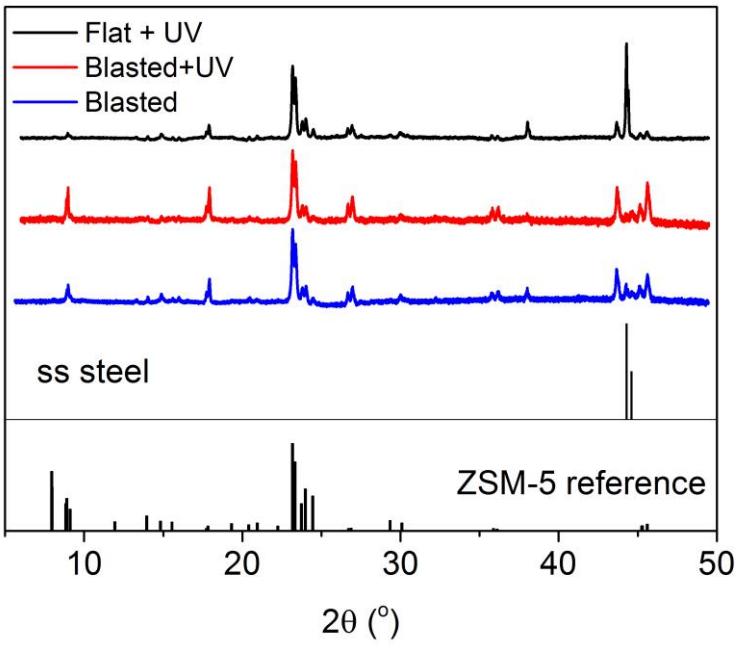


**Figure 4.19**. XRD patterns of coating samples with different pretreatment and reference patterns of ZSM-5 catalyst

substrate. The relative crystallinity of sample is defined as the ratio between the area of peaks at 2θ of 20-25° to the one of the reference sample. From the intensity of characteristic peaks between 20-25° 2θ, it can be concluded that ZSM-5 coating on UV pre-treated, blasted substrate exhibits a higher relative crystallinity of 100% while it is only 71% on the substrate without UV treatment. After UV treatment, the $TiO_2$ layer becomes super hydrophilic [195,196]. Strong peaks from the stainless steel substrate suggest a low coating thickness on flat substrate. These results indicate a thick and uniform coating formed on blasted substrates where nucleation is preferable at higher roughness.

*4.3.1.2 Effect of synthesis time*

XRD patterns of a zeolite coating obtained at a Si/Al ratio of 20, an $H_2O$/Si ratio of 30 and the synthesis time in the range of 24-120 h are shown in **Figure 4.20**. These patterns agree with the XRD patterns of the corresponding crystals without other phases formed on a stainless steel plate. The ZSMC-20-1.04 sample obtained with a synthesis time of 72 h is selected as the reference sample for its highest crystallinity. These data demonstrate that zeolite coatings can be obtained using conventional

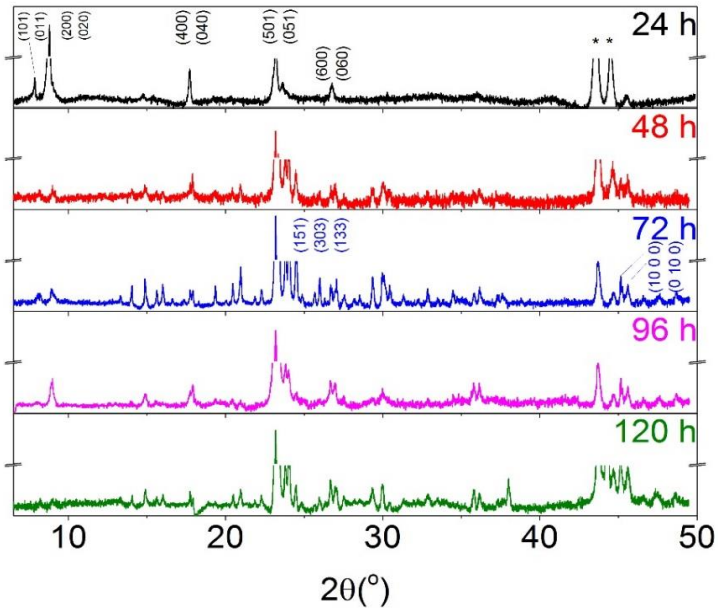


**Figure 4.20**. XRD patterns of zeolite coating on substrates obtained in different synthesis time (*: reflection of stainless steel)

hydrothermal synthesis without the introduction of zeolite seeds on the substrate. A few lattice plane orientations with Miller indices including the main peaks (501) and (051) at 2θ 23.18$^{o}$ are observed in coating synthesised for 24 h (**Figure 4.20**). For the synthesis of 72 h, the main characteristic peaks (151), (303) and (133) in the 2θ range of 23-25$^{o}$ indicates the formation of highly crystalline ZSM-5 coating.

Using this seedless method, zeolite coatings were obtained on stainless steel microreactor plates with the semi-circular microchannels (**Figure 4.21**). The coating was very uniform and contained no uncoated areas. A cross-sectional view is also shown in the insert figure in **Figure 4.21**.

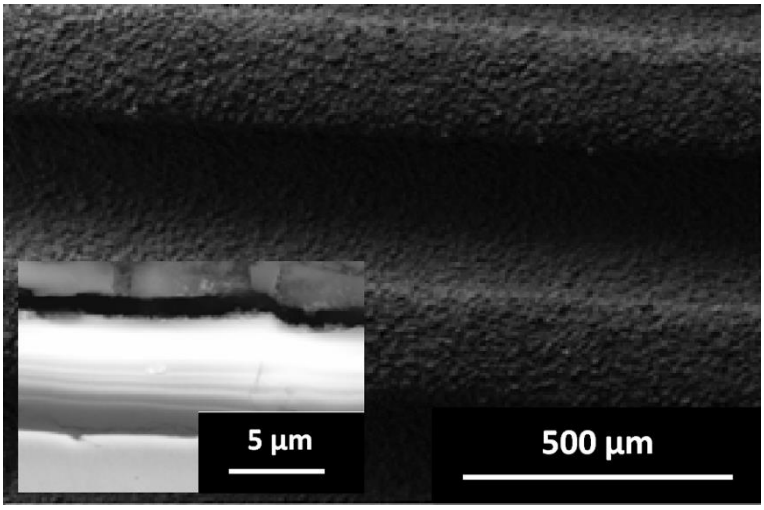


**Figure 4.21**. SEM images of ZSM-5 coating on microchannel with cross-section

The effect of synthesis time on coating thickness obtained on stainless steel plates and crystal size of ZSM-5 are presented in **Figure 4.3**. The thickness increased up to the synthesis time of 72 h, which was likely caused by the build-up of the zeolite nuclei from the precursor solution. For the synthesis time longer than 72 h, however, the average coating thickness decreased. The conversion of Si precursor, was always below 50 %, which shows that the observed effect cannot be explained by the exhaustion of the precursors. A similar effect of stopped zeolite growth much earlier than the depletion of the precursor mixture was observed by Moor et al. and is likely caused by the achieved equilibrium between the dissolved and the formed crystalline zeolite species [197]. The crystallinity of zeolite decreases for higher synthesis time above 72 h, likely because zeolite crystals could be partially dissolved to form a new, thermodynamically stable, phase of the amorphous aluminosilicate or just a mixture of silica and alumina. This hypothesis is supported by the data reported by Jacobs et al. [198], who observed the formation of non-zeolite aluminosilicates at longer synthesis times. Therefore, it can be concluded

that the optimal synthesis time for the ZSM-5 zeolite coatings is 72 h from this study.

*4.3.1.3 Multi step synthesis*

Compared to a fixed-bed reactor with pellets, one of the drawbacks of microreactors with zeolite coatings is their low catalyst loading. This also predicts that the reactor could suffer from a low yield of hydrocarbons which could limit the subsequent scale-up. According to the effect of crystallization time studied in section **4.2.1**, the growth of coating stops after 72 h due to the presence of crystallization equilibrium as discussed in section **4.2.2**. In order to increase the coating loading on the substrates, a multi cycle synthesis coating should be performed by repeating synthesis procedures on the substrate with synthesised coating. A zeolite coating with a thickness of 65 µm was formed after 5 synthesis cycles. The cross-section of this coating is shown in **Figure 4.22a** where the layers obtained in different synthesis cycles are clearly seen. The total thickness of the bottom two layers is 15 µm while the three top layers have a thickness of 15 µm each (**Figure 4.22b**). The faster growth of coating in the subsequent synthesis cycles could be explained by seeded synthesis and the higher surface roughness due to zeolite particles present on the surface of the previous coating.

However, a microporous ZSM-5 catalyst with a large coating thickness could experience internal diffusion limitations in MTH. Therefore, prior to catalytic tests, the maximum thickness of zeolite coating was calculated from the Thiele Modulus (Φ) using reaction rate data over a ZSM-5 powder sample. The Thiele modulus describes the relationship between diffusion and reaction rate in a porous catalyst where effective diffusivity ($D_{eff}$) accounts for the unavailable area for diffusion flux, tortuous path and pores

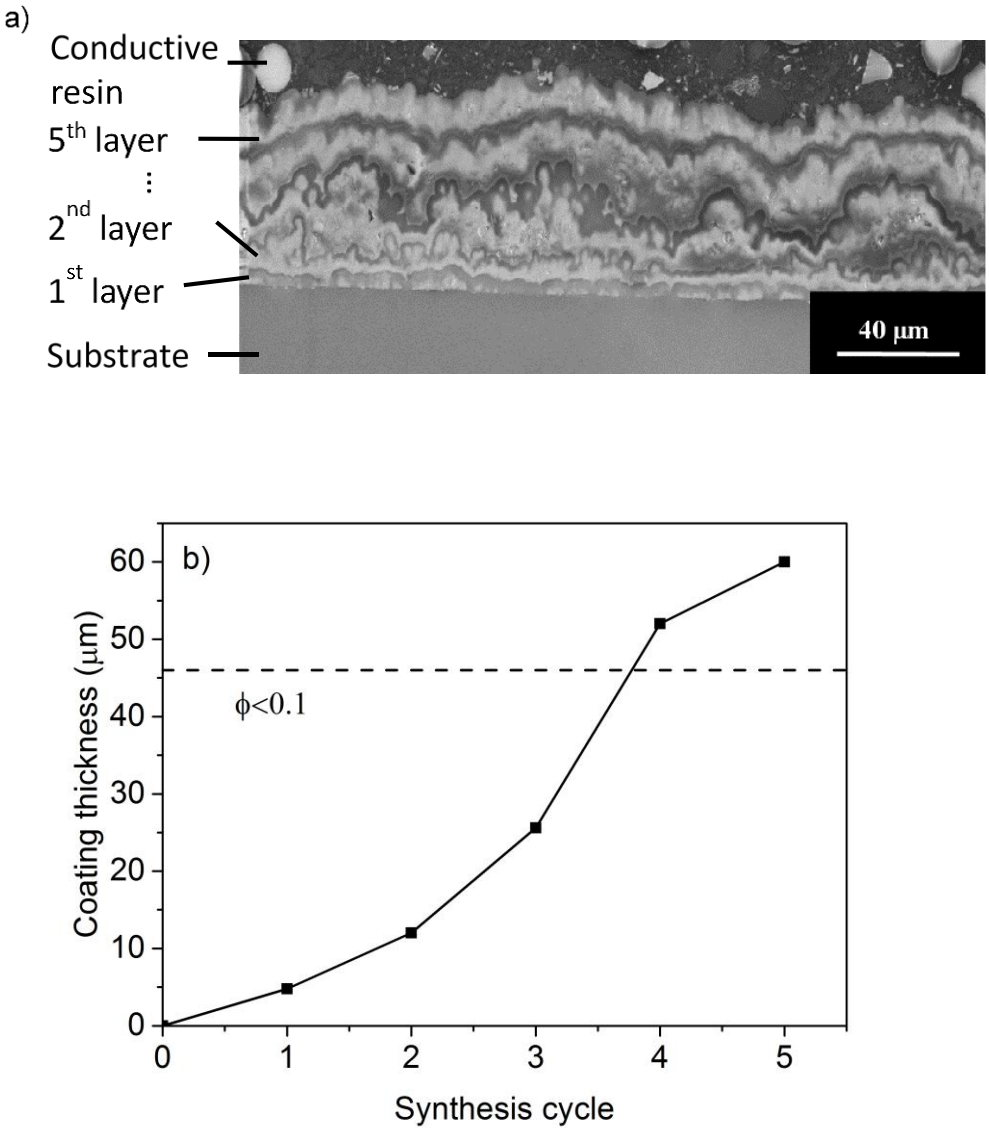


**Figure 4.22**. a) SEM image of the cross-section of 5-layer coating and b) coating thickness as a number of synthesis cycles

with varying cross-section area in a catalyst [199]. 100% utilisation of catalytic coating represents a situation where the observed reaction rate equals to the intrinsic reaction rate without diffusion limitation and the value of Thiele modulus is 0. On the contrary, a Thiele modulus of 10 represents a situation where only 10% of the catalytic coating is utilised effectively [200].

$$\Phi = h\sqrt{\frac{k}{D_{eff}}} < 0.1 \tag{4.6}$$

$$D_{eff} = \frac{D_m \varepsilon \delta}{\tau} = 4.87 \times 10^{-8} \ (\mathrm{m^2 \cdot s^{-1}}) \tag{4.7}$$

**Table 4.5**. Parameters for Thiele modulus calculation

| Notation | Description | Value | Reference |
|---|---|---|---|
| $D_m$ | Molecular diffusion coefficient (T=643 °C and P=4 bar) ($m^2 \cdot s^{-1}$) | ~$7.3\times10^{-7}$ | [257] |
| ε | Particle porosity (dimensionless) | 0.25[i] | [This study] |
| δ | Constrictivity (dimensionless) | ~0.8 | [258] |
| τ | Catalyst tortuosity (dimensionless) | 3.0 | [258] |
| k | Reaction rate constant ($s^{-1}$) | 0.224 [ii] | [This study] |

i. Obtained from nitrogen physisorption

ii. From experimental data over ZSM-5 powder catalyst

where $h$ is the coating thickness, $k$ is the fisrt-order reaction rate constant obtained from experiments, $D_m$ is the molecular diffusion coefficient of methanol in nitrogen, ε is the porosity of catalyst, δ is the constrictivity describing transport process in porous media, τ is the tortuosity as a property of tortuous curves in pore structure. These parameters are listed in **Table 4.5**.

For the reaction rate observed over experimental results in section **4.2.3**, the maximum thickness of the coating that could be accessible to the reactant is 47 µm. Therefore, thick zeolite coatings with a thickness above 47 µm would suffer from internal diffusion limitations in the MTH reaction.

Approaches aimed at increasing effective diffusivity such as introducing mesoporosity into zeolite could allow application of thicker coatings in the MTH reaction without diffusion limitations. However, with thick zeolite coatings, the hot-spot issue becomes more pronounced so further research including heat transfer modelling and modification of coating morphology is required as presented in the following chapter.

### 4.3.2. Catalytic performance

Microporous ZSM-5 zeolite with large particle size may experience diffusion limitations in the MTH reaction. As discussed earlier, a maximum coating thickness to avoid internal diffusion limitation is estimated to be 47 µm at a temperature of 370 $^{o}$C and a pressure of 4 bar.

**Table 4.6**. Initial conversion and selectivity over ZSM-5 catalyst in the MTH reaction (T=370 $^{o}$C, WHSV of methanol=7.0 $h^{-1}$, P=1 bar)

| Sample | Conversion (%) | $S_{1-4}$ (%) | $S_{5-7}$ (%) | $S_{8-11}$ (%) | $S_{6-10A}$ (%) |
|---|---|---|---|---|---|
| ZSM-50-2.4 | 89.0 | 43.9 | 25.7 | 10.9 | 19.1 |
| ZSMC-50-2.4 | 83.3 | 58.4 | 21.7 | 10.1 | 9.6 |

The catalytic performance of powder ZSM-5 sample and coating sample with the same composition was compared in the MTH reaction under the same conditions (**Table 4.6**). The conversion of methanol, overall reaction rate and selectivity towards the main hydrocarbon fractions over both samples are listed in **Table 4.6**. At similar conversion levels of 89.0% and 83.3% for powder and coating respectively, it suggests that powder samples had no diffusion limitation at the operating conditions. The selectivity to light hydrocarbons is 58.4% over the coating, compared to 43.9% over the pelleted catalyst. The selectivity towards $C_{5-7}$ and $C_{8-11}$ gasoline fractions over the coating sample are both slightly lower than over the pelleted catalyst. The higher selectivity to light olefins as intermediates of reaction is anticipated due to shorter residence time in coating compared to one in pellets [201]. The shorter residence time of molecules in catalytic coating prevents the build-up of small molecules into larger fractions. The production of aromatic hydrocarbons, especially toluene and xylene over the pellets are around twice on comparing with the zeolite coating. This indicates that over zeolite pellets, in dual-cycle of hydrocarbon pool, alkene cycle is suppressed when more carbon takes part in the aromatic cycle involving methylation and demethylation of aromatics [202]. At a small characteristic dimension of zeolite coating, the possibility of re-adsorption

of light olefins to form aromatics decreases due to a higher leak rate of smaller fractions [201]. This finding is in line with a previous report where the undesired aromatic production was suppressed at lower space time in zeolite coating deposited onto the inner walls of a monolith reactor [203].

## 4.4 Conclusions

A series of ZSM-5 catalyst with different Si/Al ratios (20-60) and the mean crystal size ranging from 0.8 to 2.6 μm has been synthesized on AISI-304 stainless steel substrates by hydrothermal synthesis. The coatings obtained have MFI structure without the presence of other phases. A higher Si/Al ratio in the initial sol gives larger mean crystal size. A higher $H_2O$/Si ratio leads to larger crystal size with a wide crystal size distribution. Continuous coatings were obtained with an average coating thickness of 14 μm. The crystallisation of ZSM-5 zeolite was stopped after 72 hours when the liquid phase was exhausted of Al species, even an incomplete conversion of Si species was observed. An increased catalyst loading up to 0.09 $kg \cdot m^{-2}$ was achieved by repeated synthesis resulting in a coating thickness of 60 μm.

High Al content in the catalysts (Si/Al ratio below 30) resulted in a fast equilibrium between methanol and DME in the MTH reaction at 370 $^oC$. These catalysts also showed a fast deactivation within 50 h on stream. The catalysts with Si/Al ratio above 50 showed an initial induction period over which an increase in catalyst activity was observed. They demonstrated improved stability with no deactivation for more than 80 h on stream. There exists an optimal catalyst composition with a Si/Al ratio of 50, a crystal size of 2.4 μm which could be obtained at a synthesis time of 72 h from a sol with a nominal composition of 50 $SiO_2$: 1 $AlO_2$: 6 TPAOH: 1500 $H_2O$.

The H-ZSM-5 catalyst with a Si/Al ratio of 50 provided the maximum yield of gasoline range hydrocarbons. The $C_{8-11}$ selectivity increases to 18.6% at a pressure of 4 bar and a residence time of 3 s. Any further increase in residence time does not change the selectivity pattern. While the $C_{8-11}$

selectivity over the ZSM-5 coatings is slightly lower than over the powder sample with the same composition, the amount of undesired aromatic fraction was considerably reduced to 9.6% over the coatings as compared to 19.2% over the pellets. This illustrates that the application of thin zeolitic layers gives considerable potential for tailoring and optimizing the catalytic performance in the MTH reaction.

# Chapter 5
# Post-synthesis modification of ZSM-5 catalysts

## 5.1 Introduction

It is well known that it is the acid site in zeolite that catalyses the MTH reactions [15, 94,104]. Fast deactivation in ZSM-5 catalysts with high Al content requires further modification to inhibit aromatisation and coke formation over strong acid sites. However, low Al content results in large crystal size that demonstrates internal diffusion limitations resulting in low catalyst utilisation. The acidity can be modified by a post-synthesis treatment with metal salts by replacing a proportion of protons at strong acid sites with metal ions [84,85,189]. This changes the product pattern and enhances the catalyst lifetime. Especially Ca-ZSM-5 catalysts were reported to show higher resistance against coke formation and hence an enhanced lifetime [204–207].

Due to the low internal diffusion limitation in the microporous ZSM-5 catalyst, the development of a micro-mesoporous zeolite structure has been investigated introducing mesoporosity in ZSM-5 crystals either by an application of a second structural agent [208] or by a post-treatment with an alkaline solution [209]. By introducing mesopores, the diffusion rates of the reactant and products in zeolite crystals can be considerably increased [210]. Mesoporous ZSM-5 catalysts have been reported to demonstrate better performance regarding both gasoline selectivity and lifetime compared to microporous zeolites under similar reaction conditions [94,211].

In this chapter, the effect of Ca-exchange and alkaline treatment on morphology and catalytic activity of ZSM-5 (Si/Al=50) will be studied. The reaction conditions will be optimised to obtain the maximum yield of the $C_{8-11}$ gasoline hydrocarbons.

## 5.2 Calcium ion exchange

### 5.2.1 Characterization

*XRD*

Effect of Ca ion exchange was carried out by exchanging protons by $Ca^{2+}$ on commercial ZSM-5 (Si/Al=11.5). All Ca-$NH_4$-ZSM-5 samples were analysed by ICP elemental analysis. Increase of $Ca^{2+}$ to 1.0 M in the solution does not result in full exchange of $NH_4^+$ cations with $Ca^{2+}$. This may be related to the fact that two sites should be positioned relatively close to each other in order to be replaced with a $Ca^{2+}$ ion. This is rather unlikely in the samples with a low Al content. Therefore the full ion-exchange capacity (50%) was not reached even from a very concentrated solution. The exchange ratio as a function of $Ca^{2+}$ concentration was obtained (See appendix Table C1) and all Ca-ZSM-5 samples were referred to as Ca(x), where x is the exchange ratio in percentage.

XRD patterns of Ca/$NH_4$-ZSM-5 catalysts with different Ca content and a commercial $NH_4$-ZSM-5 sample (Ca(0)) are presented in **Figure 5.1**. All

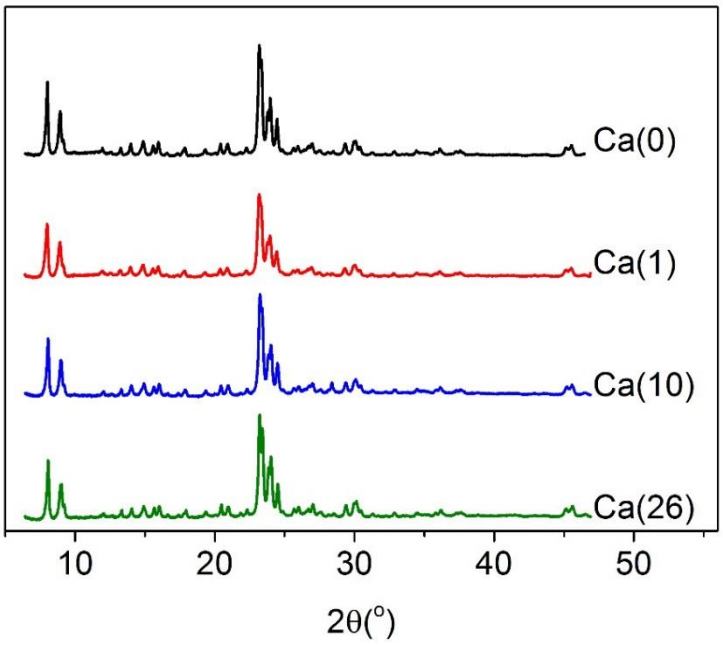


**Figure 5.1**. XRD patterns of parent and Ca-ZSM-5 samples with different Ca ion-exchange ratio

characteristic peaks in the 5-50 $^{o}$ 2θ range are present indicating the high degree of purity of ZSM-5 zeolite (MFI structure) and the absence of CaO clusters. From the relative intensity of the strongest peaks in the 20-25$^{o}$ 2θ range, it can also be concluded that the Ca-exchange step does not influence the zeolite crystallinity.

### *Pyridine-TPD*

Pyridine-TPD plots from different starting temperatures (125, 175,225 $^{o}$C) were subtracted to obtain TPD plots for separated peaks with different acid strength (**Figure 5.2**). As defined in earlier chapter, segments A and B are LTPs and C is HTP. The range of those peaks are 125-300, 200-350, 250-550 $^{o}$C respectively. The acid strength is calculated from the integral of individual peaks (**Table 5.1**). The total acidity drops gradually with increasing Ca ion-exchange ratio due to the replaced protons. However, only HTP C shows similar trend with increasing Ca ion-exchange ratio. It drops from 0.94 to 0.56 mmol·$g_{cat}^{-1}$ when Ca ion-exchange ratio increases from 0 to 26% in the catalyst. For both LTP A and B, an optimum intensity

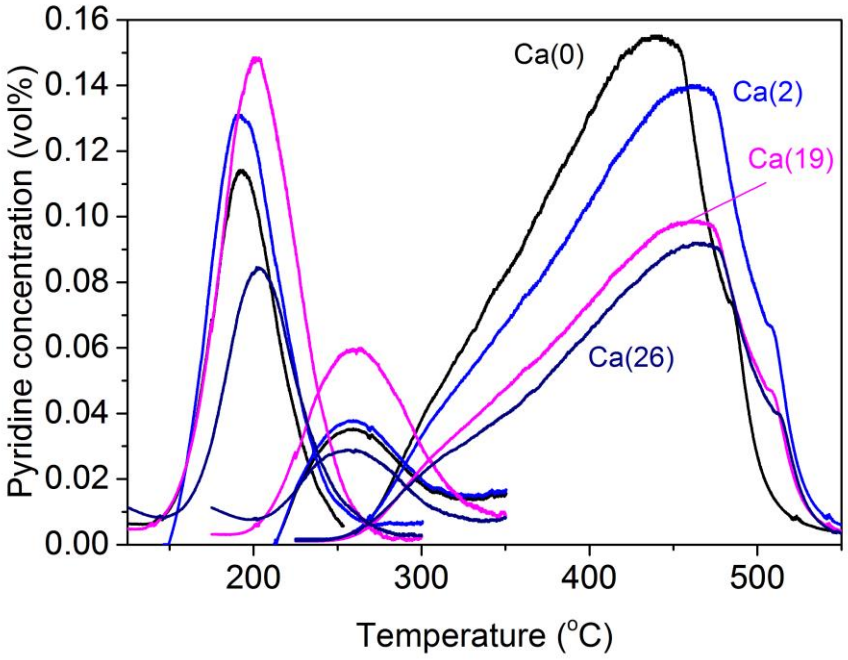


**Figure 5.2**. Differential curves of pyridine-TPD thermograms between 125-175, 175-225, 225-550 $^{o}$C starting temperatures over the samples with the increasing Ca ion-exchange ratio.

**Table 5.1.** Pyridine-TPD for different type of peaks for ZSM-5 with different Si/Al ratios

| Sample code | Total acidity (mmol·$g_{cat}^{-1}$) | LTP A (mmol·$g_{cat}^{-1}$) | LTP B (mmol·$g_{cat}^{-1}$) | HTP C (mmol·$g_{cat}^{-1}$) |
|---|---|---|---|---|
| Ca(0) | 1.33 | 0.26 | 0.13 | 0.94 |
| Ca(2) | 1.30 | 0.29 | 0.13 | 0.88 |
| Ca(19) | 1.18 | 0.36 | 0.17 | 0.65 |
| Ca(26) | 0.92 | 0.25 | 0.11 | 0.56 |

was observed when Ca ion-exchange ratio approached to 19%. A shift of acid strength from HTP to LTP was observed when increasing Ca ion-exchange ratio. Ca ion-exchange weakens the strong acid sites (HTP C) in line with the previous literature [206,207,212]. This also explains the shift and the increasing intensity of weak acid sites at LTP A and B when increasing Ca ion-exchange ratio from 0 to 19%. For Ca ion-exchange ratio at 26%, the Ca(26) sample shows reduction in total number of acid sites due to an excessive replace of Ca ion to protons.

### 5.2.2 Catalytic performance

Deactivation behaviour of Ca/H-ZSM-5 catalysts, obtained after calcination of the respective Ca/$NH_4$-ZSM-5 catalysts, and the blank catalyst Ca(0) is shown in **Figure 5.3**. The conversion over the Ca(0) catalyst initiates at 83% and fast deactivation starts after 5 h. The deactivation is quite fast as the conversion drops to 30% within 8 h. A very similar deactivation behaviour is observed over the Ca(1) catalyst. The fast deactivation of both samples is attributed to the high acidity of zeolites with high Al content, as also reported together with high initial conversion by several groups [203, 211]. The deactivation over the Ca(10) and Ca(19) catalysts is much slower compared to the Ca(0) and Ca(1) samples. The conversion of methanol maintains above 80% for 10 h over the Ca(19) catalyst. It takes another 20

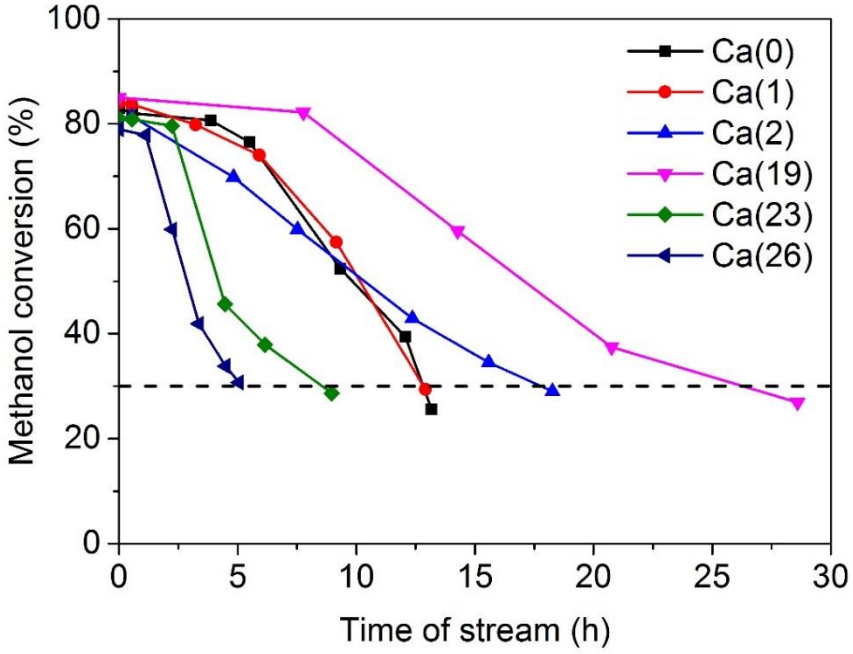


**Figure 5.3**. Methanol conversion over Ca-ZSM-5 samples with different Ca exchange ratios (T=370 $^{o}$C, P=1 bar, WHSV=3 $h^{-1}$)

h for it to drop below 30%. With higher Ca content in the Ca(23) and Ca(26) catalysts, even faster deactivation is observed. As expected, with the drop in total acidity, the total catalytic activity is limited. This interplay between the two effects on deactivation behaviour during results in the existence of an optimal ion-exchange ratio in H-ZSM-5 zeolites. The catalyst lifetime ($t_{0.3}$) of Ca-H-ZSM-5 catalyst is defined as the time on stream when the methanol conversion drops to 30%. As shown in **Figure 5.4**, the value of $t_{0.3}$ is improved from 13 h over the Ca(0) catalyst to 28 h over the Ca(19) catalyst. Further increasing Ca exchange ratio to 26% leads to a decrease of lifetime to 5 h due to the insufficient amount of acid sites. The catalytic performance is quantified using Janssens deactivation model [192]. As discussed in Chapter 4, the model describes the first-order reaction rate and the deactivation coefficient for Ca ion-exchanged ZSM-5 catalysts (**Table 5.2**). The deactivation coefficient of the samples drops from 0.782 in the parent ZSM-5 sample to a minimum value at Ca ion-exchange ratio of 19%. This could be attributed to the reduced strong acid sites observed in our pyridine-TPD results. The first-order reaction rate drops slightly from 0.236 to 0.202 $mol \cdot g_{cat}^{-1} \cdot h^{-1}$ indicating a decrease in catalytic activity due

**Table 5.2** Calculated values of the rate constant, deactivation coefficient and conversion capacity for ZSM-5 catalysts ($W_0$=0.1 g, $\tau_0$=7.7 g·h·mol$^{-1}$)

| Sample | $t_{0.5}$ (h) | $t_{0.3}$ (h) | k (mol·$g_{cat}^{-1}$·$h^{-1}$) | a (mmol·$g^{-1}$) |
|---|---|---|---|---|
| Ca(0) | 10 | 13 | 0.223 | 0.738 |
| Ca(1) | 10 | 13 | 0.236 | 0.769 |
| Ca(2) | 11 | 16 | 0.212 | 0.700 |
| Ca(19) | 14 | 19 | 0.219 | 0.542 |
| Ca(23) | 7 | 14 | 0.211 | 1.183 |
| Ca(26) | 4 | 9 | 0.202 | 2.079 |

to reduced number of total acid sites. $t_{0.5}$ calculated from the deactivation model also shows a similar trend with an optimum value for the sample Ca(19) as $t_{0.3}$ which is obtained in the experimental.

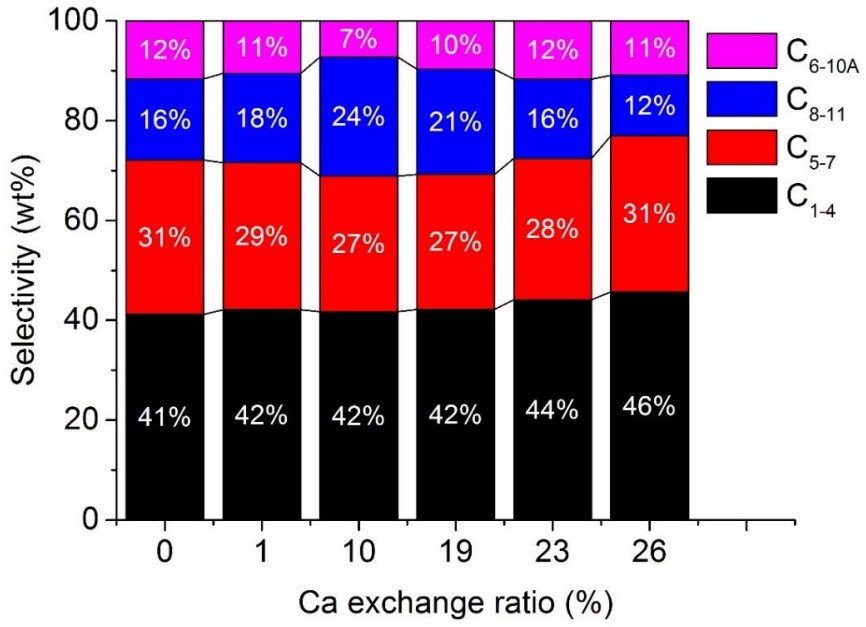


**Figure 5.5**. Selectivity of hydrocarbons over Ca-ZSM-5 with different exchange ratio

The effect of Ca exchange ratio in Ca-H-ZSM-5 catalysts on products distribution was also studied (**Figure 5.5**). The selectivity towards $C_{1-4}$ fraction increases to 46% with increasing Ca content. The selectivity towards $C_{5-7}$ decreases from 31 to 27% as the $Ca^{2+}$ exchange ratio increases from 0 to 10%. On the contrary, the selectivity towards $C_{8-11}$ increases from 16 to 24%. In this range, $Ca^{2+}$ has clearly promoted hydrocarbon pool build-up from light to heavy molecules. However a further addition of $Ca^{2+}$ decreases the catalytic activity. The higher $S_{8-11}$ of 24 and 21% are observed over the Ca(10) and Ca(19) samples respectively. For these two samples, the aromatics production is also heavily suppressed comparing to either blank or Ca(26) samples. It should be mentioned that the Si/Al ratio of the blank sample is 11.5 and the aromatics is the main product over Ca(0) due to its high acidity. Low $C_{6-10A}$ selectivity and fast deactivation suggest that aromatic products have been instantly converted to poly-aromatics species which could result in production of smaller molecules due to narrowed channels and pores. Modified by small amount of Ca ions, strong acid sites are eliminated resulting in less coke precursors. This is confirmed by increasing smaller aromatics such as benzene, toluene and xylene. As a result, the lifetime was improved over the Ca(10) catalyst.

Comparing the activity results with textual properties of these catalysts (**Table 5.3**), the shift in product distribution could be explained by changing pore size and specific surface area as more Ca is introduced in the

**Table 5.3**. Textual properties of blank and Ca-ZSM-5 samples

| Sample | $S_{BET}$ ($m^2 \cdot g^{-1}$) | $S_{micro}$ ($m^2 \cdot g^{-1}$) | $S_{meso}$ ($m^2 \cdot g^{-1}$) | $V_{micro}$ ($cm^3 \cdot g^{-1}$) | $V_{meso}$ ($cm^3 \cdot g^{-1}$) |
|---|---|---|---|---|---|
| Ca(0) | 388 | 293 | 71 | 0.13 | 0.066 |
| Ca(1) | 358 | 288 | 61 | 0.12 | 0.055 |
| Ca(10) | 330 | 256 | 53 | 0.10 | 0.042 |
| Ca(19) | 275 | 170 | 37 | 0.09 | 0.029 |
| Ca(26) | 279 | 216 | 10 | 0.09 | 0.010 |

catalysts. The reduction in the efficient dimensions of micropores due to the replacement of protons (0.02 nm) by larger $Ca^{2+}$ ions (0.20 nm) [214], in confirmed by decreasing micropore volume in the Ca-ZSM-5 catalysts. The $C_{8-11}$ selectivity reduces by half when Ca exchange ratio was increased from 10 to 26%. This is explained by loss of total acid sites catalysing hydrocarbon build-up. Much higher deactivation rates over the Ca(23) and Ca(26) catalysts are therefore observed.

Regarding selectivity towards the target $C_{8-11}$ fraction, both Ca(10) and Ca(19) catalysts show similar performance. When taking stability into consideration, the Ca(19) catalyst with the longest lifetime on stream in MTH reaction is considered to be an optimal catalyst. Therefore it could be concluded that $Ca^{2+}$ exchange ratio in the range between 10 and 19% is optimal for the production of $C_{8-11}$ fraction gasoline products.

## 5.3 Desilication

The desilicated samples will be referred to as Meso(x)-y, where index x stands for average diameter of pores and index y stands for crystal size of desilicated catalysts. The sample treated with a mixture of TPAOH and NaOH will be referred to as Meso(3.1)-2.4. The blank sample (ZSM-50-2.4) will be referred to as Micro(0.5)-2.4 since it has little mesoporous structure and mainly micropores with a diameter of 0.5 nm. The desilication method was adopted to H-ZSM-5 coatings in order to introduce mesoporosity and enhance their lifetime. Desilication was performed with a total concentration of $OH^-$ of 0.2 M. The coating samples will be called by two indexes representing the modification method and the coating thickness. For example, MicroC-10 is a microporous coating with a thickness of 10 µm and Ca-MesoC-30 is the modified coating by the alkaline treatment followed by Ca ion-exchange with a coating thickness of 30 µm.

### 5.3.1 ZSM-5 powder

An alkaline treatment of zeolite removes silicon species from the zeolite framework. The removal of silicon species forms mesopores with a diameter in the nanometre range. The surface area, pore size distribution and pore volume could be changed [89, 97]. The removal of framework Si and Al by a TPAOH solution was reported to be more moderate than a NaOH solution [215]. The presence of TPAOH in the treatment solution could lead to secondary crystallization of amorphous species and extra framework Si and Al in the zeolite [216]. Therefore the effect of the addition of TPAOH structuring template during alkaline treatment was also studied at a concentration of $OH^-$ of 0.2 M. A ratio of TPAOH/(NaOH+TPAOH) of 0.4 was chosen in this study based on literature data [217].

#### *5.3.1.1 Characterisation*

The property summary of blank and desilicated samples are shown in **Table 5.4**.

**Table 5.4**. Textural properties of blank and desilicated ZSM-5 samples

| Sample | $C_{OH^-}$ | Si/Al[a] | $S_{BET}$ | $S_{meso}$ | $V_{tot}$ | $V_{meso}$[b] | $\overline{D}$ | $\overline{D_1}$ | $\overline{D_2}$ |
|---|---|---|---|---|---|---|---|---|---|
| | (mol·$L^{-1}$) | (-) | ($m^2 \cdot g^{-1}$) | | ($cm^3 \cdot g^{-1}$) | | | (nm) | |
| Micro(0.5)-2.4 | - | 49.6 | 379 | 18 | 0.17 | 0.01 | 0.5 | - | - |
| Meso(3.1)-2.4 | 0.2 | 44.7 | 346 | 116 | 0.19 | 0.09 | 3.1 | 3.7 | 6.6 |
| Meso(4.1)-2.4 | 0.1 | 45.3 | 318 | 46 | 0.18 | 0.07 | 4.1 | 3.6 | - |
| Meso(4.4)-2.4 | 0.2 | 31.9 | 357 | 88 | 0.21 | 0.10 | 4.4 | 3.7 | 8.7 |
| Meso(5.0)-2.4 | 0.4 | 19.4 | 544 | 85 | 0.30 | 0.10 | 5.0 | 3.7 | 10 |
| Micro(0.5)-1.1 | - | 28.9 | 507 | 69 | 0.18 | 0.03 | 0.5 | - | - |
| Micro(0.5)-0.8 | - | 19.6 | 326 | 32 | 0.15 | 0.02 | 0.5 | - | - |
| MesoC-30 | 0.2 | - | 383 | 66 | 0.18 | 0.04 | 2.7 | - | - |

a. Obtained by EDS-SEM

b. Obtained by BJH method

*XRD*

XRD patterns show preserved MFI structure for all ZSM-5 samples **(Figure 5.6)**. The desilication treatment does not influence the crystallinity of samples due to the local removal of Si from the zeolite framework. The microporous structure was preserved [209].

*SEM*

**Figure 5.7** clearly shows the difference between microporous and desilicated H-ZSM-5 samples. Smooth external surface is observed (**Figure 5.7a)** with clear edges of crystals. In the Meso(4.1)-2.4 sample (**Figure 5.7b)**, roughness at edges of crystals is observed (**Figure 5.7b**) due to extraction of the framework Si and Al atoms. In **Figure 5.7c**, an increase in surface roughness could be seen on every crystal indicating the formation of mesopores. However, desilication at highly alkaline conditions (0.4 M) results in the formation of macropores with a diameter above 50 nm (**Figure 5.7d**). This effect could be explained by the fact that the Si extraction rate is much faster than the rate of realumination resulting in larger and deeper pores [91]. These data are also in line with the nitrogen

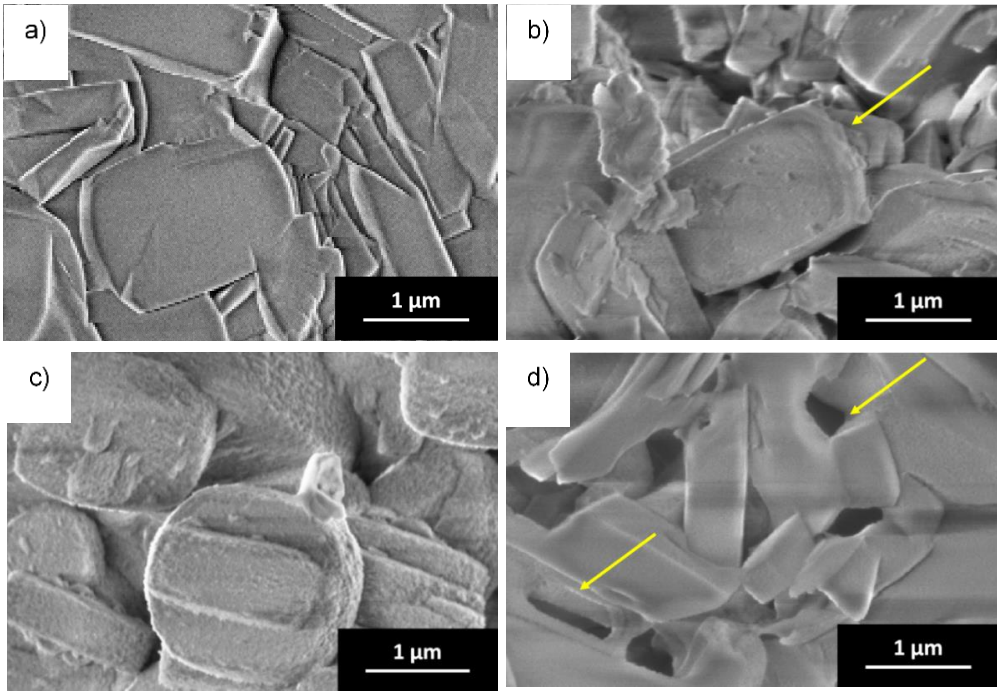


**Figure 5.7**. SEM images of a) Micro(0.5)-2.4 and desilicated samples, b) Meso(4.1)-2.4, c) Meso(4.4)-2.4, d) Meso(5.0)-2.4

adsorption data over the Meso(5.0)-2.4 catalyst. It can be concluded that high alkalinity is not desirable in the desilication process because it would substantially reduce the total amount of catalyst.

### *Nitrogen adsorption-desorption*

Nitrogen adsorption-desorption isotherms of mesoporous H-ZSM-5 samples are shown in **Figure 5.8.** The blank microporous zeolite shows typical Type I adsorption isotherms while all desilicated samples show typical Type IV isotherms as defined by IUPAC nomenclature [218]. The isotherm of the blank sample shows a highly uniform distribution of pore size in the micropore range without noticeable mesoporosity. The hysteresis loops positioned in the range of relative pressure of $P/P_0$ between 0.4 and 1.0 in the isotherms of desilicated samples are due to capillary condensation of the nitrogen in mesopores [219]. These hysteresis loops could be assigned into H4 adsorption type which is characteristic for the narrow slit-like pores. Moreover, the parallel shift of both adsorption and desorption branches suggests the presence of open (cylindrical) mesopores connecting to the external surface [220]. The

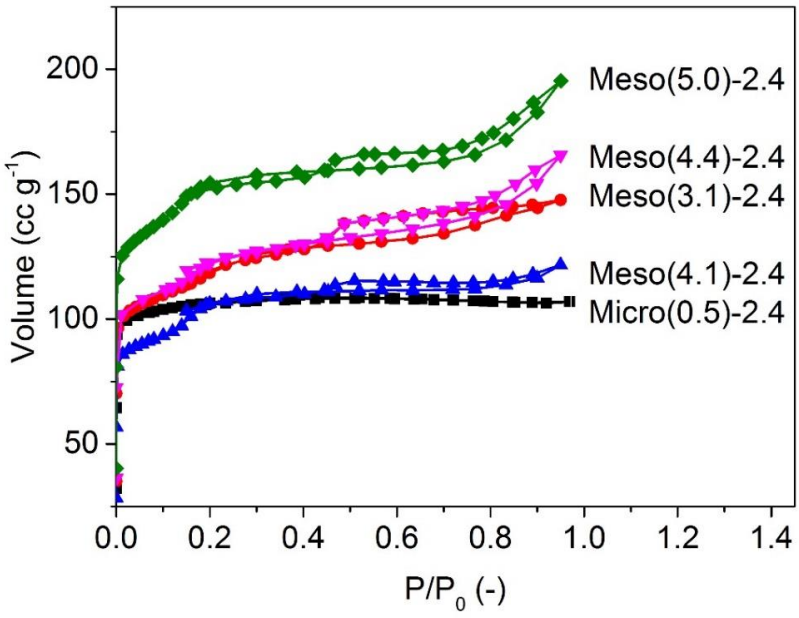


**Figure 5.8**. Nitrogen adsorption-desorption isotherms of micro-mesoporous ZSM-5 catalysts

Meso(3.1)-2.4 catalyst, obtained in the presence of TPAOH, shows the hysteresis loop of H2 type indicating the existence of a complex porous network and a wide pore distribution due to secondary crystallization of Si and Al atoms initially removed from the zeolite framework [221].

The pore size distribution (**Figure 5.9**) confirms the microporous nature of the blank H-ZSM-5 catalyst and induced mesoporosity in the desilicated H-ZSM-5 samples. There are no pores in the blank ZSM-5 sample in the mesoporous range. Two type of mesopores with different average diameters ($\overline{D_1}$, $\overline{D_2}$) are observed in the desilicated catalysts. Type 1 mesopores are defined by a diameter of ca 4 nm while type 2 mesopores have a mean diameter above 8 nm (shown in the frame, see **Figure 5.9**). All desilicated samples show Type 1 mesopores with a $\overline{D_1}$ of 3.6 nm. The mesopore volume decreases in the order of Meso(5.0)-2.4> Meso(3.1)-2.4> Meso(4.1)-2.4> Meso(4.4)-2.4. The Meso(4.4)-2.4 and Meso(5.0)-2.4 samples show the presence of type 2 mesopores with a diameter of 8.7 and 10.3 nm respectively. With the addition of $TPA^+$, the Meso(3.1)-2.4 sample has smaller (type 2) mesopore diameter of 6.6 nm. The Meso(4.1)-

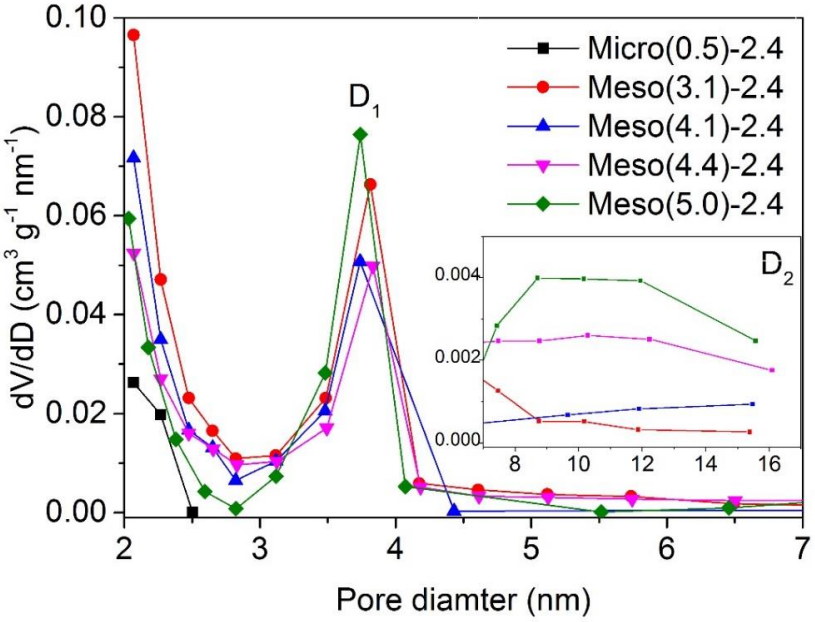


**Figure 5.9**. BJH pore size distribution curves of the blank and desilicated ZSM-5 samples

2.4 c barely has any type 2 mesopores due to much lower concentration of alkaline solution. By increasing the alkaline concentration to 0.4 M, the amount of type 1 of mesopores increases while larger type 2 mesopores are also formed. The Meso(3.1)-2.4 sample obtained in the presence of TPAOH has remarkably more type 1 mesopores and a much smaller amount of type 2 mesopores comparing to Meso(4.4)-2.4 obtained with the same total $OH^-$ concentration. This result indicates that the presence of the template introduces a much higher density of mesopores at a very narrow mesopore size range, without generating larger pores. These findings agree well with a previous study performed by Schmidt et al. [97].

As previously reported in the literature [97], the alkaline treatment could remove both framework silicon and aluminium atoms. The framework Si is more favourable to be removed in this process due to weaker Si-O-Si bonds in hydrolysis than Si-O-Al bonds [217]. Moreover, the negative charge of $AlO_4^-$ tetrahedrals protects nearby Al and Si atoms against $OH^-$ attack by negatively charged hydroxyl ions [217]. Therefore, extraction of Si could be mild in zeolite with a low Si/Al ratio. As shown in **Table 5.4**, as the alkaline concentration increases to 0.2 M, the Si/Al ratio in desilicated samples drops to 31.9. With the addition of TPAOH, a milder desilication is observed and the Si/Al ratio only drops to 44.7. The milder desilication happens due to the protecting reaction of $TPA^+$ cations and recrystallization of Si and Al during desilication. The $TPA^+$ cations have high affinity to the surface of ZSM-5 zeolite resulting in sealing off most of the external surface [222] and therefore preventing further diffusion of $OH^-$ ions.

The concentration of NaOH in desilication process has a major effect on textural properties of the samples. There is a noticeable increase both in the surface area and the mesopore volume in the Meso(4.1)-2.4 sample obtained from the diluted NaOH solution. By increasing the pH, both the total pore volume and the mesopore volume increase to 0.302 and 0.107 $cm^3 \cdot g^{-1}$ respectively. In the concentrated NaOH solution, the specific surface area increases to 544 $m^2 \cdot g^{-1}$ and both the total volume and the mesopore volume show a substantial increase to 0.302 and 0.107 $cm^3 \cdot g^{-1}$ respectively compared to those obtained from the diluted solution. The

average pore diameter increases to 5.0 nm. Comparing the Meso(4.4)-2.4 and Meso(5.0)-2.4 catalysts, it can be concluded that both the surface area and the total pore volume could be increased by 40% in the highly alkaline solution. However, the volume and the surface area of mesopores remains almost the same and the specific surface area of Meso(5.0)-2.4 even decreases. This suggests that larger macropores are formed that cannot be measured by BJH adsorption with its detection range of pores below 300 nm. Influenced by the TPAOH addition, the surface area of mesopores increases by 2.5 times from 45.6 to 116 $m^2 \cdot g^{-1}$. A decrease in the average pore diameter suggests the formation of small mesopores (**Figure 5.9**). The textual properties of microporous H-ZSM-5 samples with the Si/Al ratios (20 and 30) are also listed in **Table 5.4** for comparison.

*Pyridine-TPD*

**Figure 5.10** shows the pyridine-TPD profiles in a range of 125-550 °C of the parent and desilicated ZSM-5 catalysts. For microporous ZSM-5 catalysts, two distinct pyridine desorption peaks are observed in the profiles: a LTP at 150-300 °C and a HTP over 450 °C corresponding to the

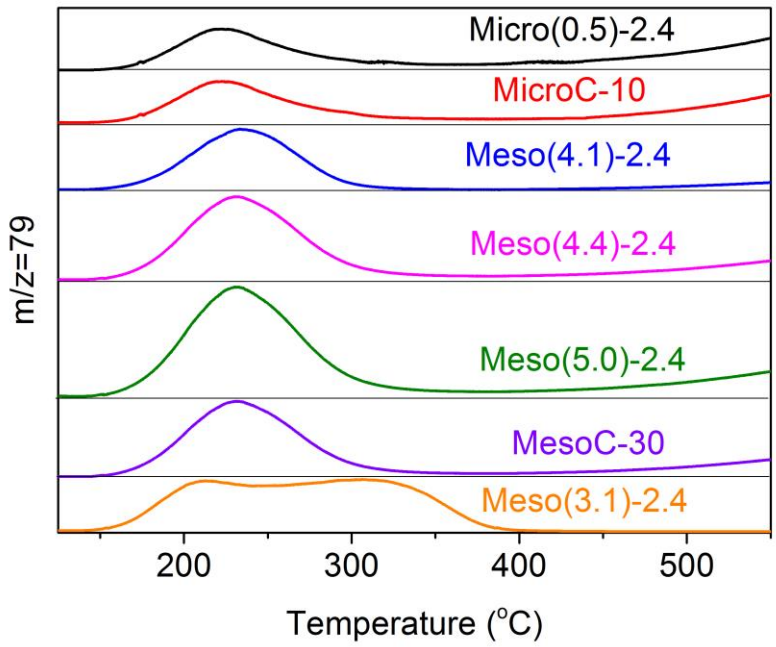


**Figure 5.10**. Pyridine-TPD profiles of parent and desilicated ZSM-5 powder and coating catalysts

weak and strong acid sites respectively. By comparing profiles of the sample Micro(0.5)-2.4 and Meso(4.1)-2.4, the HTP decreases while the LTP increases after the desilication treatment. With a higher NaOH concentration during desilication, the LTP shows a gradual increase. The increase in total population of acid sites is mainly caused by the formation of weak Lewis sites due to richer Al deposits [177,209]. All these results indicates that desilication treatment could either converts strong acid sites into weak acid sites, or improve accessibility of acid sites due to the partial removal of silica, affirmed by other authors [223]. A much stronger HTP emerges at 250-400 $^{o}$C for the sample Meso(3.1)-2.4 desilicated by TPAOH/NaOH mixture when there is no observation of the HTP over 450 $^{o}$C. Its LTP at 150-300 is reduced comparing to the sample Meso(4.4)-2.4 which is desilicated by 0.2 M NaOH only. The shift of HTP which indicates a weakened strong acidity is due to the Al redistribution under the protection effect by structural template against Al removal during desilication, which is also reported in literature [215]. The coating samples MicroC-10 and MesoC-30 show identical pyridine-TPD profiles as their powder counterparts Micro(0.5)-2.4 and Meso(4.4)-2.4 respectively.

*5.2.1.2 Catalytic performance*

The methanol conversion over the blank and desilicated samples is shown in **Figure 5.11**. Similar to the previous discussion, a methanol conversion of 30% is shown with a dash line. Based on Janssens's deactivation model [192], both the highest first-order reaction rate of 4.84 mol·$g_{cat}^{-1}$·$h^{-1}$ and deactivation coefficient of 0.884 mmol·$g^{-1}$ are calculated compared to desilicated samples, which could be attributed to presence of strong acid sites. The methanol conversion drops to 30% within 4 h indicating a substantial fraction of micropores becomes inaccessible due to blockage by the strong adsorption of large molecules and carbon deposits. The deactivated catalysts show much lower deactivation coefficients in a range of 0.126-0.219 mmol·$g^{-1}$ (**Table 5.5**). The catalyst lifetime ($t_{0.3}$) is improved to 7.5 and14 h for the Meso(4.1)-2.4 and Meso(4.4)-2.4 sample repectively. However the Meso(5.0)-2.4 catalyst with larger mesopores shows a similar

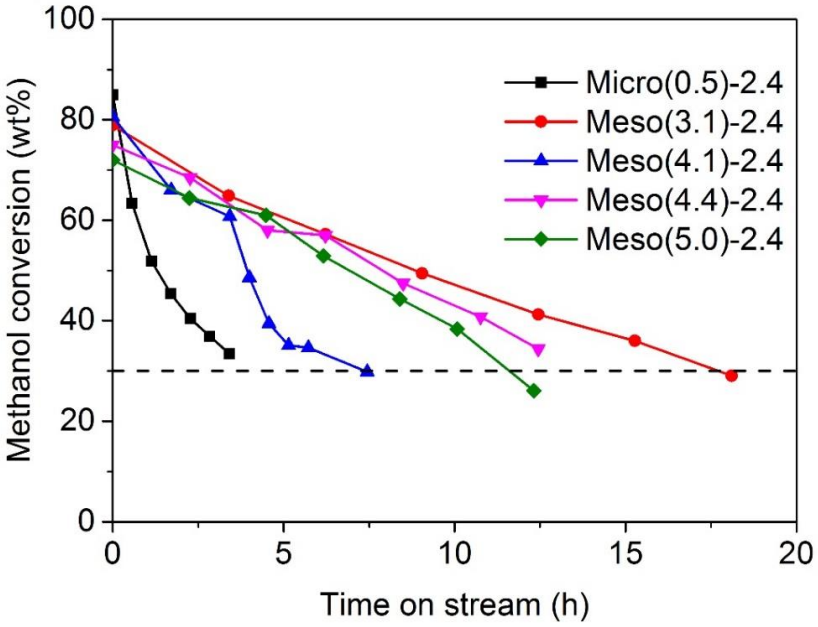


**Figure 5.11**. Conversion of methanol over the blank and desilicated ZSM-5 samples along time on stream in MTH reaction (T=370 $^{o}$C K, WHSV=20 $h^{-1}$, P=4 bar)

lifetime of 12 h as the Meso(4.4)-2.4 sample. It is very clear that the formation of mesopores improves the mass transfer of large molecules

**Table 5.5**. Calculated values of the rate constant, deactivation coefficient and turnover number (TON) for $C_{8-11}$ fraction of ZSM-5 catalysts ($W_0$=0.1 g, $\tau_0$=1.15 g·h·$mol^{-1}$)

| Sample | $t_{0.5}$ (h) | $t_{0.3}$ (h) | k ($mol \cdot g_{cat}^{-1} \cdot h^{-1}$) | a ($mmol \cdot g^{-1}$) | TON for $C_{8-11}$ ($g \cdot gcat^{-1}$) |
|---|---|---|---|---|---|
| Micro(0.5)-2.4 | 1.3 | 4 | 4.84 | 0.884 | 4.2 |
| Meso(3.1)-2.4 | 9.1 | 18 | 1.19 | 0.126 | 15.0 |
| Meso(4.1)-2.4 | 4.0 | 7.5 | 1.40 | 0.219 | 6.4 |
| Meso(4.4)-2.4 | 7.9 | 14 | 2.78 | 0.146 | 12.2 |
| Meso(5.0)-2.4 | 7.5 | 12 | 3.60 | 0.153 | 14.5 |

such as poly-aromatics in these zeolites and consequently improves the coke resistance. The lifetime for the Meso(3.1)-2.4 catalyst shows the highest value of 18 h among all samples. This improvement is explained by enhanced surface area, which is in a good agreement with several studies in MTP [217] and MTH reactions [99, 200]. The $TPA^+$ surfactant molecules with positive charge and hydrophobic tails could self-assemble to micelles interacting with negatively charged zeolite framework during the alkaline treatment, which prevents formation of extra framework Al [225].

The alkaline treatment could distinctly decrease the strength of strong acid sites which are responsible for the promotion of hydride transfer and cyclization reactions [217]. Consequently, the formation of aromatics from light olefins is suppressed, resulting in minimum amount of coke precursors and minimum deactivation [215,226]. Besides reduced acidity, structural properties including mean pore diameter and length would also attribute to the high resistance against coking of desilicated H-ZSM-5 [227]. **Scheme 5.1** demonstrates the interplay control of reaction rate by acidity and pore size. In the Micro(0.5)-2.4 catalyst, the micropores allocate sufficient density and amount of acid sites which provides high intrinsic reaction rate. However, the overall reaction rate is hindered by low diffusion of reaction

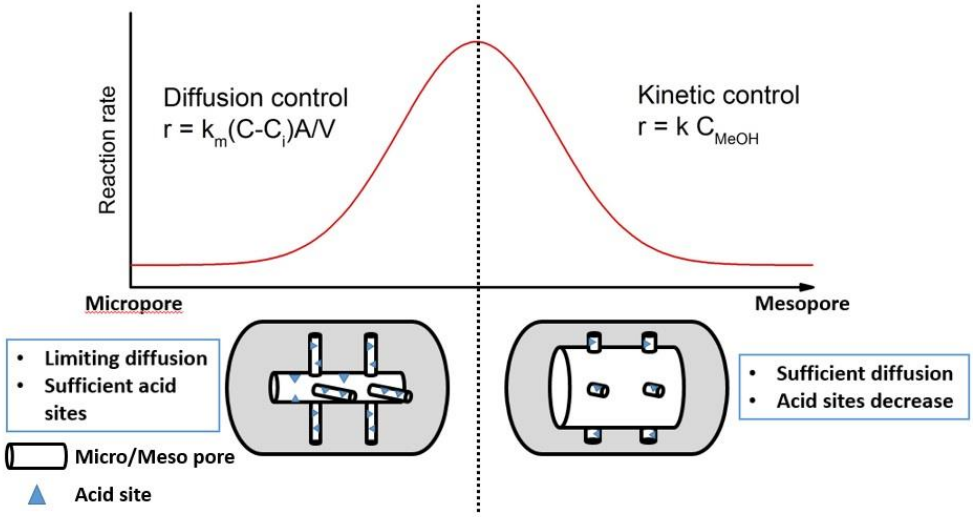


**Scheme 5.1**. Reaction rate under diffusion and kinetic control in transformation from micropore to mesopore ZSM-5 zeolite

products out of catalyst pores. In other words, the overall reaction rate is governed by diffusion control. In the mesoporous catalysts, the number of acid sites decreased significantly due to fewer micropores while the diffusion rate of reaction products is improved by the presence of larger cavities and pores. In this case, the overall reaction rate and the ratio of products is governed by kinetic control where the overall reaction rate equals to the intrinsic reaction rate. A much higher effective diffusivity in the mesoporous catalysts also improves the selectivity towards larger molecules and minimises coke formation rate increasing the catalyst lifetime in the MTH reaction [228].

The product distribution is shown in **Figure 5.12**. The selectivity changes with time on stream due to coke build-up [187]. The build-up of heavier hydrocarbons (both $C_{8\text{-}11}$ and $C_{6\text{-}10A}$ fractions) may take several hours while smaller molecules are consumed through methylation and aromatisation pathways. The selectivity is not greatly affected by desilication which is in line with previously published data [229]. The selectivity to the $C_{1\text{-}4}$ fraction of 54% is observed over all samples. The selectivity to the $C_{5\text{-}7}$ products

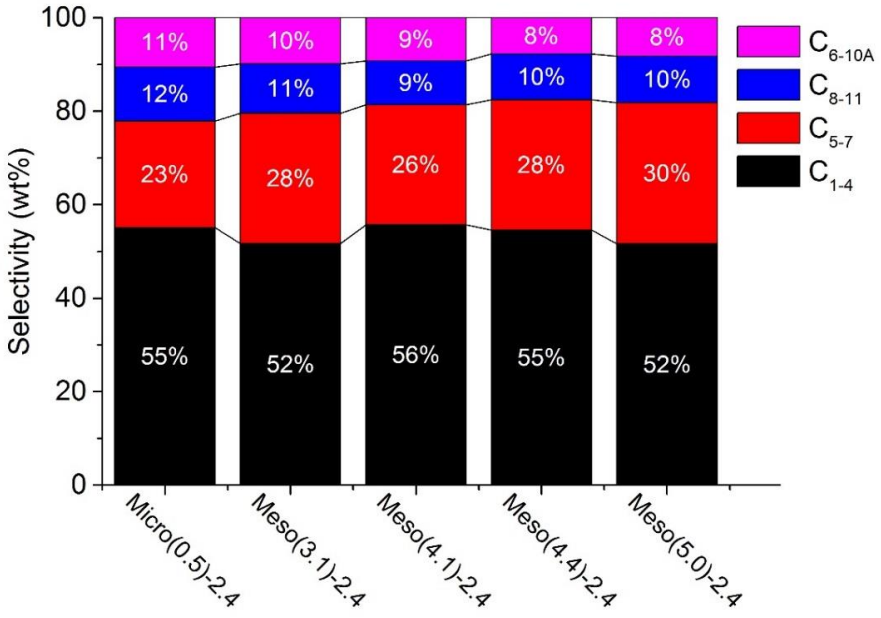


**Figure 5.12**. Selectivity of hydrocarbons over blank and desilicated ZSM-5 samples obtained in MTH reaction at conversion of 50%

increased from 23 to 30% with enhanced mesoporosity. This is explained by reduced structural restrains for molecules formed inside the pores. Typical molecule size for the $C_{5-7}$ paraffins is 0.42-0.71 nm [230]. Therefore larger molecules have very low diffusivity in the H-ZSM-5 micropores with a diameter of 0.55 nm. The selectivity to the $C_{8-11}$ products is slightly lower in the desilicated samples when comparing to the microporous catalyst due to a decreased micropore length and residence time. The aromatics fraction also drops from 11 to 8% with increasing mesopore size.

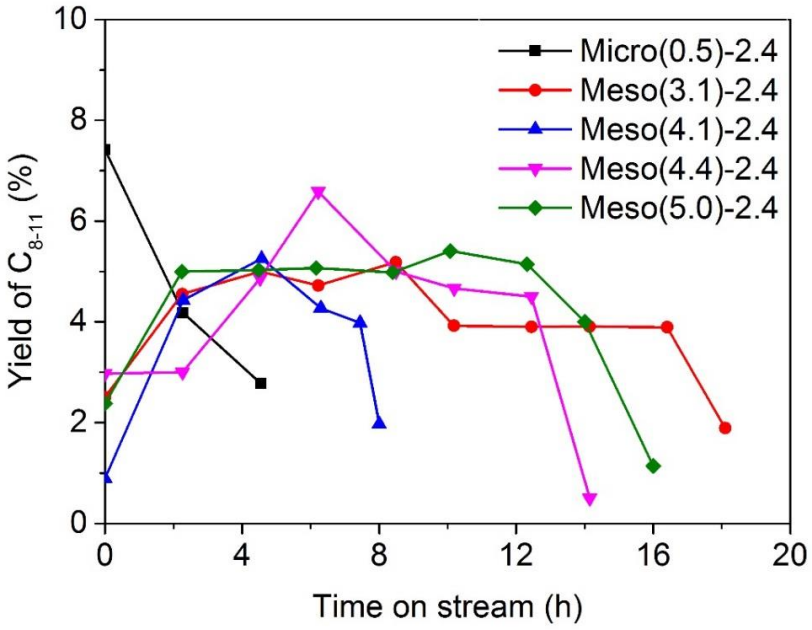


**Figure 5.13**. Product yield of $C_{8-11}$ fraction over blank and desilicated samples (T=370 $^{o}$C, WHSV=20 $h^{-1}$, P=2 bar)

The yield of the target $C_{8-11}$ fraction is shown in **Figure 5.13**. A higher yield of 7.5% was initially observed over the microporous sample as compared to the desilicated samples. However, the yield drops to 3% within 5 h on stream due to a fast drop in reaction rate. Over the desilicated samples, the $C_{8-11}$ fraction yield of ca 5% remains rather constant for a considerable period of time, followed by a deactivation period. The duration of the stable yield period is in following order: Meso(3.1)-2.4> Meso(5.0)-2.4> Meso(4.4)-2.4> Meso(4.1)-2.4. The highest turnover number (TON) of 15.0 is observed over the Meso(3.1)-2.4 catalyst obtained in the presence of TRAOH. With the influence of the template, the framework Si and Al atoms

are preserved and more active sites is present in the Meso(3.1)-2.4 catalyst. Increasing TON with increasing mesopore size also suggests that the reaction is in the transition regime between kinetic and diffusion controlled regimes (**Table 5.5**).

### 5.3.2 Micro-mesoporous ZSM-5 coating

*5.3.2.1 Characterisation*

After the alkaline treatment, transport pores with a diameter of 5 µm were present in the coatings (**Figure 5.14**). This noticeable change is in line with the previously proposed formation mechanism of mesopores where Al atoms released from the zeolite framework form a protective shell of $AlO_4$ species to prevent massive dissolution [91]. The surface roughness increases as it was previously observed in the Meso(4.4)-2.4 sample (**Figure 5.7c**) indicating larger surface area. The smaller crystals exhibit higher resistance to desilication due to a lower gradient of Al atoms from the external to internal surface [231]. The micro-mesoporous ZSM-5 coating has a mean pores size of 2.4 µm and a specific surface area of 383 $m^2 \cdot g^{-1}$ (**Table 5.4**). After the alkaline treatment with a shorter time, the MesoC-30 catalyst shows higher specific surface area than either microporous sample or Meso(4.4)-2.4 catalyst. However, the mesopore

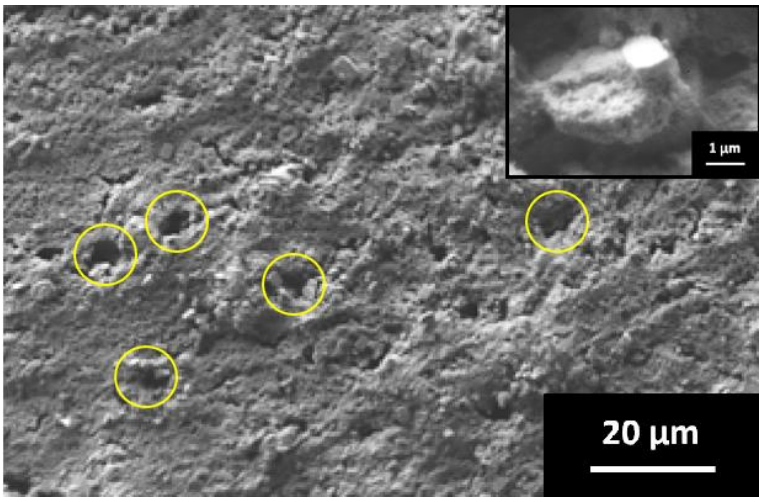


**Figure 5.14**. SEM images of coating sample MesoC-10 on its surface

surface area and volume reduces at the short treatment time. This suggests that in this micro-mesoporous catalyst, mesopores are mainly created near the outer surface while the alkaline solution may have limited access to the inner layer of coating.

*5.3.2.2 Catalytic performance*

The conversion of methanol over the microporous and hierarchical coatings is shown in **Figure 5.15**. An initial conversion of 80% is observed over the thin microporous coating (MicroC-10) indicating full catalyst utilisation and the absence of internal diffusion limitations. However, the initial conversion of methanol decreases to 45% over the thick H-ZSM-5 coating (MicroC-30). Almost complete deactivation of both MicroC-10 and Micro-30 coatings occurs within 4 h on stream. It appears that the coke formation is preferably localised at the external layer of zeolite crystals. This hinders the diffusion of reactants into the inner coating layers [232].

The MesoC-30 coating shows a similar initial conversion as the microporous coating however it demonstrates a longer lifetime of 28 h. The

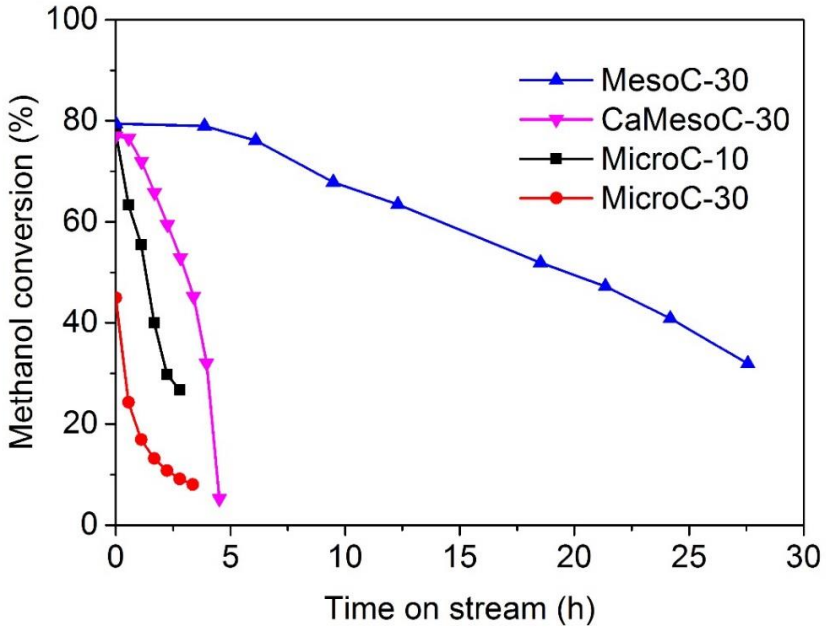


**Figure 5.15**. Conversion of methanol over blank and modified coating samples (T=370 $^{o}$C, WHSV=28 $h^{-1}$, P=4 bar)

mesoporous structure has considerably improved utilisation of coating resulting in much higher conversion levels. The mesoporous network also facilitates the diffusion of heavier products and coke precursors leading to an improved lifetime in the MTH reaction. It should be noted that the ion-exchanged Ca-MesoC-30 coating demonstrates much lower stability than the mesoporous MesoC-30. The Ca-MesoC-30 coating fully deactivates within 5 h on stream. This result is expected based on the similar effect of Ca ion-exchange and desilication on strong acid sites of catalysts. The strong acid sites (HTP over 450 $^{o}$C in **Figure 5.10**) is suppressed by desilication. A following Ca ion-exchange treatment would only replace protons of weak acid sites. Therefore the additional Ca-exchange step results in a low amount of acid sites in the Ca-MesoC-30 coating and thus reduces its catalytic activity.

In the subsequent experiments, the MTH reaction was carried out at a pressure of 1-4 bar and a WHSV in the range between 5 and 40 $h^{-1}$ to optimise reaction conditions. The product distribution is considerably influenced by the methanol flow rate and reaction pressure. The selectivity to $C_{1-4}$ above 50% was obtained at a high methanol flow rate due to a low residence time of product in the catalyst (**Figure 5.16a**) when light hydrocarbons are purged out of catalyst without further methylation. The formation of the $C_{5-7}$ fraction was highly promoted by a higher pressure. The highest selectivity of 25.3% was observed at the highest pressure of 4 bar (**Figure 5.16b**). It can be seen that both pressure and residence time play a major role on the $C_{8-11}$ selectivity. The highest $S_{8-11}$ of 18.5% was observed at 4 bar and a WHSV of 10 $h^{-1}$. On the other hand, the $C_{6-10}$ aromatic hydrocarbons are preferably formed at a small WHSV of 5 $h^{-1}$

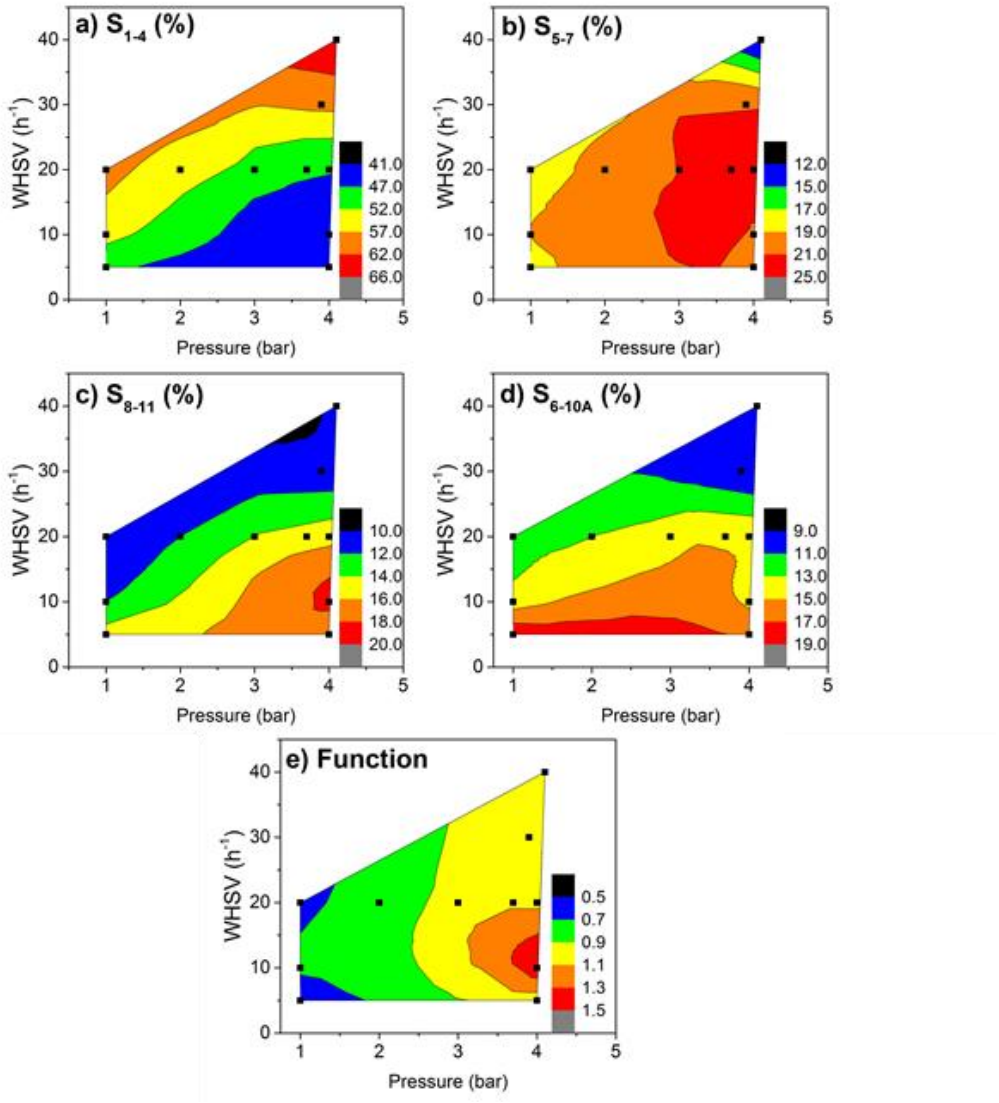


**Figure 5.16**. Product distribution of a) $C_{1-4}$, b) $C_{5-7}$, c) $C_{8-11}$ and d) $C_{6-10A}$ in MTH reaction over the MesoC-30 coating under different conditions (T= 370 $^{o}$C) e) the values of the design parameter (Eq. 5.3)

when the residence time is much longer in the reactor indicating a different kinetic.

**Figure 5.16e** shows the values of the design parameter given by Eq. 5.1 as a function of reaction pressure and WHSV. The optimal conditions correspond to reaction pressure of 4 bar and a WHSV of 10 $h^{-1}$ which provides the highest value of design parameter 1.4. In other words, these conditions provide the maximum yield of $C_{8-11}$ fraction with the minimum formation of aromatics by-products.

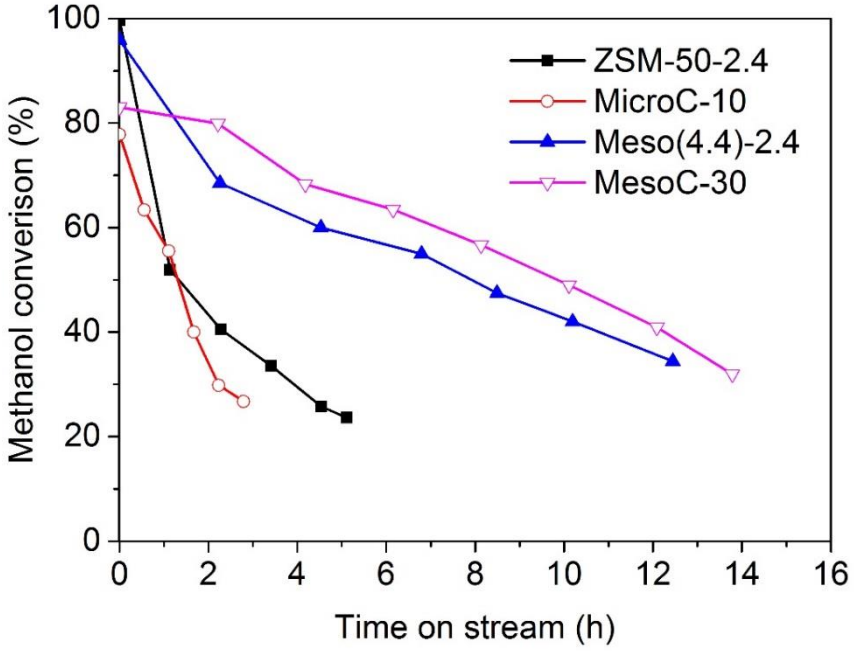


**Figure 5.17**. Methanol conversion over micro and micro-mesoporous pellets (Solid symbols) and coatings (Open symbols) in MTH reaction (T=370 $^{o}$C, WHSV=28 $h^{-1}$, P=4 bar)

The methanol conversion over the microporous and hierarchical (micro mesoporous) ZSM-5 coating and pellets was also compared (**Figure 5.17**). The initial methanol conversion of 95% was observed over both types of ZSM-5 pellets. The deactivation behaviour was similar for both ZSM-5 coatings and pellets. Selectivity distribution (**Table 5.6**) shows that mesoporous structure improves selectivity to $C_{5+}$ range products and reduces aromatics. However, the thin microporous coating, shows lower $S_{8-11}$ due to short diffusion time in the porous network. With the presence

**Table 5.6**. Summary of selectivity over ZSM-5 catalyst in different reactor (T=370 $^{o}$C, WHSV=28 $h^{-1}$, P=4 bar)

| Sample | Porosity | Catalyst form | $S_{1-4}$ (%) | $S_{5-7}$ (%) | $S_{8-11}$ (%) | $S_{6-10A}$ (%) |
|---|---|---|---|---|---|---|
| Micro(0.5)-2.4 | Microporous | Pellets | 53.5 | 23.1 | 11.5 | 11.0 |
| Meso(4.4)-2.4 | Micro-mesoporous | Pellets | 49.1 | 27.7 | 12.7 | 9.2 |
| MicroC-10 | Microporous | Coating | 56.7 | 25.1 | 6.1 | 6.7 |
| MesoC-30 | Micro-mesoporous | Coating | 42.4 | 24.7 | 16.6 | 15.2 |

of mesopores and longer diffusion time in a thicker coating, the MesoC-30 sample shows higher selectivity towards both $C_{8-11}$ and $C_{6-10A}$ fractions. More aromatic is released from reaction with less formation of poly-aromatics considering larger diffusivity in mesopores. The exact control of selectivity is further possible by adjusting reaction conditions.

## 5.4 Conclusions

It has been found that ion-exchange with Ca provides controllable Ca exchange ratio in Ca-H-ZSM-5 catalyst. The resulting catalysts exhibited similar structural and morphological patterns to the parent H-ZSM-5. By increasing the Ca content, the catalyst lifetime and selectivity to the $C_{8-11}$ hydrocarbons were considerably improved. Ca-ZSM-5 catalysts with an exchange ratio in the range of 0.15-0.20 were found to be the most stable in the MTH reaction, maintaining an initial conversion level for over 7 h and having the highest selectivity of ca. 46% to the $C_{8-11}$ gasoline fraction due to the presence of weak Brønsted acidity.

Experimental evidence shows that the performance of mesoporous H-ZSM-5 catalysts can be improved by regulating porous network. The presence of mesopores introduced by desilication with an alkaline solution enhanced effective diffusivity for larger hydrocarbons. The average mesopore diameter and volume as well as the surface area increased with increasing the concentration of the alkaline solution. Low catalyst loading was observed from a very concentrated alkaline solution due to a massive dissolution of ZSM-5 catalyst and the formation of larger macropores. While the selectivity to the $C_{8-11}$ hydrocarbons did not change, a higher turnover number for the $C_{8-11}$ fraction was observed over the desilicated samples. The presence of the structural template in the alkaline solution reduced the mesopore diameter and preserved the microporous ZSM-5 structure. The longest lifetime and the highest TON for the $C_{8-11}$ were found with a mean mesopore size of 3.1 nm and a crystal size of 2.4 µm.

The selectivity to gasoline fraction and the catalyst lifetime improves over ZSM-5 coatings as compared to pelleted catalysts. The meso-microporous H-ZSM-5 coatings with a thickness of 30 µm show a 5-fold increase in catalyst lifetime and two times higher selectivity to $C_{8-11}$ fraction compared to the microporous coating with the same thickness and composition. The highest selectivity to gasoline range hydrocarbons of 18.5% with a minimum formation of aromatics by-products was obtained in the MTH reaction at a temperature of 370 $^{o}$C at a pressure of 4 bar and a WHSV of 10 $h^{-1}$.

# Chapter 6
# Modelling of heat transfer in a microstructured reactor/ heat-exchanger

## 6.1 Introduction

In recent years microreactor technologies are being widely investigated in chemical process engineering to build microchannel devices, e.g. mixers, heat-exchangers, and reactors with advantaged capabilities as compared to those of conventional macroscopic systems. Microstructured heat-exchangers were first developed in 1985 by Swift et al. [233]. Due to their high heat transfer area per unit volume, standalone microreactors and microstructured reactors combined with heat-exchangers (MRHE) have been favoured for exothermic reactions. Compared to conventional-sized reactors and heat-exchangers, overall heat transfer coefficient in microstructured devices could be up to 2 orders higher [234]. This is a characteristic feature of both microreactors and MRHEs and it could be beneficial for applications such as fast, highly exothermic reactions. The development of microreactors shows large promise when several unit operations are integrated with sensors and actuators to form a micro chemical plant [235]. These miniplants offer opportunities for small-scale fuel processing and portable power generation.

Deactivation due to coking is one of the main reasons reducing catalyst lifetime in the MTH reaction. Temperature hot-spots could occur in a fixed-bed reactor due to insufficient heat transfer to the environment. In adiabatic conditions, the reaction heat causes a temperature gradient over 600 K in the reactor. At a low temperatures, the MTH reaction yields mainly gasoline products ($C_{1-4}$) that are of low commercial value. When shifted further up, the reaction temperature results in the formation of carbon deposits that are blocking micropores in the catalyst structure which leads to a fast catalyst deactivation. To better understand the hot-spot issue, a comprehensive reactor design was carried out in separated studies where

a reaction kinetic model is combined with a reactor heat transfer model [236–239].

To support the reactor design, modelling will be indispensable. By means of modelling, the effect of different reactor operating conditions, such as reactor diameter and length, temperature and reactant flow ratio can be predicted, which can then be checked experimentally. In this chapter, a compact MRHE is designed to generate gasoline range hydrocarbons from methanol. The MTH reaction takes place on a surface of H-ZSM-5 catalytic coating. A simplified kinetic scheme was chosen with products lumped to $C_8$ hydrocarbons. An air flow is used as a cooling agent.

MRHEs differ from larger-scale heat-exchangers, as axial conduction of heat through the solid material plays a very important role in a microdevice. Therefore as it was discussed in the literature review section, 1D convective heat transfer models often fail as they are not able to predict the temperature gradients measured experimentally. Therefore 2D heat transfer models of the MRHE were also developed. The 2D heat-transfer model describes a single periodic unit with simplified hydrodynamics and conductive heat transfer. The corresponding differential equations are solved numerically in a COMSOL Multiphysics software. The actual device to be manufactured in cooperation with the Institut for Mikrotechnik Mainz (IMM-Fraunhofer).

## 6.2 2D modelling

### 6.2.1 Reactor design

The reactor is to be designed for a methanol feed rate of 2 $kg \cdot h^{-1}$ with a product yield of the $C_8$ hydrocarbon fraction of 0.83 $kg \cdot h^{-1}$. It is assumed a methanol conversion of 95% as an amount of 3% of methanol is allowed in fuels according to the European Fuel Quality Directive [240].

**Initial conditions:**

- Methanol WHSV of 2.4 $h^{-1}$
- Outlet pressure: 1 bar
- Inlet temperature: 653K

*Kinetic model*

The kinetic model used in this study is a simplified lumped model (**Scheme 6.1**). As the major desired product, $C_8$ olefin ($C_8H_{16}$) was taken as the model pseudocomponent (pseudocomponent C). Physical properties of all reaction species and reaction rate constants are listed in Appendix B.

$$2CH_3OH(A) \underset{k_{-1}}{\overset{k_1}{\Longleftrightarrow}} CH_3OCH_3(B) + H_2O(D)$$

$\Delta_rH_2$ (653 K) =-7.254 kJ·mol$^{-1}$

$$CH_3OCH_3(B) \xrightarrow{k_2} \frac{1}{4}C_8H_{16}(C) + H_2O(D)$$

$\Delta_rH_2$ (653 K) =-68.364 kJ·mol$^{-1}$

**Scheme 6.1**. Lumped reaction scheme for methanol to hydrocarbon process.

The mole balance (**Eq.6.1**) in the reactor are described using Plug Flow Reactor (PFR) rate equations. The volume expansion is defined as a function of methanol conversion ($X$) to octene (**Eqs.6.2, 6.3**). Formation rate of each species and their relationship to the reaction rates are described as **Eqs.6.4-6.9** [241].

$$F_{i,0} - F_i + \int_0^{L=0.2}(r_i \cdot A_{cat})dL = 0 \quad \text{(i=A, B, C)} \tag{6.1}$$

$$F_i = C_i \cdot V = C_i \cdot V_0(1 + \frac{X}{8}) \tag{6.2}$$

$$\mathrm{X} = 1 - \frac{C_A}{C_{A,0}} \tag{6.3}$$

$$\mathrm{r}_A = \ -2R_1 \ = -2k_1 \cdot {C_A}^2 + 2k_{-1} \cdot C_B \cdot C_D \tag{6.4}$$

$$\mathrm{r}_B = R_1 - R_2 = k_1 \cdot {C_A}^2 - k_{-1} \cdot C_B \cdot C_D - k_2 \cdot C_B \tag{6.5}$$

$$r_C = \frac{1}{4}R_2 = \frac{1}{4}k_2 \cdot C_B \quad (6.6)$$

$$r_D = R_1 + R_2 = k_1 \cdot {C_A}^2 - k_{-1} \cdot C_B \cdot C_D + k_2 \cdot C_B \quad (6.7)$$

$$K_{eq} = \frac{k_1}{k_{-1}} = \frac{16.8}{2.5} = 6.60 \quad (6.8)$$

$$k_2 = 8.2\ s^{-1} \quad (6.9)$$

where $F_{i,0}$ and $V_0$ are the initial molar and volumetric flow rate of the species i respectively. $F_i$ and $C_i$ are the molar flow rate and the concentration of species i at the position $L$ in the reactor. $r_i$ is the formation rate of the species i. $A_{cat}$ is the cross-section area of catalyst coating. Water is considered as the fourth species and its concentration is calculated as a by-product released during formation of DME and octene.

By solving above equations, the concentration profile was derived (**Figure 6.1**). Methanol is initially rapidly consumed to form an fast equilibrium with DME at around L=0.025 m in the reactor. Octene and water are continuously formed in the reactor.

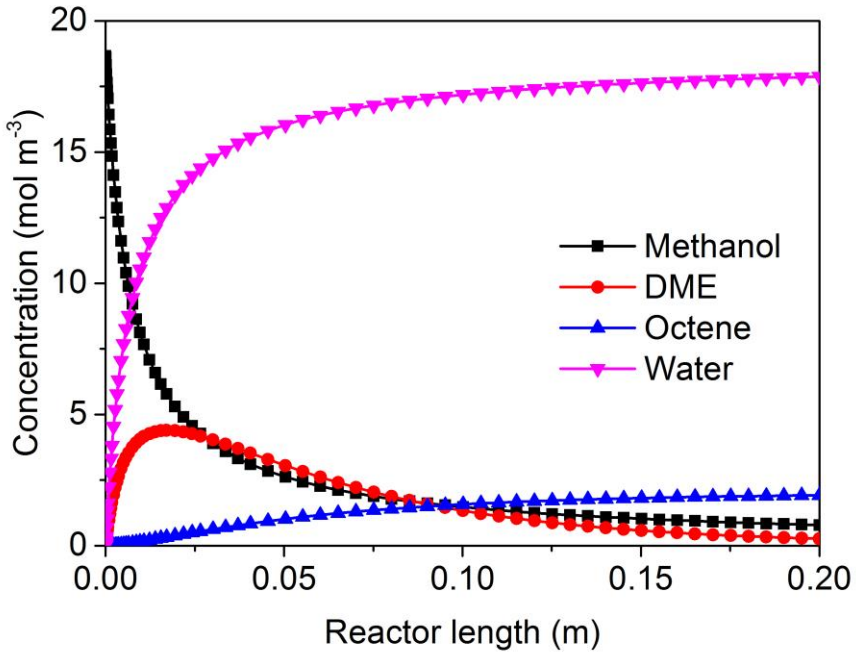


**Figure 6.1**. An example of concentration profiles for methanol and reaction products as a function of reactor length. (T=653 K, $F_{v,M}$=2.66*10$^{-9}$ m$^3$ s$^{-1}$, P=1 bar)

*Properties of gas mixture*

The density, heat capacity, thermal conductivity and dynamic viscosity of the gas mixture were calculated as a function of temperature. The details of the calculations are presented in Appendix B. All initial properties were estimated at 1 bar and 653 K. The temperature dependencies of physical properties are also presented in Appendix B. In the reaction channel, fluid composition goes through a transition from pure methanol to a mixture of diluted hydrocarbons and water. The average value of each property through the whole reactor is listed in **Table 6.1**. Then, the properties of gas mixture were presented as a function of reactor coordinate (L) considering changing gas composition during the reaction as shown in Appendix B.

**Table 6.1**. Properties of gas phases species at 653 K

| Vapor | Molecular weight ($g \cdot mol^{-1}$) | Density ($kg \cdot m^{-3}$) | Heat capacity ($J \cdot K^{-1} \cdot mol^{-1}$) | Dynamic viscosity ($Pa \cdot s$) | Thermal conductivity ($W \cdot m^{-1} \cdot K^{-1}$) |
|---|---|---|---|---|---|
| Methanol | 32 | 0.597 | 2200 | 2.01 | 0.0583 |
| DME | 46 | 0.859 | 2480 | / | 0.0493 |
| Octene | 112 | 2.090 | 1030 | / | 0.0313 |
| Water | 18 | 0.336 | 2050 | 2.36 | 0.0539 |

*Reactor geometry*

The geometry of the MRHE is shown in **Figure 6.2**. A single microchannel plate made of the AISI 304 steel has 14 semi-cylindrical channels with a diameter of 0.5 mm. Two plates stacked together form a single reactor unit of parallel channels. The plates with reaction channels are sandwiched with the ones with cooling channels. The A-A cross section is chosen to represent 2D geometry. The design parameters are shown in **Figure 6.2** and also listed in **Table 6.2**. The following assumptions are made in the design:

- Steady-state fully developed flow
- Heat losses to surrounding are neglected (adiabatic reactor).
- Pressure drop in reaction channel could be neglected due to laminar gas flow at low flow rate. The supporting calculations are provided in Appendix B.

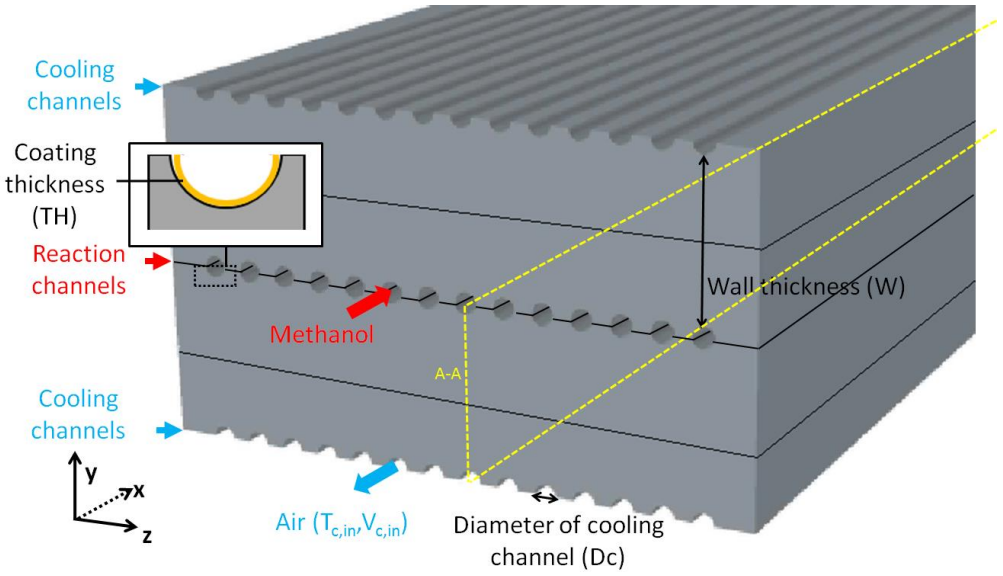


**Figure 6.2.** Schematic view of sandwich microchannel reactor/heat-exchanger geometry. Plate dimensions (w×h) are 14 × 8 $mm^2$, with 14 microchannels with a diameter of 0.5 mm and a length of 200 mm

Due to the highly exothermic nature of this process, the energy released from the reaction should be removed by the coolant.

Laminar flow conditions in the reaction channels was determined from a low value of Reynolds number by **Eq. 6.10**.

$$Re = \frac{\rho \cdot v \cdot D_r}{\mu} = 0.38 \qquad (6.10)$$

**Table 6.2**. Reactor design specifications and fluid properties

| Parameter | | Range |
|---|---|---|
| Solid thermal conductivity (W $m^{-1}$ $s^{-1}$) | Fixed | 30 |
| Fluid thermal conductivity (W $m^{-1}$ $s^{-1}$) | Fixed | 0.0624 |
| Reaction channel diameter (mm) | Fixed | 0.5 |
| Plate length (m) | Fixed | 0.2 |
| Plate thickness (mm) | Variable | 0.5-2.0 |
| Catalytic coating thickness (mm) | Variable | 0.005-0.025 |
| Cooling channel diameter (mm) | Variable | 0.2-0.5 |
| Coolant superficial velocity (m $s^{-1}$) | Variable | 1.0-4.0 |

where $\rho$ is density of fluid, $v$ is velocity of fluid, $D_r$ is the diameter of reaction channel, $\mu$ is the dynamic viscosity. The reactor is insulated which makes heat loss to the environment negligible compared to the heat generated in the reaction (Assumption 2). The heat diffusion and mass diffusion are much higher inside catalyst coating compared to the packed catalyst. Thiele modulus and heat transfer coefficient have been discussed in **Chapter 3.5**.

To compare the effect of different design parameters on the temperature distribution, the difference of temperature between the local temperature at the catalyst position in the channel and the reactor set-point was expressed via the temperature non-uniformity parameter ($\delta$):

$$\delta(\%) = \frac{1}{\bar{T}}\sqrt{\frac{1}{N-1}\sum_{j-1}^{N}(\bar{T} - T_j)^2} \times 100 \qquad (6.11)$$

where $\bar{T}$ is average temperature, $T_j$ is the temperature at position $j$ along the axial reactor coordinate and $N$ is the total number of positions taken in the optimisation.

The reaction rate constant of 0.224 $s^{-1}$ was taken from experimental results in section **4.2.3.3**. The maximum coating loading was limited by a thickness of 0.05 mm corresponding a Thiele Modulus of 0.1. In these conditions, the reactor operates in the kinetics regime providing full utilisation of catalyst coating.

*Mesh independence*

Prior to the parametric study, the dependence of computational mesh level was examined in the model. Three levels of mesh density (coarse, normal, fine) are presented in **Figure 6.3**. The relative level of meshing elements follows the order: coating > reaction channel = cooling channel > reactor wall. Theoretically, smaller size of computational cells would require more

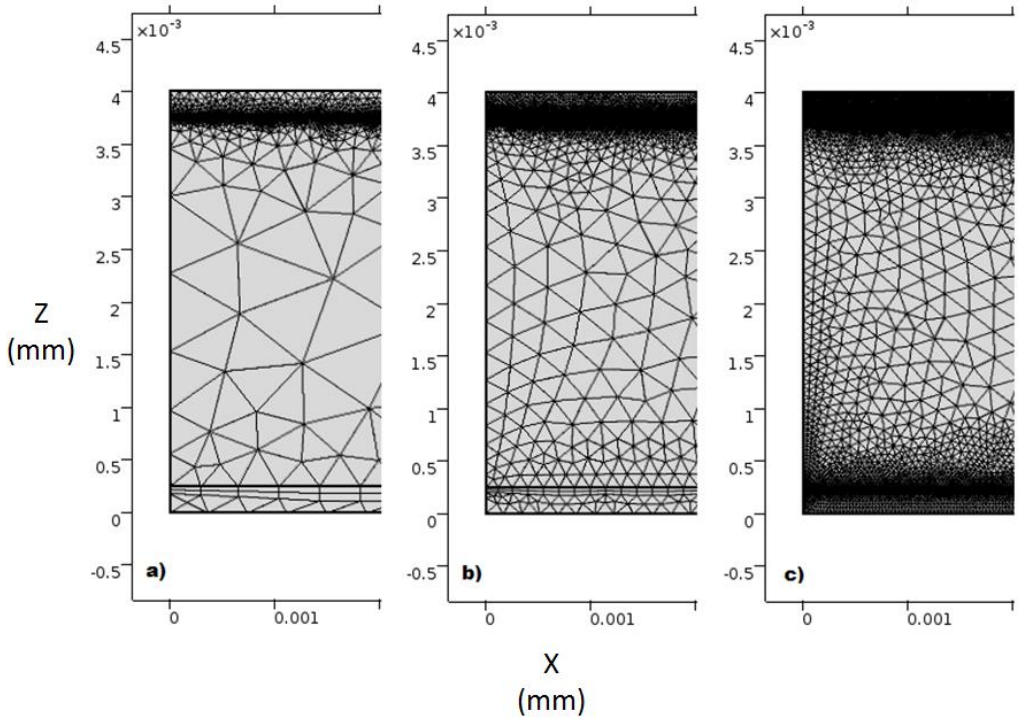


**Figure 6.3**. Different meshing levels: a) Coarse, b) Normal, c) Fine.

computational steps leading to higher accuracy. However, the computation time may take days to reach convergence depending on the complexity of models, which could be inconvenient in the parametric study. To estimate the effect of meshing density on the accuracy of computation, computed temperature profiles are compared. The temperature profile shifts by 1 and 2.5 K to higher temperatures for the normal and fine meshes, respectively comparing to the coarse mesh. The shift of temperature profiles suggests that increasing level of mesh improves the accuracy. However, this difference of 2.5 K was neglected and a coarse mesh (**Figure 6.3a**) was chosen for 2D modelling.

### 6.2.3 Heat transfer modelling

*Initial single reactor model*

To reach isothermal conditions, heat management is the critical issue of the process as the reaction is very exothermic. The heat of reaction is 1.2 MJ· kg-methanol$^{-1}$. In the first reactor design, we defined a maximum and a minimum temperature limit, 643 and 663 K respectively. A cooling gas system is needed to control the catalyst temperature. A plug flow was assumed for both gases and the axial dispersion was neglected.

Due to the fast radial heat transport, axial temperature dispersion introduced by the laminar flow profile could also be neglected. The temperature profile of the gases is determined by convective heat transport and heat exchange with the metal walls. When the length coordinate is made dimensionless with the length of the heat-exchanger, the equations for the reactant ($T_r$) and coolant gas ($T_c$) temperatures become

$$(\dot{m}Cp)_r \frac{dT_r}{d\hat{x}} = -h_r A_r (T_r - T_m) \tag{6.12}$$

$$(\dot{m}Cp)_c \frac{dT_c}{d\hat{x}} = -h_c A_c (T_m - T_c) \tag{6.13}$$

where $\hat{x}$ is the dimensionless reactor coordinate, $(\dot{m}Cp)_i$ the heat transport capacity (mass flow rate times heat capacity) of fluid i (W·K$^{-1}$), $h$ the gas–solid heat transfer coefficients (W·m$^{-2}$·K$^{-1}$), and $A_i$ the respective heat exchange surface areas (m$^2$). To calculate the heat transfer coefficients, entrance effects were neglected and a constant Nusselt number of 3.66 was assumed for the circular microchannels.

The model for the metal plates takes into account axial heat conduction through the plates, heat exchange with the two gases, and for the reactor part, heat production due to reaction, to yield

$$-\frac{\lambda_m A_m}{L} \frac{d^2 T_m}{d\hat{x}^2} = h_r A_r (T_r - T_m) - h_c A_c (T_m - T_c) + \dot{Q}_P(X) \tag{6.14}$$

with $\lambda_m$ the conductivity of the reactor material (W·m$^{-1}$·K$^{-1}$), $A_m$ the cross-sectional area of the reactor material perpendicular to the x-axis (m$^2$), and $L$ is the heat-exchanger length (m).

The heat generation function (**Eq. 6.15**) derived from the reaction kinetics and the reaction enthalpy calculated as the sum of the formation enthalpies of all species. The reaction enthalpies at 653 K are 3.6 and 34.2 kJ·mol$^{-1}$ for the first and second reaction steps respectively.

$$\dot{Q}_P\ (W \cdot m^{-3}) = \Delta_r H_1(653\ K) \cdot R_1 + \Delta_r H_2(653\ K) \cdot R_2 \qquad (6.15)$$

To verify the numerical model, a single reaction channel geometry was adopted to estimate the adiabatic temperature rise in the reaction channel.

$$\Delta T = \frac{\Delta H(653\ K)}{\sum m_i \int Cp_i(T)dT} = 510\ K \qquad (6.16)$$

where $m$ is the mass flow rate of fluid i and $Cp_i(T)$ is its heat capacity at temperature $T$. In the adiabatic case, the predicted outlet temperature rise corresponds well with the results obtained by **Eq 6.16**. This showed that the accuracy of numerical calculations is high enough for the purpose of this study.

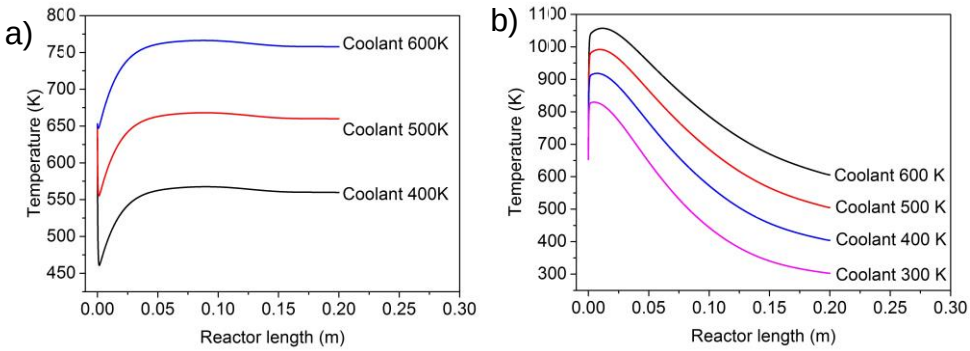


**Figure 6.4**. Effect of coolant temperature on reactant temperature in different cooling mode a) Co-current, b) Counter-current ($v_c$=1.0 m s$^{-1}$, $D_c$=0.5 mm, W=3.5 mm, TH=0.01 mm

The effect of coolant flow mode (co-current vs counter-current) and inlet coolant temperature on the temperature distribution was studied with the 1 D model. In the co-current case, a sharp temperature drop is observed near an axial position of 0.01 m in the reaction channel (**Figure 6.4a**). However, the temperature decreases too far below the desired temperature. The temperature profiles in the counter-current case are smoother yet a hot spot is observed at the channel inlet (**Figure 6.4b**). Changing the coolant

temperature shifts the whole temperature profiles rather than narrowing the temperature difference.

It can be concluded that the target temperature difference could not be achieved in a single reactor/heat-exchanger. The optimised geometry still gives a high temperature non-uniformity with a temperature gradient of 100

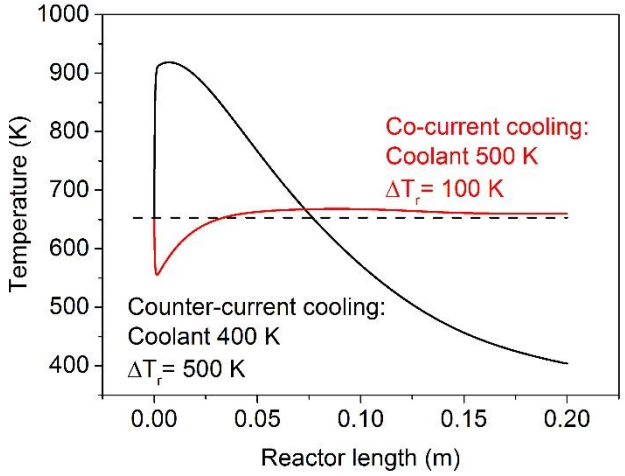


**Figure 6.5**. Optimised temperature profiles in a single reactor configuration with co-current and counter-current coolant configuration. ($v_c$=1.0 m $s^{-1}$, $D_c$=0.5 mm, W=3.5 mm, TH=0.01 mm)

K in the reaction channels (**Figure 6.5**). To reduce the axial temperature gradient, the reactor should be split in two parts with an additional coolant feeding stage between them.

The temperature profiles show the effect of the length of the first reactor on temperature non-uniformity in the coating (**Figure 6.6a** & **Figure 6.6b**).

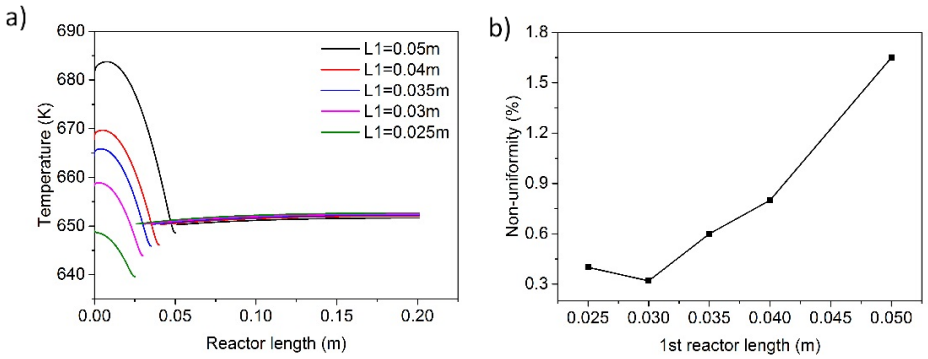


**Figure 6.6**. a) Temperature profiles plotted with different length of the first reactor (b) The effect of the length of the first reactor on temperature non-uniformity in the coating ($v_c$=1.0 m·s$^{-1}$, $D_c$=0.5 mm, W=3.5 mm, Th=0.01 mm)

It can be seen that a reactor length of 0.03 m results in a temperature gradient of about 14K along the reactor length. A higher length of the first reactor would result in a higher temperature gradient: for example, a length of 0.04 m gives a temperature gradient of 22 K (**Figure 6.6a**). The temperature gradient is hardly observed since the inlet cooling of the second reactor could efficiently compensate the decreased reaction heat due to the dropped methanol and DME conversion. The temperature non-uniformity (**Figure 6.6b**) can always be efficiently handled with adjustment of coolant flow rate in the second reactor.

Therefore, the length of two reactors was fixed at 0.03 and 0.17 m to keep the total length of 0.2 m. The minimum length is determined by limitations on the manufacturing method. This corresponds to a methanol conversion of 50% in the first reactor and 95% in the second reactor. The heat generation rate is 5.84·10$^{-4}$ W (per channel) in the first reactor and 1.28·10$^{-3}$ W (per channel) in the second reactor. In the following simulations, a 2D model has been developed describing the temperature field in a single periodic unit.

*2D heat transfer model for two reactor design*

The model geometry consists of the channel areas, a catalyst layer and a wall between the two channels. Like in the 1D model, the 2D model takes into account convective heat transport by the flowing gases, heat transfer between the gases and the reactor material, heat conduction through the reactor material and the heat generation in the catalytic coating layer. The

geometry is represented by the A-A cross section shown in **Figure 6.2**. The geometry consists of four domains listed in **Table 6.3**. Two physical models are laminar flow (**Figure 6.7a**).and heat transfer (**Figure 6.7b**). Laminar flow conditions are applied in the reactant and coolant flow domains while heat transfer exists in all domains as listed in **Table 6.3**.

**Table 6.3**. Computational domains and corresponding physical models

| Domains | Name | Physics | Parameters | Notations | Range |
|---|---|---|---|---|---|
| R1&R2 | Semi cylindrical reaction channel | Laminar flow<br>Heat convection | Length of first reactor | $L_{R1}$ | 0.03-0.05 m |
| F1&F2 | Catalytic film | Heat conduction | Thickness of zeolitic coating | TH | 0.01-0.025 mm |
| M1&M2 | Metal wall | Heat conduction | Wall thickness | W | 1-5 mm |
| C1&C2 | Semi cylindrical cooling channel | Laminar flow<br>Heat convection | Diameter of diameter<br>Temperature<br>Velocity<br>Flow mode | Dc<br>Tc<br>vc<br>- | 0.2-0.8 mm<br><653 K<br>0-4 $m \cdot s^{-1}$<br>Co-/Counter current |

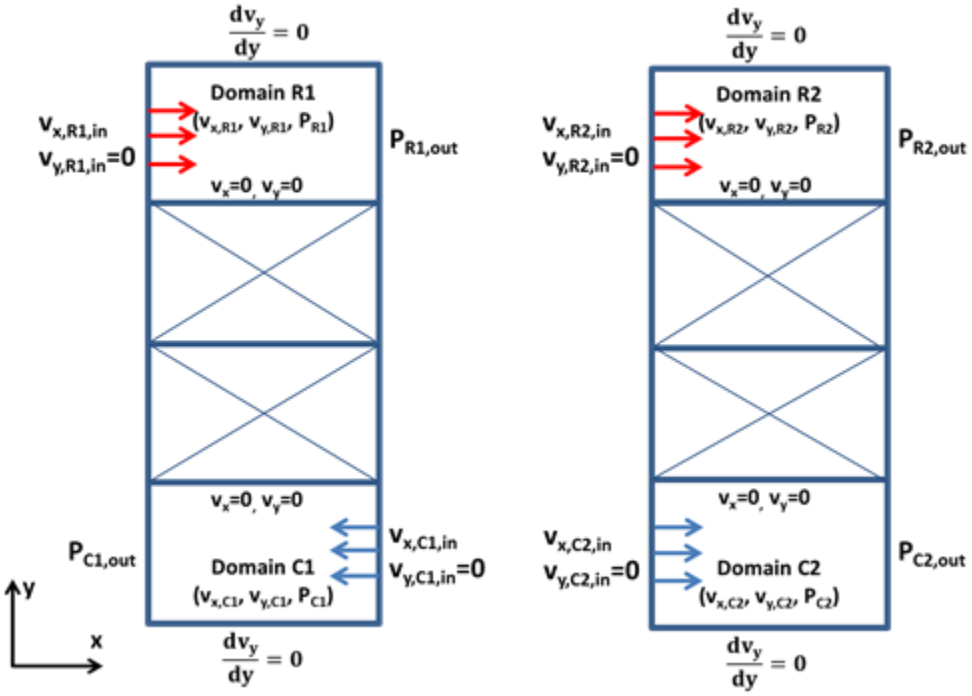


**Figure 6.7a**. Schematic view of boundary conditions in laminar flow domains. The left image part represents the first reactor, the right part represents the second reactor. The images are not on scale. Domains (from top to bottom): Semi cylindrical reaction channel (R1, R2), catalytic film (F1, F2), Metal wall (M1, M2), Semi cylindrical cooling channel (C1, C2)

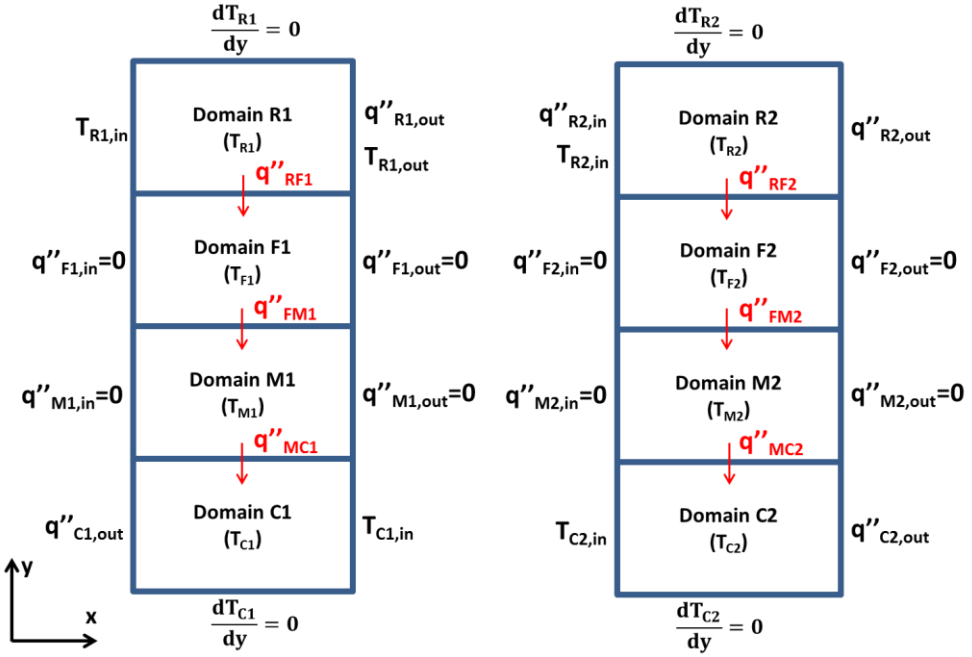


**Figure 6.7b**. Schematic view of boundary conditions in heat transfer domains. The left image part represents the first reactor, the right part represents the second reactor. The images are not on scale. Domains (from top to bottom): Semi cylindrical reaction channel (R1, R2), catalytic film (F1, F2), Metal wall (M1, M2), Semi cylindrical cooling channel (C1, C2). $T_R$, $T_F$, $T_M$,and $T_C$ are temperature of reactant, catalytic film, metal and coolant.

The following assumptions were made in all numerical simulations:

- The pressure outlet in the reaction channels and cooling channels are set at 1 bar.
- The first reactor operated in a counter-current mode, the second in a co-current mode. Other configurations resulted in much larger temperature non-uniformity, therefore they would not be considered in this study.
- The reactant flow at the outlet from the first reactor was equal to that at the inlet to the second reactor (Conservation of mass).
- There is no temperature drop between the outlet of the first reactor and inlet of the second reactor (Conservation of energy).

Laminar flow boundary conditions are given by inlet velocity and outlet pressure as **Eqs.6.17-6.19** and **Figure 6.7a**. The inlet velocity in the reaction channels is 0.0271 $m \cdot s^{-1}$:

$$v_{x,R1} = v_{x,R2} \equiv 0.0271\ m \cdot s^{-1} \tag{6.17}$$

$$v_{y,R1} = v_{y,R2} \equiv 0\ m \cdot s^{-1} \tag{6.18}$$

$$P_{R1}|_{x=LR1} = P_{R2}|_{x=L} = P_{C1}|_{x=0} = P_{C2}|_{x=L} = 1\ bar \tag{6.19}$$

The heat transfer boundary conditions in each domain are schematically shown In **Figure 6.7b**. The reactor is adiabatic with insulation at all reactor external surfaces.

General energy balances in the four domains are given by **Eqs. 6.21, 6.22**.

For domains M1 and M2:

$$-\frac{\lambda_m A_{mx}}{L_x}\frac{d^2T_m}{d\hat{x}^2} - \frac{\lambda_m A_{my}}{L_y}\frac{d^2T_m}{d\hat{y}^2} = \alpha_r A_r (T_r - T_m) - \alpha_c A_c (T_m - T_c) \tag{6.20}$$

For domains C1 and C2:

$$(\dot{m}Cp)_c \frac{dT_c}{d\hat{x}} = -\alpha_c A_c (T_m - T_c) \tag{6.21}$$

where $\hat{x}$ and $\hat{y}$ are the dimensionless coordinates (actual coordinate divided by the length in x- and y- directions respectively), and the other

terms similar as for the one-dimensional model. The boundary conditions in the heat transfer domains are listed below.

$q''_{RF1} = h_r (T_{R1}-T_{F1})$ (6.22)

$q''_{FM1} = \frac{k_{FM}}{W} (T_{F1}-T_{M1})$ (6.23)

$q''_{MC1} = h_c (T_{M1}-T_{C1})$ (6.24)

$q''_{RF2} = h_r (T_{R2}-T_{F2})$ (6.25)

$q''_{FM2} = \frac{k_{FM}}{W} (T_{F2}-T_{M2})$ (6.26)

$q''_{MC2} = h_c (T_{M2}-T_{C2})$ (6.27)

where $h_r$ &$h_c$ are the overall heat transfer coefficient in reaction and cooling channels, $k_{FM}$ is thermal conductivity in solid and $T_R$, $T_F$, $T_M$, $T_C$ are temperature of reactant, catalytic coating, metal and coolant, respectively

*Thermal resistance*

Heat transfer coefficients and thermal resistances in **Eqs. 6.28-6.32** suggest that the limiting step of heat transfer is in the boundary layers in the cooling channel domain (**Figure 6.8**). Due to a higher thermal conductivity of the reactant mixture, the thermal resistance of the reaction channel is much lower than one of the cooling channel while thermal resistance of the metal and the catalytic film is neglected due to a difference in order of magnitude to reactants and coolant (Appendix C).

$$R_r = \frac{1}{h_r \cdot A_r} \quad (6.28)$$

$$R_c = \frac{1}{h_c \cdot A_c} \quad (6.29)$$

$$R_{metal} = \frac{W}{k_M \cdot \bar{A}} \quad (6.30)$$

$$R_{film} = \frac{Z}{k_F \cdot A_r} \quad (6.31)$$

$$R_{tot} = R_r + R_c + R_{metal} + R_{film} \quad (6.32)$$

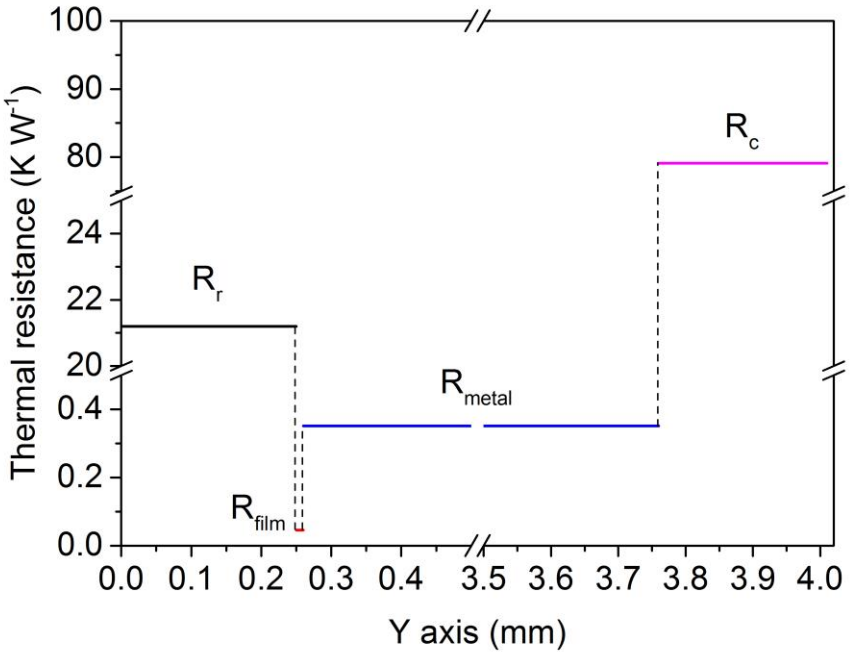


**Figure 6.8**. Schematic of thermal resistance in Y axis

### 6.2.4 Parametric study

*Effect of coolant flow mode*

The coolant flow direction has a major influence on the temperature non-uniformity in the reactors. This effect was studied by comparing reactant temperature profiles obtained under different flow configurations (**Figure 6.9**). It should be mentioned that only optimised cases are presented in the subsequent discussion.

**Figure 6.9** shows the effect of coolant flow mode in the first and second reactors. It can be seen that a minimum temperature gradient of 14 K is observed in the counter-current configuration. The counter-current mode is then determined for the first reactor when comparing flow modes in the second reactor (**Figure 6.9b**). Though the temperature gradient is relatively small in the second reactor, the co-current mode is selected for its lower temperature gradient.

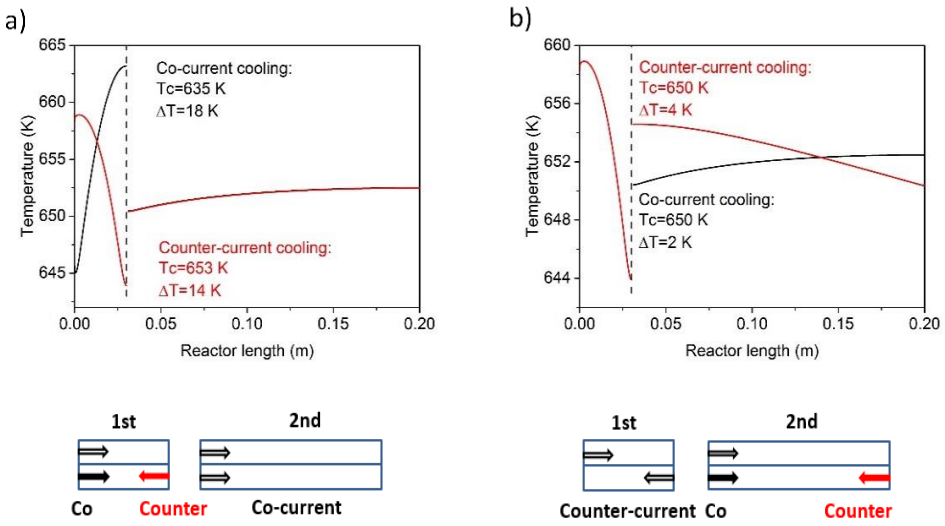


**Figure 6.9**. Reactant temperature profiles in reactors with different coolant flow mode in a) First reactor. b) Second reactor ($v_c$=1.0 m·s$^{-1}$, $D_c$=0.5 mm, W=3.5 mm, TH=0.01 mm)

This result could be explained as that injection point of coolant near the temperature hotspot provides the highest temperature difference between reactant and coolant which is the main driving force for heat flux. Therefore, the inlet of coolant in both reactors should be near the hotspot and that counter-current flow mode in the first reactor and co-current in the second reactor are concluded to be the best configuration.

*Effect of metal plate thickness*

The thickness of the metal plate helps to increase the axial heat transfer more efficiently which in turns helps to reduce the thermal gradient in the catalytic coating and in the reaction channel. The importance of heat conduction, especially axial one, in the solid wall was stated by several authors [236, 237]. In the case of an exothermic reaction in an adiabatic reactor, the solid phase axial conduction could be described by the conduction parameter ($CP$) [141] as **Eq. 6.33**. An optimal range of $CP$ between 0.1-0.5 was identified by Stief et al. [243]. In our case, stainless steel with $\lambda$ of 31.8 W·m$^{-1}$·K$^{-1}$ is used for reactor material. This leads to a CP value of 29.8 indicating a major effect of axial heat transfer.

$$CP = \frac{\lambda}{L\rho u Cp} \tag{6.33}$$

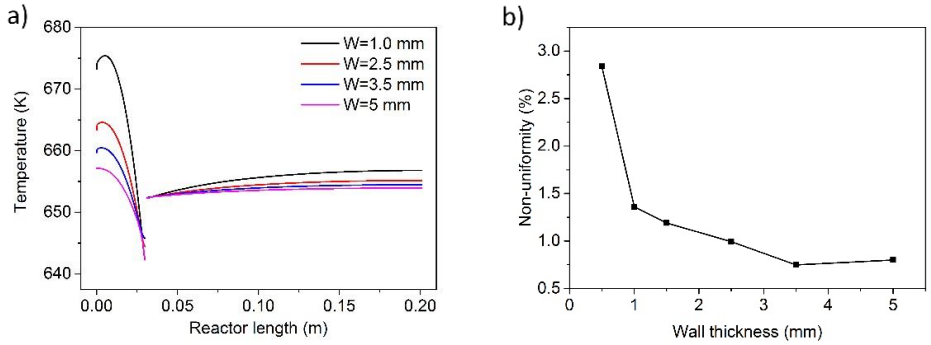


**Figure 6.10** a) Temperature profiles in reaction channel in the reactor with different wall thickness. ($v_c$=1.0 m·s$^{-1}$, $D_c$=0.5 mm, TH=0.01 mm). b) Non-uniformity as a function of W in the first reactor

A high thickness of the wall up to 5 mm between reaction and cooling channels has a positive effect on reactant temperature field as shown in **Figure 6.10a**. When increasing the wall thickness five times from 1 mm to 5 mm, the temperature gradient in the first reactor drops from 30 to 15 K. In a thicker wall, larger cross section increases heat transfer in the axial direction in metal wall, which results in more uniform temperature distribution (**Figure 6.10b**). However, too thick material would result in low space utilisation and therefore there is an optimum in the plate thickness at 3.5 mm. This allows to suppress thermal gradient in the first reactor by a factor of 2.

*Effect of diameter of cooling channel*

As it was discussed in the single reactor case, the cooling temperature and flow rate have a limited effect on the magnitude of temperature gradient in the first reactor. According to **Eqs. 6.28-6.32** the thermal resistance in the cooling channel plays a major role in the total heat transfer. By increasing the diameter of the cooling channel, the surface area of heat flux could be increased which could reduce the thermal resistance. However when decreasing the size of cooling channel from 0.5 to 0.2 mm but keeping the same volumetric flow rate of coolant, no obvious effect was observed on temperature profile. This result could be explained by the fact that the third dimension in the COMSOL numerical model cannot be adjusted in a 2D model. Therefore this effect will be discussed in 3D reactor modelling.

*Effect of coating thickness*

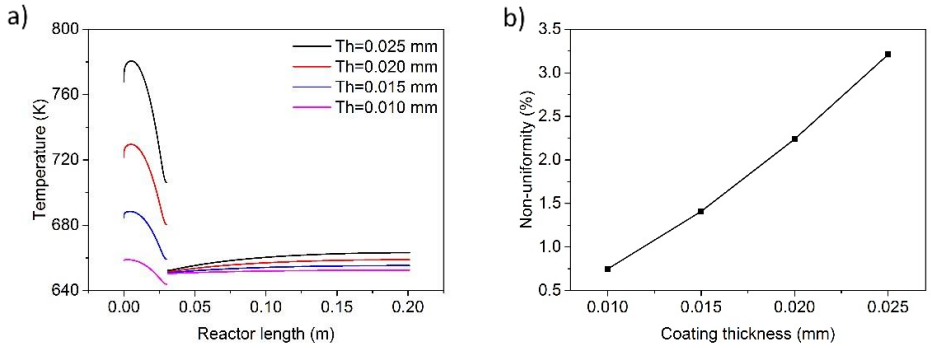


**Figure 6.11**. a) Temperature profiles in reaction channel with catalyst film of different thickness. (W=3.5 mm, $D_c$=0.5 mm, $v_c$=1.0 m·s$^{-1}$, $T_{C1,\,in}$ = 635 K, $T_{C2,\,in}$=652 K). b) Non-uniformity as a function of C in the first reactor

The coating thickness has a major influence on temperature distribution as a thicker coating would result in much larger heat generation rate in the reaction channels. (**Figure 6.11a**). Therefore the temperature gradient rises to 75 K when coating thickness of 0.025 mm is applied. Non-uniformity of temperature profile (**Figure 6.11b**) increases for the thicker coatings. The thickness of 0.01 mm is selected for further optimisation.

*Effect of coolant temperature*

When increasing coolant temperature ($T_c$) from 610 to 650 K in both reactors, the reactant temperature ($T_R$) increases by the same magnitude (**Figure 6.12**). This result suggests that temperature of coolant could help to adjust the reaction temperature but it does not reduce the temperature gradient. This simplifies the process control as the drop in the reactor temperature due to catalyst deactivation could be easily compensated by increasing the coolant temperature.

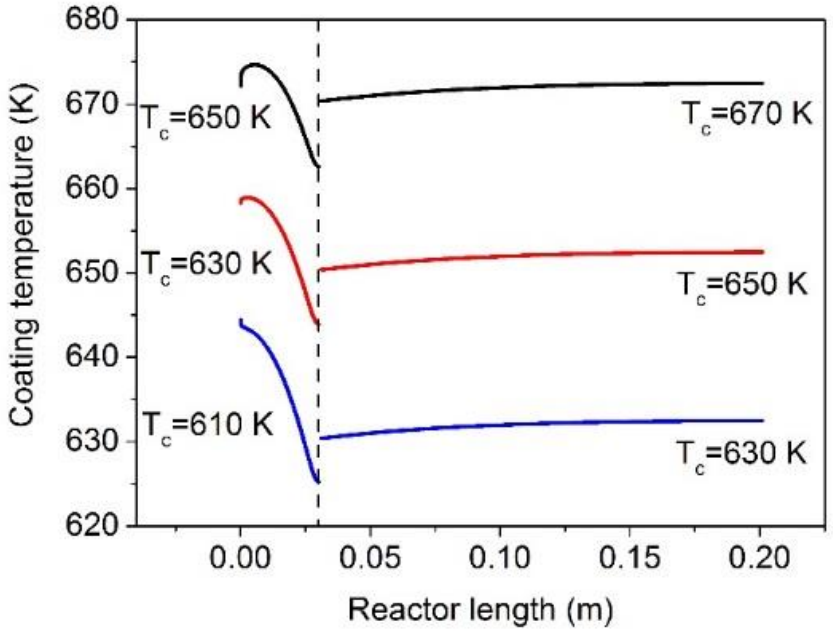


**Figure 6.12.** a) Temperature profiles in coating domain when coolant at different temperature. (W=3.5 mm, $D_c$=0.5 mm, $v_c$=1.0 m·s$^{-1}$, TH =0.01 mm).

*Effect of coolant velocity*

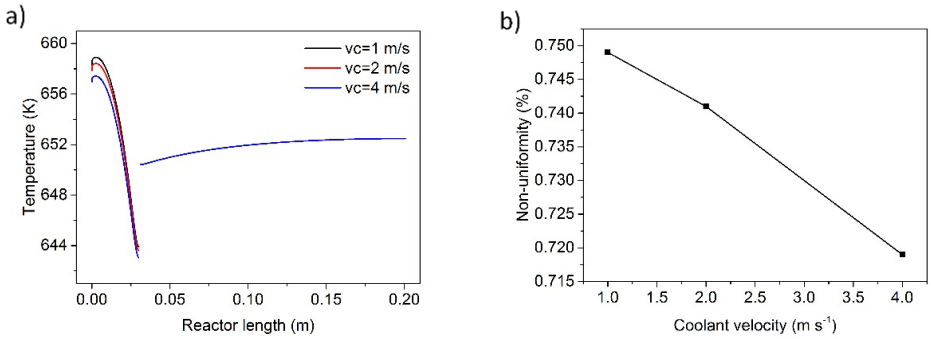


**Figure 6.13.** a) Temperature profiles in first reactor when coolant at different velocity. (W=1.0 mm, $D_c$=0.5 mm, TH =0.01 mm, $T_{C1,\,in}$ = 635 K, $T_{C2,\,in}$=652 K). b) Non-uniformity as a function of $v_c$ in the first reactor

The coolant velocity showed a little impact on the catalyst temperature (**Figure 6.13a**). When the coolant velocity is four times higher, the reactant temperature dropped by 2 K. This implies that velocity of coolant could not be used as an efficient controlling parameter. As the velocity decreases, the outlet temperature of the coolant increases. **Figure 6.13b** shows that higher coolant velocity gives a slightly more uniform distribution of reactor

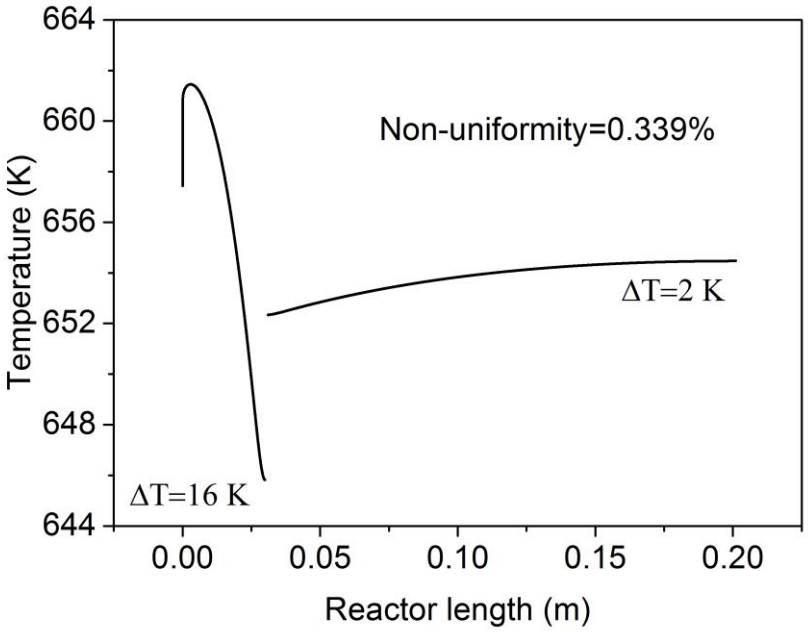


**Figure 6.14.** Temperature profiles in coating domain with optimise parameters. (W=3.5 mm, $D_c$=0.5 mm, $v_c$=4.0 m·s$^{-1}$, TH =0.01 mm, $T_{C1,\,in}$ = 635 K, $T_{C2,\,in}$=652 K)

temperature. Therefore the minimum of coolant velocity of 1 m·s$^{-1}$ was selected.

**Table 6.4.** Overview of design unit (half channel) in micro-reactor/heat-exchanger

| | First reactor | Second reactor |
|---|---|---|
| Methanol conversion rate ($h^{-1}$) | 2.3 | 2.3 |
| Reactor length (m) | 0.03 | 0.17 |
| Wall thickness (m) | $3.5 \cdot 10^{-3}$ | $3.5 \cdot 10^{-3}$ |
| Reaction channel diameter | $5 \cdot 10^{-4}$ | $5 \cdot 10^{-4}$ |
| Catalytic film thickness (m) | $10^{-5}$ | $10^{-5}$ |
| Mass of catalyst coating (kg) | $3.53 \cdot 10^{-7}$ | $2.00 \cdot 10^{-6}$ |
| Reactant flow velocity ($m \cdot s^{-1}$) | 0.0271 | 0.0271 |
| Methanol feeding rate ($kg \cdot h^{-1}$) | $5.76 \cdot 10^{-6}$ | - |
| Total methanol conversion to DME (%) | 49.3 | 94.7 |
| Total DME conversion to C8H16 (%) | 55.6 | 99.8 |
| Heat generation (W) | $5.81 \cdot 10^{-4}$ | $1.28 \cdot 10^{-3}$ |
| Heat reactant adsorbed (W) | $3.30 \cdot 10^{-5}$ | $1.65 \cdot 10^{-5}$ |
| Heat coolant absorbed (W) | $5.48 \cdot 10^{-4}$ | $1.26 \cdot 10^{-3}$ |
| Coolant flow direction | Counter- | Co- |
| Cooling channel diameter | $5 \cdot 10^{-4}$ | $5 \cdot 10^{-4}$ |
| Coolant temperature (K) | 635 | 652 |
| Coolant flow velocity ($m \cdot s^{-1}$) | 4.0 | 4.0 |
| Product (n-Octene) output rate ($kg \cdot h^{-1}$) | - | $2.47 \cdot 10^{-6}$ |

According to the studies above, an optimisation of studies parameters was applied to the model as stated in the caption of **Figure 6.14**. Overview of design is listed in **Table 6.4**.

The temperature gradient of 16 K was observed. With adjustment of coolant temperature to 635 K in the first reactor, reactant temperature is ±7 K from desired reaction temperature at 653 K. The temperature non-uniformity parameter also drops to 0.339% which is the lowest among all designs.

## 6.3 3D modelling

2D modelling on MRHE provides an estimation of the magnitude of the temperature profile in reaction channels. However, the practical solution exceeds the stationary and laminar limit of 2D modelling where simplification may conflict with realistic complex 3D gaseous dynamic. Moreover, the cross-section chosen in 2D modelling may not reproduce 3D effects. 3D simulation could provide a more accurate approach for the MRHE design. A full scale 3D model describes the actual hydrodynamics in the both channels coupled with heat transfer via convection and conduction.

### 6.3.1 Geometry and physics

The 3D model represents a single periodic unit of the MRHE. The inlet and outlet tubes, which are perpendicular to the reaction channel plane, are not included in the model. Instead, the inflow and outflow are modelled as straight surfaces in line with the plate. Without the inlet and outlet tubes, the geometry is symmetrical in a centre plane, allowing simulation of the half geometry. The model had about 23 computational nodes and it took about 10 minutes to reach convergence from a previous solution.

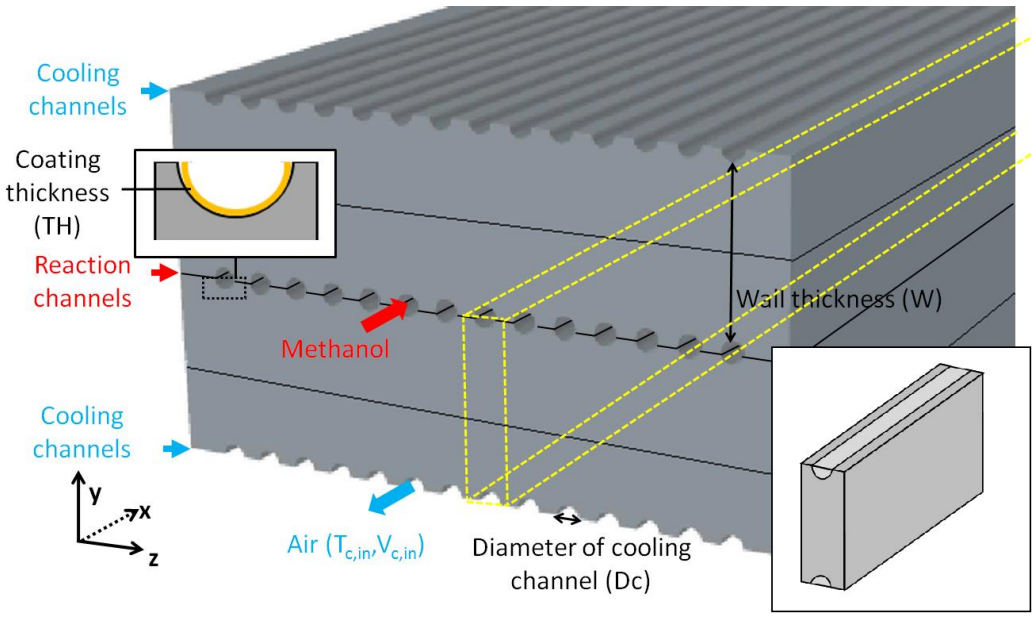


**Figure 6.15**. Geometry of 3D modelling with design unit and parameters

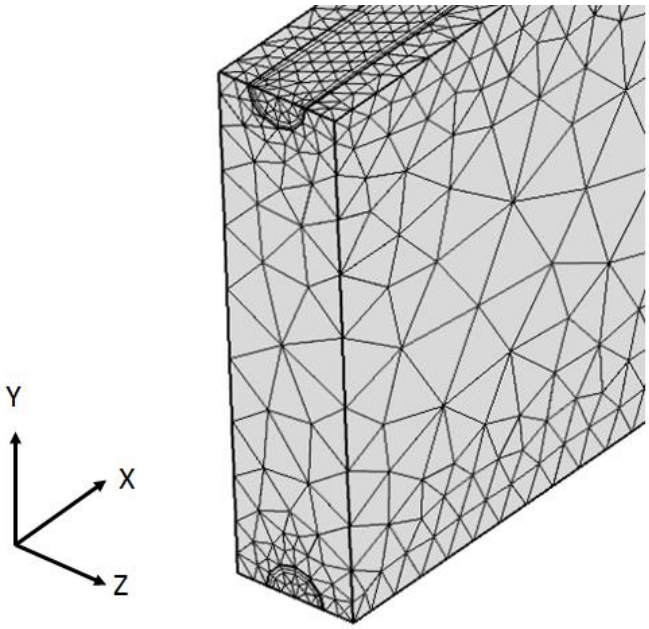


**Figure 6.16**. Mesh of 3D geometry

The 3D model was constructed based on the same physics and domain arrangement as it was presented in the 2D modelling section. The 3D geometry of a single periodic unit of the MRHE is shown in **Figure 6.15** with the design unit shown in the frame. It should be noted that the catalyst layer is considered as a 'thin layer' domain which acts as a boundary heat source. Similar to the 2D model, two reactors in series and four domains were considered. The 3D meshing scheme is shown in **Figure 6.16**.

### 6.3.2 Parametric study

A parametric study in 3D modelling is mainly focused on the optimisation of the geometry of cooling channels and the coolant flow rate that were not applicable in 2D modelling. Other parameters will be compared in 2D and 3D. Parameters to be studied in 3D modelling are listed below.

**Table 6.5**. Studied parameters and range in 3D modelling

| Parameter | Notation | Studies range |
|---|---|---|
| Diameter of cooling channel | $D_c$ | 0.2-0.8 (mm) |
| Number of cooling channel | $N_c$ | 1-3 |

*Diameter of cooling channels*

The cooling channel diameter was changed in the range from 0.5 to 0.8 mm keeping the same coolant flow rate. It can be seen in **Figure 6.17**, an increase of the diameter of the cooling channel leads to a temperature drop around 10 K in the entire reactor. Due to an increase in surface area for convective heat flux at the cooling channel wall the heat transfer is improved. No major improvement in the temperature non-uniformity parameter was observed meaning that this effect is not beneficial in reducing the hot-spot magnitude. The thickness of the fluid boundary layer increases in the channels with larger diameter which reduces the positive effect of increasing the surface area. Therefore, this parameter was kept at 0.5 mm in further optimisation.

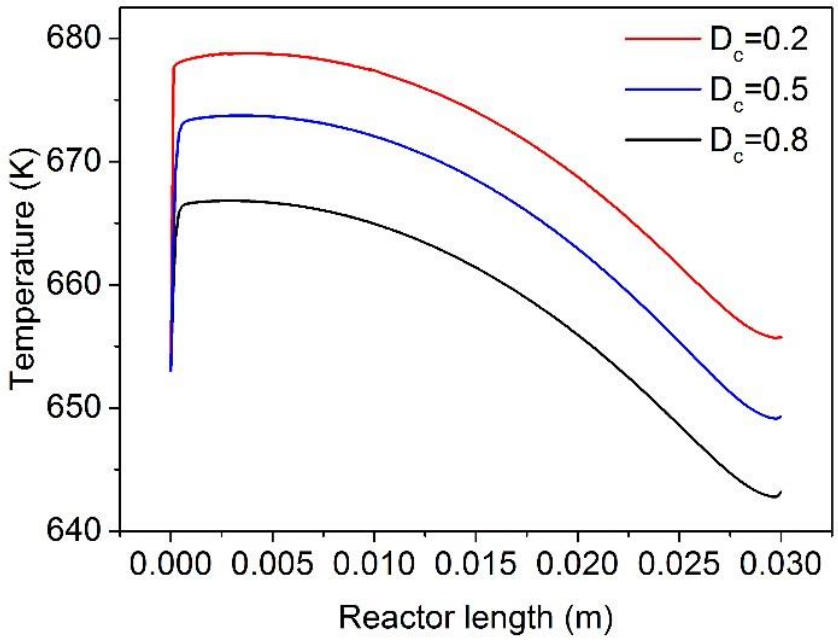


**Figure 6.17**. Temperature distribution profile in the first reactor with different diameters of cooling channel (W=3.5 mm, $v_c$=4.0 m·s$^{-1}$, TH =0.01 mm)

*Multiple cooling channels*

The limiting step in overall heat transfer is the heat convection at the interface between the metal wall and the coolant. In order to improve heat transfer rate, a design with multiple cooling channels was made to increase the surface area for convective heat flux without increasing the thickness

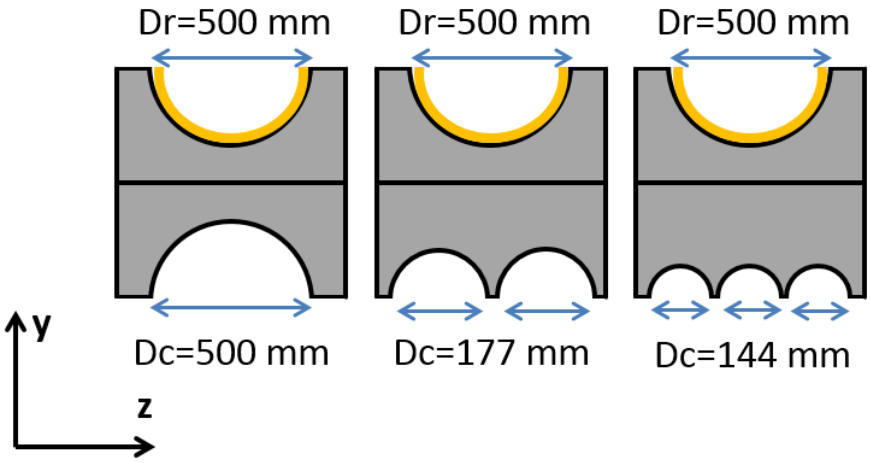


**Figure 6.18.** 2D Sketch of geometries with one (left), two (middle) and three (right) cooling channels

of the boundary layer in the cooling channel (**Figure 6.18**). The corresponding temperature profiles in the coating domain are shown in **Figure 6.19**. A significant improvement was observed as the gradient was

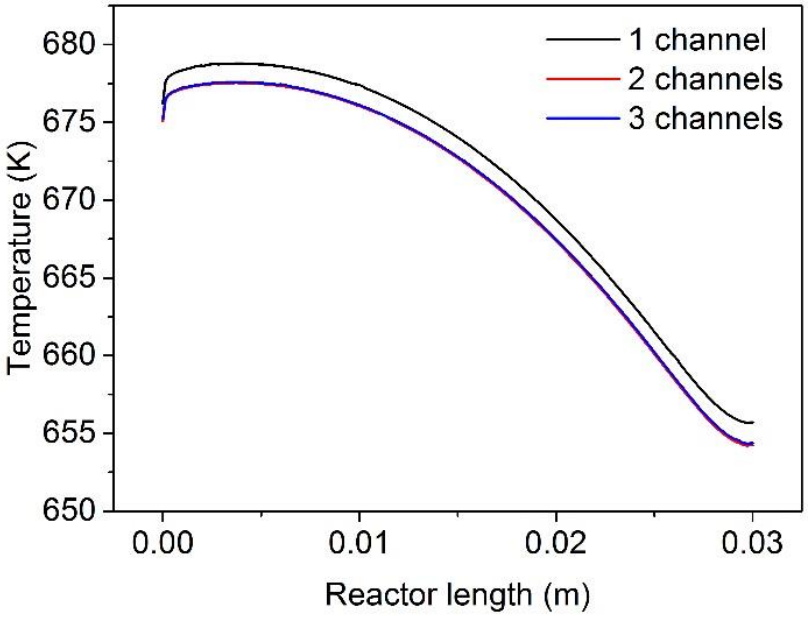


**Figure 6.19**. Temperature profiles in the coating with one, two and three cooling channels obtained with the 3D model (Dc=0.3 mm, W=3.5 mm, $v_c$=4.0 m·s$^{-1}$, TH =0.01 mm)

reduced by 15% as compared to the single cooling channel configuration. The high surface to volume ratio of cooling microchannels has a positive effect on the temperature field in the MRHE. However, a further increase in the number of cooling channels would not reduce the temperature gradient as the main thermal resistance shifts to the reaction channels.

### 6.3.3 Optimised model

The temperature distribution in the first reactor is shown **Figure 6.20**. The colour legend shows the temperature range in the cooling channel is within the 600-660 K range. The right scale bar shows the temperature in the reaction channel is within the 635-665 K range. The catalyst suffers from a fast rise in temperature to 665 K within 5 mm in the reaction channel due to fast heat generation in the area with high concentration of methanol. A temporary equilibrium is reached when the heat generation rate by the exothermic reactions and the heat removal rate the coolant channels are equal. With methanol being consumed towards the downstream locations, the reaction temperature in the coating drops to 635 K due to a significant

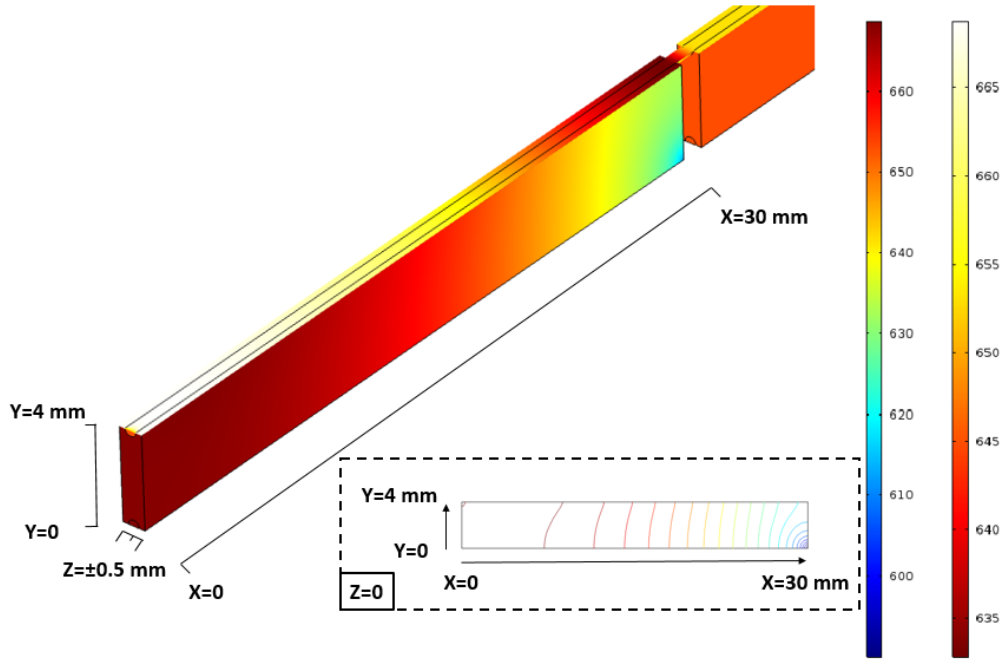


**Figure 6.20**. Temperature distribution in first reactor with optimised conditions with temperature contour in YZ cross-section obtained with the 3D model (v=0.0271m·s$^{-1}$, Dc=0.8 mm, W=3.5 mm, TH=0.01 mm)

reduction in the reaction rate. The lowest temperature of coolant is observed near the injection point of coolant at a distance of 30 mm as shown in **Figure 6.20**. Flowing to the other end (L=0 mm), the coolant temperature increases to 660 K. The heat transfer through the metal wall is visualized by temperature contours aligned in the XY plane passing through the origin (z=0). It can be seen, the contour lines in the first reactor are parallel to each other indicating sufficient heat transfer while they are bended near the hot-spot and the coolant entrance due to the presence of a substantial transverse heat flux in the metal which helps to reduce the hot spot.

The temperature profiles in the coating, the reactor wall and in the cooling channel are shown in **Figure 6.21**. A hot-spot of 21 K is observed at the entrance of the first reactor. The temperature gradient in the second reactor is nearly zero due to a reduced heat generation rate. In the first reactor, the temperature difference is merely observed between those domains, indicating a sufficient heat transfer from the heat source in coating layer to

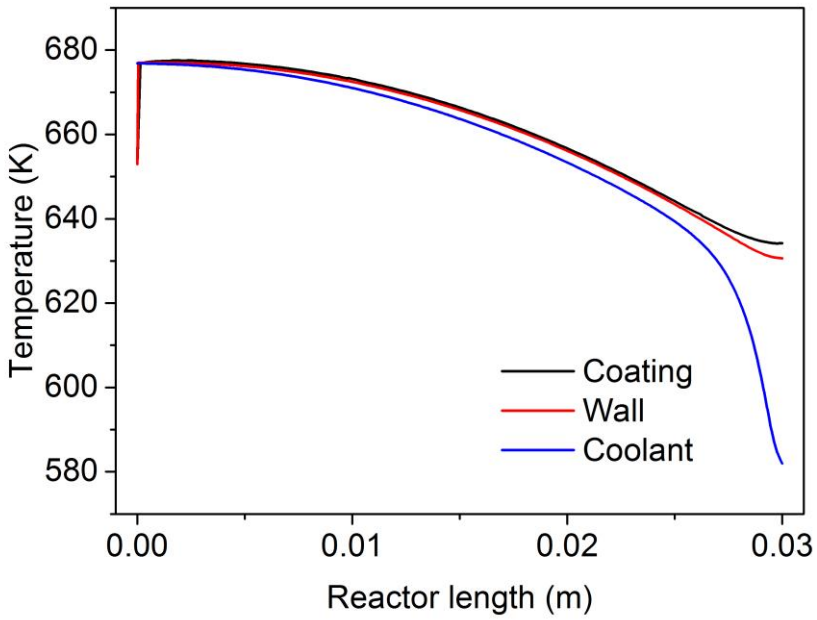


**Figure 6.21**. Temperature profiles of coating, wall and coolant domains with optimised parameters in the first reactor obtained with the 3D model (v=0.0271m·s$^{-1}$, Dc=0.8 mm, W=3.5 mm, TH=0.01 mm)

metal wall and cooling channel. Coolant is injected at L=30 mm at 600 K always resulting in excessive cooling below the desired temperature in that section. The same situation is observed in the second reactor which is not shown due to the long length of the reactor.

### 6.3.4 Comparison to 2D modelling

The optimisation process gave the same optimum values of parameters in both 2D and 3D models (v=0.0271m·s$^{-1}$, Dc=0.8 mm, W=3.5 mm, Th=0.01 mm). However, the temperature gradient in the 3D model of ±20 K is higher than that in the 2D model of ±8 K. The reason for the deviation between the 2D and 3D models is related to two aspects. The area for convective and conductive heat flux could not be represented in the 2D model. As a consequence, the heat flux which is always considered orthogonal to the reactor wall is overestimated in the 2D model. In the actual geometry this area is not a constant over the entire domain, so the characteristic length for conductive heat transfer is considerably reduced between the cooling

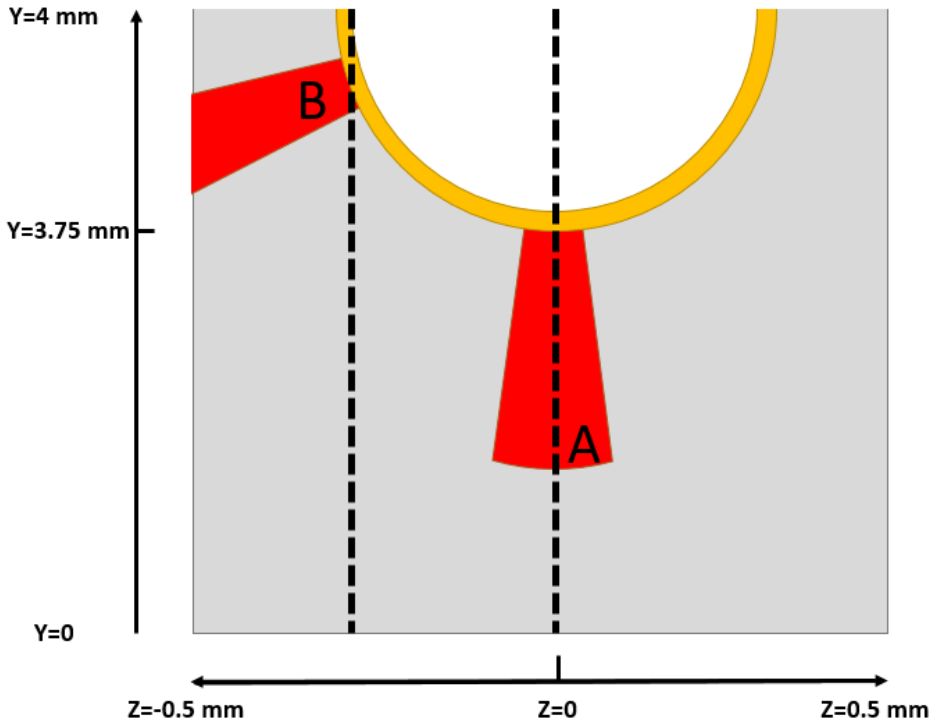


**Figure 6.22**. Sketch of heat transfer path from different locations of heat source

channels (in the y-range from 3.75 and 4.00 mm, section B in **Figure 6.22**) as compared to the space between the cooling and reaction channels (in the y-range below 3.75 mm, section A in **Figure 6.22**). In the 2D model, the cross-section was represented by section A. While in the case of cross-section B, if modelled separately in 2D geometry, the temperature gradient would be two to three times higher depending on the distance between the reaction channels (which cannot be specified either in the 2D model). Therefore, 2D modelling is considered to be a straightforward tool for initial parametric study while 3D modelling is a more accurate tool for quantitative study.

## 6.4 Pilot unit

Even though with a strong control of reaction conditions and improved yield studied in many studies, small production scale has been an obstacle for micro-structured reactors [244–246]. Based on the optimised geometry, the dimensions and the weight of the MRHE are estimated in **Table 6.6**. The reaction plates with 14 semicircle microchannels and cooling plates with 28 semicircle microchannels are assembled to form a reactor. Due to the large mass of the device, a single reactor would require a start-up time of about 15 min by available electric power with a 3 kW output. In order to achieve the target conversion rate of methanol of 2 $kg \cdot day^{-1}$, a reactor module with 88 MRHEs is needed. The final design represent a series of individual MRHEs with a volume of 0.002 $m^3$ and a weight of 15 kg. To scale up the current model to pilot scale, a higher coating would be desirable even it would not provide the full catalyst utilisation.

**Table 6.6**. Summary of pilot scale of MRHE

| | **Parameter** | **Value** |
|---|---|---|
| Reaction channel plate | Length of channel | 200 mm |
| | Diameter of channel | 0.5 mm |
| | Thickness | 4 mm |
| | Number of channel per plate | 14 |
| | **Methanol conversion rate per channel** | **67 mg·h$^{-1}$** |
| | Weight | 84 g |
| Cooling channel plate | Length of channel | 200 mm |
| | Diameter of channel | 0.8 mm |
| | Thickness | 4 mm |
| | Number of channel per plate | 14 |
| | Weight | 84 g |
| Assembled MRHE module | **Conversion capacity** | **2 kg·day$^{-1}$** |
| | Number of MRHEs | 88 |
| | Total weight | 15 kg |
| | Dimension of module (W*H*L) | ~0.1 * 0.2 * 0.1 m$^3$ |
| | Heating output | 3 kW |
| | Start-up time | 15 min |

## 6.5 Conclusions

A parametric study has been carried out to investigate effect of coolant temperature and velocity, wall thickness, cooling channel diameter and coating thickness on temperature non-uniformity parameter. The effect of flow mode configuration was studied as well. An optimum reactor configuration is a two reactor assembly with a counter-current coolant flow in the first reactor and a co-current coolant flow in the second reactor. The length of the first reactor is 0.03 m and the length of the second reactor is 0.17 m. An optimal plate thickness is in the range 1.0-1.5 mm. The optimal catalyst thickness is in the range 10-15 micron. Such configuration would result in a temperature gradient of 14 K in the first reactor and less than 2 K in the second reactor.

A difference in computation results was observed between 2D and 3D models as 2D model does not represent the actual area available for heat transfer. The temperature gradient in the 3D model was ±13 K in the first reactor while the optimal parameters remained the same. A prospective

miniplant configuration for a conversion rate of methanol at 2 $kg \cdot day^{-1}$ has been suggested.

# Chapter 7
# Conclusions and outlook

## 7.1 Conclusions

A series of ZSM-5 coatings with different Si/Al ratios (20-60) and the mean crystal size ranging from 0.8 to 2.6 μm have been synthesized on AISI-304 stainless steel substrates by hydrothermal synthesis. The coatings obtained have a MFI structure without the presence of other phases. A higher Si/Al ratio in the initial sol gives a larger mean crystal size. A higher $H_2O$/Si ratio leads to a larger crystal size with a wide crystal size distribution. Continuous coatings were obtained with an average coating thickness of 14 μm. The crystallisation of ZSM-5 zeolite was stopped after 48 hours when the liquid phase was exhausted in Al species, even an incomplete conversion of Si species was observed. An increased catalyst loading up to 0.09 $kg \cdot m^{-2}$ was achieved by repeated synthesis resulting in a coating thickness of 60 μm.

A high Al content in the coatings (Si/Al ratio below 30) resulted in a fast equilibrium between methanol and DME in the MTH reaction at 370 $^oC$. These catalysts also showed a fast deactivation within 50 h on stream. The catalysts with Si/Al ratio above 40 showed an initial induction period over which an increase in catalyst activity was observed. They demonstrated improved stability with no deactivation for more than 80 h on stream. There exists an optimal catalyst composition with a Si/Al ratio of 50, a crystal size of 2.4 μm which could be obtained at a synthesis time of 72 h from a sol with a nominal composition of 50 $SiO_2$: 1 $AlO_2$: 6 TPAOH: 1500 $H_2O$.

The H-ZSM-5 coating with a Si/Al ratio of 50 provided the maximum yield of gasoline range hydrocarbons. The $C_{8-11}$ selectivity increases to 18.6% at a pressure of 4 bar and a residence time of 3 s. Any further increase in residence time does not change the selectivity pattern. While the $C_{8-11}$ selectivity over the H-ZSM-5 coatings is slightly lower than over the powder sample with the same composition, the amount of undesired aromatic fraction was considerably reduced to 9.6% over the coatings as compared

to 19.2% over the pellets. This illustrates that the application of thin zeolitic layers gives considerable potential for tailoring and optimizing the catalytic performance in the MTH reaction.

It has been found that ion-exchange with Ca provides controllable Ca exchange ratio in Ca-H-ZSM-5 catalyst. The resulting catalysts exhibited similar structural and morphological patterns to the parent H-ZSM-5. By increasing the Ca content, the catalyst lifetime and selectivity to $C_{8-11}$ hydrocarbons were considerably improved. Ca-ZSM-5 catalysts with an exchange ratio in the range of 0.15-0.20 were found to be the most stable in the MTH reaction, maintaining an initial conversion level for over 7 h and having the highest selectivity of ca. 46% to $C_{8-11}$ gasoline fraction due to the presence of weak Brønsted acidity.

Hierarchical structures were introduced to H-ZSM-5 with Si/Al ratio at 50 by a desilication treatment. Experimental evidences show that the performance of mesoporous H-ZSM-5 catalysts can be improved by regulating the porous network. The presence of mesopores introduced by desilication with an alkaline solution enhanced effective diffusivity for larger hydrocarbons. The average mesopore diameter and volume as well as the surface area increased with increasing the concentration of the alkaline solution. Low desilication efficiency was observed from a very concentrated alkaline solution due to a massive dissolution of ZSM-5 catalyst and the formation of larger macropores. While the selectivity to $C_{8-11}$ hydrocarbons did not change, a higher turnover number for $C_{8-11}$ fraction was observed over the desilicated samples. The presence of the structural template in the alkaline solution reduced the mesopore diameter and preserved the microporous ZSM-5 structure. The longest lifetime and the highest TON for $C_{8-11}$ were found with a mean mesopore size of 3.1 nm and a crystal size of 2.4 µm.

The optimised desilication method was applied to ZSM-5 coating. Meso-microporous coating is observed to have similar textual properties as mesoporous H-ZSM-5 pelleted catalyst. The selectivity to gasoline fraction and the catalyst lifetime improves over ZSM-5 coatings as compared to

pelleted catalysts. The meso-microporous H-ZSM-5 coatings with a thickness of 30 μm show a 5-fold increase in catalyst lifetime and two times higher selectivity to $C_{8-11}$ fraction compared to the microporous coating with the same thickness and composition. The highest selectivity to gasoline range hydrocarbons of 18.5% with a minimum formation of aromatics by-products was obtained in the MTH reaction at a temperature of 370 $^{o}$C at a pressure of 4 bar and a WHSV of 10 $h^{-1}$.

A compact microstructured reactor/heat-exchanged was designed to generate gasoline range hydrocarbons from methanol. The MTH reaction takes place on the surface of H-ZSM-5 catalytic coating deposited onto the inner wall of reaction channels. A simplified kinetic scheme was suggested with products lumped to $C_8$ hydrocarbons. An air flow is used as a cooling agent. A parametric study has been carried out to investigate effect of coolant temperature and velocity, reactor wall thickness, cooling channel diameter and coating thickness on temperature non-uniformity parameter. The effect of flow mode configuration was studied as well.

An optimum reactor configuration is a two reactor assembly with a counter-current coolant flow in the first reactor and a co-current coolant flow in the second reactor. The length of the first reactor is 0.03 m and the length of the second reactor is 0.17 m. An optimal plate thickness is in the range 1.0-1.5 mm. The optimal catalyst thickness is in the range 15 micron. Such configuration would result in a temperature gradient of 14 K in the first reactor and less than 2 K in the second reactor.

A difference in computation results was observed between 2D and 3D models as the 2D model does not represent the actual area available for heat transfer. The temperature gradient in the 3D model was ±13 K in the first reactor while the optimal parameters remained the same. A prospective miniplant configuration for a conversion rate of methanol at 2 kg·$day^{-1}$ has been suggested.

## 7.2 Outlook

At the sight of depleting fossil fuel reserves and facing increasing environmental problems connected to their usage, novel strategies to power our society are presently being developed based on renewable energy sources [247]. Renewable energies in combination with chemical energy conversion will play a crucial role in such future energy scenarios [248]. Future catalytic processes involved in chemical storage of renewable energy and in the (subsequent) transformation to chemicals and fuels, will have to provide fast start up and shut down times and be modular so they can be deployed in remote areas with the availability of feedstocks from renewable resources. This requires more decentralized plants with among others microstructured reactors.

A fluctuating supply of energy, affects both heat and mass transport processes within the reactor and the porous catalysts. Dynamic changes on the molecular catalyst level often resulting in deactivation. With the availability of new analytical methods, it is possible to gain further insights into catalytic systems and to obtain a deep understanding of the effect of variable reaction conditions [249]. The MTH reaction is an example of process where the catalyst encounters varying reaction conditions. The catalyst is periodically regenerated by passing air through the reactor to burn off coke deposits.

As the microstructure of the catalyst and the acid sites are strongly dependent on the environment (temperature, pressure, reactant concentrations), the catalytic performance will vary depending on the local reaction conditions. This requires both the development of a fundamental understanding at an atomic level and its integration into the theoretical and kinetic description of the catalyst under dynamic conditions. Therefore the catalysts should be investigated under dynamic conditions so the averaged optimum can be found which can be expressed, for example, in turnover number (TON) rather than turnover frequency (TOF). An attempt to characterize the catalyst performance in terms of TONs has been made in this thesis. The reaction kinetics (if not solely used for reactor design

purposes) should also be based on reaction sites that can vary their activity in time and not on static ones as observed under steady-state conditions and implemented in kinetic models discussed in the literature review section.

Computational fluid dynamics (CFD) packages are already widely used both at the design phase, and for interpretation of experimental data when complex coupling of momentum, heat and mass transfer cannot be described by simple engineering correlations, such as pressure drop, Nusselt and Sherwood numbers. While 3D models are demonstrated to be a powerful tool in reactor design, some assumptions have still to be made on boundary conditions that later on require experimental verification of 3D models in the reactors with known hydrodynamics. Various studies proved the importance of the design phase via simulation prior to fabrication as was also demonstrated in this thesis. Such a design approach can avoid costly, iterative experimental design procedures where components are fabricated, tested and then redesigned to improve performance.

Despite the recent developments in the area of microstructured reactors, the reactor performance is often limited by the activity of the standard catalysts. Therefore the catalyst development remains the key issue to improve further the product yield in a chemical reactor. For understanding catalysts under dynamic reaction conditions different scientific disciplines such as (operando) spectroscopy, theory and kinetic modelling have to work hand in hand in order to provide a basic understanding of the relevant processes at the catalyst surface and the bulk.

Deposition of ZSM-5 coatings on micro-channels does not require a binder - the crystals are chemically bonded to the support, i.e. the wall of the channel; thus, there will be no interference between the catalytic activity of the zeolite and any binder. Methods need to be further optimized for the deposition of the thin catalyst layers and the incorporation of other elements within these layers. Ion-exchange was found to be a superior method for control of concentration of metal ions in ion-exchanged zeolites. It would be useful to extend the range of operating conditions to obtain

relationships between the degree of exchange and external parameters (temperature, metal concentration, pH). The porosity has also a major impact on the product distribution. Existing literature describes two approaches either by addition of hard templating [250] or surfactant [251]. Mesoporous ZSM-5 catalysts obtained by hard templating (Carbon Black) and microwave digestion were claimed to have high mesoporosity however further study need to be done on whether the method can be translated to zeolitic coatings. Mesoporous ZSM-5 obtained by addition of cetyltrimethylammonium bromide (CTAB) as a surfactant was claimed to have extraordinary textual properties such as a specific surface area of 949 $m^2g^{-1}$ however the catalytic activity and stability have to be confirmed in a long term operation under real MTH conditions. Synthesis of mesoporous ZSM-5 coatings on substrates could improve their efficiency as compared to post-synthesis desilication and could provide a better control over catalyst loading. Finally, the metal substrate may also affect the coating activity in numerous ways, such as by having an electron deficient or donating nature, via additional roughness or application of additional intermediate layers. This creates another degree of freedom to modify catalytic properties as compared to powder catalysts.

# References


[1] U. Vie, Towards a methanol economy : Zeolite catalyzed production of synthetic fuels Methanol Fuels and chemicals Uffe Vie Mentzel, Technical University of Denmark, 2010.

[2] A. Demirbas, Biofuels securing the planet's future energy needs, Energy Convers. Manag. 50 (2009) 2239–2249.

[3] X. Liu, G.Q. Lu, Z. Yan, J. Beltramini, Recent Advances in Catalysts for Methanol Synthesis via Hydrogenation of CO and CO 2, (2003) 6518–6530.

[4] S. Czernik, a V Bridgwater, Overview of applications of biomass fast pyrolysis oil, Energy & Fuels. 18 (2004) 590–598.

[5] A.M. Zainoodin, S.K. Kamarudin, W.R.W. Daud, Electrode in direct methanol fuel cells, Int. J. Hydrogen Energy. 35 (2010) 4606–4621.

[6] U. Olsbye, S. Svelle, M. Bjørgen, P. Beato, T.V.W. Janssens, F. Joensen, S. Bordiga, K.P. Lillerud, Conversion of Methanol to Hydrocarbons: How Zeolite Cavity and Pore Size Controls Product Selectivity, Angew. Chemie Int. Ed. 51 (2012) 5810–5831.

[7] International Zeolite Association online database, (n.d.).

[8] Kokotailo.G.T, Lawton.S.L, Olson.D.H, Structure of synthetic zeolite ZSM-5, Nature. 272 (1978) 437–438.

[9] M.M. Walter, ATLAS of Zeolite Framework Types, 2007.

[10] L. Kristallographie, I.G. Der, Nomenclature of sturctural and compositional characteristics of ordered microporous and mesoporous materials with inorganic hosts, Pure Appl. Chem.,. 73 (2001) 381–394.

[11] B. Arstad, S. Kolboe, Methanol-to-hydrocarbons reaction over SAPO-34. Molecules confined in the catalyst cavities at short time on stream, Catal. Letters. 71 (2001) 209–212.

[12] W. Song, H. Fu, J.F. Haw, Selective synthesis of methylnaphthalenes in HSAPO-34 cages and their function as reaction centers in methanol-to-olefin catalysis, J. Phys. Chem. B. 105 (2001) 12839–12843.

[13] E.M. Flanigen, R.W. Broach, S.T. Wilson, Zeolites in Industrial Seperations and Catalysis, (2010) 584.

[14] S. Teketel, M. Westgård Erichsen, F.L. Bleken, S. Svelle, Shape selectivity in zeolite catalysis. The Methanol to Hydrocarbons (MTH) reaction, in: Catalysis, 2014: pp. 179–217.

[15] M. Elanany, M. Koyama, M. Kubo, E. Broclawik, A. Miyamoto, Periodic density functional investigation of Lewis acid sites in zeolites: Relative strength order as revealed from NH3 adsorption, Appl. Surf. Sci. 246 (2005) 96–101.

[16] C. Martinez, J. Perez-pariente, Zeolites And Ordered Porous Solids, 2011.

[17] R. Gounder, E. Iglesia, The catalytic diversity of zeolites: confinement and solvation effects within voids of molecular dimensions, Chem. Commun. Chem. Commun. 49 (2013) 3491–3509.

[18] W. Alharbi, E.F. Kozhevnikova, I. V. Kozhevnikov, Dehydration of Methanol to Dimethyl Ether over Heteropoly Acid Catalysts: The Relationship between Reaction Rate and Catalyst Acid Strength, ACS Catal. 5 (2015) 7186–7193.

[19] A.S. Al-dughaither, H. De Lasa, HZSM‑5 Zeolites with Different SiO2/Al2O3 Ratios. Characterization and NH3 Desorption Kinetics, (2014).

[20] T. Miyamoto, N. Katada, J.H. Kim, M. Niwa, Acidic property of MFI-type gallosilicate determined by temperature-programmed desorption of ammonia, J. Phys. Chem. B. 102 (1998) 6738–6745.

[21] N. Katada, M. Niwa, Analysis of acidic properties of zeolitic and non-zeolitic solid acid catalysts using temperature-programmed desorption of ammonia, Catal. Surv. from Asia. 8 (2004) 161–170.

[22] L. Rodríguez-González, F. Hermes, M. Bertmer, E. Rodríguez-Castellón, A. Jiménez-López, U. Simon, The acid properties of H-ZSM-5 as studied by NH3-TPD and 27Al-MAS-NMR spectroscopy, Appl. Catal. A Gen. 328 (2007) 174–182.

[23] L. Rodríguez-González, E. Rodríguez-Castellón, A. Jiménez-López, U. Simon, Correlation of TPD and impedance measurements on the desorption of NH3 from zeolite H-ZSM-5, Solid State Ionics. 179 (2008) 1968–1973.

[24] W.O. Haag, R.M. Lago, P.B. Weisz, The active site of acidic aluminosilicate catalysts, Nature. 309 (1984) 589–591.

[25] J.P. van den Berg, J.P. Wolthuizen, J.H.. van Hooff, No Title, in: Proc. 5th Int. Zeolite Methanol to Ethyl. with a Sel. as High Conf., London, 1980: p. 649.

[26] M. Stöcker, Methanol-to-hydrocarbons: catalytic materials and their behavior, Microporous Mesoporous Mater. 29 (1999) 3–48.

[27] G.A. Olah, H. Doggweiler, J.D. Felberg, S. Frohlich, M.J. Grdina, R. Karpeles, T. Keumi, S. ichi Inaba, W.M. Ip, K. Lammertsma, G. Salem, D.C. Tabor, Onium Ylide Chemistry. 1. Bifunctional Acid-Base-Catalyzed Conversion of Heterosubstituted Methanes into Ethylene and Derived Hydrocarbons. The Onium Ylide Mechanism of the C1 to C2 Conversion, J. Am. Chem. Soc. 106 (1984) 2143–2149.

[28] F.A. Swabb, B.C. Gates, No Title, Ind. Eng. Chem. Foundament. 11 (1972) 540.

[29] C.D. Chang, A.J. Silvestri, The Conversion of Methanol and Other

O-Compounds to Hydrocarbons over Zeolit Catalysts, J. Catal. 47 (1977) 249–259.

[30] P.B. Venuto, P.S. Landis, Organic Catalysis over Crystalline Aluminosilicates, Adv. Catal. 18 (1968) 259–371.

[31] C.D. Chang, C.T.W. Chu, On the mechanism of hydrocarbon formation from methanol over zeolite catalysts: Evidence for carbene intermediacy, J. Catal. 74 (1982) 203–206.

[32] I. DAHL, S. KOLBOE, On the Reaction Mechanism for Hydrocarbon Formation from Methanol over SAPO-34: I. Isotopic Labeling Studies of the Co-Reaction of Ethene and Methanol, J. Catal. 149 (1994) 458–464.

[33] I.M. Dahl, S. Kolboe, On the reaction mechanism for propene formation in the MTO reaction over SAPO-34, Catal. Letters. 20 (1993) 329–336.

[34] D.M. Bibby, C.D. Chang, R.F. Howe, S. Yurchak, Methane Conversion, 1988.

[35] S. Kolboe, Methanol Reactions on ZSM-5 and Other Zeolite Catalysts: Autocatalysis and Reaction Mechanism, Acta Chem. Scand. A. 40 (1986) 711–713.

[36] S. Svelle, F. Joensen, J. Nerlov, U. Olsbye, K.-P.P. Lillerud, S. Kolboe, M. Bjørgen, Conversion of methanol into hydrocarbons over zeolite H-ZSM-5: Ethene formation is mechanistically separated from the formation of higher alkenes, J. Am. Chem. Soc. 128 (2006) 14770–14771.

[37] M. Bjørgen, S. Svelle, F. Joensen, J. Nerlov, S. Kolboe, F. Bonino, L. Palumbo, S. Bordiga, U. Olsbye, Conversion of methanol to hydrocarbons over zeolite H-ZSM-5: On the origin of the olefinic species, J. Catal. 249 (2007) 195–207.

[38] Y. Liu, S. Müller, D. Berger, J. Jelic, K. Reuter, M. Tonigold, M. Sanchez-Sanchez, J.A. Lercher, Formation Mechanism of the First Carbon-Carbon Bond and the First Olefin in the Methanol Conversion into Hydrocarbons, Angew. Chemie - Int. Ed. 55 (2016) 5723–5726.

[39] M. Boronat, C. Martínez-Sánchez, D. Law, A. Corma, Enzyme-like specificity in zeolites: A unique site position in mordenite for selective carbonylation of methanol and dimethyl ether with CO, J. Am. Chem. Soc. 130 (2008) 16316–16323.

[40] A.D. Chowdhury, K. Houben, G.T. Whiting, M. Mokhtar, A.M. Asiri, S.A. Al-Thabaiti, S.N. Basahel, M. Baldus, B.M. Weckhuysen, Initial Carbon–Carbon Bond Formation during the Early Stages of the Methanol-to-Olefin Process Proven by Zeolite-Trapped Acetate and Methyl Acetate, Angew. Chemie - Int. Ed. 55 (2016) 15840–15845.

[41] S.R. Blaszkowski, R. Van Santen, R. a VanSanten, R. a van Santen, Theoretical study of CC bond formation in the methanol-to-gasoline

process, J. Am. Chem. Soc. 119 (1997) 5020–5027.

[42] Z. Wei, Y.Y. Chen, J. Li, W. Guo, S. Wang, M. Dong, Z. Qin, J. Wang, H. Jiao, W. Fan, Stability and Reactivity of Intermediates of Methanol Related Reactions and C-C Bond Formation over H-ZSM-5 Acidic Catalyst: A Computational Analysis, J. Phys. Chem. C. 120 (2016) 6075–6087.

[43] J.S. Martinez-Espin, K. De Wispelaere, M. Westgård Erichsen, S. Svelle, T.V.W. Janssens, V. Van Speybroeck, P. Beato, U. Olsbye, Benzene co-reaction with methanol and dimethyl ether over zeolite and zeotype catalysts: Evidence of parallel reaction paths to toluene and diphenylmethane, J. Catal. 349 (2017) 136–148.

[44] P. Pérez-Uriarte, A. Ateka, A.T. Aguayo, A.G. Gayubo, J. Bilbao, Kinetic model for the reaction of DME to olefins over a HZSM-5 zeolite catalyst, Chem. Eng. J. 302 (2016).

[45] P. Pérez-Uriarte, A. Ateka, M. Gamero, A.T. Aguayo, J. Bilbao, Effect of the Operating Conditions in the Transformation of DME to olefins over a HZSM-5 Zeolite Catalyst, Ind. Eng. Chem. Res. 55 (2016) 6569–6578.

[46] W. Guo, W. Wu, M. Luo, W. Xiao, Modeling of diffusion and reaction in monolithic catalysts for the methanol-to-propylene process, Fuel Process. Technol. 108 (2013) 133–138.

[47] S. Svelle, P.O. Rønning, S. Kolboe, Kinetic studies of zeolite-catalyzed methylation reactions: 1. Coreaction of [12C]ethene and [13C]methanol, J. Catal. 224 (2004) 115–123.

[48] T.V.W. Janssens, S. Svelle, U. Olsbye, Kinetic modeling of deactivation profiles in the methanol-to-hydrocarbons (MTH) reaction: A combined autocatalytic–hydrocarbon pool approach, J. Catal. 308 (2013) 122–130.

[49] Y. Tavan, S.H. Hosseini, From laboratory experiments to simulation studies of methanol dehydration to produce dimethyl ether reaction-Part II: Simulation and cost estimation, Chem. Eng. Process. 73 (2013) 144–150.

[50] A.T. Aguayo, D. Mier, A.G. Gayubo, M. Gamero, J. Bilbao, Kinetics of methanol transformation into hydrocarbons on a HZSM-5 zeolite catalyst at high temperature (400-550 C), Ind. Eng. Chem. Res. 49 (2010) 12371–12378.

[51] N.Y. Chen, W.J. Reagan, Evidence of autocatalysis in methanol to hydrocarbon reactions over zeolite catalysts, J. Catal. 59 (1979) 123–129.

[52] L. Bonaccorsi, L. Calabrese, A. Freni, E. Proverbio, Hydrothermal and microwave synthesis of SAPO (CHA) zeolites on aluminium foams for heat pumping applications, Microporous Mesoporous Mater. 167 (2013) 30–37.

[53] M.N. Katariya, A.K. Jana, P.A. Parikh, Corrosion inhibition

effectiveness of zeolite ZSM-5 coating on mild steel against various organic acids and its antimicrobial activity, J. Ind. Eng. Chem. 19 (2013) 286–291.

[54] J. Wang, Z. Wang, S. Guo, J. Zhang, Y. Song, X. Dong, X. Wang, J. Yu, Antibacterial and anti-adhesive zeolite coatings on titanium alloy surface, Microporous Mesoporous Mater. 146 (2011) 216–222.

[55] H.B. Pande, P.A. Parikh, Novel application of ZSM-5 zeolite: Corrosion-resistant coating in chemical process industry, J. Mater. Eng. Perform. 22 (2013) 190–199.

[56] L. Bonaccorsi, L. Calabrese, E. Proverbio, Low temperature single-step synthesis of zeolite y coatings on aluminium substrates, Microporous Mesoporous Mater. 144 (2011) 40–45.

[57] F. Ribeiro, J.M. Silva, E. Silva, M.F. Vaz, F.A.C. Oliveira, Catalytic combustion of toluene on Pt zeolite coated cordierite foams, Catal. Today. 176 (2011) 93–96.

[58] V. Valtchev, S. Mintova, The effect of the metal substrate composition on the crystallization of zeolite coatings, Zeolites. 15 (1995) 171–175.

[59] I. Aartun, T. Gjervan, H. Venvik, Catalytic conversion of propane to hydrogen in microstructured reactors, Chem. Eng. J. 101 (2004) 93–99.

[60] G. Chen, S. Li, F. Jiao, Q. Yuan, Catalytic dehydration of bioethanol to ethylene over TiO2/γ-Al2O3 catalysts in microchannel reactors, Catal. Today. 125 (2007) 111–119.

[61] T. Giornelli, A. Löfberg, L. Guillou, S. Paul, V. Le Courtois, E. Bordes-Richard, Catalytic wall reactor. Catalytic coatings of stainless steel by VOx/TiO2 and Co/SiO2 catalysts, Catal. Today. 128 (2007) 201–207.

[62] O. Schwarz, B. Frank, C. Hess, R. Schomäcker, Characterisation and catalytic testing of VOx/Al2O3 catalysts for microstructured reactors, Catal. Commun. 9 (2008) 229–233.

[63] P. Pfeifer, K. Schubert, M.A. Liauw, G. Emig, PdZn catalysts prepared by washcoating microstructured reactors, Appl. Catal. A Gen. 270 (2004) 165–175.

[64] L. Kiwi-Minsker, O. Wolfrath, A. Renken, Membrane reactor microstructured by filamentous catalyst, Chem. Eng. Sci. 57 (2002) 4947–4953.

[65] E. Cao, A. Gavriilidis, Oxidative dehydrogenation of methanol in a microstructured reactor, Catal. Today. 110 (2005) 154–163.

[66] M.T. Janicke, H. Kestenbaum, U. Hagendorf, F. Schüth, M. Fichtner, K. Schubert, The Controlled Oxidation of Hydrogen from an Explosive Mixture of Gases Using a Microstructured Reactor/Heat Exchanger and Pt/Al2O3 Catalyst, J. Catal. 191 (2000) 282–293.

[67] E. V. Rebrov, Sol-gel synthesis of zeolite coatings and their application in catalytic microstructured reactors, Catal. Ind. 1 (2009) 322–347.

[68] Y. Jiao, C. Jiang, Z. Yang, J. Zhang, Controllable synthesis of ZSM-5 coatings on SiC foam support for MTP application, Microporous Mesoporous Mater. 162 (2012) 152–158.

[69] H.P.A. Calis, Z. Shan, W.E.J. Van Kooten, O.L. Oudshoorn, J.C. Jansen, H. Van Bekkum, C.M. Van den Bleek, Optimization of the preparation of binderless ZSM-5 coatings on stainless steel monoliths by in situ hydrothermal synthesis, Microporous Mesoporous Mater. 34 (2000) 81–91.

[70] R.M. Mohamed, O.A. Fouad, A.A. Ismail, I.A. Ibrahim, Influence of crystallization times on the synthesis of nanosized ZSM-5, Mater. Lett. 59 (2005) 3441–3444.

[71] N.L. Chauhan, J. Das, R. V. Jasra, P.A. Parikh, Z.V.P. Murthy, Synthesis of small-sized ZSM-5 zeolites employing mixed structure directing agents, Mater. Lett. 74 (2012) 115–117.

[72] Y. Cheng, L.J. Wang, J.S. Li, Y.C. Yang, X.Y. Sun, Preparation and characterization of nanosized ZSM-5 zeolites in the absence of organic template, Mater. Lett. 59 (2005) 3427–3430.

[73] T. Xue, Y.M. Wang, M.-Y. He, Facile synthesis of nano-sized NH4-ZSM-5 zeolites, Microporous Mesoporous Mater. 156 (2012) 29–35.

[74] Y. Meng, H.C. Genuino, C. Kuo, H. Huang, S. Chen, L. Zhang, A. Rossi, S.L. Suib, One-Step Hydrothermal Synthesis of Manganese-Containing MFI- Type Zeolite, Mn−ZSM-5, Characterization, and Catalytic Oxidation of Hydrocarbons, J. Am. Chem. Soc. 135 (2013) 8594–8605.

[75] R. Karimi, B. Bayati, N. Charchi Aghdam, M. Ejtemaee, A.A. Babaluo, Studies of the effect of synthesis parameters on ZSM-5 nanocrystalline material during template-hydrothermal synthesis in the presence of chelating agent, Powder Technol. 229 (2012) 229–236.

[76] A. Petushkov, S. Yoon, S.C. Larsen, Synthesis of hierarchical nanocrystalline ZSM-5 with controlled particle size and mesoporosity, Microporous Mesoporous Mater. 137 (2011) 92–100.

[77] K.F.M.G.J. Scholle, W.S. Veeman, P. Frenken, G.P.M. Van der Velden, Characterization of the intermedieate TPAZSM-5 type structure during crystallization, Appl. Catal. 17 (1985) 233–259.

[78] L. Shirazi, E. Jamshidi, M.R. Ghasemi, The effect of Si/Al ratio of ZSM-5 zeolite on its morphology, acidity and crystal size, Cryst. Res. Technol. 43 (2008) 1300–1306.

[79] A.S. Al-Dughaither, H. de Lasa, Neat dimethyl ether conversion to olefins (DTO) over HZSM-5: Effect of SiO2/Al2O3 on porosity, surface chemistry, and reactivity, Fuel. 138 (2014) 52–64.

[80] U. Olsbye, S. Svelle, K.P. Lillerud, Z.H. Wei, Y.Y. Chen, J.F. Li, J.G. Wang, W.B. Fan, The formation and degradation of active species during methanol conversion over protonated zeotype catalysts, Chem. Soc. Rev. 44 (2015) 7155–7176.

[81] D. Rojo-Gama, S. Etemadi, E. Kirby, K.P. Lillerud, P. Beato, S. Svelle, U. Olsbye, Time- and space-resolved study of the methanol to hydrocarbons (MTH) reaction – influence of zeolite topology on axial deactivation patterns, Faraday Discuss. 197 (2017) 421–446.

[82] S. Namba, A. Inaka, T. Yashima, Effect of selective removal of aluminium from external surfaces of HZSM-5 zeolite on shape selectivity, Zeolites. 6 (1986) 107–110.

[83] T. Inui, N. Morinaga, K. Fukuda, Y. Takegami, Selective Synthesis of Lower Olefins Partially from Methanol by on a High Quinoline H-ZSM-5 Catalyst, J. Japanese Pet. Inst. 27 (1984) 188–192.

[84] H. Okado, H. Shoji, Deactivation Resistance of ZSM-5-Type Zeolites containing Alkaline Earth Metals used for Methanol Conversion, 41 (1988) 121–135.

[85] D.L. Hoang, H. Berndt, H. Miessner, E. Schreier, J. V??lter, H. Lieske, Nickel modified H-ZSM-5 catalysts, Appl. Catal. A, Gen. 114 (1994) 295–311.

[86] A.J. Maia, B. Louis, Y.L. Lam, M.M. Pereira, Ni-ZSM-5 catalysts: Detailed characterization of metal sites for proper catalyst design, J. Catal. 269 (2010) 103–109.

[87] T.M. Gur, R.A. Huggins, Methane Synthesis on Nickel by a Solid-State Ionic Method Reviewed work ( s ): Source : Science , New Series , Vol . 219 , No . 4587 ( Feb . 25 , 1983 ), pp . 967-969 Published by : American Association, Science (80-. ). 219 (1983) 967–969.

[88] A. a. Rownaghi, F. Rezaei, J. Hedlund, Uniform mesoporous ZSM-5 single crystals catalyst with high resistance to coke formation for methanol deoxygenation, Microporous Mesoporous Mater. 151 (2012) 26–33.

[89] W.C. Yoo, X. Zhang, M. Tsapatsis, A. Stein, Synthesis of mesoporous ZSM-5 zeolites through desilication and re-assembly processes, Microporous Mesoporous Mater. 149 (2012) 147–157.

[90] M. Ogura, S. Shinomiya, J. Tateno, Y. Nara, E. Kikuchi, M. Matsukata, Formation of Uniform Mesopores in ZSM-5 Zeolite through Treatment in Alkaline Solution., Chem. Lett. (2000) 882–883.

[91] D. Verboekend, J. Pérez-Ramírez, Desilication mechanism revisited: Highly mesoporous all-silica zeolites enabled through pore-directing agents, Chem. - A Eur. J. 17 (2011) 1137–1147.

[92] L. Zhao, C. Xu, S. Gao, B. Shen, Effects of concentration on the alkali-treatment of ZSM-5 zeolite: A study on dividing points, J. Mater. Sci. 45 (2010) 5406–5411.

[93] B. Gil, Ł. Mokrzycki, B. Sulikowski, Z. Olejniczak, S. Walas, Desilication of ZSM-5 and ZSM-12 zeolites: Impact on textural, acidic and catalytic properties, Catal. Today. 152 (2010) 24–32.

[94] M. Bjørgen, F. Joensen, M. Spangsberg Holm, U. Olsbye, K.-P. Lillerud, S. Svelle, Methanol to gasoline over zeolite H-ZSM-5: Improved catalyst performance by treatment with NaOH, Appl. Catal. A Gen. 345 (2008) 43–50.

[95] J. Zhuang, Y. Xu, Creating Mesopores in ZSM-5 Zeolite by Alkali Treatment: A New Way to Enhance the Catalytic Performance of Methane, Eur. Sci. Ed. 38 (2012) 35–37.

[96] J.C. Groen, T. Sano, J.A. Moulijn, J. Pérez-Ramírez, Alkaline-mediated mesoporous mordenite zeolites for acid-catalyzed conversions, J. Catal. 251 (2007) 21–27.

[97] F. Schmidt, M.R. Lohe, B. Büchner, F. Giordanino, F. Bonino, S. Kaskel, Improved catalytic performance of hierarchical ZSM-5 synthesized by desilication with surfactants, Microporous Mesoporous Mater. 165 (2013) 148–157.

[98] S. Sartipi, K. Parashar, M.J. Valero-Romero, V.P. Santos, B. Van Der Linden, M. Makkee, F. Kapteijn, J. Gascon, Hierarchical H-ZSM-5-supported cobalt for the direct synthesis of gasoline-range hydrocarbons from syngas: Advantages, limitations, and mechanistic insight, J. Catal. 305 (2013) 179–190.

[99] K. Sadowska, K. Góra-Marek, M. Drozdek, P. Kuśtrowski, J. Datka, J. Martinez Triguero, F. Rey, Desilication of highly siliceous zeolite ZSM-5 with NaOH and NaOH/tetrabutylamine hydroxide, Microporous Mesoporous Mater. 168 (2013) 195–205.

[100] Z. Di, C. Yang, X. Jiao, J. Li, J. Wu, D. Zhang, A ZSM-5/MCM-48 based catalyst for methanol to gasoline conversion, Fuel. 104 (2013) 878–881.

[101] a. G. Gayubo, A.T. Aguayo, M. Olazar, R. Vivanco, J. Bilbao, Kinetics of the irreversible deactivation of the HZSM-5 catalyst in the MTO process, Chem. Eng. Sci. 58 (2003) 5239–5249.

[102] A. de Lucas, P. Canizares, a. Durán, a. Carrero, Dealumination of HZSM-5 zeolites: Effect of steaming on acidity and aromatization activity, Appl. Catal. A Gen. 154 (1997) 221–240.

[103] M.A. Aukett, Y.A. Parks, P.H. Scott, B.A. Wharton, Treatment with Iron Increases Weight-Gain and Psychomotor Development, Arch. Dis. Child. 61 (1986) 849–857.

[104] G.F. Froment, J. De Meyer, E.G. Derouane, Deactivation of zeolite catalysts by coke formation, J. Catal. 124 (1990) 391–400.

[105] G.F. Froment, Coke formation in catalytic processes: kinetics and catalyst deactivation, Stud Surf Sci Catal. 111 (1997) 53–68.

[106] H. Schulz, “Coking” of zeolites during methanol conversion: Basic reactions of the MTO-, MTP- and MTG processes, Catal. Today. 154

(2010) 183–194.

[107] F. Bleken, M. Bjørgen, L. Palumbo, S. Bordiga, S. Svelle, K.P. Lillerud, U. Olsbye, The effect of acid strength on the conversion of methanol to olefins over acidic microporous catalysts with the CHA topology, Top. Catal. 52 (2009) 218–228.

[108] Q. Zhu, J.N. Kondo, R. Ohnuma, Y. Kubota, M. Yamaguchi, T. Tatsumi, The study of methanol-to-olefin over proton type aluminosilicate CHA zeolites, Microporous Mesoporous Mater. 112 (2008) 153–161.

[109] I.M. Dahl, H. Mostad, D. Akporiaye, R. Wendelbo, Structural and chemical influences on the MTO reaction: a comparison of chabazite and SAPO-34 as MTO catalysts, Microporous Mesoporous Mater. 29 (1999) 185–190.

[110] S. Wilson, P. Barger, The characteristics of SAPO-34 which influence the conversion of methanol to light olefins, Microporous Mesoporous Mater. 29 (1999) 117–126.

[111] F. Schmidt, C. Hoffmann, F. Giordanino, S. Bordiga, P. Simon, W. Carrillo-Cabrera, S. Kaskel, Coke location in microporous and hierarchical ZSM-5 and the impact on the MTH reaction, J. Catal. 307 (2013) 238–245.

[112] A.T. Aguayo, A.G. Gayubo, M. Olazar, J.M. Ortega, A.L. Moran, J. Bilbao, Coke Combustion and Reactivation Kinetics of a Zsm-5 Zeolite Based Catalyst Used for the Transformation of Methanol Into Hydrocarbons, Chem. Eng. Commun. 176 (1999) 43–63.

[113] S. Müller, Y. Liu, M. Vishnuvarthan, X. Sun, A.C. Van Veen, G.L. Haller, M. Sanchez-Sanchez, J.A. Lercher, Coke formation and deactivation pathways on H-ZSM-5 in the conversion of methanol to olefins, J. Catal. 325 (2015) 48–59.

[114] S. Müller, Y. Liu, F.M. Kirchberger, M. Tonigold, M. Sanchez-Sanchez, J.A. Lercher, Hydrogen Transfer Pathways during Zeolite Catalyzed Methanol Conversion to Hydrocarbons, J. Am. Chem. Soc. 138 (2016) 15994–16003.

[115] R. Hunter, G.J. Hutchings, Hydrocarbon formation from methanol using WO3/Al2O3 and zeolite H-ZSM-5 catalysts: further evidence on the reaction mechanism, (1987) 377–379.

[116] G.J. Hutchings, L.J. Van Rensburg, W. Pick, R. Hunter, Hydrocarbon formation from methanol and dimethyl ether using WO3/Al2O3 and H-ZSM-5 catalysts. A mechanistic investigation using model reagents, Africa (Lond). 84 (1988) 1311–1328.

[117] X. Sun, S. Mueller, Y. Liu, H. Shi, G.L. Haller, M. Sanchez-Sanchez, A.C. Van Veen, J.A. Lercher, On reaction pathways in the conversion of methanol to hydrocarbons on HZSM-5, J. Catal. 317 (2014) 185–197.

[118] H. Schulz, “Coking” of zeolites during methanol conversion: Basic

reactions of the MTO-, MTP- and MTG processes, Catal. Today. 154 (2010) 183–194.

[119] Y. M., L. H., Z. Y., Z. T., L. Z., MTO Processes Development: The Key of Mesoscale Studies, Academic Press, 2015.

[120] M. Bjørgen, U. Olsbye, D. Petersen, S. Kolboe, The methanol-to-hydrocarbons reaction: Insight into the reaction mechanism from [12C]benzene and [13C]methanol coreactions over zeolite H-beta, J. Catal. 221 (2004) 1–10.

[121] F.C. Patcas, The methanol-to-olefins conversion over zeolite-coated ceramic foams, J. Catal. 231 (2005) 194–200.

[122] J. Li, Y. Wei, G. Liu, Y. Qi, P. Tian, B. Li, Y. He, Z. Liu, Comparative study of MTO conversion over SAPO-34, H-ZSM-5 and H-ZSM-22: Correlating catalytic performance and reaction mechanism to zeolite topology, Catal. Today. 171 (2011) 221–228.

[123] S. Fathi, M. Sohrabi, C. Falamaki, Improvement of HZSM-5 performance by alkaline treatments: Comparative catalytic study in the MTG reactions, Fuel. 116 (2014) 529–537.

[124] T. Mildner, H. Ernst, D. Freude, U. Winkler, Time-Resolved 13 C MAS NMR Investigation of Chemical Reactions : the MTG Process, Magetic Reson. Chem. 37 (1999) s38–s42.

[125] A.G. Gayubo, J.M. Ortega, A.T. Aguayo, J.M. Arandes, J. Bilbao, MTG fluidized bed reactor-regenerator unit with catalyst circulation: Process simulation and operation of an experimental setup, Chem. Eng. Sci. 55 (2000) 3223–3235.

[126] S. Yurchak, Development of Mobil's Fixed-Bed Methanul-to-Gasoline (MTG) Process, in: Stud. Surf. Sci. Catal., 1988: pp. 251–272.

[127] C.D. Chang, The New Zealand Gas-to-Gasoline plant: An engineering tour de force, Catal. Today. 13 (1992) 103–111.

[128] D. Mohan, C.U. Pittman, P.H. Steele, Pyrolysis of Wood / Biomass for Bio-oil : A Critical Review, Energy & Fuesl. 20 (2006) 848–889.

[129] Exxon Mobil Research and Engineering, Proven process . Proven plants . Proven performance ., (2014).

[130] Exxon Mobil Research and Engineering, Methanol to Gasoline (MTG) Production of Clean Gasoline from Coal, Technology. (2009).

[131] J.Q. Chen, A. Bozzano, B. Glover, T. Fuglerud, S. Kvisle, Recent advancements in ethylene and propylene production using the UOP/Hydro MTO process, Catal. Today. 106 (2005) 103–107.

[132] American Chemical Society, Concentrates, Chem. Eng. News. 83 (2005) 18.

[133] H. Keompel, W. Liebner, Lurgi's Methanol To Propylene (MTP) Report on a successful comercialisation, Stud. Surf. Sci. Catal. 167 (2007) 261–267.

[134] V. Hessel, S. Hardt, H. Lowe, Chemical Micro Process Engineering, Fundamentals, Modelling and Reactions, WILEY-VCH, 2004.

[135] J.C. Charpentier, In the frame of globalization and sustainability, process intensification, a path to the future of chemical and process engineering (molecules into money), Chem. Eng. J. 134 (2007) 84–92.

[136] S. Senkan, K. Krantz, S. Ozturk, V. Zengin, I. Onal, High-throughput testing of heterogeneous catalyst libraries using array microreactors and mass spectrometry, Angew. Chemie - Int. Ed. 38 (1999) 2794–2799.

[137] S.M. Senkan, S. Ozturk, Discovery and Optimization of Heterogeneous Catalysts by Using Combinatorial Chemistry, 20 (1999) 791–795.

[138] J.R. Burns, C. Ramshaw, Development of a Microreactor for Chemical Production, Chem. Eng. Res. Des. 77 (1999) 206–211.

[139] J. West, M. Becker, S. Tombrink, A. Manz, Micro total analysis systems: Latest achievements, Anal. Chem. 80 (2008) 4403–4419.

[140] E. V. Rebrov, S.A. Duinkerke, M.H.J.M. de Croon, J.C. Schouten, Optimization of heat transfer characteristics, flow distribution, and reaction processing for a microstructured reactor/heat-exchanger for optimal performance in platinum catalyzed ammonia oxidation, Chem. Eng. J. 93 (2003) 201–216.

[141] E. V. Rebrov, J.C. Schouten, M.H.J.M. de Croon, Single-phase fluid flow distribution and heat transfer in microstructured reactors, Chem. Eng. Sci. 66 (2011) 1374–1393.

[142] A.G. Fedorov, R. Viskanta, Three-dimensional conjugate heat transfer in the microchannel heat sink for electronic packaging, Int. J. Heat Mass Transf. 43 (2000) 399–415.

[143] A. Weisberg, H.H. Bau, J.N. Zemel, Analysis of microchannels for integrated cooling, Int. J. Heat Mass Transf. 35 (1992) 2465–2474.

[144] W. Qu, I. Mudawar, Experimental and numerical study of pressure drop and heat transfer in a single-phase micro-channel heat sink, Int. J. Heat Mass Transf. 45 (2002) 2549–2565.

[145] I. Tiselj, G. Hetsroni, B. Mavko, A. Mosyak, E. Pogrebnyak, Z. Segal, Effect of axial conduction on the heat transfer in micro-channels, Int. J. Heat Mass Transf. 47 (2004) 2551–2565.

[146] P. van Male, M.H.J.M. de Croon, R.M. Tiggelaar, A. van den Berg, J.C. Schouten, Heat and mass transfer in a square microchannel with asymmetric heating, Int. J. Heat Mass Transf. 47 (2004) 87–99.

[147] P.S. Lee, S. V. Garimella, D. Liu, Investigation of heat transfer in rectangular microchannels, Int. J. Heat Mass Transf. 48 (2005) 1688–1704.

[148] A. Karim, J. Bravo, D. Gorm, T. Conant, A. Datye, Comparison of

wall-coated and packed-bed reactors for steam reforming of methanol, Catal. Today. 110 (2005) 86–91.

[149] D. Liu, S. V. Garimella, Investigation of liquid flow in microchannels, J. Thermophys. Heat Transf. 18 (2004) 65–72.

[150] X.F. Peng, G.P. Peterson, Convective heat transfer and flow friction for water flow in microchannel structures, Int. J. Heat Mass Transf. 39 (1996) 2599–2608.

[151] A. Vatani, H.A. Mohammed, Turbulent nanofluid flow over periodic rib-grooved channels, Eng. Appl. Comput. Fluid Mech. 7 (2013) 369–381.

[152] J. Lee, I. Mudawar, Assessment of the effectiveness of nanofluids for single-phase and two-phase heat transfer in micro-channels, Int. J. Heat Mass Transf. 50 (2007) 452–463.

[153] D. Kumar, A. Panigrahi, Numerical investigation of heat transfer enhancement and pressure drop increment in finned rectangular ... Numerical Investigation of Heat Transfer Enhancement and Pressure drop Increment in Finned Rectangular Micro-channel with Nanofluids under Constant , (2016).

[154] G.D. Stefanidis, D.G. Vlachos, Millisecond methane steam reforming via process and catalyst intensification, Chem. Eng. Technol. 31 (2008) 1201–1209.

[155] K.A. Alfadhel, M. V. Kothare, Microfluidic modeling and simulation of flow in membrane microreactors, Chem. Eng. Sci. 60 (2005) 2911–2926.

[156] C.Y. Hsueh, H. Sen Chu, W.M. Yan, Numerical study on micro-reformer performance and local transport phenomena of the plate methanol steam micro-reformer, J. Power Sources. 187 (2009) 535–543.

[157] J.Y. Jang, Y.X. Huang, C.H. Cheng, The effects of geometric and operating conditions on the hydrogen production performance of a micro-methanol steam reformer, Chem. Eng. Sci. 65 (2010) 5495–5506.

[158] X. Zhang, K. Cooke, P. Carmichael, I.P. Parkin, The deposition of crystallized TiO2 coatings by closed field unbalanced magnetron sputter ion plating, Surf. Coatings Technol. 236 (2013) 290–295.

[159] E. V. Rebrov, G.B.F. Seijger, H.P. a Calis, M.H.J.M. De Croon, C.M. Van Den Bleek, J.C. Schouten, Preparation of highly ordered single layer ZSM-5 coating on prefabricated stainless steel microchannels, Appl. Catal. A Gen. 206 (2001) 125–143.

[160] J. Peréz-Ramírez, D. Verboekend, A. Bonilla, S. Abelló, Zeolite catalysts with tunable hierarchy factor by pore-growth moderators, Adv. Funct. Mater. 19 (2009) 3972–3979.

[161] W.D. Harkins, G. Jura, Surfaces of Solids. XIII. A Vapor Adsorption Method for the Determination of the Area of a Solid without the

Assumption of a Molecular Area, and the Areas Occupied by Nitrogen and Other Molecules on the Surface of a Solid, J. Am. Chem. Soc. 66 (1944) 1366–1373.

[162] S. Brunauer, P.H. Emmett, E. Teller, Adsorption of Gases in Multimolecular Layers, J. Am. Chem. Soc. 60 (1938) 309–319.

[163] J.T. Scanlon, Calculation of Flame Ionization Detector Relative Response Factors Using the Effective Carbon Number Concept, 23 (1985) 333–340.

[164] P.D. Shawn, V.R.B. Eric, L.S. Steven, Growth of zeolite crystallites and coatings on metal surfaces, Chem. Mater. 2 (1990) 712–719.

[165] M.J.M. Mies, J.L.P. Van Den Bosch, E. V. Rebrov, J.C. Jansen, M.H.J.M. De Croon, J.C. Schouten, Hydrothermal synthesis and characterization of ZSM-5 coatings on a molybdenum support and scale-up for application in micro reactors, Catal. Today. 110 (2005) 38–46.

[166] S.M. Alipour, R. Halladj, S. Askari, Effects of the different synthetic parameters on the crystallinity and crystal size of nanosized ZSM-5 zeolite, Rev. Chem. Eng. 30 (2014) 289–322.

[167] R.M. Mohamed, H. Aly, M.F. El-shahat, I.A. Ibrahim, Effect of Silica Sources on the Crystallinity of Nanosized ZSM-5, Microporous Mesoporous Mater. 79 (5AD) 7–12.

[168] A.A. Ismail, R.M. Mohamed, O.A. Fouad, I.A. Ibrahim, Synthesis of nanosized ZSM-5 using different alumina sources, Cryst. Res. Technol. 41 (2006) 145–149.

[169] H. Aly, M.E. Moustafa, E.A. Abdelrahman, Influence of aluminum source on the synthesis of nanosized ZSM-5 zeolite, 2011.

[170] Y. Hu, C. Liu, Y. Zhang, N. Ren, Y. Tang, Microwave-assisted hydrothermal synthesis of nanozeolites with controllable size, Microporous Mesoporous Mater. 119 (2009) 306–314.

[171] M.M.J. Treacy, J.B. Higgins, Collection of Simulated XRD Powder Patterns for Zeolites, Fifth, Elsevier, 1984.

[172] Y. Furumoto, Y. Harada, N. Tsunoji, A. Takahashi, T. Fujitani, Y. Ide, M. Sadakane, T. Sano, Effect of acidity of ZSM-5 zeolite on conversion of ethanol to propylene, Appl. Catal. A Gen. 399 (2011) 262–267.

[173] Z. Wan, W. Wu, G.K. Li, C. Wang, H. Yang, D. Zhang, Effect of SiO2/Al2O3 Ratio on the Performance of Nanocrystal ZSM-5 Zeolite Catalysts in Methanol to Gasoline Conversion, Appl. Catal. A Gen. (2016).

[174] A.F.P. Ferreira, M.C. Mittelmeijer-Hazeleger, J.V.D. Bergh, S. Aguado, J.C. Jansen, G. Rothenberg, A.E. Rodrigues, F. Kapteijn, Adsorption of hexane isomers on MFI type zeolites at ambient temperature: Understanding the aluminium content effect, Microporous Mesoporous Mater. 170 (2013) 26–35.

[175] J. Shao, T. Fu, J. Chang, W. Wan, R. Qi, Z. Li, Effect of ZSM-5 crystal size on its catalytic properties for conversion of methanol to gasoline, J. Fuel Chem. Technol. 45 (2017) 75–83.

[176] X. Niu, J. Gao, K. Wang, Q. Miao, M. Dong, G. Wang, W. Fan, Z. Qin, J. Wang, Influence of crystal size on the catalytic performance of H-ZSM-5 and Zn/H-ZSM-5 in the conversion of methanol to aromatics, Fuel Process. Technol. 157 (2017) 99–107.

[177] H.P. Decolatti, B.O. Dalla Costa, C.A. Querini, Dehydration of glycerol to acrolein using H-ZSM5 zeolite modified by alkali treatment with NaOH, Microporous Mesoporous Mater. 204 (2015) 180–189.

[178] F. Jin, Y. Li, A FTIR and TPD examination of the distributive properties of acid sites on ZSM-5 zeolite with pyridine as a probe molecule, Catal. Today. 145 (2009) 101–107.

[179] N.Y. Topsøe, K. Pedersen, E.G. Derouane, Infrared and temperature-programmed desorption study of the acidic properties of ZSM-5-type zeolites, J. Catal. 70 (1981) 41–52.

[180] A. Auroux, V. Bolis, P. Wierzchowski, P.C. Gravelle, J.C. Vedrine, Study of the Acidity of ZSM-5 Zeolite by Microcalorimetry and Infrared Spectroscopy, J. Chem. Soc., Farad.T. 1. 75 (1979) 2544.

[181] M.D. Oleksiak, J.D. Rimer, Synthesis of zeolites in the absence of organic structure-directing agents: factors governing crystal selection and polymorphism, Rev. Chem. Eng. 30 (2014).

[182] Y. Li, H; Zhang, Y; Xiang, S; Tao, K; Liang, S; Wang, Synthesis of large-crystal ZSM-5 zeolite and studies on its catalytic behavior, Ranliao Huaxue Xuebao. 13 (1985) 187–91.

[183] P.L. Benito, A.G. Gayubo, A.T. Aguayo, M. Olazar, J. Bilbao, Deposition and Characteristics of Coke over a H-ZSM5 Zeolite-Based Catalyst in the MTG Process, Ind. Eng. Chem. Res. 35 (1996) 3991–3998.

[184] K. Barbera, F. Bonino, S. Bordiga, T.V.W. Janssens, P. Beato, Structure-deactivation relationship for ZSM-5 catalysts governed by framework defects, J. Catal. 280 (2011) 196–205.

[185] M. Bjørgen, F. Joensen, K.P. Lillerud, U. Olsbye, S. Svelle, The mechanisms of ethene and propene formation from methanol over high silica H-ZSM-5 and H-beta, Catal. Today. 142 (2009) 90–97.

[186] M. Guisnet, P. Magnoux, Deactivation by coking of zeolite catalysts. Prevention of deactivation. Optimal conditions for regeneration, Catal. Today. 36 (1997) 477–483.

[187] J. Li, Z. Wei, Y. Chen, B. Jing, Y. He, M. Dong, H. Jiao, X. Li, Z. Qin, J. Wang, W. Fan, A route to form initial hydrocarbon pool species in methanol conversion to olefins over zeolites, J. Catal. 317 (2014) 277–283.

[188] F.L. Bleken, S. Chavan, U. Olsbye, M. Boltz, F. Ocampo, B. Louis, Conversion of methanol into light olefins over ZSM-5 zeolite:

Strategy to enhance propene selectivity, Appl. Catal. A Gen. 447–448 (2012) 178–185.

[189] D. Goto, Y. Harada, Y. Furumoto, A. Takahashi, T. Fujitani, Y. Oumi, M. Sadakane, T. Sano, Conversion of ethanol to propylene over HZSM-5 type zeolites containing alkaline earth metals, Appl. Catal. A Gen. 383 (2010) 89–95.

[190] a. W. Chester, E.G. Derouane, eds., Zeolite Characterization and Catalysis: A Tutorial, 1st ed., Springer US, 2009.

[191] F.J. Keil, Methanol-to-hydrocarbons : process technology, 29 (1999) 49–66.

[192] T.V.W. Janssens, A new approach to the modeling of deactivation in the conversion of methanol on zeolite catalysts, J. Catal. 264 (2009) 130–137.

[193] J.F. Haw, J.B. Nicholas, W. Song, F. Deng, Z. Wang, T. Xu, C.S. Heneghan, Roles for cyclopentenyl cations in the synthesis of hydrocarbons from methanol on zeolite catalyst HZSM-5, J. Am. Chem. Soc. 122 (2000) 4763–4775.

[194] D.M. Bibby, N.B. Milestone, J.E. Patterson, L.P. Aldridge, Coke formation in zeolite ZSM-5, J. Catal. 97 (1986) 493–502.

[195] C. Zhou, Y. Bashirzadeh, T.A. Bernadowski, X. Zhang, UV light-induced aggregation of titania submicron particles, Micromachines. 7 (2016).

[196] T. Zubkoy, D. Stahl, T.L. Thompson, D. Panayotov, O. Diwald, J.T. Yates, Ultraviolet light-induced hydrophilicity effect on TiO 2(110) (1×1). Dominant role of the photooxidation of adsorbed hydrocarbons causing wetting by water droplets, J. Phys. Chem. B. 109 (2005) 15454–15462.

[197] P.-P.E.A. de Moor, T.P.M. Beelen, R.A. van Santen, In situ Observation of Nucleation and Crystal Growth in Zeolite Synthesis. A Small-Angle X-ray Scattering Investigation on Si-TPA-MFI, J. Phys. Chem. B. 103 (1999) 1639–1650.

[198] P.A. Jacobs, E.G. Derouane, J. Weitkamp, Evidence for X-Ray - amorphous Zeolites, J. Chem. Soc. Chem. Commun. (1981) 591–593.

[199] H.S. Folger, M.N. Gurmen, Diffusion and Reaction 12, Essentials Chem. React. Eng. (2008) 813–866.

[200] J. Pérez-Ramírez, C.H. Christensen, K. Egeblad, C.H. Christensen, J.C. Groen, Hierarchical zeolites: Enhanced Utilisation of Microporous Crystals in Catalysis by Advances in Materials Design., Chem. Soc. Rev. 37 (2008) 2530–2542.

[201] F.C. Patcas, The methanol-to-olefins conversion over zeolite-coated ceramic foams, J. Catal. 231 (2005) 194–200.

[202] U. Olsbye, S. Svelle, M. Bjrgen, P. Beato, T.V.W. Janssens, F.

Joensen, S. Bordiga, K.P. Lillerud, Conversion of methanol to hydrocarbons: How zeolite cavity and pore size controls product selectivity, Angew. Chemie - Int. Ed. 51 (2012) 5810–5831.

[203] W. Guo, W. Xiao, M. Luo, Comparison among monolithic and randomly packed reactors for the methanol-to-propylene process, Chem. Eng. J. 207–208 (2012) 734–745.

[204] H. Okado, H. Shoji, T. Sano, S. Ikai, H. Hagiwara, H. Takaya, Deactivation resistance of ZSM-5-type zeolites containing alkaline earth metals used for methanol conversion, Appl. Catal. 41 (1988) 121–135.

[205] T. Sano, T. Murakami, K. Suzuki, S. Ikai, H. Okado, K. Kawamura, H. Hagiwara, H. Takaya, Improvement of catalyst stability of ZSM-5 zeolite containing calcium by modification with CaCO3., Appl. Catal. 33 (1987) 209–217.

[206] K. Omata, Y. Yamazaki, Y. Watanabe, K. Kodama, M. Yamada, Artificial neural network (ann)-aided optimization of zsm-5 catalyst for the dimethyl ether to olefin (dto) reaction from neat dimethyl ether (dme), Ind. Eng. Chem. Res. 48 (2009) 6256–6261.

[207] S. Hajimirzaee, M. Ainte, B. Soltani, R.M. Behbahani, G.A. Leeke, J. Wood, Dehydration of methanol to light olefins upon zeolite/alumina catalysts: Effect of reaction conditions, catalyst support and zeolite modification, Chem. Eng. Res. Des. 93 (2015) 541–553.

[208] A.A. Rownaghi, F. Rezaei, J. Hedlund, Uniform mesoporous ZSM-5 single crystals catalyst with high resistance to coke formation for methanol deoxygenation, Microporous Mesoporous Mater. 151 (2012) 26–33.

[209] D. Verboekend, S. Mitchell, M. Milina, J.C. Groen, J. Pérez-Ramírez, Full compositional flexibility in the preparation of mesoporous MFI zeolites by desilication, J. Phys. Chem. C. 115 (2011) 14193–14203.

[210] S. van Donk, A.H. Janssen, J.H. Bitter, K.P. de Jong, Generation, Characterization, and Impact of Mesopores in Zeolite Catalysts, Catal. Rev. 45 (2003) 297–319.

[211] S. Fathi, M. Sohrabi, C. Falamaki, Improvement of HZSM-5 performance by alkaline treatments: Comparative catalytic study in the MTG reactions, Fuel. 116 (2014) 529–537.

[212] K. Suzuki, Y. Kiyozumi, K. Matsuzaki, S. Shin, Effect of modification of ZSM-5 type zeolite with calcium phosphate on its physico-chemical and catalytic properties, Appl. Catal. 42 (1988) 35–45.

[213] K. Omata, Y. Yamazaki, Y. Watanabe, K. Kodama, M. Yamada, Artificial neural network (ann)-aided optimization of zsm-5 catalyst for the dimethyl ether to olefin (dto) reaction from neat dimethyl ether (dme), Ind. Eng. Chem. Res. 48 (2009) 6256–6261.

[214] B.Y.R.D. Shannon, M. H, N.H. Baur, O.H. Gibbs, M. Eu, V. Cu, Revised Effective Ionic Radii and Systematic Studies of Interatomie

Distances in Halides and Chaleogenides Central Research and Development Department , Experimental Station , E . L Du Pont de Nemours The effective ionic radii of Shannon & Prewitt [ Acta, (1976).

[215] Y. He, M. Liu, C. Dai, S. Xu, Y. Wei, Z. Liu, X. Guo, Modification of nanocrystalline HZSM-5 zeolite with tetrapropylammonium hydroxide and its catalytic performance in methanol to gasoline reaction, Cuihua Xuebao/Chinese J. Catal. 34 (2013) 1148–1158.

[216] X.L. Huang, MS Dissertation, Xiangtan University, 2008.

[217] J. Ahmadpour, M. Taghizadeh, Selective production of propylene from methanol over high-silica mesoporous ZSM-5 zeolites treated with NaOH and NaOH/tetrapropylammonium hydroxide, Comptes Rendus Chim. 18 (2015) 834–847.

[218] K.S.W. Sing, D.H. Everett, R. a. W. Haul, L. Moscou, R. a. Pierotti, J. Rouquérol, T. Siemieniewska, Reporting Physisorption Data for Gas / Solid Systems with Special Reference to the Determination of Surface Area and Porosity, Pure Appl. Chem. 54 (1982) 2201–2218.

[219] T. Fu, Y. Jiang, J. Lv, Z. Li, Effect of carbon support on Fischer-Tropsch synthesis activity and product distribution over Co-based catalysts, Fuel Process. Technol. 110 (2013) 141–149.

[220] J.C. Groen, L.A.A. Peffer, J.A. Moulijn, J. Pérez-Ramírez, Mechanism of hierarchical porosity development in MFI zeolites by desilication: The role of aluminium as a pore-directing agent, Chem. - A Eur. J. 11 (2005) 4983–4994.

[221] Physical Adsorption Characterization of Mesoporous Materials: Comments on Hysteresis Scanning, Part 1, (2007) 1–5.

[222] D. Verboekend, G. Vilé, J. Pérez-Ramírez, Mesopore formation in usy and beta zeolites by base leaching: Selection criteria and optimization of pore-directing agents, Cryst. Growth Des. 12 (2012) 3123–3132.

[223] X. Zhu, L.L. Lobban, R.G. Mallinson, D.E. Resasco, Tailoring the mesopore structure of HZSM-5 to control product distribution in the conversion of propanal, J. Catal. 271 (2010) 88–98.

[224] M. Milina, S. Mitchell, P. Crivelli, D. Cooke, J. Pérez-Ramírez, Mesopore quality determines the lifetime of hierarchically structured zeolite catalysts, Nat. Commun. 5:3922 (2014) doi:10.1038/ncomms4922.

[225] J. García-Martínez, M. Johnson, J. Valla, K. Li, J.Y. Ying, Mesostructured zeolite Y—high hydrothermal stability and superior FCC catalytic performance, Catal. Sci. Technol. 2 (2012) 987.

[226] F. Yaripour, Z. Shariatinia, S. Sahebdelfar, A. Irandoukht, Effect of boron incorporation on the structure, products selectivities and lifetime of H-ZSM-5 nanocatalyst designed for application in methanol-to-olefins (MTO) reaction, Microporous Mesoporous Mater. 203 (2015) 41–53.

[227] M. Dyballa, E. Klemm, J. Weitkamp, M. Hunger, Effect of phosphate modification on the Brønsted acidity and methanol-to-olefin conversion activity of zeolite ZSM-5, Chemie-Ingenieur-Technik. 85 (2013) 1719–1725.

[228] S. Mitchell, N.-L. Michels, K. Kunze, J. Pérez-Ramírez, Visualization of hierarchically structured zeolite bodies from macro to nano length scales, Nat. Chem. 4 (2012) 825–831.

[229] F. Lønstad, K. Barbera, F. Bonino, U. Olsbye, K. Petter, S. Bordiga, P. Beato, T.V.W. Janssens, S. Svelle, Catalyst deactivation by coke formation in microporous and desilicated zeolite H-ZSM-5 during the conversion of methanol to hydrocarbons, 307 (2013) 62–73.

[230] F. Jiménez-Cruz, G.C. Laredo, Molecular size evaluation of linear and branched paraffins from the gasoline pool by DFT quantum chemical calculations, Fuel. 83 (2004) 2183–2188.

[231] J.C. Groen, T. Bach, U. Ziese, A.M. Paulaime-Van Donk, K.P. De Jong, J.A. Moulijn, J. Pérez-Ramírez, Creation of hollow zeolite architectures by controlled desilication of A1-zoned ZSM-5 crystals, J. Am. Chem. Soc. 127 (2005) 10792–10793.

[232] F. Schmidt, C. Hoffmann, F. Giordanino, S. Bordiga, P. Simon, W. Carrillo-Cabrera, S. Kaskel, Coke location in microporous and hierarchical ZSM-5 and the impact on the MTH reaction, J. Catal. 307 (2013) 238–245.

[233] G.W. Swift, A. Migliori, J.C. Wheatley, Microchannel crossflow fluid heat exchanger and method for its fabrication, US 4516632 A, 1985.

[234] P.X. Jiang, M.H. Fan, G.S. Si, Z.P. Ren, Thermal-hydraulic performance of small scale micro-channel and porous-media heat-exchangers, Int. J. Heat Mass Transf. 44 (2001) 1039–1051.

[235] J.W. Ashmead, J.K. Nyquist, J.A. Perrotto, C.T. Blaisdell, M.H. Johnson, J.F. Ryley, Integrated chemical processing apparatus and processes for the preparation thereof, 5, 1995.

[236] M. Kaarsholm, B. Rafii, F. Joensen, R. Cenni, J. Chaouki, G.S. Patience, Kinetic modeling of methanol-to-olefin reaction over ZSM-5 in fluid bed, Ind. Eng. Chem. Res. 49 (2010) 29–38.

[237] H. Hu, W. Ying, D. Fang, Mathematical modeling of multi-bed adiabatic reactor for the Methanol-to-Olefin process, React. Kinet. Mech. Catal. 101 (2010) 49–61.

[238] Y. Zhao, H. Li, M. Ye, Z. Liu, 3D Numerical Simulation of a Large Scale MTO Fluidized Bed Reactor, Ind. Eng. Chem. Res. 52 (2013) 11354–11364.

[239] M. Jayamurthy, S. Vasudevan, Methanol-to-gasoline (MTG) conversion over ZSM-5. A temperature programmed surface reaction study, Catal. Letters. 36 (1996) 111–114.

[240] N. Board, E. Format, H. Isbn, A. Pacific, B. Press, The Complete Book on Biomass Based Products ( Biochemicals , Biofuels ,

Activated Carbon ), 2015th ed., Delhi, 2008.

[241] Y. Tavan, R. Hasanvandian, Two practical equations for methanol dehydration reaction over HZSM-5 catalyst – Part I: Second order rate equation, Fuel. 142 (2015) 208–214.

[242] R.B. Peterson, Numerical Modeling of Conduction Effects in Microscale Counterflow Heat Exchangers, Microscale Thermophys. Eng. 3 (1999) 17–30.

[243] T. Stief, O. Langer, K. Schubert, Numerical Investigations of Optimal Heat Conductivity in Micro Heat Exchangers, Chem. Eng. Tech. 21 (1999) 297–303.

[244] S. Taghavi-Moghadam, A. Kleemann, K.G. Golbig, Microreaction technology as a novel approach to drug design, process development and reliability, Org. Process Res. Dev. 5 (2001) 652–658.

[245] S. Suga, A. Nagaki, J. Yoshida, Highly selective Friedel – Crafts monoalkylation using micromixing † Highly selective Friedel – Crafts monoalkylation of aromatic compounds with N -acyliminium ions has been achieved by, (2003) 354–355.

[246] T. Fukuyama, M. Shinmen, S. Nishitani, M. Sato, I. Ryu, A copper-free Sonogashira coupling reaction in ionic liquids and its application to a microflow system for efficient catalyst recycling, Org. Lett. 4 (2002) 1691–1694.

[247] J.M. Thomas, Heterogeneous catalysis and the challenges of powering the planet, securing chemicals for civilised life, and clean efficient utilization of renewable feedstocks, ChemSusChem. 7 (2014) 1801–1832.

[248] K.F. Kalz, R. Kraehnert, M. Dvoyashkin, R. Dittmeyer, R. Gläser, U. Krewer, K. Reuter, J.D. Grunwaldt, Future Challenges in Heterogeneous Catalysis: Understanding Catalysts under Dynamic Reaction Conditions, ChemCatChem. 9 (2017) 17–29.

[249] F. Tao, P.A. Crozier, Atomic-Scale Observations of Catalyst Structures under Reaction Conditions and during Catalysis, Chem. Rev. 116 (2016) 3487–3539.

[250] J.B. Koo, N. Jiang, S. Saravanamurugan, M. Bejblová, Z. Musilová, J. Čejka, S.E. Park, Direct synthesis of carbon-templating mesoporous ZSM-5 using microwave heating, J. Catal. 276 (2010) 327–334.

[251] M.L. Gonçalves, L.D. Dimitrov, M.H. Jordão, M. Wallau, E.A. Urquieta-González, Synthesis of mesoporous ZSM-5 by crystallisation of aged gels in the presence of cetyltrimethylammonium cations, Catal. Today. 133–135 (2008) 69–79.

[252] K. Singh, N.K. Sood, Viscosity and thermal conductivity of gas mixtures, Indian J. Pure Appl. Phys. 41 (2003) 121–127.

[253] W. Shen, Physical Chemistry, Second, Science probulication, Beijing, 2004.

[254] Dimethyle ether. https://en.wikipedia.org/wiki/Dimethyl_ether (Last accessed: 08-2016), (n.d.).

[255] http://ruby.chemie.uni-freiburg.de/Vorlesung/silicate_8_9.html, (n.d.).

[256] Methanol to Gasoline (MTG) Production of Clean Gasoline from Coal, Exxon Mob. Res. Eng. (n.d.).

[257] Mass diffusivity data. http://webserver.dmt.upm.es/~isidoro/dat1/Mass diffusivity data.pdf (Last accessed: 11-2017), (n.d.).

[258] H.S. Fogler, Elements of Chemical Reaction Engineering, Pearson Education Inc., 2010.

# Appendices

*Appendix A - GC analysis*

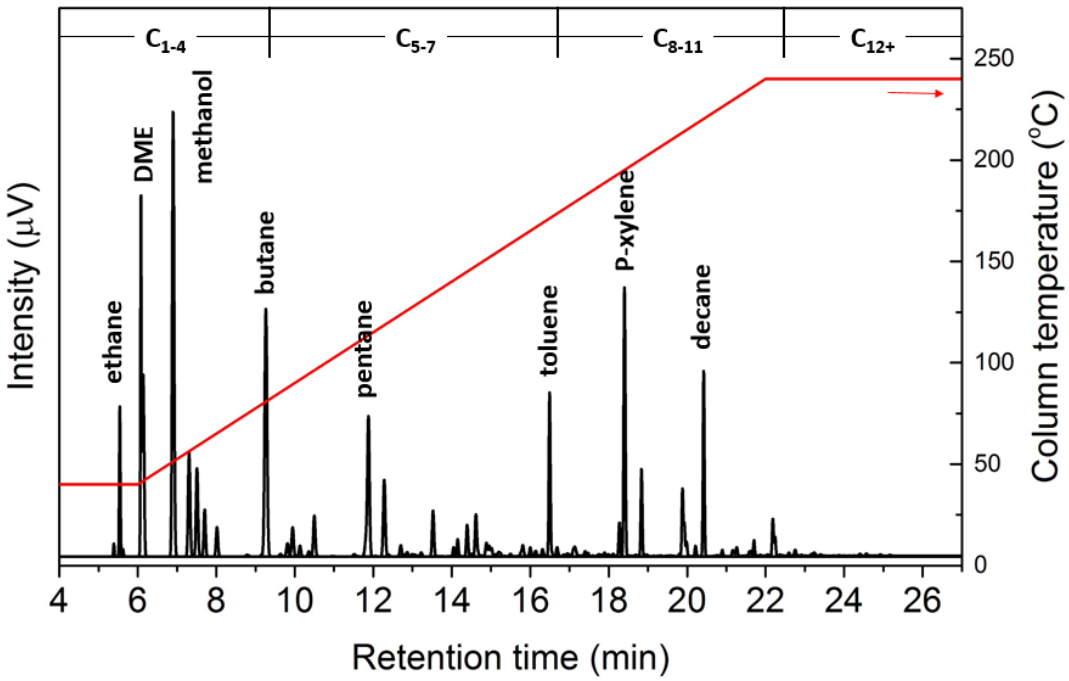


**Figure A1**. Typical GC chromatogram for hydrocarbons from $C_1$ to $C_{11}$

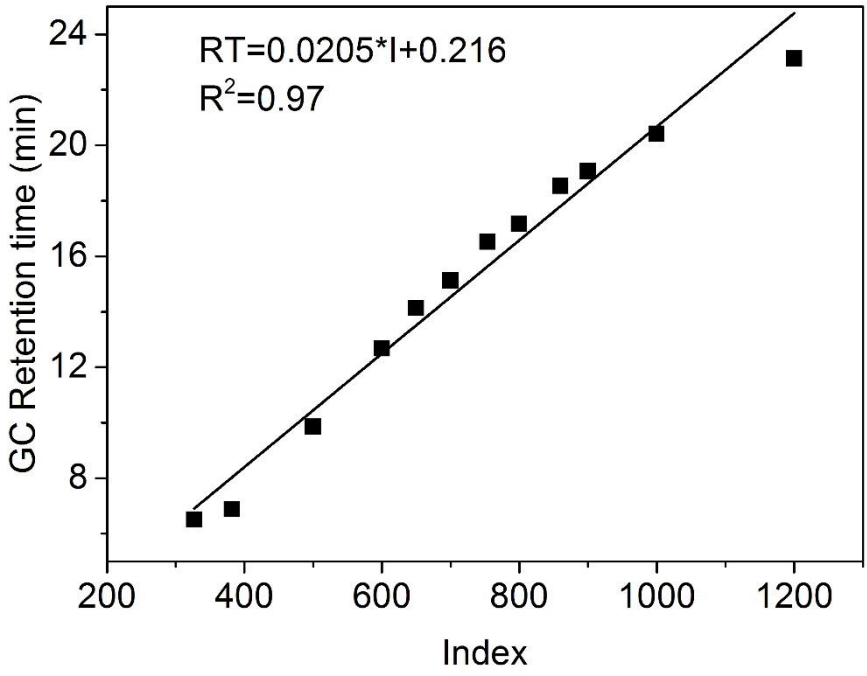


**Figure A2**. GC calibration curve of hydrocarbons

*Appendix B – Calculation of physical properties*

*Molecular diffusivity of gas*

$$D_m(T,P) = D_m^0(T_0,P_0) \cdot \frac{(T/T_0)^{1.5}}{P/P_0} \quad \text{(B0.1)}$$

where $D_m^0$ is the molecular diffusivity of gas at the temperature of $T_0$ and the pressure of $P_0$. $D_m$ is the molecular diffusivity of gas at the temperature of $T$and the pressure of $P$.

*Pressure drop*

Darcy friction pressure drop for laminar flow:

$$\Delta P\ (\mathrm{Pa}) = 32\frac{\mu v L}{D^2} = 2.1 \quad \text{(B0.2)}$$

Where $\Delta$P is pressure drop, L is reactor length, $\mu$ is dynamic viscosity, v is flow velocity, D is diameter of channel.

*Properties of individual gas*

Data of properties were fitted into functions of temperature below

Function (T) = $A_0+A_1 \cdot T+A_2 \cdot T^2$

- Heat capacity (J $mol^{-1}$ $K^{-1}$)

| | **$A_0$** | **$A_1$** | **$A_2$** |
|---|---|---|---|
| Methanol | 17.3 | $9.90\times10^{-2}$ | $-2.70\times10^{-5}$ |
| DME | 25.7 | $1.35\times10^{-1}$ | 0 |
| Octene | 34.8 | $5.52\times10^{-1}$ | $-1.80\times10^{-4}$ |
| Water | 30.0 | $1.06\times10^{-2}$ | 0 |

- Viscosity ($10^{-6}$ kg $s^{-1}$ $m^{-1}$)

| | **$A_0$** | **$A_1$** | **$A_2$** |
|---|---|---|---|
| Methanol | 1.043 | $2.92\times10^{-2}$ | 0 |
| Water | -3.16 | $4.10\times10^{-2}$ | 0 |

- Thermal conductivity ($10^{-4}$ W m$^{-1}$ K$^{-1}$)

| | $A_0$ | $A_1$ | $A_2$ |
|---|---|---|---|
| Methanol | 248 | 1.27 | 0 |
| DME | -298 | 1.21 | 0 |
| Octene | -46.3 | $2.88\times10^{-1}$ | $8.42\times10^{-4}$ |
| Water | -155 | 1.06 | 0 |

*Properties of gas mixture* [252]

$$\bar{\rho} = \sum C_B M_B \tag{B0.3}$$

$$\overline{Cp} = \sum Cp_B \frac{C_B}{\sum C_B} \tag{B0.4}$$

$$\overline{\mu_{12}} = K\sqrt{\mu_1\mu_2}\left(\frac{4M_1M_2}{(M_1+M_2)^2}\right)^{\frac{1}{4}} \tag{B0.5}$$

$$\overline{k_{12}} = k_1\left(1 + A_{12}\frac{C_{B2}}{C_{B1}}\right)^{-1} + k_2\left(1 + A_{21}\frac{C_{B1}}{C_{B2}}\right)^{-1} \tag{B0.6}$$

where $C_B$ are concentration for each species. μ is dynamic viscosity. $k_1, k_2$ are thermal conductivities for methanol and water with value of 0.058 and 0.052 W m$^{-1}$ K$^{-1}$. $A_{\mathrm{ij}}$ is coefficient depending upon mass ratio $M_2/M_1$ (>1) and inter-molecular potential parameters below.

Coefficient A for thermal conductivity of mixture gas:

$$A_{ij} = \frac{1}{K}\sqrt{\frac{\lambda_i}{\lambda_j}}\left\{F_{ij} + \frac{1-\left(\frac{\lambda_j F_{ij}}{\lambda_i F_{ji}}\right)^{\frac{1}{2}}}{\frac{(M_i+M_j)^{\frac{1}{2}}}{2.6M_iM_j} + \left(\frac{\lambda_j}{\lambda_i}\right)^{\frac{1}{4}}\left(\frac{1}{KF_{ji}}\right)^{\frac{1}{2}}}\right)\} \tag{B0.7}$$

where

$$F_{ij} = 1 + \frac{M_i - M_j}{(M_i+M_j)^2}(2.375M_i - 0.225M_j) \tag{B0.8}$$

$$K = \frac{1}{L^2}(1.01546L - 0.01403) \tag{B0.9}$$

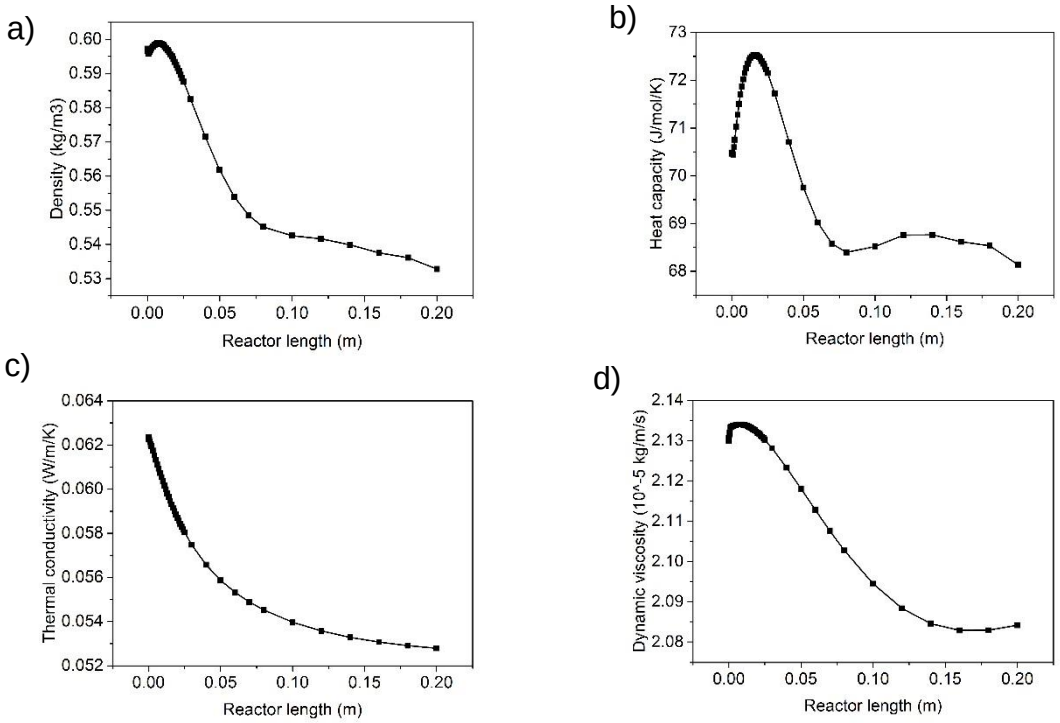


**Figure B1**. Profiles of physical properties a) Density, b) Heat capacity, c) Thermal conductivity, d) Dynamic viscosity of mixture fluid in reaction channel

*Reaction enthalpy*

$$H_{f,B}(T) = H_{f,B}(298\ K) + \int_{298}^{T} Cp_B(T)dT \quad \text{(B0.10)}$$

$$\Delta_r H(T) = \sum n_B H_{f,B}(T) \quad \text{(B0.11)}$$

where $H_{f,B}$ formation enthalpy of substance, standard value at 298 K could be found in **Table B1**. $\Delta_r H$ is reaction enthalpy, $n_B$ is stoichiometric number in reaction.

**Table B1**. Formation enthalpy of substances at 298 K

| **Substance** | **$H_{f,B}$ at 298 K (kJ·mol$^{-1}$)** | **References** |
|---|---|---|
| Methanol (g) | -200.7 | [253] |
| DME (g) | -184.1 | [254] |
| Octene (g) | -82.93 | [253] |

| | | |
|---|---|---|
| Water (g) | -241.8 | [253] |

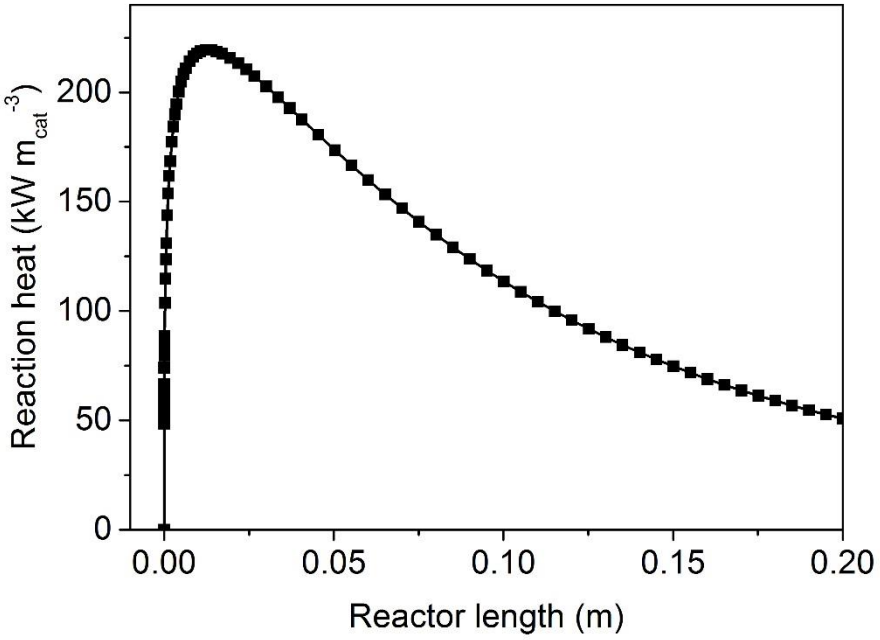


**Figure B2**. Heat generation profile in reaction channel (T=653 K, $F_{v,methanol}$=2.66*10$^{-9}$ m$^3$ s$^{-1}$, P=1 bar)

**Table B2**. Thermal resistance in the reactor for different configuration

| **Parameter** | **$D_r$=$D_c$=0.5 mm** |
|---|---|
| W (mm) | 3.5 |
| Z (mm) | 0.01 |
| $\mathrm{R_r} = \frac{1}{\mathrm{h_r \cdot A}_r}$ (K·W$^{-1}$) | 21.2 |
| $\mathrm{R_c} = \frac{1}{\mathrm{h_c \cdot A}_c}$ (K·W$^{-1}$) | 79.1 |
| $\mathrm{R_{metal}} = \frac{\mathrm{W}}{\mathrm{k_M \cdot \bar{A}}}$ (K·W$^{-1}$) | 0.351 |
| $\mathrm{R_{film}} = \frac{Z}{\mathrm{k_F \cdot A}_r}$ (K·W$^{-1}$) | 0.046 |
| $\mathrm{R_{tot}} = \mathrm{R_r} + \mathrm{R_c} + \mathrm{R_{metal}} + \mathrm{R}_{film}$ (K·W$^{-1}$) | 101.2 |

*Appendix C - Calcium ion-exchange ratio*

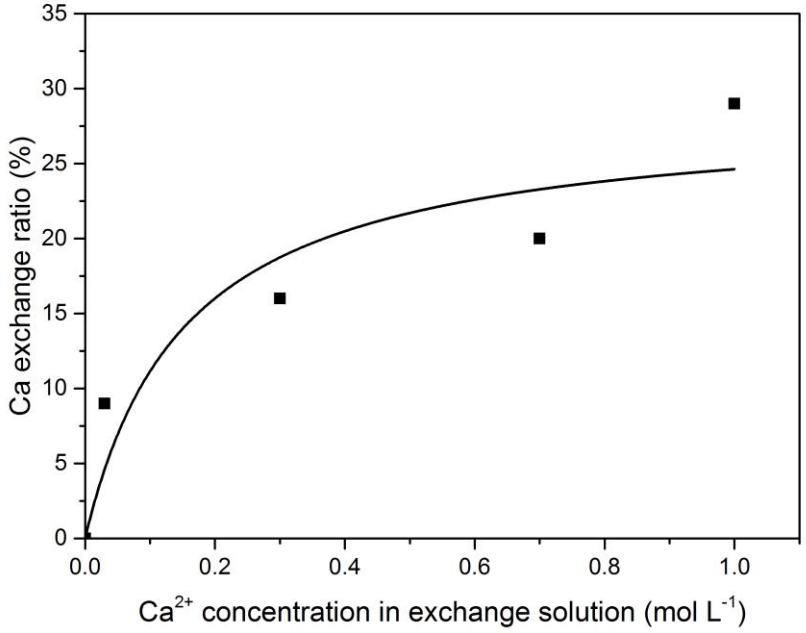


**Figure C1**. Calcium exchange ratio in the zeolite along different $Ca^{2+}$ concentration in the exchanging solution

**Table C1**. Calcium ion-exchange ratio

| Sample | Concentration of $Ca^{2+}$ in solution | Ca (wt%)[a] | Exchange ratio (%) |
|---|---|---|---|
| Ca(0) | 0 | 0 | 0 |
| Ca(8) | 0.03 | 0.22 | 9 |
| Ca(16) | 0.3 | 0.43 | 16 |
| Ca(20) | 0.7 | 0.54 | 20 |
| Ca(29) | 1 | 0.78 | 29 |

a) Obtained by ICP

b) Fitted function exchange ratio (%) = $29*C_{Ca2+}/(0.24+C_{ca2+})$

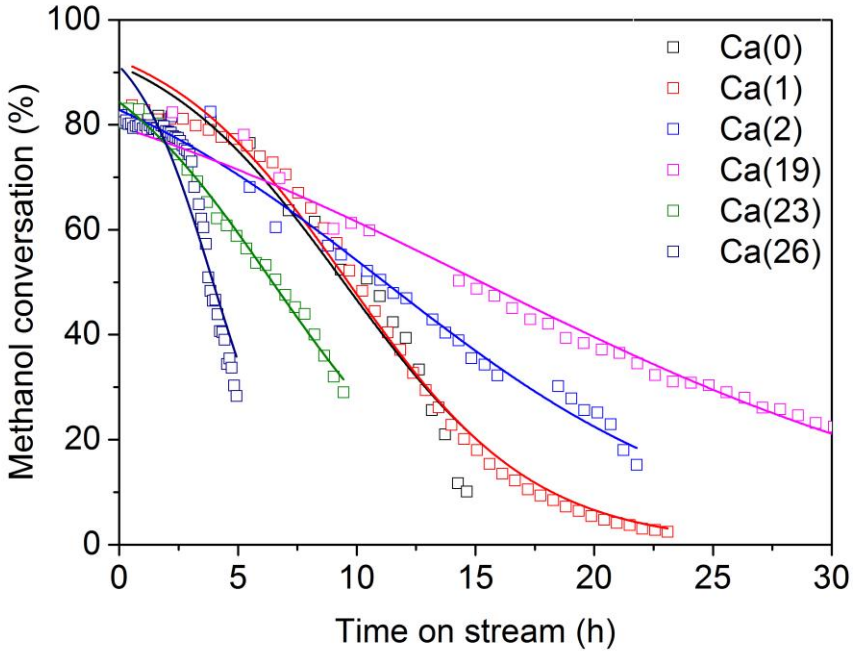


**Figure C2**. Comparison of the calculated methanol conversion (solid line) with measured methanol conversion (open symbols) with time on stream over Ca ion-exchanged ZSM-5 catalysts at 370 $^{o}$C and 4 bar

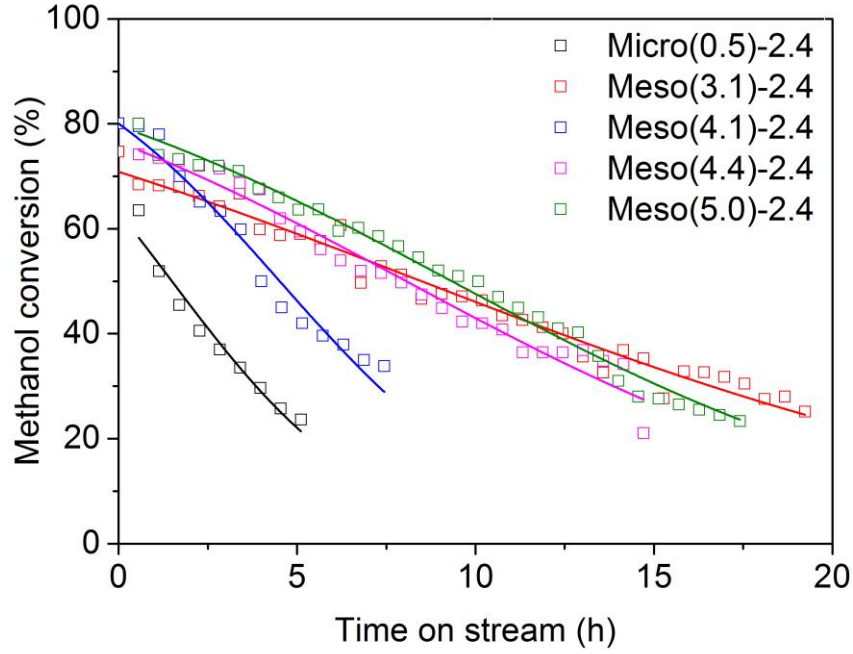


**Figure C3**. Comparison of the calculated methanol conversion (solid line) with measured methanol conversion (open symbols) with time on stream over desilicated ZSM-5 catalysts at 370 $^{o}$C and 4 bar